Measurement of Polarisation Observables for a circularly polarised Photon Beam and a transversally polarised Target in the Photoproduction of Neutral Pion Pairs off the Proton

Inauguraldissertation

zur
Erlangung der Würde eines Doktors der Philosophie
vorgelegt der
Philosophisch-Naturwissenschaftlichen Fakultät
der Universität Basel

von

Stefanie Nicole Garni

aus Lörrach, Deutschland

Basel, 2017

Genehmigt von der Philosophisch-Naturwissenschaftlichen Fakultät
auf Antrag von

Prof. Dr. B. Krusche
Prof. Dr. M. Ostrick

Basel, den 21.02.2017

Prof. Dr. Martin Spiess
Dekan

Abstract

The inner structure of nucleons and thus the fundamental interaction between the constituents, the quarks, can be investigated by means of the hadron spectroscopy. On the basis of the hadron spectroscopy, the different excitation states of the proton, the so-called resonances, can be determined, and thus also the possible degrees of freedom. Since the degrees of freedom determine the number of excited states, conclusions can then be done about the structure of the nucleons. However, the previously measured excitation spectrum of the proton cannot yet be fully described with the theoretical predictions of the quark models or the lattice gauge theories. Significantly more resonances are predicted at higher energies which so far could not be found in the experiments. This phenomenon is known as the problem of the $missing\,resonances$. But so far it is unclear, if these discrepancies are caused by assumed degrees of freedom in the theoretical models which are not realisable in nature or from the experimental bias. Due to their low lifetime, the different resonances of the excitation spectrum overlap and are difficult to identify.

Through the polarisation observable measurements, the individual resonance contributions can be identified more easily because they are more sensitive to interference terms and therefore also to the weak resonance contributions. For this purpose the polarisation observable for the double π^0 photoproduction off the free proton were analysed. The double π^0 photoproduction is one of the most interesting reaction for the measurement of these observables. It allows to search for excited nucleon states which decay preferentially via cascades involving intermediate excited states. Furthermore, the background of non-resonant terms is small since the photon does not couple directly to neutral pions.

The measurement of the double polarisation observable F and the single polarisation observable T were performed at the MAMI tagged photon facility in Mainz, Germany, using circularly polarised bremsstrahlung photons with incident energies from 450 up to 1450 MeV and a transversally polarised butanol target. The double π^0 reaction was identified using a combined setup of the Crystal Ball calorimeter and a TAPS forward wall and additionally the PID and the MWPCs for the charged particle tracking, which results in an almost 4π acceptance.

The polarisation observables were extracted from the data sets by the use of two different methods, the carbon subtraction method and the hydrogen normalisation method. It could be shown that the polarisation observable results for both methods are consistent. In order to check possible systematic uncertainties from the measurement with butanol targets also the absolutely normalised unpolarised cross sections were extracted and composed to results from measurements with liquid hydrogen

targets.

The experimental results were measured for further studies of the partial wave content of the double pion photoproduction in the second and third resonance regions. Therefore, the measured polarisation observables are compared to two different predictions of partial waves analysis, the isobar MAID model and the Bonn-Gatchina partial wave analysis. The measured results show distinct differences to the predictions and deliver new information for partial wave analysis.

Acknowledgements

I would like to thank Prof. Dr. Bernd Krusche who gave me the opportunity to work in his research group and letting me grow as a research scientist. This work was only possible with his supervision and support. I would also like to thank Prof. Dr. Michael Ostrick for his support and for serving as my co-referrer.
Special thanks to Victor Kashevarov for his support and the many helpful discussions. I must also thank Natalie Walford who has been everything I could wish for in a Post-Doc. I would also like to thank Susanna Constanza for her help with the MWPCs, especially for the calibration. Thanks to Philippe Martel for all the helpful discussions. Special thanks go also to the theorists Aleksandr I. Fiks and Victor Nikonov for their fast respond and the calculation of the theoretical models corresponding to my calculations. I would also like to thank Pier Paolo Bortoluzzi for the helpful programming advice.
Finally, to my friends and family, thank you for your patience and supporting me through this entire process.

Contents

1 Introduction

In this chapter, an introduction of the structure of the nucleon and the underlying theory for the measurement of the polarisation observables F and T will be given. An overview of the current experimental results and theoretical knowledge of the structure of the nucleon and the excitation spectrum is shown in Section 1.1.1. The differences of the nucleon excitation spectrum between the measured experimental results and the predictions of the quark model and lattice Quantum Chromodynamics (QCD) will be discussed in Section 1.1.1. Section 1.2 introduces the formalism to describe the double π^0 reaction in the context of kinematical consideration and the different amplitude representations. In Section 1.3, the formalism and the idea for the measurement of the polarisation observables are discussed. In Section 1.4.1, the used models will be described. In the last Section 1.5 the current results of the double π^0 reaction channel will be shown.

1.1 The Structure of the Nucleon

Protons and neutrons referred to as nucleons are the basic elements of the atomic nuclei. The proton, the only stable hadron and the lightest baryon, was identified around 1919 experimentally by Ernest Rutherford [1] as a constituent of atomic nuclei. Ernest Rutherford was also the first person who recognized that atoms have small cores with positive charge and formulated the Rutherford atom model on the basis of his scattering experiments [1]. In the 1932, existence of the neutron as a neutral nuclear particle was experimentally confirmed by James Chadwick [2].
The first evidence of the substructure of the nucleons was given by the measurement of the magnetic moment in 1933 by R. Frisch and O.Stern [3]. Their measurements of the magnetic moment of the nucleons disagree with the prediction of a structure-less spin $1/2$ particles. It has been shown that the proton has a different than expected magnetic moment as the electron of $\mu_N = e\hbar/2m_pc$, where e is the electron charge, $\hbar$ is the reduced Planck constant, m_p is the proton mass, and c is the speed of light. No magnetic moment was ever expected for the neutron. Therefore, the measured magnetic moments of the proton $\mu_p = 2.792\ \mu_N$ and of the neutron $\mu_n = -1.913\ \mu_N$ are in contradiction to point-like particles.
The electron scattering experiments in the 1950 by Hofstadter et al. [4] confirmed the existence of the substructure of the protons. The measured cross section of the

proton was not compatible with a point-like particle and a charge radius for the proton of $\sqrt{\langle r_p^2 \rangle} = 0.74$ fm could be extracted.
Until today, the nucleon properties based on the composition of the quarks and gluons and their interaction are not well understood. Therefore, the current tasks of nuclear physics is the understanding of the inner structure of the nucleons by means of experiments and the explanation of the measured results by models.

1.1.1 Nucleon Resonances

For the nucleon, a similar system of excited states for different energy levels as the atom can be observed. In the atom, the transition between the different excitation states are given by the emission and absorption of photons, the quantum field of the electromagnetic field [5]. In atomic spectroscopy, the emitted photons with defined energies from the excited atom can be investigated as emission lines and information about the electromagnetic interaction between the nucleons and the atomic electron shell of an atom can be obtained. For the atom, the masses of the involved elementary particles are essentially larger than the energy distances in between the levels and thus, atom spectroscopy shows discrete emission lines, which can be assigned to different excitation states. For the nucleon, the situation is much more complicated since the energy distances of the different excited states are on the order of magnitude of the masses from the involved constituents. For the nucleon, the transitions in the excitation spectra involve the emission of mesons by the strong interaction. For hadron spectroscopy, baryons are excited by means of high energy projectiles such as photons or pions and the final states were then investigated. Through this information over the inner construction of the nucleons, the proton and the neutron and the nature of the interaction between the constituents can be studied.
Whereas in the absorption spectrum of the atom, sharp absorption lines corresponding to certain energies are visible, can only a few broad peaks at low energies be recognized in the excitation spectrum of the proton or neutron. These peaks correspond to nucleon resonances which can be assigned to single particles with defined quantum numbers such as the spin, isospin, peak widths, and masses. Since the dominant decay channel of nucleon resonances is defined by the hadronic decay via the emission of mesons, the excited states have a very short lifetime of $\tau \approx 10^{-24}$s and the spacing of the resonance peaks is either more than 10 MeV [6]. Therefore, the resonance peaks have a large overlap especially in the high energy ranges where the level density of the excited states is larger. This makes it difficult to identify and investigate the individual states, as demonstrated in the total photoabsorption cross section shown in Fig. 1.1. It can be seen that decay modes involving different mesons make different constitutions to the total photoabsorption, thus carrying complementary information about the excitation of nucleon resonances. In general,

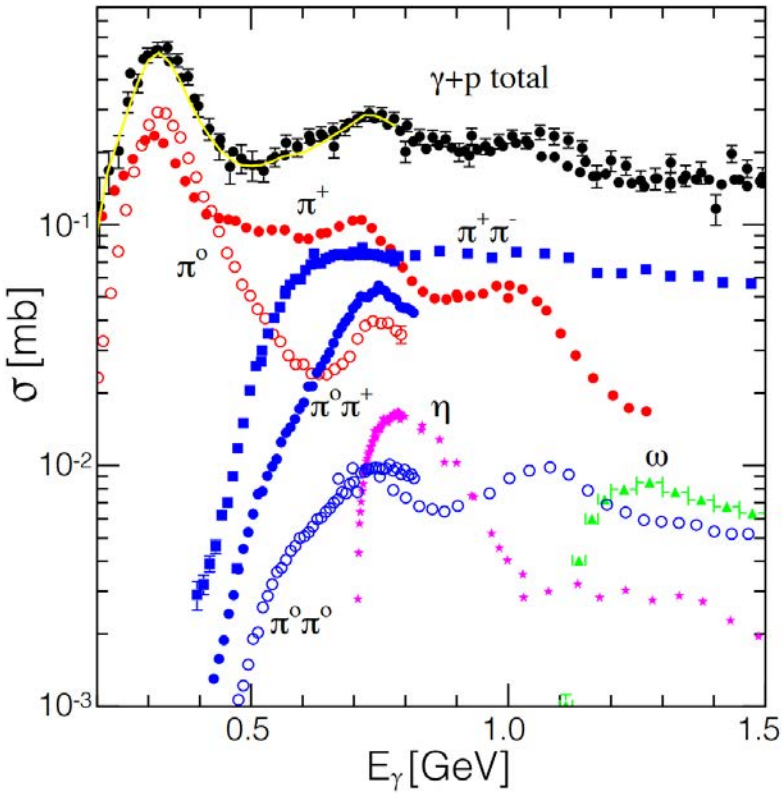

Figure 1.1.: Total photoabsorption cross section for the free proton and contributions from different meson final states. Figure taken from [7].

nucleon resonances cannot be simply identified as resonance bumps in total cross sections. This is only the case in a few exceptional cases as the $\Delta(1232)$ in pion production or the $S_{11}(1535)$ in η-production [6]. Identification of the overlapping resonances at higher energies requires detailed studies of angular distributions and polarisation observables.

The low energy excitation schema of the nucleon with the dominating transition, the hadronic decay via the emission of mesons is summarized in Fig. 1.2. The excited states of the nucleon are divided in isospin $I = 1/2$ referred to as N^*-resonances and isospin $I = 3/2$ states referred to as Δ-resonances. For the nucleon resonances, the following notation is used [6]:

$$L_{2I2J}(W), \tag{1.1}$$

where L is the orbital angular momentum from the decay of the resonance from the corresponding nucleon-meson pair, I is the isospin, and J is the spin of the resonances, respectively, and W is the mass of the resonance in MeV/c^2. The orbital angular momentum L is generally given in the spectroscopically notation as $S, P, D, ...$

The photoproduction of the double π^0 mesons allows for the investigation of sequential and direct decay of resonances. In the sequential decay of the resonances, the

excited nucleon state decays in a first step into the intermediate nucleon excited state via the emission of a first pion and then back into the nucleon ground state via the emission of a second pion. The sequential decay channel over the Δ resonance $\gamma p \rightarrow N^*, \Delta \rightarrow \Delta(1232) \rightarrow p\pi^0\pi^0$ is allowed for all higher lying resonances and allows the study of the sequential resonance-resonance decays. For the direct decay of the resonance, the excited nucleon state decays into two pions to the nucleon ground state. For the direct decay of $\gamma p \rightarrow P_{11}(1440) \rightarrow p(\pi^0\pi^0)_s^{I=0}$, the two final state pions are correlated in a relative s-wave [8]. This direct decay channel is the only one of this kind which is allowed in the second resonance region for the photoproduction of two π^0 mesons. The direct decay over the ρ meson only contributes to the charged pion channels, since the ρ meson cannot decay into two neutral pions.

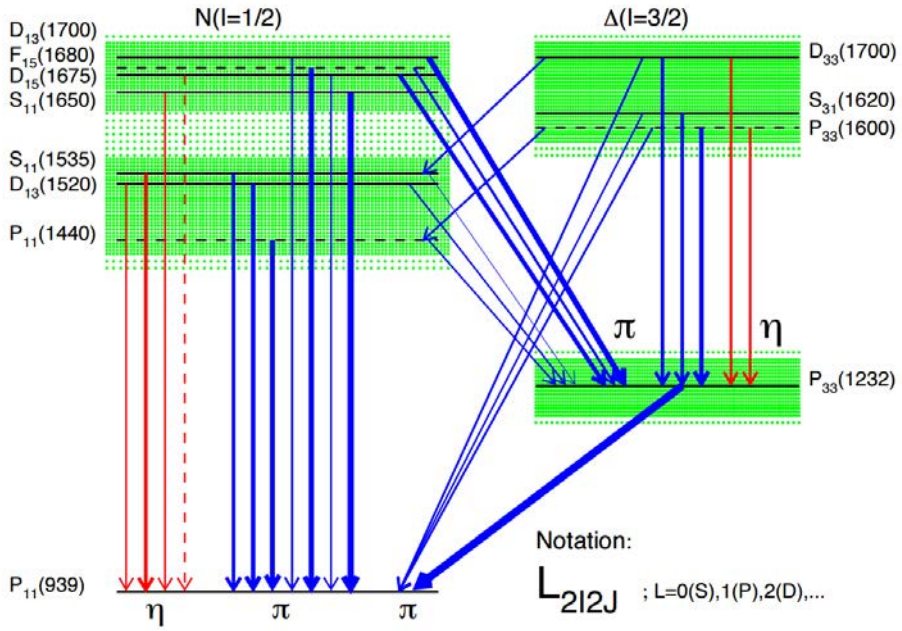

Figure 1.2.: Low lying excited states of the nucleon and the shown decay modes via the emission of mesons. The solid red arrows indicate the decays via pion emission and η-emission is shown by the red lines with isospin $I = 1/2$ on the left hand side and isospin $I = 3/2$ on the right hand side. Figure taken from [9].

1.1.2 Description of Models

Hadron spectroscopy provides an experimental possibility to get more information of the inner structure of the nucleons and the strong interaction between the involved constituents. However, the perturbative calculations of the underlying theory of the strong interaction of the QCD can only be calculated and compared with the experimental results for small distances of $r \ll 1$ fm between the quarks. The distances are the so called "asymptotic freedom" as the quarks can move quasi freely

[10]. For greater distances of $r \geq 1fm$, the potential between the quarks increases. This effect is denoted as the "confinement" and cannot be described by perturbative calculations of QCD. This can be seen in Fig. 1.3 by the large coupling constants α_s for the strong interaction of QCD. For these cases, only phenomenological models such as quark models and numerical solutions of QCD formulated in lattice gauge theory exists. The quark model and lattice gauge theory will be explained in the following sections.

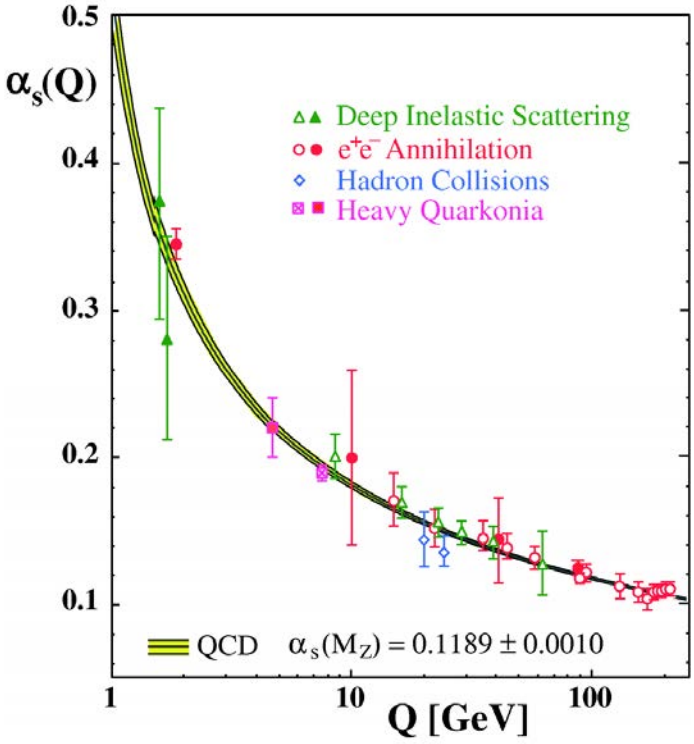

Figure 1.3.: Summary of the measurement results of the coupling constant α_s as a function of the energy scale Q. The open symbols indicate next-to-leading order QCD calculations and the closed symbols indicate the next-to-next-to-leading order QCD calculations. The yellow curves are the QCD predictions for the combined world average values of the coupling constants α_s for the strong interaction of the energy scale $Q = M_{Z^0}$ defined by the mass of the Z^0 boson. Figure taken from [11].

Quark Models

The quark models are used to predict the masses and the quantum numbers of the different resonances. The most basic version of the quark model was originally proposed by Murray Gell-Mann [12], [13] and George Zweig [14] in the 1960s. They suggested quarks as the fundamental components of mesons and baryons, whereby mesons are compound of a quark-antiquark pair $(q\bar{q})$ and baryons of three quarks (qqq). Therefore, the three varieties of quarks were introduced, the up (u), down (d) and strange (s) quarks with spin $1/2$ and the electric charge of $+2/3$ for the up

quark, $-1/3$ for the down quark, and $-1/3$ for the strange quark. The three lightest quarks defined by Gell-Mann and additional quarks of the Standard Model of particle physics are shown in Table 1.1. In their quark model, they arranged these bound

Generation	Name	Symbol	Charge	Flavour	Hypercharge	Mass (MeV)
1	Up	u	$+2/3$	$l_Z = +1/2$	$1/3$	$2.3^{+0.7}_{-0.5}$
	Down	d	$-1/3$	$l_Z = -1/2$	$1/3$	$4.8^{+0.5}_{-0.3}$
2	Charm	c	$+2/3$	$C = +1$	$4/3$	1275 ± 25
	Strange	s	$-1/3$	$S = -1$	$-2/3$	95 ± 5
3	Top	t	$+2/3$	$T = +1/2$	$4/3$	173070 ± 890
	Bottom	b	$-1/3$	$B' = -1$	$-2/3$	4180 ± 30

Table 1.1.: Three generations of the grouped quarks. Table taken from [15].

quark systems of the mesons and baryons into the so called hadrons in a multiplet structure by using the representation of the Lie group $SU(3)$. With this quark model by Gell-Mann and Zweig, all the known particles could be classified and the existence of the Ω^- particle could be predicted by the quantum number arrangement of the baryon-$3/2$ decupled. When the Ω^- particle was then experimentally discovered in 1964, the quark model gained acceptance. From the arrangement of the leptons at that time, Sheldon Glashow and James Bjorken concluded that the quarks must have the same arrangement and postulated the existence of a fourth quark, the charm quark with electrical charge of $-1/3$, which was discovered much later. O.W. Greenberg [16], M.Y. Han, and Yoichiro Namu [17] introduced the quark property, the color charge with the classification of red (r), blue (b) and green (g) in 1965. The introduction of the color charge solved the problem of an additional quantum number with the symmetric wave function of the Δ^{++} particle, which offends the Pauli principle.

In $1968 - 69$ at the Standford Linear Accelerator (SLAC), it was discovered that the electrons, which were scattered on protons are rebound on point like constituents inside the proton. Based on this experimental result, James Bjorken and Richard P. Feynamn [18] concluded that the proton consists of spin $1/2$-particles, which they called partons. The existence of these patrons can be explained by the scaling of the deep inelastic scattering cross sections, which were derived from J. Bjorken and E. Paschos [19] from the current theory. The Bjorken-Scaling theory was confirmed in 1969 by the experiment of Jerome I. Friedman, Henry W. Kendall, and Richard E. Taylor [20] and since then, it was clear that the so called patrons were quarks.

In 1973, the quantum field theory for the strong interaction based on the theory of the quarks and gluons was formulated. This quantum field theory has the same underlying theory as the quantum electrodynamics (QED), but is called QCD because of the additional consideration of the color charge. David Politzer, David Gross, and Frank Wilczek [21],[22] explained the asymptotic freedom of the strong interaction. Based on this asymptotic freedom, the small forces between the quarks can be

explained at large momentum transfers. In the standard model of the elementary particles, the strong, weak, and electromagnetic interactions between all the known elementary particles are described by quantum field theories.

For the understanding of the nucleon structure, the relevant effective degrees-of-freedom which reflect the internal symmetries of the underlying fundamental interaction have to be identified. Therefore, a constituent quark model based on a harmonic oscillator potential was introduced for the determination of the effective degrees-of-freedom of the nucleon by Gell-Mann [13], Greenberg [23], Darlitz [24], and collaborators. For the description of the quark model, it is assumed that the nucleon consists of three equivalent constituent quarks bound in a collective potential. On the basis of this model, the masses of the ground state baryons could be explained, but not the excited states of the baryons. Further non-relativistic harmonic models were developed by Greenberg [16], Darlitz [24], Fairmann and Hendry [25] for the theoretical explanation of the nucleon excited states. The first assumption was that in addition to the collective potential, a gluon exchange between the quarks is possible. The calculation of the strong coupling constant from the hyperfine structure and the first nucleon excited state, the Δ resonance shows that the assumption of the additional gluon exchange between the quarks leads only to a strong simplification of the fine splitting and the excited states of the baryons could not be explained. The model of Isgur and Karl [26] is based on the spin-spin interactions. As a result of the large contribution of the spin-spin interactions, the spin-orbit interactions are then less important. With this model, the baryon spectra has been described for the very first time and predictions about resonances could be made.

The number of excited states are determined by the degrees of freedom of the nucleons and are given by their residual quark-quark interaction. Therefore, the degrees of freedom can be increased by the consideration of different interaction models of the quark. For the quark-diquark model, a closely bound diquark-cluster plus one free quark is assumed, which leads to fewer excited states. In the flux tube model, the three constituent quarks and flux tubes are excited. This description leads to much more excited states. The relativistic quark model by Löring, Metsch and Petry [27] is based on the flux tube definitions, whereby the confinement is a linearly rising three-body string potential. The interaction between the quarks is described by instanton interactions and therefore, the quarks are bound in the baryon by a linear increasing potential. The predictions of the quark model of Löring, Metsch and Petry and the measured results of the nucleon resonances for the different orbital angular momentum and parities are shown in Fig. 1.4. Plotted are the calculated resonance masses shown by the blue lines against the measured resonance mass, shown by the red and green lines for different spins and parities. The wide range of the measured resonance masses is indicated by the colored bar for the different experimental resonance masses. It can be seen that the theoretical predictions only in the low energy range match in a good approximation. However, for higher lying energies,

discrepancies occur and much more resonances are predicted by the quark model than were measured. This is known as the problem of the missing resonances.

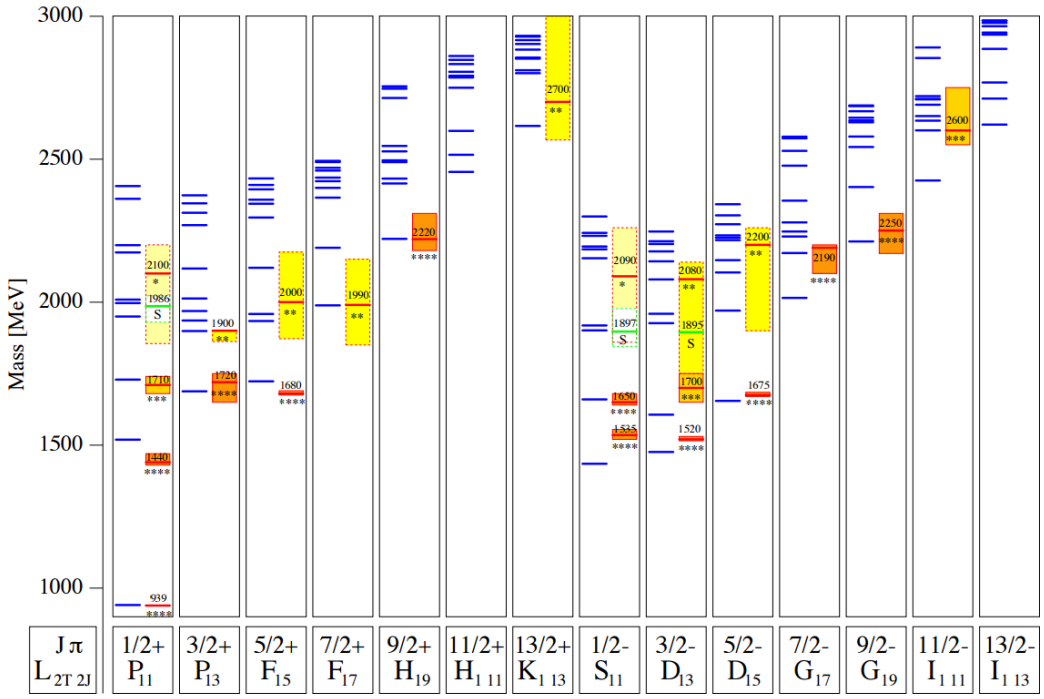

Figure 1.4.: Definition of the nucleon resonances after Löring, Metsch and Petry [27]. Plotted are the calculated resonance masses shown by the blue lines against the measured resonance masses shown by the red and green lines for different spins and parities. The measurement uncertainties are shown by the high of the colored bar for the different experimental resonance masses. Figure taken from [27].

Lattice QCD

In addition to the quark model, the calculation of the lattice gauge theory, lattice QCD, can also be used as an underlying theory for the prediction of the excitation spectra and the corresponding resonances of the nucleons. Lattice gauge theories are essentially non-perturbative numerical methods to solve the quantum field theory of QCD [5]. In the basis of the lattice gauge theory, fundamental features of the lower energy nucleon spectrum for the strong interaction can be calculated. The mathematical description of the lattice gauge theories of discrete time and space points defined on a cubic lattice allows for calculations, which cannot be solved by perturbation theory. In the lattice gauge theory, the quarks are described as points on the four-dimensional lattice which interacts via gluons. Therefore, the degrees of freedom of the quarks are defined by the fields on the lattice points and the degree of freedom of the gluons is defined by the fields of the connection lines between the quarks. For the calculation of the physical properties of the quarks, QCD chance calculations are then used. In this calculation, the lattice distances and the masses

of the quarks are extrapolated (e.g. with chiral perturbation theory) to the physical point. The effective mass of the pions is usually used in these calculations. A specific nucleon excitation spectrum of the lattice gauge theory, extrapolated to a pion mass of $m_\pi = 396$ MeV by Edwards et. al. [28] is shown in Fig. 1.5. The prediction of the excited nucleon spectra of the lattice gauge theory has the same structure as the one obtained by the quark models, despite the pion mass used for the lattice QCD calculations was $m_\pi = 396$ MeV and not yet matched with the physical pion mass of $m_\pi = 134.9766$ [15]. Especially for the low-lying states of the N^* and Δ resonances, the lattice QCD and the quark model predicts the same pattern of states. The constituent quark models and the lattice QCD predict for the first excitation state of the N^* resonance with two negative parity states for $J = 1/2$ and $J = 3/2$ and one singlet state for $J = 5/2$ and no state for $J = 1/2$. Even for the second excited states of the N^* resonances with positive parity, the predictions of lattice QCD and the quark model show the same prediction pattern of four states with $J = 1/2$, five states with $J = 3/2$, three states with $J = 5/2$, and one state with $J = 7/2$. Due to the difference between the used pion mass and the physical pion mass, the obtained lattice QCD results could not be compared with the experimentally measured results. The results of lattice QCD are similar to the quark model and predict much more states at higher energies, which have not been observed experimentally.
In summary, the quark model and lattice QCD predict more resonances than experimentally found. The difference between the predicted and the measured resonances can appear through wrong assumptions in the quark models and in the lattice QCD or from the inadequate experimental measurements.

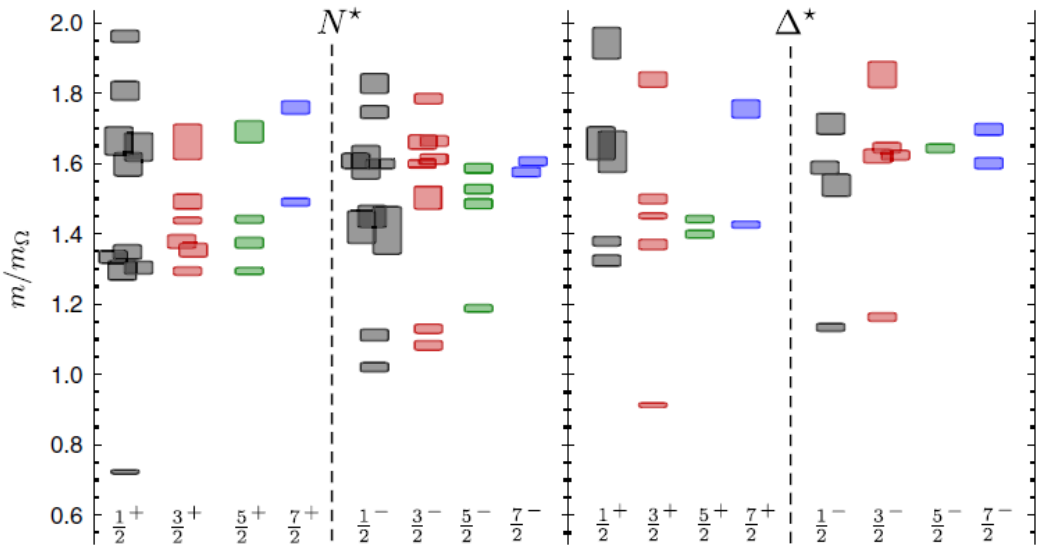

Figure 1.5.: Predictions of the N^* and Δ resonances from the lattice gauge theory by Edwards et. al. [28] at a pion mass of $m_\pi = 396$ MeV. Figure taken from [28].

1.2 Formalism of the Double π^0 Meson Photoproduction

In this section, the underlying formalism of the double π^0 meson photoproduction will be discussed. For the creation of the resonances of a certain reaction, multipole excitations are necessary, which will be discussed in Section 1.2.1. For the determination of the contributing resonances of reactions, amplitudes have to be generated from the multipoles. The generation of the CGLN amplitudes and the helicity amplitudes from the multipoles are discussed in Sections 1.2.3 and 1.2.4, respectively. In order to finally reconstruct the resonances from the measured amplitudes, partial wave analysis is necessary, which is discussed in more detail in Section 1.4.

1.2.1 Electromagnetic Multipoles

The excited states of the nucleon can be studied with the photoproduction of mesons. The nucleon is excited by the interaction with a high energy photon, forming a resonance, and decays back into the nucleon ground state via the emission of a meson. The process of the photoproduction of mesons via excitation of nucleon resonances is shown in Fig. 1.6 for the single π^0-photoproduction.

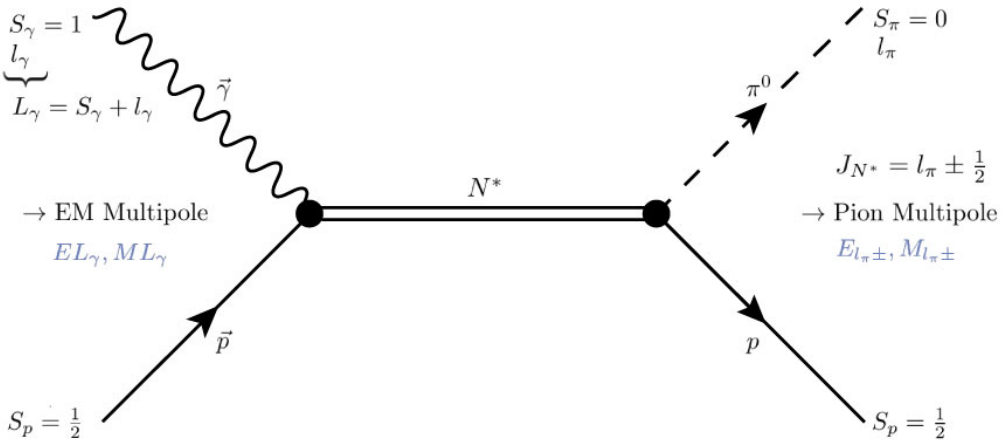

Figure 1.6.: Principle of the meson photoproduction with an intermediate nucleon resonance for the single π^0-photoproduction. Figure taken from [29].

The intermediate resonances can be defined by parity and angular momentum based on the multipole components of the initial and final states. The initial state is defined by a photon with parity P_γ and total angular momentum $\vec{L}_\gamma = \vec{l} + \vec{s}_\gamma$ given by the photon spin $\vec{s}_\gamma$ and the orbital angular momentum $\vec{l}$ relative to the target nucleon, and a nucleon with parity P_N. In the process, the photon with parity P_γ and total angular momentum $\vec{L}_\gamma$ couples electromagnetically to the nucleon with parity P_N

and nucleon spin $\vec{J}_N$ $(J = 1/2)$ and produces a resonance with parity P_{N^*} and spin $\vec{J_{N^*}}$. For the initial state and the intermediate resonance of the meson photoproduction process, the following selection rules obey [6]:

$$|L_\gamma - J_N| = |L_\gamma - \frac{1}{2}| \leq J_{N^*} \leq |L_\gamma + \frac{1}{2}| = |L_\gamma + J_N| \tag{1.2}$$

and

$$P_{N^*} = P_N \cdot P_\gamma = P_\gamma. \tag{1.3}$$

The resonance decays via the strong interaction to the nucleon ground state with the emission of a meson. For pseudoscalar mesons like pions the decay meson has spin $\vec{s}_{\pi^0}$ $(s = 0)$, parity P_{π^0}, and relative orbital angular momentum L_{π^0}. For the final state, the decay meson and the nucleon, the following selection rules have to be fulfilled [6]:

$$|L_{\pi^0} - J_N| = |L_{\pi^0} - \frac{1}{2}| \leq |J_{N^*}| \leq |L_{\pi^0} + \frac{1}{2}| = |L_{\pi^0} + J_N| \tag{1.4}$$

and

$$P_{N^*} = P_N \cdot P_{\pi^0} \cdot (-1)^{L_{\pi^0}} = (-1)^{L_{\pi^0}+1}. \tag{1.5}$$

Thus, the following condition applies by combining the selection rules of the initial and finals states, given by Equations 1.2 and 1.4 [6]:

$$L_\gamma \pm \frac{1}{2} = J_{N^*} = L_{\pi^0} \pm \frac{1}{2}, \tag{1.6}$$

where both $\pm$ signs are independent. Consequently, the parity conditions for the photoproduction process can be obtained by combing Equations 1.3 and 1.5 [6]:

$$P_\gamma = P_{N^*} = (-1)^{L_{\pi^0}+1}. \tag{1.7}$$

For the excitation of certain spin and parity states, electromagnetic multipole transition of the initial photon are necessary. Due to the parity and angular momentum conservation, two multipoles possibilities are allowed: electric multipoles (E_l) and magnetic multipole (M_l), whereby l stands for the total angular momentum of the incident photons. The difference between the two multipole types lies in the parity. For the electric multipoles, the parity is defined by $P_\gamma = (-1)^{L_\gamma}$, while for the magnetic multipoles, the parity is defined by $P_\gamma = (-1)^{L_\gamma+1}$ with the total angular

momentum of the photon L_γ. Therefore, the conditions of the electric and magnetic multipoles are given by [6]:

$$E_l : L = L_{\pi^0} \pm 1 \tag{1.8}$$

$$M_l : L = L_{\pi^0}, \tag{1.9}$$

where for pseudoscalar photoproduction the notation of $E_{l\pm}$ and $M_{l\pm}$ is used. $E_{l\pm}$ and $M_{l\pm}$ indicates whether the nucleon spin has to be added or subtracted from the orbital momentum $\vec{l}$ to obtain the total angular momentum J_{N^*} of the intermediate state. For the identification of the generated resonances, the contributing multipoles have to be clearly determined. An overview of the lowest order multipole amplitudes for the single π^0 peseudoscalar photoproduction is given in Table 1.2. Resonances with a total angular momentum of $J_{N^*} > 1/2$ can be generated by an electric and by a magnetic multipole.

photon M-pole	initial state (L^P_γ, J^P_N)	interm. state $J^P_{N^*}$	final state $(J^P_N, L^P_{\pi^0})$	multi-pole	$(k^*/q^*)d\sigma/d\Omega$
E1	$\left(1^-, \frac{1}{2}^+\right)$	$\frac{1}{2}^-$	$\left(\frac{1}{2}^+, 0^-\right)$	E_{0+}	$\lvert E_{0+}\rvert^2$
		$\frac{3}{2}^-$	$\left(\frac{1}{2}^+, 2^-\right)$	E_{2-}	$\frac{1}{2}\lvert E_{2-}\rvert^2\,(5-3x^2)$
M1	$\left(1^+, \frac{1}{2}^+\right)$	$\frac{1}{2}^+$	$\left(\frac{1}{2}^+, 1^+\right)$	M_{1-}	$\lvert M_{1-}\rvert^2$
		$\frac{3}{2}^+$	$\left(\frac{1}{2}^+, 1^+\right)$	M_{1+}	$\frac{1}{2}\lvert M_{1+}\rvert^2\,(5-3x^2)$
E2	$\left(2^+, \frac{1}{2}^+\right)$	$\frac{3}{2}^+$	$\left(\frac{1}{2}^+, 1^+\right)$	E_{1+}	$\frac{9}{2}\lvert E_{1+}\rvert^2\,(1+x^2)$
		$\frac{5}{2}^+$	$\left(\frac{1}{2}^+, 3^+\right)$	E_{3-}	$\frac{9}{2}\lvert E_{3-}\rvert^2\,(1+6x^2-5x^4)$
M2	$\left(2^-, \frac{1}{2}^+\right)$	$\frac{3}{2}^-$	$\left(\frac{1}{2}^+, 2^-\right)$	M_{2-}	$\frac{9}{2}\lvert M_{2-}\rvert^2\,(1+x^2)$
		$\frac{5}{2}^-$	$\left(\frac{1}{2}^+, 2^-\right)$	M_{2+}	$\frac{9}{2}\lvert M_{2+}\rvert^2\,(1+6x^2-5x^4)$

Table 1.2.: Lowest order electromagnetic multipole amplitudes for pseudoscalar meson photoproduction. Figure taken from [6].

1.2.2 Amplitude Representation

As mentioned before, the multipole can be summarized in amplitudes represented of CGLN amplitudes or in helicity amplitudes. These two representations of the multipole amplitudes will be discussed in the next sections.
The differential cross section is defined by the quadratic scattering amplitude $f(\theta)$ as [30]:

$$\frac{d\sigma}{d\Omega} = |f(\theta)|^2. \tag{1.10}$$

The scattering amplitude is described as a vector in the complex plane, whereby the angle dependence can be described by Legendre polynomials. By reference to the

angle dependence, given by the Legendre polynomials P_l, the scattering amplitude can be written as the sum of the different partial waves f_l [30]:

$$f(\theta) = \sum_{l=0}^{\infty}(2l+1)f_l P_l\left(\cos(\theta)\right), \tag{1.11}$$

where l is defined by the different angular momentums. The representation of the scattering amplitude in the different partial waves of certain angular momentum is defined as partial wave analysis (PWA).
For the photoproduction of pseudoscaler mesons, the cross section can be expressed in terms of the scattering matrix $\mathcal{F}$ of the eigen states of the Pauli spin operators of the initial state m_i and the final state m_f of the reaction as [31]:

$$\frac{d\sigma}{d\Omega} = \frac{q}{k}|\langle m_f|\mathcal{F}|m_i\rangle|, \tag{1.12}$$

where k and q are the contribution of the momentum of the incoming, and outgoing meson in the centre of mass system, respectively. The Lorentz and gauge invariant scattering matrix element $\mathcal{F}$ contains all the information of the scattering processes and can be expressed for different amplitude representations.

1.2.3 CGLN-Amplitudes

The matrix element $\mathcal{F}$ for the photoproduction of pseudoscalar mesons in the representation of the Chew-Goldberger-Nambu-Low (CGNL) [32] parametrisation is given by:

$$\mathcal{F} = iF_1 \cdot \vec{\sigma} \cdot \vec{\epsilon} + F_2(\vec{\sigma}\cdot\vec{q})(\vec{\vec{\sigma}}\cdot(\vec{k}\times\vec{\epsilon})) + iF_3(\vec{\sigma}\cdot\vec{k})(\vec{q}\cdot\vec{\epsilon}) + iF_4(\vec{\sigma}\cdot\vec{q})(\vec{q}\cdot\vec{\epsilon}), \tag{1.13}$$

where F is a two-dimensional matrix with the unity vectors $\hat{k} = \vec{k}/|\vec{k}|$ and $\hat{q} = \vec{q}/|\vec{q}|$ of the incoming and outgoing meson, $\vec{\epsilon}$ is the polarisation vector of a real photon with $\pm$ helicity, and $\vec{\sigma} = (\sigma_x, \sigma_y, \sigma_z)$ are the Pauli matrices [33]. The Pauli matrices $\vec{\sigma}$ for the nucleon spin are given by:

$$\sigma_x = \begin{pmatrix} 0 & 1 \\ 1 & 0 \end{pmatrix}, \quad \sigma_y = \begin{pmatrix} 0 & -i \\ i & 0 \end{pmatrix}, \quad \sigma_z = \begin{pmatrix} 1 & 0 \\ 0 & -1 \end{pmatrix} \tag{1.14}$$

The four complex CGLN amplitudes F_1, F_2, F_3, and F_4 are structure functions which contain all the information of the energy W and the polar angle θ dependence of the meson in the centre of mass.

The unpolarised differential cross section in the parametrisation of the CGLN amplitudes can written as [32]:

$$\begin{aligned}\frac{k^*}{q^*}\frac{d\sigma}{d\Omega} &= [|F_1|^2 + |F_2|^2 + \frac{1}{2}|F_3|^2 + \frac{1}{2}|F_4|^2 + \mathrm{Re}(F_1F_3^*)] \\ &+ [\mathrm{Re}(F_3F_4^*) - 2\,\mathrm{Re}(F_1F_2^*)]\cos(\theta^*) \\ &- [\frac{1}{2}|F_3|^2 + \frac{1}{2}|F_4|^2\,\mathrm{Re}(F_1F_4^*) + \mathrm{Re}(F_2F_3^*)]\cos^2(\theta^*) \\ &- [\mathrm{Re}(F_3F_4^*)]\cos^3(\theta^*).\end{aligned} \tag{1.15}$$

The CGLN amplitudes can be expanded in angle dependent terms of derivatives of the Legendre polynomials $P_l'(z)$ and $P"_l(z)$ with $z = \cos(\theta)$ and the energy dependent magnetic $M_{l\pm}$ and electric $E_{l\pm}$ multipole amplitudes as [32]:

$$F_1(W,\theta) = \sum_{l=0}^{\infty}[lM_{l+} + E_{l+}]P'_{l+1}(\cos(\theta^*)) + [(l+1)M_{l-} + E_{l-}]P'_{l-1}(\cos(\theta)) \tag{1.16}$$

$$F_2(W,\theta) = \sum_{l=0}^{\infty}[(l+1)M_{l+} + lM_{l-}]P'_l(cos(\theta^*)) \tag{1.17}$$

$$F_3(W,\theta) = \sum_{l=0}^{\infty}[E_{l+} - M_{l+}]P"_{l+1}(\cos(\theta^*)) + [E_{l-} - M_{l-}]P"_{l-1}(\cos(\theta^*)) \tag{1.18}$$

$$F_4(W,\theta) = \sum_{l=0}^{\infty}[M_{l+} - E_{l+} - M_{l-} - E_{l-}]P"_{l-1}(cos(\theta^*)). \tag{1.19}$$

For the determination of the multipoles $E_{l\pm}$ and $M_{l\pm}$, the four complex structure functions F_i for the reaction over the complete energy and angle range has to be defined. The spin and parity information of the resonance can then be determined by the multipole expansion.

1.2.4 Helicity Amplitudes

Another representation of the matrix element $\mathcal{F}$ is the parametrisation in terms of the helicity of the initial and final state. For circular polarised photons with positive and negative helicity, the matrix element is defined in spherical components as [34]:

$$F_\pm = \pm\frac{1}{\sqrt{2}}(F_x \pm iF_y) \quad \text{and} \quad F_0 = F_z, \tag{1.20}$$

where the scattering plane lies in the $x-z$ plane and thus, F_z is not defined for photoproduction. The matrix element for linear polarised photons can be described by:

$$F_\pm = F_x\cos(\phi_\gamma) + F_y\sin(\phi_\gamma), \tag{1.21}$$

where ϕ_γ defines the polarisation direction of the photons. The four helicity amplitudes H_1, H_2, H_3, and H_4 [35] define the components of the operators F and can be written as two dimensional matrices as:

$$F_+ = \begin{pmatrix} H_1 & H_2 \\ H_3 & H_4, \end{pmatrix}, \quad F_- = \begin{pmatrix} H_4 & -H_3 \\ -H_2 & H_1 \end{pmatrix}, \tag{1.22}$$

where H_1 and H_2 represent helicity amplitudes with a spin flip, where the initial photon and nucleon spin are arranged parallel or antiparallel, respectively, H_2 represents the helicity amplitude without a spin-flip and H_3 represents the helicity amplitude with a double spin flip. The helicity amplitudes can also be expressed in the CGLN amplitude representation as [35]:

$$H_1 = -\frac{1}{\sqrt{2}} \sin\theta (F_3 + F_4 \cos\theta), \tag{1.23}$$

$$H_2 = -\frac{1}{\sqrt{2}} (2F_1 - 2F_2 \cos\theta + F_4 \sin^2\theta), \tag{1.24}$$

$$H_3 = -\frac{1}{\sqrt{2}} (F_4 \sin^2\theta), \tag{1.25}$$

$$H_4 = \frac{1}{\sqrt{2}} \sin\theta (2F_2 + F_3 + F_4 \cos\theta). \tag{1.26}$$

The cross section can therefore be represented by the helicity amplitudes in the following form [35]:

$$\frac{d\sigma}{d\Omega} = \frac{1}{2}\frac{q}{k} \sum_{i=1}^{4} |H_i|^2, \tag{1.27}$$

where q is the momenta of the meson and k is the momenta of the photon.

1.3 Polarisation Observables

In this section the formalism of the polarisation observables will be discussed. Since the photoproduction of pseudoscalar meson pairs of nucleons is much more complex than for the single pseudoscalar meson photoproduction, in this section, the formalism of the polarisation observables of the later will be discussed first. The formalism of the double pseudoscalar meson photoproduction contains more complex amplitudes than the single pseudoscalar meson photoproduction and thus more polarisation observables are required to obtain the full information of the amplitudes.

1.3.1 Single Pseudoscalar Meson Photoproduction

Cross sections, as shown in the previous Section, are defined as the sum of squares of amplitudes, which is obvious in the helicity representation. Therefore, the cross section is dominated by high amplitudes and the contribution of the small amplitudes are supressed. For that reason, contribution of the small amplitudes cannot be determined from the cross sections. The measurement of the polarisation observables allows the determination of the small amplitudes. Since the polarisation observables are given by the product of different amplitudes, even small amplitudes have an impact on the high ones and thus can be easier determined.
For the single pseudoscalar meson photoprodction polarisation observables are defined for the different polarisation of the photon beam, target and recoil nucleon. For photoproduction, the photon beam can be linearly or circularly polarised. For linearly polarised photons, the electric field vector is always in a plane perpendicular to the propagation direction. For circularly polarised photons, the same amplitude of two wave planes is shifted by $\pi/2$ difference in phase. Therefore, the electric field vector is rotating around the propagation axis. The target nucleon can be polarised in three different directions defined by (x, y, z). Similarly the recoil nucleon can be polarised in three directions $((x', y', z'))$. The used coordinate system for the definition of the polarisation observables for the single pseudoscalar meson photoproduction with the different polarisation definitions are shown in Fig. 1.7.

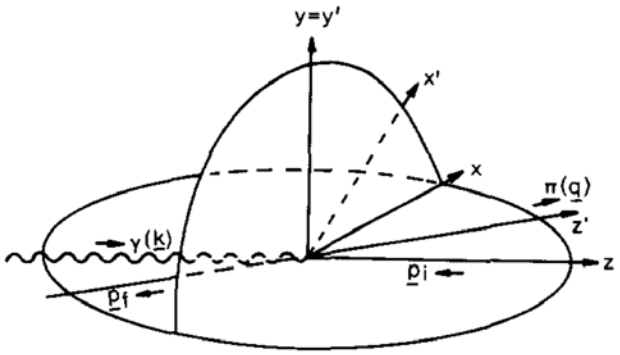

Figure 1.7.: Definition of the axis used for the determination of the polarisation observables: $x = y \times z$, $x' = y \times z'$, $y = k \times q/|k \times q|$, $y' = y$, $z = k/|k|$ and $z' = q/|q|$ whereby k defines the momentum of the incoming photon and q the outgoing meson momentum in the center of mass system. Figure taken from [36]

Due to the different polarisation possibilities, three single polarisation observables can be defined in addition to the unpolarised cross section σ: the beam asymmetry Σ, the target polarisation observable *T*, and the recoil polarisation observable *P*. The unpolarised angle dependent differential cross section $d\sigma/d\Omega$ and these polarisation observables are defined as the *S*-type of observables. Additionally to the *S*-type of observables, double polarisation observables can be measured in the pseudoscalar meson photoproduction, which are divided into three groups of four observables,

namely Beam-Target ($\mathcal{BT}$), Beam Recoil ($\mathcal{BR}$) and Target-Recoil ($\mathcal{TR}$) [36]. An overview of the different single and double polarisation observables of the single pseudoscaler meson photoproduction is shown in Table 1.3.

photon		target			recoil			target + recoil			
		x	y	z	$-$	$-$	$-$	x	z	x	z
		$-$	$-$	$-$	x'	y'	z'	x'	x'	z'	z'
-	σ	$-$	T	$-$	$-$	P	$-$	$T_{x'}$	$-L_{x'}$	$T_{z'}$	$L_{z'}$
linearly	Σ	H	$-P$	$-G$	$O_{x'}$	$-T$	$O_{z'}$	$-$	$-$	$-$	
circularly	-	F	$-$	$-E$	$-C_{x'}$	$-$	$-C_{z'}$	$-$	$-$	$-$	

Table 1.3.: Overview of the different single and double polarisation observables of the pseudoscaler meson photoproduction.

Thus in all, $2 \times 3 \times 3 = 18$ different polarisation observables can be defined by the different polarisation possibilities of the photon beam, the target nucleon, and the recoil nucleon. Since the 18 polarisation observables are not independent and through some combinations no additionally information can be obtained, the measurement of 12 double polarisation observables is enough. These double polarisation observables can be investigated by the following angle dependent cross sections [36].

Beam and Target Polarisation (Beam-Target ($\mathcal{BT}$))

The cross section with a linearly polarised photon beam and a polarised target can be written as:

$$\begin{aligned} \left.\frac{d\sigma}{dt}\right|_{pol} = \left.\frac{d\sigma}{dt}\right|_{unpol} \cdot \{1 &- P_T \Sigma \cos(2\phi) \\ &+ P_x[-P_T H \sin(2\phi) + P_{circ} F] \\ &- P_y[-T + P_T P \cos(2\phi)] \\ &- P_z[-P_T G \sin(2\phi) + P_{circ} E]\}, \end{aligned} \tag{1.28}$$

where P_T is the transverse polarisation degree of the photon beam, P_{circ} is the circular polarisation degree of the photon beam, and (P_x, P_y, P_z) is the direction of the target nucleons.

Beam- and Recoil Polarisation (Beam-Recoil ($\mathcal{BR}$))

The cross section for polarised photon beams and polarised recoil nucleons is given by:

$$\begin{aligned} p_f \left.\frac{d\sigma}{dt}\right|_{pol} = \left.\frac{d\sigma}{dt}\right|_{unpol} \cdot \{1 + \sigma_y P - P_T \cos(2\phi)(\Sigma + \sigma_y T) \\ - P_T \sin(2\phi)(O_x\sigma_x + O_z\sigma_z) \\ - P_{circ}(C_x\sigma_x + C_z\sigma_z)\}, \end{aligned} \tag{1.29}$$

where $(\sigma_x, \sigma_y, \sigma_z)$ describes the degree and direction of the recoil nucleon. The density matrix of the recoil nucleon including its polarisation degree P_f is defined by $\rho_f = (1 + \sigma P_f)$, where 1 is the unitary matrix and σ are the Pauli matrices.

Target- and Recoil Polarisation (Target-Recoil ($\mathcal{TR}$))

For an experiment with polarised target nucleons and recoil nucleon polarisation, the total cross section can be written as:

$$\begin{aligned} p_f \left.\frac{d\sigma}{dt}\right|_{pol} = \left.\frac{d\sigma}{dt}\right|_{unpol} \cdot \{1 + \sigma_y P + P_x(T_x\sigma_x + T_z\sigma_z) \\ + P_y(T + \Sigma\sigma_y) \\ - P_z(L_x\sigma_x - L_z\sigma_z)\}. \end{aligned} \tag{1.30}$$

The total cross section for the single pseudoscalar photoproduction, including all polarisation observables, can be written as [37]:

$$\begin{aligned} d\sigma \propto (d\sigma_0 + \hat{\Sigma}[-P_L^\gamma \cos(2\phi)] + \hat{T}[P_y^T] + \hat{P}[P_{y'}^R] \\ + \hat{E}[-P_c^\gamma P_z^T] + \hat{G}[P_L^\gamma P_z^T \sin(2\phi)] + \hat{F}[P_c^\gamma P_x^T] + \hat{H}[P_L^\gamma P_x^T \sin(2\phi)] \\ + \hat{C}_{x'}[P_c^\gamma P_{x'}^R] + \hat{C}_{z'}[P_c^\gamma P_{z'}^R] + \hat{O}_{x'}[P_L^\gamma P_{x'}^r \sin(2\phi)] + \hat{O}_{z'}[P_L^\gamma P_{z'}^R \sin(2\phi)] \\ + \hat{L}_{x'}[P_z^T P_{x'}^R] + \hat{L}_{z'}[P_z^T P_{z'}^R] + \hat{T}_{x'}[P_x^T P_{x'}^R] + \hat{T}_{z'}[P_x^T P_{z'}^R]), \end{aligned} \tag{1.31}$$

where the same nomenclature was used for the description of the different polarisations. The cross section for the single pesudocalar meson photoproduction including higher order terms is shown in Appendix A.1.

1.3.2 Double Pseudoscalar Meson Photoproduction

The general formalism for photoproduction of pseudoscalar meson pairs off nucleons was introduced by W. Roberts and T. Oed [38]. The polarisation observables for the two pseudoscalar meson photoproduction are defined for the same polarisation conditions of the photon beam, the target and the recoil nucleon as for the single pseudoscalar photoproduction. However, the number of polarisation observables of the single and double pseudoscalar meson photoproduction differs due to the different scattering amplitudes of the single $(2 \times 2 = 4)$ and double pseudoscalar meson photoproduction $(2 \times 2 \times 2 = 8)$. Hence, 64 polarisation observables are defined for the double pseudoscalar meson photoproduction by taking the bilinear combinations of the eight complex amplitudes into account. For that reason, the formalism of the polarisation observables of the double pseudoscalar meson photoproduction is much more complicated than for the single pseudoscalar photoproduction where only 16 polarisation observables are defined considering the bilinear combination of the four complex amplitudes. Since the polarisation observables are products of amplitudes, 15 and 63 independent polarisation observables can be defined for the single and double pseudoscalar meson photoproduction. For the single and double pseudoscalar meson photoproduction, the double polarisation observables can be arranged into the same groups of Beam-Target ($\mathcal{BT}$), Beam-Recoil ($\mathcal{BR}$), and Target-Recoil ($\mathcal{TR}$), according to which pair of particles are polarised. However, for the double pseudoscalar meson photoproduction additional to the single and double polarisation observables, the triple polarisation observables, consisting of the polarisation of the photon beam, the target and the recoil, have to be considered. In contrast to the single pseudoscalar meson photoproduction, where the triple polarisation observables are identical with other double polarisation observables.
The representation of the single and double polarisation observables for the single and double pseudoscalar meson photoproduction in terms of the helicity amplitudes $H_1, H_2, ..., H_4$ and transversal amplitudes $b_1, b_2, ..., b_3$ are shown in Table 1.4 and 1.5. However, in these Tables not all the possible polarisation observables for the photoproduction are represented, the Tables only including the polarisation observables (the double polarisation observable F and the single polarisation observable T) which were extracted in this work. In Table 1.4 only the polarisation observables which require at least a polarised target or the measurement of the recoil nucleon are shown and in Table 1.5 only the polarisation observables which require at least a circular polarised photon beam B_{circ} are shown.
In both Tables the polarisation observables which require a polarised target or the measurement of the recoil polarisation are denoted by $\mathcal{T}$ and $\mathcal{R}$, respectively. Polarisation observables denoted by $\mathcal{TR}$ require the measurement of the target and the recoil nucleon. For these target polarisation observables, the x, y and z axes are

so chosen that the momentum of the first meson has positive X-projection and is orthogonal to the y-axes and the z axes is directed along the photon momentum.

Observable	Helicity form	Transversity form	Expt.	Type
I_0	$\|H_1\|^2+\|H_2\|^2+\|H_3\|^2+\|H_4\|^2$	$\|b_1\|^2+\|b_2\|^2+\|b_3\|^2+\|b_4\|^2$	$\{-;-\}$	
I_0P_x	$2R(H_1H_3^*+H_2H_4^*)$	$-2F(b_1b_3^*+b_2b_4^*)$	$\{x;-\}$	$\mathcal{T}$
I_0P_y	$-2F(H_1H_3^*+H_2H_4^*)$	$\|b_1\|^2+\|b_2\|^2-\|b_3\|^2-\|b_4\|^2$	$\{y;-\}$	
I_0P_z	$-\|H_1\|^2-\|H_2\|^2+\|H_3\|^2+\|H_4\|^2$	$-2R(b_1b_3^*+b_2b_4^*)$	$\{z;-\}$	
$I_0P_{x'}$	$-2R(H_1H_2^*+H_3H_4^*)$	$-2F(b_1b_2^*+b_3b_4^*)$	$\{-;x'\}$	$\mathcal{R}$
$I_0P_{y'}$	$2F(H_1H_2^*+H_3H_4^*)$	$\|b_1\|^2-\|b_2\|^2+\|b_3\|^2-\|b_4\|^2$	$\{-;y'\}$	
$I_0P_{z'}$	$\|H_1\|^2-\|H_2\|^2+\|H_3\|^2+\|H_4\|^2$	$-2R(b_1b_2^*+b_3b_4^*)$	$\{-;z'\}$	
$I_0O_{xx'}$	$-2R(H_2H_3^*+H_1H_4^*)$	$2R(-b_2b_3^*+b_1b_4^*)$	$\{x;x'\}$	$\mathcal{TR}$
$I_0O_{xy'}$	$-2F(-H_2H_3^*+H_1H_4^*)$	$-2R(b_1b_3^*+b_2b_4^*)$	$\{x;y'\}$	
$I_0O_{xz'}$	$2F(H_1H_3^*-H_2H_4^*)$	$2R(b_2b_3^*+b_1b_4^*)$	$\{x;z'\}$	
$I_0O_{yx'}$	$2F(H_2H_3^*+H_1H_4^*)$	$2F(b_1b_2^*+b_3b_4^*)$	$\{y;x'\}$	
$I_0O_{yy'}$	$2R(-H_2H_3^*+H_1H_4^*)$	$\|(b_1\|^2+\|b_2\|^2-\|b_3\|^2+\|b_4\|^2$	$\{y;y'\}$	
$I_0O_{yz'}$	$-2F(H_1H_3^*-H_2H_4^*)$	$2R(-b_1b_2^*+b_3b_4^*)$	$\{y;z'\}$	
$I_0O_{zx'}$	$2R(H_1H_2^*-H_3H_4^*)$	$2F(b_2b_3^*-b_1b_4^*)$	$\{x;z'\}$	
$I_0O_{zy'}$	$-2F(H_1H_2^*-H_3H_4^*)$	$2R(-b_1b_3^*+b_2b_4^*)$	$\{z;y'\}$	
$I_0O_{zz'}$	$-\|H_1\|^2+\|H_2\|^2+\|H_3\|^2-\|H_4\|^2$	$2R(b_2b_3^*+b_1b_4^*)$	$\{z;z'\}$	

Table 1.4.: Definition of the polarisation observables in terms of helicity and transversity amplitudes in single- and double-pion photoproduction using a pion beam. For the polarisation observables denoted $\mathcal{T}$, a polarised target is required but not the measurement of the recoil polarisation. For the polarisation observables labeled with a $\mathcal{R}$ an unpolarised target is required, but the polarisation of the recoil has to be measured. For the variables denoted with $\mathcal{TR}$ the target has to be polarised and the polarisation of the recoil has to be measured. The required experimental conditions are described by the brackets $\{t,r\}$ including the polarisation information of the target (t) and the recoil (r). For the target polarisation, the x, y axes are so chosen that the momentum of the first meson has positive x-projection and is orthogonal to y-axes and the z-axes is directed along the photon momentum. Table taken from [38].

Observable	Helicity form	Transversity form	Expt.	Type
I_0I^{circ}	$-\|H_1^-\|^2+\|H_1^+\|^2-\|H_2^-\|^2+\|H_2^+\|^2$ $-\|H_3^-\|^2+\|H_3^+\|^2-\|H_4^-\|^2+\|H_4^+\|^2$	$-\|b_1^-\|^2+\|b_1^+\|^2-\|b_2^-\|^2+\|b_2^+\|^2$ $-\|b_3^-\|^2+\|b_3^+\|^2-\|b_4^-\|^2+\|b_4^+\|^2$	$\{c;-;-\}$	B_{circ}
$I_0P_x^{circ}$	$2R(-H_1^-H_3^{-*}+H_1^+H_3^{+*}-H_2^-H_4^{-*}+H_2^+H_4^{+*})$	$2F(b_1^-b_3^{-*}-b_1^+b_3^{+*}+b_2^-b_4^{-*}-b_2^+b_4^{-*})$	$\{c;x;-\}$	$B_{circ}\mathcal{T}$
$I_0P_y^{circ}$	$2R(H_1^-H_3^{-*}-H_1^+H_3^{+*}+H_2^-H_4^{-*}-H_2^+H_4^{+*})$	$-\|b_1^-\|^2+\|b_1^+\|^2-\|b_2^-\|^2+\|b_2^+\|^2$ $+\|b_3^-\|^2-\|b_3^+\|^2+\|b_4^-\|^2-\|b_4^+\|^2$	$\{c;y;-\}$	
$I_0P_z^{circ}$	$\|H_1^-\|^2-\|H_1^+\|^2+\|H_2^-\|^2-\|H_2^+\|^2$ $-\|H_3^-\|^2+\|H_3^+\|^2-\|H_4^-\|^2+\|H_4^+\|^2$	$2R(b_1^-b_3^{-*}-b_1^+b_3^{+*}+b_2^-b_4^{-*}-b_2^+b_4^{-*})$	$\{c;z;-\}$	
$I_0P_{x'}^{circ}$	$2R(H_1^-H_2^{-*}-H_1^+H_2^{+*}+H_3^-H_4^{-*}-H_3^+H_4^{+*})$	$-2F(b_1^-b_2^{-*}-b_1^+b_2^{+*}+b_3^-b_4^{-*}-b_3^+b_4^{-*})$	$\{c;-;x'\}$	$B_{circ}\mathcal{R}$
$I_0P_{y'}^{circ}$	$-2F(H_1^-H_2^{-*}-H_1^+H_2^{+*}+H_3^-H_4^{-*}-H_3^+H_4^{+*})$	$-\|b_1^-\|^2+\|b_1^+\|^2+\|b_2^-\|^2-\|b_2^+\|^2$ $+-\|b_3^-\|^2+\|b_3^+\|^2+\|b_4^-\|^2-\|b_4^+\|^2$	$\{c;y;-\}$	
$I_0P_{z'}^{circ}$	$-\|H_1^-\|^2+\|H_1^+\|^2+\|H_2^-\|^2-\|H_2^+\|^2$ $-\|H_3^-\|^2+\|H_3^+\|^2-\|H_4^-\|^2+\|H_4^+\|^2$	$2R(b_1^-b_2^{-*}-b_1^+b_2^{+*}+b_3^-b_4^{-*}-b_3^+b_4^{-*})$	$\{c';-;z'\}$	
$I_0O_{xx'}^{circ}$	$2R(H_2^-H_3^{-*}-H_2^+H_3^{+*}+H_1^-H_4^{-*}-H_1^+H_4^{+*})$	$2R(b_2^-b_3^{-*}-b_2^+b_3^{+*}-b_1^-b_4^{-*}+b_1^+b_4^{-*})$	$\{c;x;x'\}$	$B_{circ}\mathcal{TR}$
$I_0O_{xy'}^{circ}$	$2F(H_2^-H_3^{-*}-H_2^+H_3^{+*}-H_1^-H_4^{-*}+H_1^+H_4^{+*})$	$2F(b_1^-b_3^{-*}-b_1^+b_3^{+*}-b_2^-b_4^{-*}+b_2^+b_4^{-*})$	$\{c;x;y'\}$	
$I_0O_{xz'}^{circ}$	$2R(-H_1^-H_3^{-*}+H_1^+H_3^{+*}+H_2^-H_4^{-*}-H_2^+H_4^{+*})$	$-2R(b_2^-b_3^{-*}-b_2^+b_3^{+*}+b_1^-b_4^{-*}-b_1^+b_4^{-*})$	$\{c;x;z'\}$	
$I_0O_{yx'}^{circ}$	$-2F(H_2^-H_3^{-*}-H_2^+H_3^{+*}+H_1^-H_4^{-*}-H_1^+H_4^{+*})$	$-2F(b_1^-b_2^{-*}-b_1^+b_2^{+*}-b_3^-b_4^{-*}+b_3^+b_4^{-*})$	$\{c;y;x'\}$	
$I_0O_{yy'}^{circ}$	$2R(H_2^-H_3^{-*}-H_2^+H_3^{+*}-H_1^-H_4^{-*}+H_1^+H_4^{+*})$	$-\|b_1^-\|^2+\|b_1^+\|^2+\|b_2^-\|^2-\|b_2^+\|^2$ $\|b_3^-\|^2-\|b_3^+\|^2-\|b_4^-\|^2+\|b_4^+\|^2$	$\{c;y;y'\}$	
$I_0O_{yz'}^{circ}$	$2F(H_1^-H_3^{-*}-H_1^+H_3^{+*}-H_2^-H_4^{-*}+H_2^+H_4^{+*})$	$2R(b_1^-b_2^{-*}-b_1^+b_2^{+*}-b_3^-b_4^{-*}+b_3^+b_4^{-*})$	$\{c;y;z'\}$	
$I_0O_{zx'}^{circ}$	$2R(-H_1^-H_2^{-*}+H_1^+H_2^{+*}+H_3^-H_4^{-*}-H_3^+H_4^{+*})$	$-2F(b_2^-b_3^{-*}-b_2^+b_3^{+*}-b_1^-b_4^{-*}+b_1^+b_4^{-*})$	$\{c;z;x'\}$	
$I_0O_{zy'}^{circ}$	$2F(H_1^-H_2^{-*}-H_1^+H_2^{+*}-H_3^-H_4^{-*}+H_3^+H_4^{+*})$	$2R(b_1^-b_3^{-*}-b_1^+b_3^{+*}-b_2^-b_4^{-*}+b_2^+b_4^{-*})$	$\{c;z;y'\}$	
$I_0O_{zz'}^{circ}$	$\|M_1^-\|^2-\|M_1^+\|^2-\|M_2^-\|^2+\|M_2^+\|^2$	$2R(-b_2^-b_3^{-*}+b_2^+b_3^{+*}-b_1^-b_4^{-*}+b_1^+b_4^{-*})$	$\{c;z;z'\}$	

Table 1.5.: Polarisation observables of single- and double pion photoproduction using a circularly polarised photon beam, in terms of the helicity and transversity amplitudes. The same notation as in Table 1.4 is used. The required experimental conditions are described by the brackets $\{b,t,r\}$, including the polarisation information of the photon beam (b) (B_{circ} indicates a circularly polarised photon beam), target (t) and recoil (r). Table taken from [38].

As mentioned before, in this work only the polarisation observables for a circular polarised photon beam and a transversal polarised target were extracted for the double π^0 meson photoproduction from free protons. The possible polarisation observables, the double polarisation observable $I_0 P_x^{circ}$ and the single polarisation observable $I_0 P_z$, were only extracted for ϕ angle distributions of the π^0 mesons and the recoil proton and not over all degrees of freedom. Hence, the polarisation observables $I_0 P_x^{circ}$ and $I_0 P_z$ are equivalent to the ordinary F and T polarisation observables in the single pseudoscalar meson photoproduction. Since the extracted polarisation observables $I_0 P_x^{circ}$ and $I_0 P_z$ in this work are limited to ϕ angle distributions of the π^0 mesons and the recoil proton, the F and T notation is used.
For a circularly polarised photon beam and transversally polarised target nucleons, the differential cross section can be simplified to the following equation [36]:

$$\left.\frac{d\sigma}{d\Omega}\right|_{pol} = \left.\frac{d\sigma_0}{d\Omega}\right|_{unpol} \{1 + \frac{1}{\sqrt{2}} P_T [P_{circ} P_x F \cos(\phi) + P_y T \sin(\phi)]\}, \tag{1.32}$$

where *F* and *T* are the polarisation observables, σ_0 denote the unpolarised differential cross section, and P_{circ} and P_T are the polarisation degree of the photon beam and the target nucleons, respectively.
The double polarisation observable F is a circular polarised photon beam and transversally polarised target nucleon dependent asymmetry and can be described by:

$$F \cos(\phi) = \frac{1}{P_T P_{circ}} \frac{d\sigma^+(\phi) - d\sigma^-(\phi)}{d\sigma^+(\phi) + d\sigma^-(\phi)}, \tag{1.33}$$

where P_T and P_{circ} are the degree of the photon beam and nucleon polarisation, respectively, the ϕ angle depend on the direction of the polarisation of the nucleon spin and $d\sigma(\phi)^+ = d\sigma^{+\uparrow}(\phi) + d\sigma^{-\uparrow}(\phi)$ and $d\sigma(\phi)^- = d\sigma^{+\downarrow}(\phi) + d\sigma^{-\downarrow}(\phi)$ are the differential polarised cross sections including the photon beam with positive and negative helicity ($\pm$) and the nucleon target spin polarisation ($\uparrow, \downarrow$) vertically up or down.
The single polarisation observable T is a transversally polarised target spin dependent asymmetry and can be described by:

$$T \sin(\phi) = \frac{1}{P_T} \frac{\sigma^{\uparrow}(\phi) - \sigma^{\downarrow}(\phi)}{\sigma^{\uparrow}(\phi) + \sigma^{\downarrow}(\phi)}, \tag{1.34}$$

where P_T is the degree of polarisation of the target nucleons, ϕ angle depend on the direction of the polarisation of the nucleon target spin, and $d\sigma^{\uparrow}$ and $d\sigma^{\downarrow}$ are the differential cross section with nucleon spin polarisation $\uparrow, \downarrow$ vertically up or down, respectively. The connection between the measured polarisation observables F and T and the different amplitudes will be explained in the following section.

1.4 The Complete Experiment

For the double pseudoscalar meson photoproduction the determination of the required polarisation observables is much more complicated in contrast to the single pseudoscalar meson photoproduction. In the single pseudoscalar meson photoproduction, only 15 independent polarisation observables exists, whereby the measurement of eight appropriately selected polarisation observables are sufficient for the determination of the four complex amplitudes [39]. Since in the double pseudoscalar meson photoproduction 63 independent polarisation observables exists, more polarisation observables have to be measured in contrast to the single pseudoscalar meson photoproduction to determine the eight complex amplitudes [38]. However, not all required polarisation observables can be measured for the double pseudoscalar meson photoproduction which would define the complete experiment including the eight complex amplitudes. Since the extraction of the magnitude of all amplitudes would require the measurement of eight independent observables in a unique way and requires fixing the phase by measuring the 15 polarisation observables [40]. But the measurement of at least some polarisation observables can give more information about the contribution amplitudes in the photoproduction of double pseudoscalar mesons.

1.4.1 Extraction of Resonance Parameters

Contributions from nucleon resonances can then be reconstructed by partial wave analysis (PWA) from the measured amplitudes. In PWA the measured observables are decomposed into different multipoles, including contributions from nucleon resonances and non-resonant backgrounds. The models used then different parametrisations for the determination of the resonant and background terms. In the following sections, the most common PWA analysis for the double π^0 photoproduction and their parametrisations will be discussed.

MAID

The Mainz MAID isobar model [41] is based on an effective Lagrangian approach and has been developed at the Johannes Gutenberg University in Mainz, Germany by A. Fix and H. Arenhövel [41]. The model includes contributions of several nucleon resonances and background contributions. The non-resonant background arise e.g. from N- and Δ- nucleon Born terms as well as from t-channel effects like vector-meson exchange and parametrised by effective Lagrangians. For the total cross section of the double π^0-meson reaction the MAID model includes resonances

contribution of the N^* from $D_{13}(1520)$, $S_{11}(1650)$, $D_{15}(1675)$, $F_{15}(1680)$, $D_{13}(1700)$, $P_{11}(1710)$, and $P_{13}(1720)$ whereby the second resonance region is dominated by the $D_{13}(1700)$. However, the predictions of the MAID model cannot reproduce the experimental total cross section in the region below the resonances $N(1520)3/2^-$ [42].

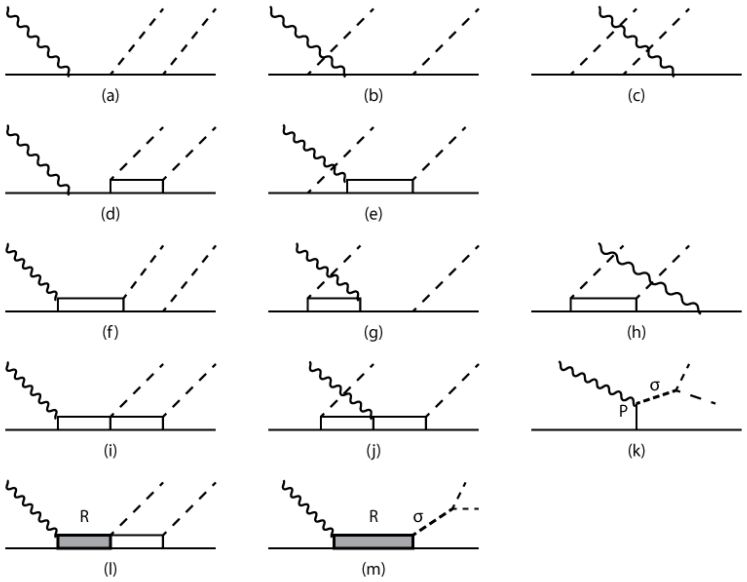

Figure 1.8.: Diagrams for the $\gamma p \to \pi^0\pi^0 p$ reaction of free proton used in the theoretical isobar MAID models [41][42] of the polarisation observables F and T. The empty rectangles represent the $\Delta(1232)$ resonances and other resonances in the s channel are represented by the shaded rectangles. Figure taken from [42].

In the MAID isobar model for the polarisation observables *F* and *T*, the reaction amplitude consists of two main terms from two main groups. The first group contains the nucleon and Δ-nucleon Born diagrams, shown in Fig. 1.8 by the diagrams from (a) to (k). The second group contains the sum of s-channel Breit-Wigner resonances for $J \leq 5/2$, shown in Fig. 1.8 by the diagrams (l) and (m). The used parameters for the description of the γN coupling as the partial decay widths of the resonances were taken from the Particle Data Group [15].

Bonn-Gatchina Partial Wave Analysis

The coupled partial channel wave analysis Bonn-Gatchina (BnGa) model has been developed in a collaboration between the Rheinische Friedrich-Wilhelms-Universität in Bonn, Germany, and the Petersburg Nuclear Physics Institute in Gatchins, Russia. The model is a coupled-channel reaction model including background terms and uses simultaneous fits from experimental results of baryon spectroscopy. In the analysis, the K-matrix-approach is used for the partial waves at low energies and for

high energies, resonances with masses above 2.2 GeV, the relativistic multi-channel Breit-Wigner amplitudes are used.
For the polarisation observables *F* and *T*, the general coupled partial wave analysis BnGa model is available with the general fits to previous ELSA data and an additional BnGa model fit without the resonances of $N(1900)3/2^+$. Therefore, the contribution of the $N(1900)3/2^+$ resonance can be estimated in the polarisation observables *F* and *T*.

1.5 Current Experimental Data

The double π^0 photoproduction from the free proton has been studied rather intensively during the last decade with the DAPHNE [43], [44], TAPS [45]-[46], Crystal Ball/TAPS [47]-[48] detectors at MAMI, GRAAL [49] experiment, and with the Crystal Barell/TAPS [50]-[51] detectors at ELSA. The reaction was first measured from the threshold up to the second resonance region and later also to the third energy region. The $\pi^0\pi^0 N$ reaction has the advantage that the different sequential decays via the intermediate N^*- and Δ^*-resonances can be investigated by the measurement of the total cross sections and invariant mass distributions.
A previously measured total cross section for the $\gamma p \to \pi^0\pi^0 p$ reaction from the free proton as a function of the incident beam energy from the threshold region up to 800 MeV is shown in Fig. 1.9.

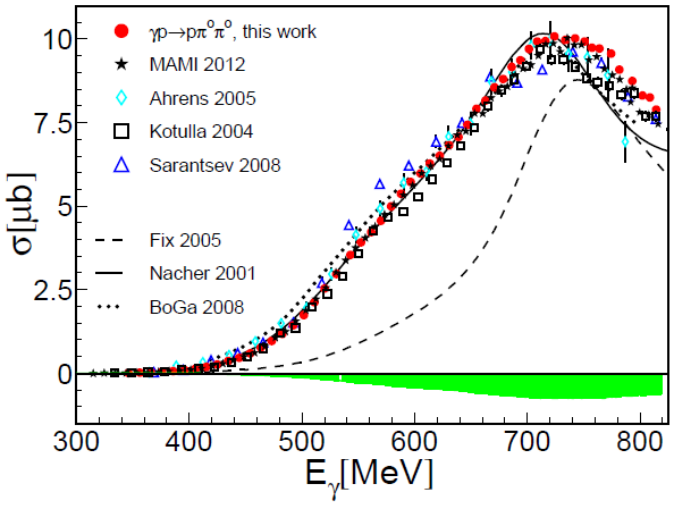

Figure 1.9.: Total cross section of the $\gamma p \to \pi^0\pi^0 p$ reaction. The measurement results are shown by the different colored symbols. (Red) dots: present measurement results of the free proton from MAMI, (black) stars: MAMI-C data [52], (black) squares: Kontulla et al. [47], [53], (blue) triangles: Sarantsev et al. [53], cyan diamonds: Ahrens et al. [44], black stars: MAMI data. The green shaded area at the bottom show the systematic uncertainty of the present measurement results. The theoretical predictionf of the Valencia model (Nacher et al. [54]), the Two-Pion-Maid (Fix and Arenhövel [41]) and the BnGa (Sarantsev et al. [53]) is shown by the solid curve, the dashed curve and the dotted curve. Figure taken from [55].

It can be seen that all the measured results from the total cross section agrees within the systematic uncertainties. The prediction of the BnGa [53] coupled channel partial wave analysis and the Valencia model [54] shown by the dotted and solid curves achieve better agreements with the experimental results as the TWO-Pion-Maid model [41] shown by the dashed curve. However, in the BnGa model and the Valencia model fit parameters form previous measured TAPS and CBELSA double π^0 data [53] were used, so that a reasonable agreement could be expected.
Additional to the total cross section, the beam helicity asymmetry of the photoproduction of the pion pairs was measured in the second resonance region from 550 up to 820 MeV [56]. This asymmetry was measured to obtain more detailed information of the double π^0 reaction. The comparison with the theoretical predictions have shown that the resonance and background contribution are not fully understood and can be seen in Fig. 1.10.

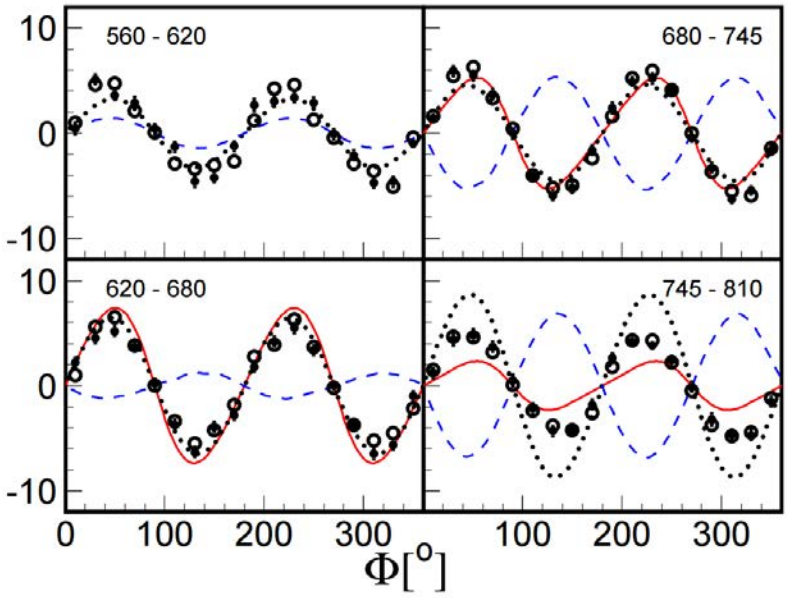

Figure 1.10.: Beam helicity asymmetry for the double π^0 reaction as a function for four different ranges of the incident photon beam energy. The filled symbols show the result of the $I^{\odot}$ and the open symbols $-I^{\odot}(2\pi - \Phi)$ The theoretical models are indicated by the different lines, the Two-Pion-Maid model [41] is described by the red solid line, the Valencia model [57] by the dashed blue line, and the BnGa [53] by the black dotted line. Figure taken from [56].

The Valencia model [57] has the best agreement with the measured total cross section, but could not reproduce the polarisation observable. The prediction from the Two-Pion-MAID [41] and the BnGa [53] show a better agreement with the measured results, but at higher energies also not a satisfactory one. This observable was then again measured for a much higher energy range by M. Oberle et. al [40]. The comparison between these results and the theoretical model show again that the BnGa model has the best agreement with the measured results, but for the high energy range, discrepancies appear.

The recent results from CBELSA/TAPS [58] show the measurement of the total and differential cross section up to the third and fourth resonance region and the first results for the polarisation observable I^S and I^C. Based on these results, the nucleon properties and the Δ resonance contribution for the double π^0 photoproduction were determined within the BnGa model. Therefore, the branching ratios of nucleon and Δ resonances with the decays via the intermediate $\Delta(1232)\pi$, $N(1440)1/2+\pi$, $N(1520)3/2^-\pi$, $N(1680)5/2^+\pi$ states, and also additional contribution from the light unflavoured mesons $pf_0(500)$, $pf_0(980)$ and $pf_2(1270)$. For the polarisation observables I^S and I^C, it could be shown that the $N(1900)3/2^+$ resonance has a non-negligible influence.
However, the resonance and background contribution of the double π^0 reaction are not fully understood and therefore, more experimental measurements are necessary.

2 Experimental Setup

The following chapter explains the experimental setup at the MAMI tagged photon facility in Mainz, Germany, which was used for the measurement of the polarisation observables F and T of the double π^0 photoproduction from the free proton. For these measurements, a circularly polarised photon beam and a transversally polarised target are required. The circularly polarised photon beam was produced via the bremsstrahlung process with a radiator and a polarised electron beam. For the polarised electron beam, electrons were accelerated using the Mainz Microtron electron accelerator. The energy of the photon beam was defined by a momentum analysis with the Glasgow Tagged Photon Spectrometer. The beam spot on the target was then defined by a collimator. The final state particles were detected with the Crystal Ball (CB) calorimeter combined with the TAPS detector and complemented with a particle identification detector (PID) made of 24 scintillations counters and multi-wire proportional chambers (MWPCs) for additional identification and tracking of charged particles. The Crystal Ball combined with the PID and MWPCs provides position, energy, and timing information for neutral and charged particles over the full ϕ range and in θ from 21° to 159°. In the beam direction, TAPS detects the particles within an angle less than 21°. This detector setup provides an excellent energy and angular resolution, which is necessary for the measurement of the polarisation observables. With this experimental setup, two butanol beam times were measured with a circularly polarised photon beam and transversally polarised protons. Additionally, a hydrogen beam time and a carbon beam time were measured to get more information about the unbound polarised hydrogen protons and the unpolarised carbon background contribution of the butanol target.

2.1 The MAMI Accelerator

The Mainz Microtron (MAMI) is a continuous wave electron accelerator at the Institut für Kernphysik at the Johannes Gutenberg Universität Mainz. The different sub-accelerator system of the MAMI accelerator can produce polarised electron beams with a polarisation degree up to 80% and with a beam current up to 20 μA and unpolarised electron beams up to 100 μA with energies of 1.6 GeV. An overview of the MAMI accelerator is shown in Fig. 2.1

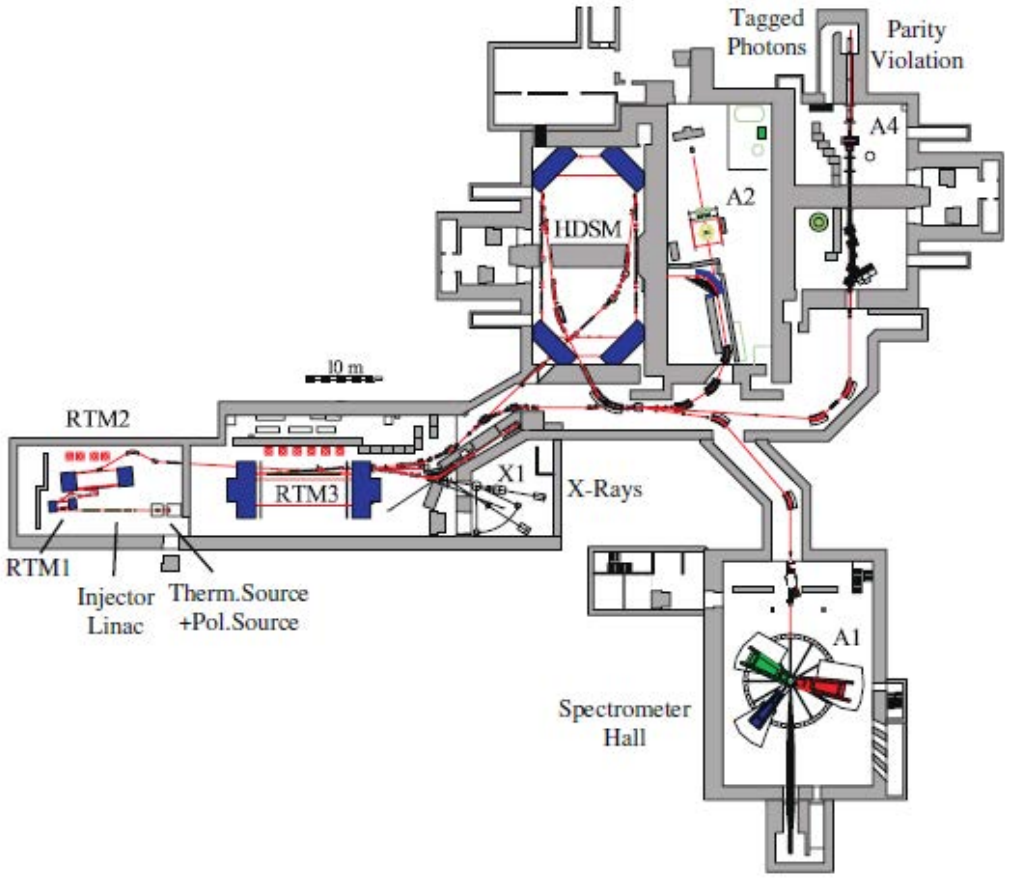

Figure 2.1.: Floorplan of the MAMI electron accelerator. MAMI comprises three racetrack microtrons and a Harmonic Double Sided Microtron, which accelerate electrons up to 1.6 GeV. The four experimental halls (X1, A1, A4, and A2) are depicted. The A1 collaboration performs electron scattering experiments, A4 performs parity violating experiments, X1 performs evaluation on the development of novel radiation sources, and A2 performs photoproduction experiments. Figure taken from [59].

2.1.1 Production of the Electron Beam

MAMI has two electron guns, one which produces unpolarised electron beams and one for the production of polarised electron beams. Unpolarised electrons are produced via thermionic emission with a thermionic electron gun, EKAN. In this process, free electrons are released from the surface of the cathode by a filament voltage, which produces high enough temperatures (higher than $1000°C$). The resulting beam current can be varied by a surrounding static electromagnetic field, which is generated by a Wehnelt cylinder. With this method, intensities of the beam current from a few pA up to $100\ \mu$A can be produced [34].
The electron gun for the production of the polarised electrons consists of a gallium arsenide (GaAs) semiconductor illuminated by circularly polarised laser light. Through the laser light, electrons in the valence band of the semiconductor with the desired spin orientation can be energetically excited to the conduction band. Some

of these electrons can be emitted by a special preparation of the semiconductor. These emitted electrons can then be further accelerated by a static electrical field. The polarisation of the electrons can be improved by the following preparation: due to the doping of the s-GaAs with zinc and by evaporating caesium, the vacuum potential can be brought slightly below the conduction band of the semiconductor, which allows a simple detachment of the polarised electrons. For the excitation and emission of the electrons in the valence band, circularly polarised laser light is necessary. To produce a circularly polarised laser light, a polarisation filter and a $45°$ to the incident optical axis rotated $\lambda/4$-plate is used to convert linearly polarised laser light to circular polarisation. The characteristics of the semiconductor and the laser light makes it possible to produce a continuous electron beam with a stable polarisation over a long period of time [60], [61].

2.1.2 Acceleration of the Electron Beam

The continuous-wave accelerator MAMI has three distinct stages for the acceleration of the electrons: (1) a pre-accelerator in the form of a linear accelerator (LINAC), (2) a cascade of three racetrack microtrons, (RTMs), and (3) the Harmonic Double Sided Microtron (HDSM) [59]. The electrons from the electron gun are first accelerated to a total energy of 3.97 MeV via an injector LINAC. These electrons enter a cascade of three racetrack microtron RTMs. The linear accelerator of the racetrack microtron is built up with several accelerator tubes behind each other where the electrons go through and are accelerated by the applied microwaves between the tubes. For a constant acceleration, the potential of the electric field changes periodically with a high frequency generator. To use the acceleration of the linear accelerator, the electrons are bent by $180°$ several times via the first large dipole magnet and passed through a focusing device after they were bent again by $180°$ via the second large dipole magnet back into the linear accelerator. Through the multiple use of the linear accelerator, the electrons gain energy and the radius of the focusing device through the bending magnet increases. The relation between the increase in path length per turn Δs and the increase in energy per turn ΔT_{RTM} is given by the following equation [62]:

$$\Delta s = 2\pi \frac{\Delta T_{RTM}}{e\beta cB}, \tag{2.1}$$

where B is the strength of the dipole magnetic field, e is the charge, and $\beta = v/c$ is the velocity, where $\beta \approx 1$ for relativistic electrons. The ejection energy of the electrons are 14.86 MeV, 180 MeV, and 855 Mev for each racetrack microtron RTM1, RTM2, and RTM3, respectively. More information about the main parameters of the different racetrack microtrons are given in Table 2.1.

	Units	Injector	RTM 1	RTM2	RTM 3	HDSM
General						
Injection Energy	[MeV]	0.511	3.97	14.86	180	855
Ejection Energy	[MeV]	3.97	14.86	180	885	1.5
Number of cycles		-	18	51	90	43
LINAC System						
Energy resp. energy gain/turn	[MeV]	3.5	0.599	3.24	7.50	13.66-16.58
LINAC length	[m]	4.93	0.80	3.55	7.75	8.57/10.1
Magnet System						
Magnetic Field	[T]	-	0.1026	0.555	1.2842	1.03-0.95
Fe/Cu weight of magnets	10^3[kg]	-	4/0.2	90/2.3	900/ 11.6	1000/27.4

Table 2.1.: Parameters for the MAMI racetrack accelerator. Values taken from [59].

The magnetic field strength in the individual RTMs is constant in time and space, but is increased as well as the radius of curvature for the further acceleration of the electrons by the different RTM' s $1, 2$ and 3. The electrons have an ejection energy of 883.1 MeV after the last racetrack RTM3 and enter the HDSM for further accelerations. The HDSM is built with four bending magnets and two linear accelerators and can be seen in Fig. 2.2.

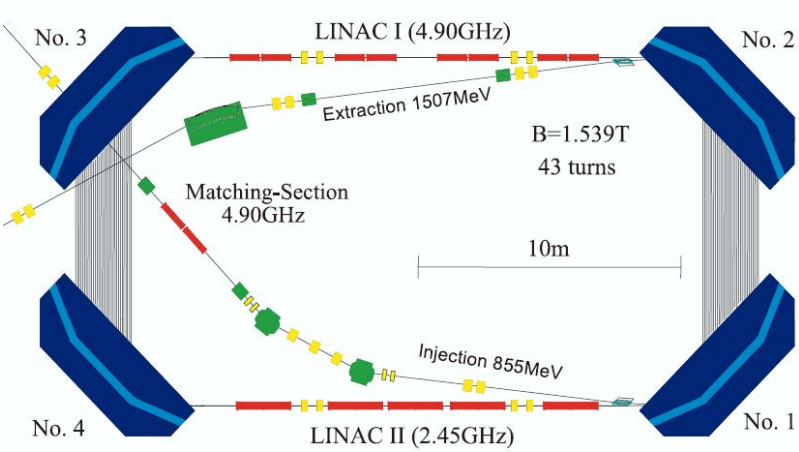

Figure 2.2.: Schematic drawing of the Harmonic Double Sided Microtron (HDSM) at MAMI. Figure taken from [63].

Each of the four bending magnets bend the electrons by $90°$. With this accelerator method, electron beam energies up to 1.6 GeV can be provided.
In contrast to the non-polarised electron beams, the acceleration of polarised electron beams is more difficult due to the effects of spin precessions. If the spin precession frequency and the momentum precession frequency are not equal to the angle of the spin, the vector changes. A spin precession exists due to the magnetic dipole moment of the electron and the applied magnetic field. The frequency of the spin precession for the acceleration of electron beams can be described by the Bargmann, Michel, and Telegdi (BMT) equation [61]:

$$\omega_s = (1 + a\gamma)\omega_p, \tag{2.2}$$

where a is the gyromagnetic anomaly of the electron ($a = (g-2)/2$), γ is the ratio of total energy to the rest mass, and ω_p is the momentum precession. The generated angle shift between the momentum and spin, which occurs through the spin precision, is predictable and is corrected by a spin rotation system. To ensure a pure longitudinal polarisation of the electron beam, a Wien filter was chosen as spin rotator and installed in the beam line before the bremsstrahlung target. A pure longitudinally polarised electron beam with the Wien filter is only possible when the electron beam energy and the strength of the applied magnetic field are properly adjusted. The settings were controlled through several measurements with the M∅ller target and then a beam energy of 1557 MeV was chosen for the measurement. The spin depolarisation effects are negligible at MAMI.

2.2 Generation of Photon Beams

The electrons, delivered by the MAMI accelerator are converted into photons for the experiment. This is done by a bremsstrahlung process using a radiator in the electron beam line. For the determination of the photon energy, the scattered electrons of the bremsstrahlung process are deflected by the tagger magnetic field and then the momentum is analysed by the photon tagger.

2.2.1 Bremsstrahlung Process

Bremsstrahlung is electromagnetic radiation produced by the deceleration of charged particles in matter. The deceleration of the charged particles is induced by the interaction with other charged particles, typically an electron by an atomic nucleus in matter, which is the so called Coulomb interaction. The deceleration of the charged particle leads to a loss of kinetic energy, which is transferred to the emitted photon. This process satisfies the law of the conservation of energy and requires the following four-momentum conversion:

$$\begin{pmatrix} E_0 \\ \vec{p_0} \end{pmatrix} = \begin{pmatrix} E \\ \vec{p} \end{pmatrix} + \begin{pmatrix} E_\gamma \\ \vec{k} \end{pmatrix} + \begin{pmatrix} T \\ \vec{q} \end{pmatrix}, \tag{2.3}$$

where $(E_0, \vec{p_0})$ is the four-momentum for an incident electron, $(E, \vec{p})$ is the four-momentum of the final state of the scattered electron, $(E_\gamma, \vec{k})$ is the four-momentum of the produced photon, and $(T, \vec{q})$ is the four-momentum corresponding to the recoil of the nucleus. The recoil energy T can be neglected because of the high nucleus mass.

2.2.2 Polarised Photons

Bremsstrahlung can be produced incoherently or coherently. With the coherent bremsstrahlung process, linearly polarised photons can be produced by scattering the electrons on a diamond radiator. Depending on whether the photon beam should be unpolarised or circularly polarised, the electrons of the incoherent bremsstrahlung process are unpolarised or longitudinally polarised. For the incoherent bremsstrahlung process, the electrons are scattered on an amorphous radiator. The different radiator materials are located in the goniometer and can be brought into the beam line. For the production of circularly polarised photons, a Møller radiator is used, which is a $10\ \mu$m thick foil made of Vacoflux50, an alloy with 49% cobalt, 49% iron, and 2% vanadium [34]. The helicity transfer of the longitudinally polarised electron to the circularly polarised photons through the bremsstrahlung process can be calculated by the Olsen and Maximon equation [64]:

$$\frac{P_\gamma}{P_e} = \frac{3 + (1-x)}{3 + 3(1-x)^2 - 2(1-x)} \cdot x \qquad \text{with} \qquad x = \frac{E_\gamma}{E_0}, \tag{2.4}$$

where E_γ and E_0 are the energy of the Bremsstrahlung photon and the energy of the electron beam, respectively, and P_γ and P_e are the degree of circular polarisation of the photon and the degree of longitudinal polarisation of the electron, respectively. The electron polarisation degree can be measured with the Møller polarimeter or with the Mott measurement, which is explained in Section 3.1.

2.2.3 The Photon Tagger

The Glasgow Tagged Photon Spectrometer is a magnetic spectrometer for electrons. It is used to determine the energy of the photon from a momentum analysis of the bremsstrahlung electron. The photon energy can be measured because the initial energy of the electron E_0 is well known from MAMI and the energy of the bremsstrahlung electron E is measured by the Glasgow Tagged Photon Spectrometer. The photon energy is given by the following equation:

$$E_\gamma = E_0 - E. \tag{2.5}$$

This determination of the photon energy is called tagging since the energy is not directly measured, but the energy of the deflected electron is, which interacts via the bremsstrahlung process. For the measurement of the energy of the bremsstrahlung electron, a large dipole magnet is used to bend the path of the electron corresponding to its energy. The deflection of low energy electrons is higher than the deflection of high energy electrons. The photon tagger has a magnetic field of 1.9 T, which deflects the main electron beam, not the scattered electrons, 79° into a beam dump [65]. The

electron beam intensity is checked by the measurement of the beam current with a Faraday cup. The scattered electrons, which interact with the radiator, are measured with a tagger ladder installed in the focal plane. A sketch of the Glasgow-Mainz photon tagger is shown in Fig. 2.3.

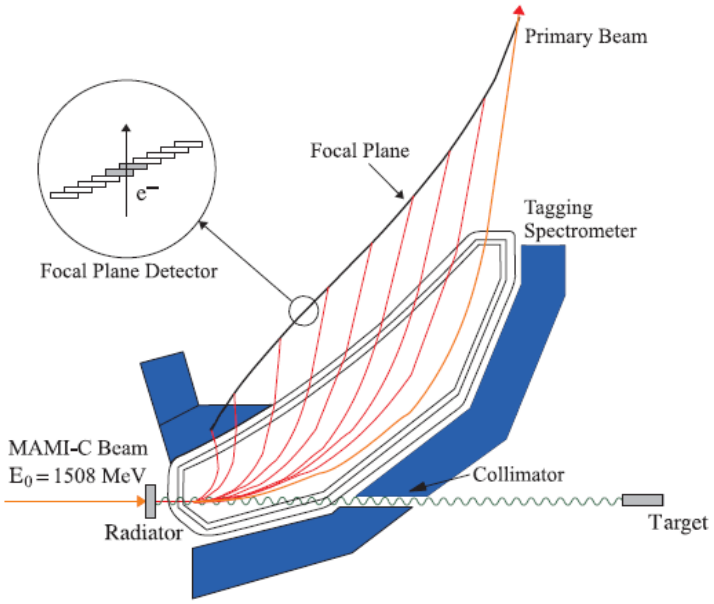

Figure 2.3.: Sketch of the Glasgow-Mainz photon tagger. The electron beam is incident upon a radiator and produces bremsstrahlung photons. The scattered electrons (red) are deflected with a dipole magnet (blue) and momentum analysed with the tagger. The bremsstrahlung photons (green) continue to the target. Figure taken from [63].

The tagger ladder consists of 353 plastic scintillators which overlap with the neighbouring scintillators by roughly 50%. The scintillators have a length of 80 mm, a thickness of 2 mm, and a variable width of 9 mm up to 52 mm because of the partially changing dispersion of the spectrometer along the focal plane. All scintillators cover a momentum range of around 7.5 MeV and 95% of the primary electron beam. Each scintillator is coupled to a Hamamatsu $R1635$ photomultiplier tube (PMT). The magnetic field of the tagger changes the radius of the electrons with different energies more accurately than the width of the single scintillators. The energy resolution is thus limited by the width of the scintillators. The incident electron beam can then be tagged with an energy resolution of 2 to 5 MeV [66]. If necessary, a "tagger microscope" with a finer momentum binning can be used, which improves the resolution by a factor $2-5$.

For the experiment in this work, the tagged incident electron beam covers an energy range between 450 to 1450 MeV. The highest tagger channels $(281-352)$ corresponding to low energy photons were not used to increase the event rate in the region of interest.

2.3 Targets

The goal of this work was the measurement of the polarisation observables F and T. For this, the nucleons in a butanol target were transversally polarised. A butanol target was chosen because of the high polarisation degree of the hydrogen protons in the butanol. For the target protons, a maximum polarisation degree of $P_T = 90\%$ and an average polarisation degree of P_T=70% can be reached with the frozen spin method. Using a butanol target has the advantage that only the unbounded hydrogen protons of the butanol target can be transversally polarised and the additional background through reactions on the unpolarised oxygen and carbon nuclei do not influence the nominator of the asymmetries. For the determination of the polarisable hydrogen contribution and the unpolarised carbon contribution of the butanol target, additional measurements with a liquid hydrogen and a carbon target with the same experimental conditions were made. The used liquid hydrogen, butanol, and carbon targets are discussed in the following sections.

2.3.1 Liquid Hydrogen Target

For the determination of the signal, the hydrogen contribution of the butanol, an unpolarised liquid hydrogen target was used with circularly polarised photons with similar experimental conditions as the butanol target. The liquid hydrogen target is a cylindrical target cell with a length of 100.0 ± 1.0 mm, made of 125 μm Kapton [67], as shown in Fig. 6.2. The full target is filled with liquid hydrogen LH_2 at a pressure of 1080 mb and has a density of $4.249 \cdot 10^{23}$ protons/cm^2. For isolation, the target was wrapped into an isolating foil (8 μm Mylar and 2 μm aluminium). During the run period, the target was cooled down with liquid nitrogen to approximately 20 K.

Figure 2.4.: The target container of liquid hydrogen, LH_2, target. The length of the target cell was 100 ± 1.0 mm, with a density of $4.249 \cdot 10^{23}$ protons/cm^2. Reproduced from [68].

2.3.2 Frozen Spin Target

For the measurement of double polarisation experiments, a special frozen spin target is used for the polarisation of the protons and deuterons of the target. A specially designed large horizontal $^3He/^4He$ dilution refrigerator was built to use the frozen spin method, through which the spin is virtually "frozen" by the low cooling of the target. A technical drawing of the frozen spin target is shown in Fig. 2.5.

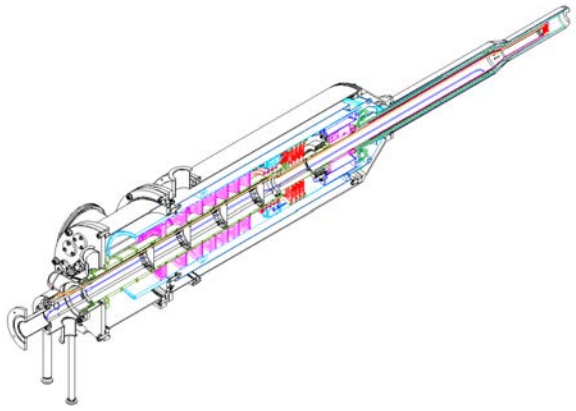

Figure 2.5.: Technical drawing of the frozen spin target. The butanol is placed into the target and cooled down with a $^3He/^4He$ mixture to $T \simeq 10$ mK. Figure taken from [68].

The highest nucleon polarisation of the target can be reached by Dynamic Nucleon Polarisation (DNP), which is a microwave pumping process. To reach the highest nucleon polarisation degrees, low temperatures and a high magnetic field are necessary. For the achievement of a high nucleon polarisation, the target is located in a cryostat with a temperature of 200 mK and an applied magnetic field of 2.5 T and polarised by applied microwaves [66]. If the target polarisation is high enough, the pumping process of the microwaves is switched off. A thin superconducting holding coil, which generates a magnetic field of 0.7 T, is put into the polarisation refrigerator to maintain the nucleon polarisation. Special spin configurations can be produced by the different superconducting holding coils, which make longitudinal and transverse target polarisation possible. More information about the DNP method and the maintenance of the polarisation in the frozen spin target are discussed in Section 3.3.

The polarisation observables are measured with a butanol (C_4H_9OH) target because of the good polarisation properties of this material: (1) the high ratio of the polarizable protons of the hydrogen contribution to the unpolarised protons of the carbon contribution (high dilution factor), (2) the high polarisation degree, which can be reached in short times, (3) the long relaxation times of the polarisation, (4) the polarisation stability over a long period of time, and (5) the easy handling and manufacturing of the material. The target container, shown in Fig. 2.6 (a) consists of Teflon, which has no free protons and does not influence the polarisation degree

of the polarised target protons. It has a length of 2 cm and a diameter of 2 cm and is filled with a filling factor of 60% with roughly 2 mm diameter butanol spheres. The target proton number of the butanol spheres, including the dilution and filling factor, is $N_t \approx 9.181 \cdot 10^{22}$ protons/cm^{-2} [67]. In the butanol target, the number of polarised protons is $N_H = 9.181 \cdot 10^{23}$ protons/cm^{-2}, the number of unpolarised carbon protons is $N_C = 3.672 \cdot 10^{-22}$ protons/cm^{-2}, and the number of unpolarised oxygen protons is $N_O = 9.181 \cdot 10^{-21}$ protons/cm^{-2}. A picture of the frozen butanol spheres is shown in Fig. 2.6 (b). From the butanol spheres, the surface is increased, which makes the cooling of the target under 1 K easier. At first, the frozen butanol spheres are cooled down in the cryostat with liquid nitrogen and later with a $^3He-^4He$ mixture. The average proton polarisation for the used butanol beamtimes is 70% with a relaxation time of about 1500 hours. The polarisation degree was measured with a Nuclear Magnetic Resonance (NMR) technique, which is explained in detail in Section 3.3.

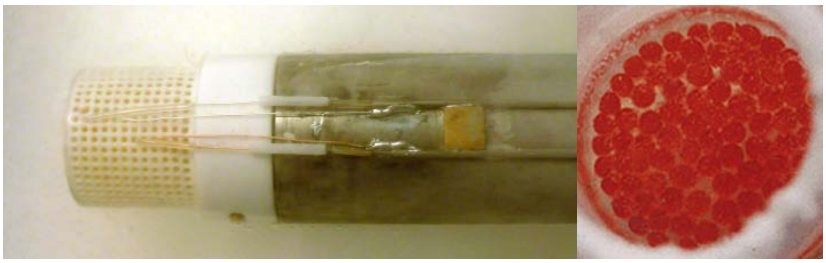

(a) Butanol container (b) Butanol spheres

Figure 2.6.: (a) Butanol container. (b) Butanol spheres. Figure taken from [34].

2.3.3 Carbon Target

A carbon target is measured with the same experimental conditions as the butanol target for the understanding of the unpolarised background in the butanol. To have the same conditions, a carbon foam cylinder is put into the same Teflon container, which is used for the butanol target [67]. The density of the foam cylinder is given by $N_T \approx 0.57$ g/cm^3 and matches with the density of the carbon in the butanol. The carbon target is shown in Fig. 2.7.

Figure 2.7.: The carbon target used for the measurement of the unpolarised carbon background. Figure taken from [68].

2.4 The Detector Setup

The detector setup of the A2 collaboration consists of the Crystal Ball (CB) as the main calorimeter [69], the Particle Identification Detector (PID) [70], the TAPS detector [71], [72], and the multi-wire proportional chamber [73], [74], as shown in Fig. 2.8.

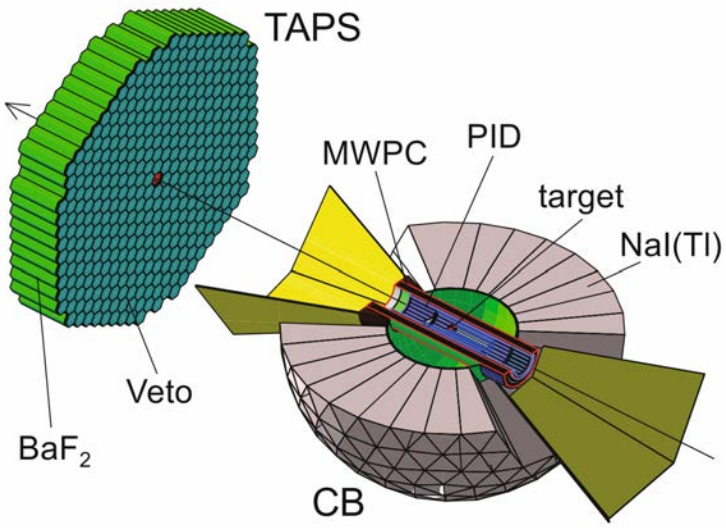

Figure 2.8.: The detector setup of the $A2$ experiment consists of the Crystal Ball as the main calorimeter, TAPS as a forward spectrometer, and the PID and MWPC for the identification of charged particles. Figure taken from [75].

2.4.1 The Crystal Ball Spectrometer (CB)

The Crystal Ball (CB) detector is one of the main components of the A2 experimental detector setup. The CB [69], [76] was built by Stanford Linear Accelerator Centre (SLAC) and was used for the first J/Ψ measurements. The spectrometer consists of two hermetically hemispheres, as shown in Fig. 2.9 (a). These two spheres consists of highly segmented optically isolated thallium doped sodium iodide (NaI(TI)) crystals. In total, the CB detector consists of 672 NaI(TI) crystals with 15.7 radiation length thickness. The geometry of the ball is based on that of an icosahedron. The surface of the CB consists of 20 triangular faces, major triangles which are divided into four minor triangles, each consisting of nine separated crystals. With this arrangement, it would be possible to install 720 crystals, but the detector has an entrance and an exit hole for the beam and so 48 crystals are not installed. Each crystal is shaped like a truncated triangular pyramid with a height of 40.6 cm, as shown in Fig. 2.9 (c). The crystals point towards the centre of the ball, where a spherical cavity is constructed for the target. The spherical shell has an inner radius of 25.3 cm and an outer radius of 66.0 cm. Each NaI(TI) crystal is read out by a PMT. The CB detector covers 92.3% of 4π steradians. The non-covered solid angle is due to the two 1.6 mm stainless

shell plates separated by the 5 mm air gap in the equator region and the missing crystals in the beam line.

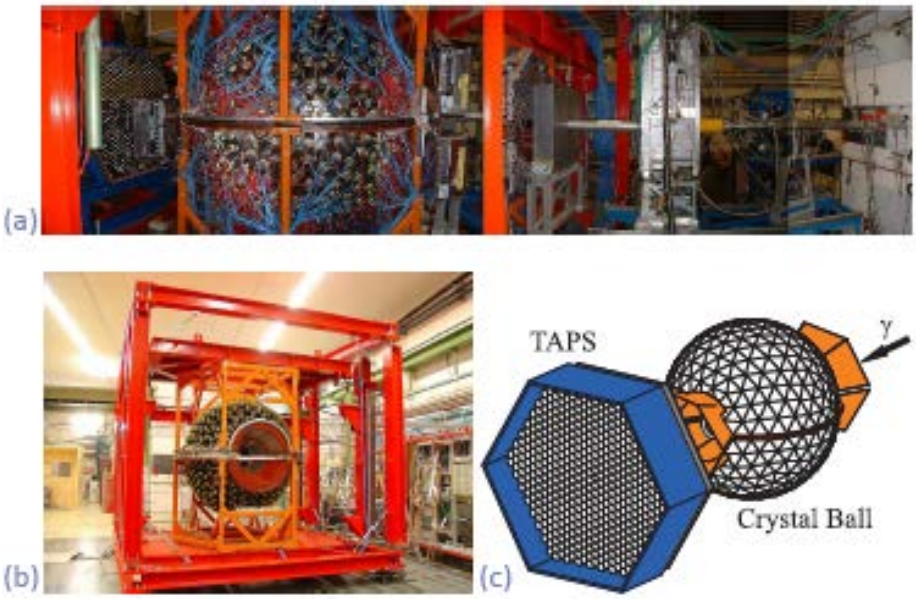

Figure 2.9.: (a) Overview of the position of the Crystal Ball in the A2 experiment. From left to right: TAPS, Crystal Ball the incident photon beam (b) Crystal Ball (c) Crystal Ball combined with the TAPS. Figure taken from [77].

2.4.2 Particle Identification Detector (PID)

In order to distinguish between neutral and charged particles detected in the Crystal Ball, the detector system is equipped with a particle identification detector (PID). The PID consists of 24 single detector elements, which are arranged parallel to the target. The detector is situated inside the CB and surrounds the target with an inner radius of 116.5 mm. A PID element consists of a EJ-204 plastic scintillation counter with a thickness of 4 mm, a width of 15.3 mm, and a length of 500 mm. For the optical isolation, every PID element is wrapped in mylar and black plastic film. One PID element covers 15° in ϕ and the full θ angle region. This results in an angle coverage of θ from 15° degree to 159° and almost complete coverage for the ϕ angles, there are only small gaps between the elements due to the isolating films they are wrapped in, for the full PID detector. The scintillator counters are read out by 9 mm diameter Hamamatsu Photonics $R1635$ PMTs. For the particle identification, the amount of energy deposited in the PID against the energy deposited in CB can be considered. Charged particles travel with a loss of energy through a PID element and will then be stopped in the ball. With this method, the energy loss can lead to an ionization, which can be measured. The different charged particles can then be distinguished in the $\Delta E/dx$ spectra.

2.4.3 The TAPS Spectrometer

The TAPS spectrometer provides particle detection in the forward polar region (angles less than $21°$), which is not covered by the Crystal Ball. TAPS is a highly segmented photon calorimeter, which is composed of 366 barium fluoride BaF_2 crystals and 72 lead tungstate $PbWO_4$ crystals. The BaF_2 crystals have a hexagonal shape with a length of 225 mm and an inner radius of 59 mm. These elements are arranged in 11 rings and in six sectors. The subdivision into six sectors is done for the trigger conditions and can be seen in Fig. 2.10 (a). The two inner rings of the TAPS detector consist of the $PbWO_4$ crystals in which four of these elements have the same size and shape as one BaF_2 crystal. The elements are surrounded by Teflon and aluminium foil to get optical isolation. The inner two rings were replaced by 72 $PbWO_4$ crystals instead of 18 BaF_2 crystals to reach a higher particle rate to handle the higher rates near the beam region. The $PbWO_4$ crystals have a better angular resolution and a higher resistivity rate because of the faster decay time, the smaller radiation length, and the higher density. Both crystal types are connected to a PMT, the BaF_2 crystals are connected to Hamamatsu $R2059-01$ PMTs and the $PbWO_4$ crystals are connected to Photonics XP 1911 PMTs. The BaF_2 crystals have two different scintillation components, one with a fast decay time of $\tau = 0.9$ ns and emission maximal wavelength of 220 nm and the other with a slow decay time of $\tau = 650$ ns and an emission maximal wavelength of 300 nm. These signals are integrated over two different time scales and used for the Pulse Shape Analysis (PSA) to distinguish between photons and neutrons. More can be seen in Fig. 2.10 (b). The angular resolution in ϕ is better than $1°$ and in the azimuthal angle, it improves with increasing θ.

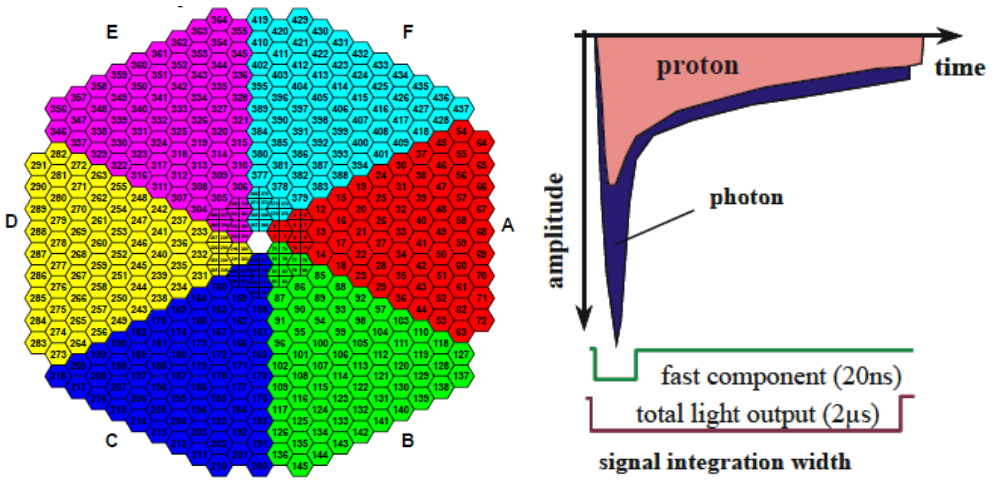

(a) TAPS (b) TAPS Signal

Figure 2.10.: (a) TAPS crystal layout. The different colored segments represent the different logical segments of the TAPS detector. Figure taken from [78]. (b) The two integrated scintillation components of the BaF_2 crystals. Figure taken from [79].

2.4.4 Multi-Wire Proportional Chambers (MWPCs)

The multi-wire proportional chambers allow for the identification and tracking of charged particles. The MWPCS are placed parallel to the beam axis and located between the PID and the CB detector. Both chambers consist of two electrodes located in an ionizing gas mixture of 66% argon, 28.5% ethane, 5% ethanol, and 0.5% freon. The chambers consist of three layers of wire where the middle wire acts as a cathode. The charged particles can then be identified by the additional voltage between the cathodes, which is created through the ionization of the gas by the charged particles. In the gas mixture, the argon contribution induces the charge avalanche by the positive and negative charged particles Ar^+ and e^-. The other gas contributions (C_2H_6 and CF_4) act as an X-ray absorber and electron absorber [73]. The applied voltage between the cathode and the anode should be large enough to prevent a charge recombination, but small enough to prevent a permanent discharging [74]. Usually a voltage of 2400 V is applied to each wire chamber. To cover all possible angles around the target, the cathode stripes are helically arranged at an angle difference of $45°$. Additionally, the inner and outer strip have counter windings. The inner chamber consists of 232 number of wires with 69 internal stripes with a radius of 70 mm and 77 external stripes with a radius of 78 mm. The outer chamber consists of 296 number of wires with 89 internal stripes with a radius of 90.5 mm and 97 external stripes with a radius of 98.5 mm. More information can be seen in Table 2.2.

	Inner chamber	Outer chamber
Number of wires	232	296
Number of internal stripes	69	89
Number of external stripes	77	97
Wire layer radius mm	74	94.5
Internal strip layer radius mm	70	90.5
External strip layer radius mm	78	98.5
Length mm	570	
Angle between wires and stripes	44.23	

Table 2.2.: General characteristics of the Multi-Wire Proportional Chambers (MWPCs). Table taken from [73].

This geometric arrangement and the characteristics of the gas mixture make it possible to not only identify the charged particles, but also reconstruct the trace and the direction of the charged particles. The chambers cover the same angle region as the CB detector, from $21°$ to $159°$ in θ and the complete ϕ range. The information from the six layers of the MWPCs can be combined with the CB detector, which achieves a very high position resolution for the charged particles.
The multi-wire proportional chambers were only operational during the run periods

of butanol (April 2011) and carbon (August 2011) and for the other measurements, the chambers were not used. Some problems occurred during the beam time of April 2011 and August 2011 due to the chemical composition of the ionizing gas mixture and the chambers could not be fully used. Only one MWPC could be used for these beamtimes for the identification and detection of the charged particles. In the used gas mixture, accrued polymer chains from the broken ethanol created an insulation layer on the cathode. This insulation layer prevented the neutralisation of positive ions and thus built an electric field on the cathode [34]. This prevents the correct measurement of the additional voltage between the cathode created by the charged particles because through the created electric field electrons can be pulled out of the cathode and increase this voltage. Thus, the current flow is increased further and further and leads to a destruction of the chambers. Because of that, the chambers often failed and could not be operated at high beam energies. For this reason, the ionizing gas mixture was replaced in 2012 by 67.1% argon, 29.0% ethane, 0.5% freon, and 3.5% methyl alcohol. Due to this change, the chambers operate reliably at higher beam energies.

2.4.5 The P2 Ionization Chamber

The P2 ionisation chamber is used to monitor the beam intensity in relative units. It is located downstream from the target with a diameter of roughly 29 cm and measures the ionisation produced by the photons in metallic plates. For the measurement of the ionisation, given by the photons, the chamber consists of a series of parallel metallic plates with air gaps in between. If a photon hits the metallic plates, an electromagnetic shower is generated and ionises the air. By applying a constant voltage of 40 V to the chamber, the ionisation of the air can be measured by the current. Through a permanent measurement of this current, the photon flux can be monitored during a run period.

2.4.6 Trigger

The measured data cannot be recorded continuously because the detector system has a so-called dead time, which is given through the readout of the detector system and digitalization of the measured data. Only the events which are of the most interest are recorded. A trigger system with good trigger conditions has to be introduced.

E-Sum Trigger

For the trigger system, the information of the total deposited energy in the Crystal Ball is used for the definition of the trigger conditions. The trigger condition is defined by the sum of all energy deposited in the NaI crystals of the Crystal Ball and is therefore, also called the energy sum trigger. The analog signal of each NaI crystal can be read out by the corresponding PMT. All analog signals from the PMT are summed up, which represents the total energy in the Crystal Ball. To select only the events of interest and suppress the background events, a Leading Edge Discriminator (LED) is used. For the decision whether an event will be recorded to a data file or discarded, the signals are discriminated with LEDs. For this, the summarized analog signal is duplicated and evaluated by two discriminators with different conditions. The first level trigger is given by a discriminator with a low threshold and forms a first level trigger condition, which is used to inhibit the system to future signals. A second level trigger condition, which is given by a discriminator with a high threshold defined as the second level trigger, forms the final experimental trigger. The information from all ADCs and TDCs in the detector system is read out and stored if the energy sum signal satisfies the condition of the first level trigger and the second level trigger. For this time, the detector system is uninhibited. If the energy sum signal only satisfies the first level trigger condition, but not the second level trigger, the ADCs and TDCs are cleared and the hardware of the detector system is reset.
For the experiments of this work, the CB energy sum trigger had a minimum trigger condition of 300 MeV. This trigger condition was set in this energy range such that only events are recorded which deposited more than 300 MeV in the Crystal Ball and rejects all events with a lower deposited energy and suppresses the high rate of events from single pion photoproduction.

Multiplicity

Additionally to the second level trigger condition, a multiplicity trigger is used to approximate the number of detected particles. For the implementation of a multiplicity trigger, the Crystal Ball is divided into logical groups consisting of 16 adjacent channels for each crystal. The logical groups contribute to the multiplicity trigger if only one of the crystals register an energy above a CB energy threshold of approximately 30 MeV. For the multiplicity trigger condition, the TAPS detector is also divided into logical groups consisting of six sectors, which have the same threshold condition. If at least one of the sectors is above a certain threshold, the threshold is defined as LED1 threshold and the sector contributes to the multiplicity trigger. Through the definition of the LED1 and LED2 thresholds, a selection of approximated

detected events in the detector system can be chosen. Only approximated detected events can be selected by the multiplicity trigger because of the division into the logical groups, it can happen that the detected particles are over or under estimated. An over estimation exists if a particle is spread out over several logical groups and is detected several times and an under estimation exists when two particles are detected in the same logical group and are detected as only one particle. An overview of the used trigger electronics is given in Fig. 2.11.

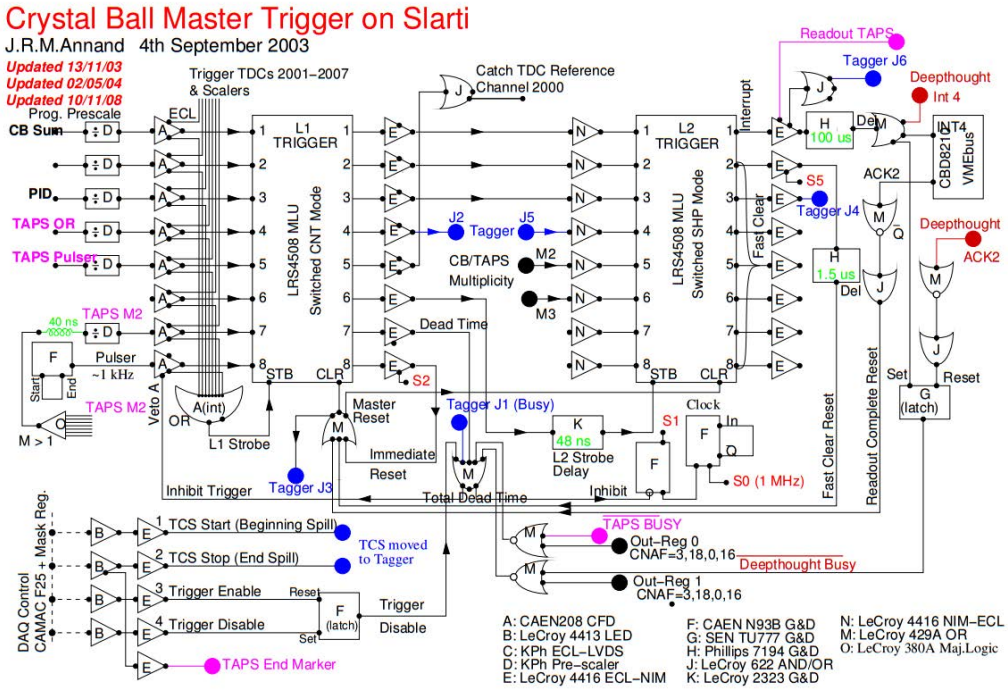

Figure 2.11.: Schematic view of the trigger electronics. Figure taken from [80].

For the experiment of this work, a M2+ multiplicity trigger was used which means that two multiplicity hits or more fulfil the combined trigger condition of the Crystal Ball and the TAPS detector. The multiplicity trigger condition was set that the two inner rings of the TAPS could not contribute to the trigger decision and the complete TAPS could not trigger alone.

2.5 Beamtime Overview

In Table 2.3, an overview of the beamtimes in this analysis is provided. The data sets were measured for the extraction of the polarisation observables F and T. Therefore, a circularly polarised photon beam and transversally polarised target nucleons were used for the measurement of the butanol data (June 2010 and April 2011). For the determination of the unbound polarisable hydrogen protons and the unpolarised carbon contribution of the butanol target, a liquid hydrogen and a carbon target

was measured under almost the same experimental conditions. The polarisation observables can be extracted in two different ways, which remove the unpolarised carbon contribution. The first method is the carbon subtraction method, where the existing carbon background in the denominator of the asymmetries is subtracted, which requires a carbon measurement. The second method is the hydrogen normalisation method, where the hydrogen cross-section is used in the denominator of the asymmetries, which requires a liquid hydrogen measurement. Before the extraction of the polarisation observables F and T, the absolute normalisation of the butanol, liquid hydrogen, and carbon data was checked by the measurement of the total unpolarised cross section of the liquid hydrogen data, as well as the total cross section of the hydrogen contribution of the butanol data.

Parameter	Apr. 2009	Jun. 2010	Apr. 2011	Aug. 2011
beamtime duration [h]	240	-	312	-
electron beam energy [MeV]	1558	1558	1557	1558
electron beam current [nA]	10	12	12	12
tagged photon energy range [MeV]	410-1401	-	-	-
collimator diameter [mm]	4	2	2.5	2.5
radiator material	10 um Cu	10 um Cu	10 um Cu	10 um Cu
target material	LH_2	C_4H_9OH	C_4H_9OH	C12foam
target length [cm]	10.0 ± 0.1	2	2	2
target radius [cm]	4.0	2	2	2
target density [barn^{-1}]	0.421	0.092	0.092	0.057
beamspot radius on target [cm]	1.3	1.3	1.3	1.3
CB energy sum threshold [MeV]	360	350	300	350
multiplicity trigger	M3+	M2+	M2+	M2+
Proportional multi-wire chamber	no	no	yes	yes
Cherenkov	no	no	no	no

Table 2.3.: Overview of the used liquid hydrogen, butanol, and carbon data sets of this work. The data sets are listed (from left to right): hydrogen beamtime 2009, butanol beamtime June 2010, butanol beamtime April 2011, and carbon beamtime August 2011.

3 Beam and Target Polarisation

In this chapter, the creation and the measurement of the beam and target polarisation of the butanol data will be explained in detail. In Section 3.1, the two measurement methods, the Mott measurement and the M∅ller measurement, are explained in relation to the respective advantages and disadvantages. In Section 3.2, the obtained polarisation degree of the photon beam from the helicity transfer from the electrons to the photons is shown. In Section 3.3, the underlying theory of the Dynamic Nucleon Polarisation (NDP) method to calculate the polarisation of the target nucleons is explained, as well as the measurement of the polarisation reached by the Nuclear Magnet Resonance (NMR) method. Finally, the obtained nucleon polarisation degrees of the butanol target are shown.

3.1 Electron Polarisation

The polarisation degree of the electron beam was measured by use of the Mott and the M∅ller measurement. The Mott measurement was performed after the linac accelerator by the use of Mott scattering. For the Mott scattering process produced by a Mott polarimeter, the electron polarisation has to be flipped to a transversal polarisation and the measurement cannot be done during a production run. In contrast to the M∅ller measurement, which measures the original longitudinal polarisation of the electron beam, and has no influence on the measured data. Therefore, the M∅ller measurement can be done during the production runs and has the advantage that the beam actual asymmetry can be continuously measured.

3.1.1 Mott Measurement

In the Mott measurement, the polarisation of the transversally polarised electrons of the beam is determined through a spin dependent Mott scattering on thin unpolarised gold foils. Therefore, the longitudinal electron polarisation was changed to a transversal polarisation. The Mott measurement was performed at beam energies of 3.65 MeV after the linac accelerator [34]. The differential cross section of the Mott

scattering [81][82], the scattering of the transversally polarised electrons on a thin unpolarised gold foil, is given by:

$$\frac{d\sigma}{d\Omega} = \frac{d\sigma_M}{d\Omega} \cdot [1 + P_t \cdot S(\theta, E) \cdot \sin(\phi)], \tag{3.1}$$

where $d\sigma_M/d\Omega$ is the differential cross section of the polarisation independent Mott scattering cross section, P_t is the degree of the transverse polarisation of the electron beam, $S(\theta, E)$ is the Sherman function, which depends on the atomic number Z of the gold foil, the scattering angle θ, and the scattering energy E, and ϕ is the azimuthal angle. The Sherman function is used for the determination of the polarisation degree, which only appears through the scattering on the gold foil with an unpolarised electron beam. The measurement of the count rate of the scattered transversally polarised electrons by two detectors, which have an angle of $\phi_1 = 90°$ and $\phi_2 = 270°$, respectively, defines an θ angle dependent asymmetry A [82] [83] according to:

$$A(\theta) = \frac{\frac{d\sigma}{d\Omega}(\phi_1) - \frac{d\sigma}{d\Omega}(\phi_2)}{\frac{d\sigma}{d\Omega}(\phi_1) + \frac{d\sigma}{d\Omega}(\phi_2)} = \frac{N_L - N_R}{N_L + N_R}. \tag{3.2}$$

By inserting the differential cross section of the Mott scattering given in Equation (3.1) into the asymmetry Equation (3.2), the asymmetry A is then proportional to the electron beam polarisation:

$$A(\phi) = P_t \cdot S(\theta, E). \tag{3.3}$$

Since thin gold foils are used for the Mott measurement, the scattering process of the transversally polarised electrons are single elastic scattering processes. For these single scattering processes, the Sherman function can also be calculated and the polarisation of the transversally polarised electrons can be determined.
To prevent an influence of the detectors, i.e. different detector efficiencies, the asymmetry A is measured for electrons with positive and negative helicity [84] according to:

$$A(\theta) = \frac{\sqrt{N_L^+ N_R^-} - \sqrt{N_R^+ N_L^-}}{\sqrt{N_L^+ N_R^-} + \sqrt{N_R^+ N_L^-}}. \tag{3.4}$$

3.1.2 Møller Measurement

In the Møller measurement, the polarisation degree of the longitudinal polarised electrons is measured at the location of the radiator. For the measurement, a Møller spectrometer consisting of a $10\ \mu$m thick ferromagnetic vacuflux foil (soft magnetic cobalt-iron-alloy) can be magnetized by an external magnetic field. The scattering

of the electrons in the MØller target is dependent on their spin orientation. The MØller cross section for the double polarisation given by the polarisation of the beam electrons and the target can be divided into a spin-dependent and spin-independent part according to [34]:

$$\left.\frac{d\sigma}{d\Omega}\right|_{pol} = \left.\frac{d\sigma_0}{d\Omega}\right|_{unpol} \left(1 + \sum_{i,j} a_{ij} P_i^B P_j^T\right), \text{ with } i,j = x,y,z \tag{3.5}$$

where a_{ij} is the analysis strength coefficient, which depends on the scattering angle and defines the strength of the coupling, P_i^B and P_j^T are the ith and jth component of the polarisation of the beam electrons and the target electrons, respectively. For the measurement of the polarisation of the beam electrons, the coincident beam and target electrons with correlated angles and energies are measured for each spin orientation (parallel or antiparallel) to the electrons in the radiator. The MØller cross section is sensitively to the longitudinal and transverse components of the beam polarisation and a large asymmetry A is measurable for parallel and antiparallel spins of electron beam and target. This asymmetry A is given by the different spin orientation of the beam electrons and the target electrons as:

$$A = \frac{N^{\uparrow\downarrow} - N^{\uparrow\uparrow}}{N^{\uparrow\downarrow} + N^{\uparrow\uparrow}}, \tag{3.6}$$

where $N^{\uparrow\uparrow}, N^{\downarrow\downarrow}$ and $N^{\uparrow\downarrow}, N^{\downarrow\uparrow}$ are the number of scattered MØller electrons with parallel and antiparallel spin orientation, respectively. Since electrons are fermions, their total wave function has to be antisymmetric due to the Pauli principle. This means that the spatial wave function of the scattered MØller electrons has to be antisymmetric due to the symmetric spin wave function of the parallel spins. The antisymmetric spatial wave function can be evaluated by Legendre polynomial expansions, which disappears for scattering angles of $90°$ [85]. Therefore, the measured number of scattered MØller electrons with antiparallel spin orientation is much higher than for parallel spin orientations.
The longitudinal polarisation of the electron beam can then be extracted from the analysis strength coefficients and the measured MØller target polarisation P_T by:

$$P_{long} = \frac{A}{P^T \cos(\alpha)\, a_{zz}}, \tag{3.7}$$

where $\alpha = 25°$ is the angle of the vacuflux foil to the beam axis [34] and a_{zz} is the asymmetry coefficient. The systematic uncertainty of the polarisation degree of the electrons by the MØller measurement compared to the Mott measurement is higher due to instable efficiencies of the tagger discriminators, the beam guidance, and the inaccuracies in the polarisation of the foil and other effects. However, with the MØller measurement, it is possible to monitor continuously the beam asymmetry.

3.2 Photon Polarisation

The photon polarisation is given via the helicity transfer by the detected scattered electrons in the tagger and the corresponding electron polarisation degree. The photon polarisation degree was then calculated by using Equation (2.4) with the polarisation degree values obtained through the Mott measurements. The energy dependent helicity transfer from the electrons to the photon beam is shown in Fig. 3.1.

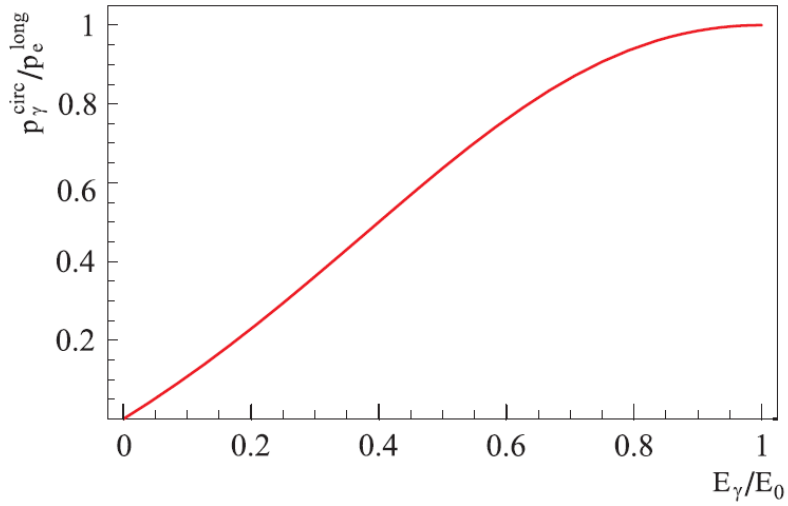

Figure 3.1.: The energy dependent helicity transfer from the electrons to the photon beam. Figure taken from [66].

The photon polarisation for the butanol data (June 2010 and April 2011) was given via the helicity transfer of a longitudinally polarised electron beam with an energy of 1557 MeV and a polarisation degree of around 80%.

3.3 Target Polarisation

Particles with a spin $\vec{s}$ have a magnetic moment μ, which interacts with an applied magnetic field. The interaction between the magnetic moment μ and the external magnetic field leads to a raising of the energy degeneracy and splits the energy levels into $(2s+1)$ Zeeman sub-levels. The energy spacing accordingly to the Zemann effect [86] is defined by:

$$\Delta E = -g\mu_m m B_z, \tag{3.8}$$

where g is the Landé factor, $m = -s, -s+1, ..., +s$ is the magnetic quantum number, and μ is the magneton of the spin particle. In the thermal equilibrium, the energy levels are occupied corresponding to the Boltzmann distribution [87]:

$$\frac{N\left(E+\Delta E\right)}{N\left(E\right)} = e^{\frac{-\Delta E}{k_B T}}, \tag{3.9}$$

where N is the occupation number, ΔE is the distance between the degenerated energy levels, k_B is the Boltzmann constant, and T is the lattice temperature. The polarisation of a spin $1/2$ particle ensemble is given by the occupation number of the two spin states, spin up $N_\uparrow$ and spin down $N_\downarrow$ according to:

$$P_{1/2} = \frac{N_\uparrow - N_\downarrow}{N_\uparrow + N_\downarrow}. \tag{3.10}$$

By inserting the corresponding Boltzmann distribution given by Equation (3.9), for the occupied spin states in Equation (3.10) the polarisation is then given by:

$$P_{1/2} = \tanh\frac{\mu B}{k_B T}. \tag{3.11}$$

A high polarisation can thus be achieved by a strong magnetic field and a low temperature.

For the extraction of the polarisation observables F and T a butanol target was used. The butanol target nucleons were polarised by the Dynamic Nucleon Polarisation (DNP) method. In the butanol target, only the free hydrogen protons can be polarised and unpolarised background occur through the bound and spinless nuclei of the carbon and oxygen of the butanol. For the calculation of the polarisation observable, the unpolarised carbon and oxygen nuclei are an advantage because otherwise they would influence the nominator of the asymmetries.

For the polarisation of the free hydrogen protons, the butanol target was put into the cryostat and cooled down to a low temperature of roughly 10 mK. The split into the Zeemann levels of the hydrogen protons is induced by an external static magnetic field in the z-direction of approximately $B_z \approx 2.5$ T [66]. The electrons in the hydrogen atoms occupy two different Zeemann levels with $m = +1/2$ and $m = -1/2$ corresponding to the electron spin of $I = 1/2$. A level transition with $\Delta m = 1$ of the electrons can be induced by applying a radio-frequency (rf) field with a frequency close to the Lamour frequency ν_e. Due to these induced transitions, the electrons are forced into a Zeemann level and thus polarise the electrons. This can be done at moderate magnetic fields and temperatures because of the electrons' small mass and thus a high magnetic moment, given by the high gyromagnetic ratio of $\gamma_s = g\mu_e/\hbar$ of the free electrons, where g is the gyromagnetic factor, μ_e is the magnetic moment of the electron, and $\hbar$ is the reduced Planck constant. The electron polarisation is transferred to the neighbouring proton in the butanol target material due to the interaction between the dipoles and the resulting coupling between them.

This has the advantage that a direct polarisation of the protons is not necessary, which would be only possible at much higher magnetic fields and lower temperatures because of their low magnetic moments of $\mu_e \approx 660\mu_p$. Due to the Zeemann effect, the two levels of the electron combined with the two levels of the proton results in four different coupled levels, as shown in Fig. 3.2.

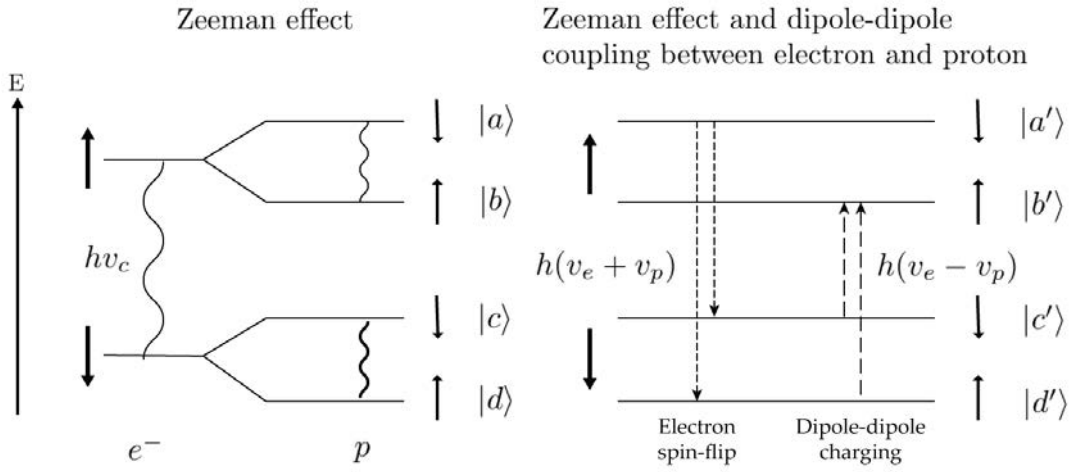

Figure 3.2.: Sketch of a coupled electron nucleon system in the magnetic field with the different Lamour-frequency to induce a spin up or a spin down polarisation. Left side: Zeemann levels of the electrons and the nucleus and Right side: Zemann splitting under the consideration of the dipole-dipole interaction between the electrons and the nucleons. Figure taken from [88] and [34].

The four different coupled levels are defined by the spin states of the electron and the protons according to:

$$|a\rangle = |\uparrow\downarrow\rangle, \qquad |b\rangle = |\uparrow\uparrow\rangle \tag{3.12}$$

$$|c\rangle = |\downarrow\downarrow\rangle, \qquad |d\rangle = |\downarrow\uparrow\rangle, \tag{3.13}$$

whereby the following notation is used: for $|\uparrow\downarrow\rangle$ the first arrow denotes the spin state of the electron and the second arrow state described the spin state of the proton. The spin states for spin-up and spin-down are parallel or antiparallel oriented to the direction of the applied magnetic field. Due to the dipole-dipole interaction between the electron and the protons, pure states cannot exist and only the following superposition's of pure states can be produced [34]:

$$|a'\rangle = |a\rangle + q|b\rangle, \qquad |b'\rangle = |b\rangle + q|a\rangle \tag{3.14}$$

$$|c'\rangle = |c\rangle + q|d\rangle, \qquad |d'\rangle = |d\rangle + q|c\rangle \tag{3.15}$$

with $q \approx 1\%$.

The mechanism to induce a nucleon polarisation caused by the polarisation of the electron in the target is described by the Solid State Effects (SSE). The spin of the

electron and thus their polarisation in the butanol target can be flipped by applying microwaves with the transition frequency [86] according to:

$$\nu_+ = \nu_e + \nu_p \quad \text{and} \quad \nu_- = \nu_e - \nu_p, \tag{3.16}$$

where ν_e and ν_p are the electron Larmour-frequency $\nu_e = \mu_e B/\pi\hbar$ with the Bohrsche magneton of the electron $\mu_e = 9.274 \cdot 10^{-24}$J/T, and the nucleon Larmour-frequency $\nu_p = \mu_p B/\pi\hbar$ with the Bohrsche magneton of the proton $\mu_p = 1.410 \cdot 10^{-26}$ J/T, respectively. This transition frequency generates a spin flip of the electrons, which is then transferred to the proton and leads to a spin-up polarisation and a spin-down polarisation, respectively. By the application of a radiofrequency field (rf) with frequencies of $\nu^{\pm}$ transitions from $|d'\rangle \rightarrow |a'\rangle$ and $|c'\rangle \rightarrow |b'\rangle$ are made possible, which then decay within their relaxation time back into the $|c'\rangle$ and $|d'\rangle$ states. Since the electrons have a much smaller relaxation time $(T \approx ms)$ compared to the protons $(T \approx h)$, the electrons transfer their polarisation to the protons and afterwards go through spin-lattice interaction radiation-free back to their unpolarised original state, where they can again be polarised by the Lamour-frequency microwaves. These interactions and therefore the polarisation of the proton target can be improved by chemical radicals, which create paramagnetic centres in the butanol target [86]. For the butanol target, pophyrexid was used as a chemical radical and the butanol target consists of 95% butanol $+4.5\%$ water $+0.5\%$ radical [88]. The microwave frequency is applied until the maximum polarisation degree of the target proton is reached and then the polarisation magnet is removed and replaced by a small holding coil with a magnetic field of approximately 0.7 T in order to maintain the polarisation [66]. For the measurement, the butanol target was further cooled down to T$\simeq 10$ mK by a $^3He/^4He$ dilution refrigerator to put the target into the frozen spin mode. Since the target polarisation has a relaxation time of approximately 1500 hours under these condition, the target has to be repolarised after this time [66].

The polarisation degree of the target protons was measured using the Nuclear Magnetic Resonance (NMR) technique. As mentioned before, for the polarisation of the target protons, a static magnetic field with $B_z = 2.5$ T is applied in the z direction and split-up the different Zeeman levels. For the hydrogen protons, there exists four Zeeman levels corresponding to the dipole-dipole interaction between the electrons and the protons, as shown in Fig. 3.2. The transitions between the four Zeeman levels are then generated by a high-frequency electromagnetic alternating field with a frequency close to the Lamour frequency perpendicular to the main magnetic field. The proton target polarisation degree can then be extracted by the measurement of the NMR signal, the resonance frequency μ_p and the Lamour frequency:

$$\mu_p = g\frac{q}{2m} \cdot B, \tag{3.17}$$

where g is the gyromagnetic factor, q is the charge, m is the mass of the proton, and B is the magnetic field. The NMR signal is measured by a Resistor Capacitor Inductor (RCL) series circuit with a small coil containing a few windings surrounding the target. The measured NMR signals at the Lamour frequency are shown in Fig. 3.3. In (a), the black curve shows the signal of the LC-resonant circuit in the region of the Lamour frequency. The purple curves show the additional signal from the NMR measurement. Depending on the polarization direction, spin-up or spin-down, the obtained signal is positive or negative. In (b), the extracted NMR signal from the target nucleons in the spin-up or spin-down state is shown.

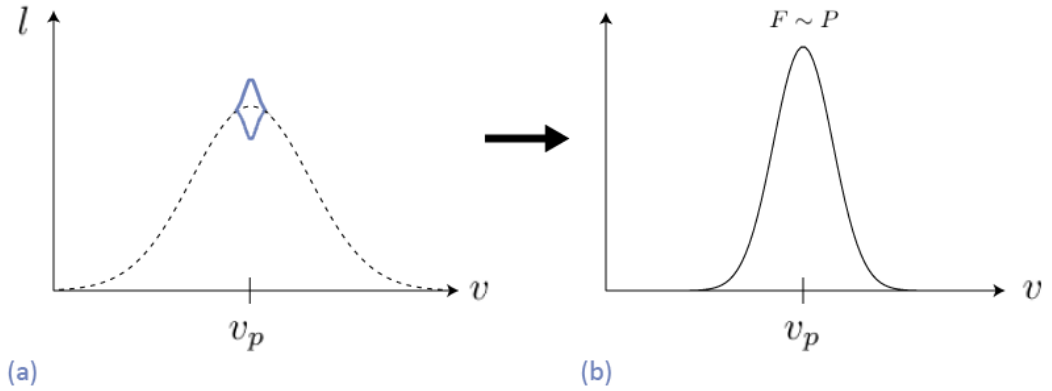

Figure 3.3.: Schematic representation of the NMR measurement [88]. (a) The complete measured resonance signal from the resonant circuit with the Lamour frequency is shown. The dashed line shows the measured resonance signal of the unpolarised target. (b) The extracted resonance signal of the target nucleons in the spin down state is shown from which the target polarisation degree is determined from.

The area under the measured NMR signal is proportional to the different population number of the energy levels and therefore, also proportional to the degree of polarization.
The target polarisation can then be extracted from the measured NMR spectra by using the Boltzmann distribution from Equation (3.9) and derives a relation between the target polarisation P_T and the ratio of the occupation number of the levels with $m = \pm 1/2$. In thermal equilibrium, the measured area F_{nat} corresponds to the polarisation degree P_{nat}. Therefore, the dynamic polarisation P_{dyn} of the butanol target can be determined by the following equation [88]:

$$P_{dyn} = P_{nat} \cdot \frac{F_{dyn}}{F_{nat}}, \tag{3.18}$$

where F_{dyn} and F_{nat} are the measured resonance signal areas with and without the measurement of the polarised butanol target, respectively. The achieved and measured proton target polarisation for the butanol data is shown in Fig. 3.4 (left) for the June 2010 beamtime and in Fig. 3.4 (right) for the April 2011 beamtime.

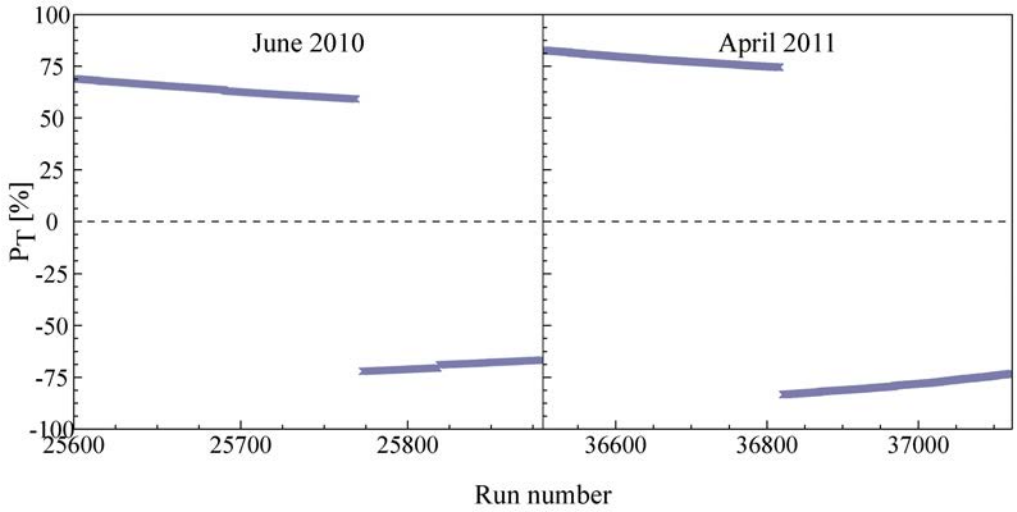

Figure 3.4.: Measured target polarisation for the butanol data June 2010 (left side) and butanol data April 2011 (right side) per run.

4 Software

The following chapter summarizes the software packages and frameworks that were used for the analysis of experimental and simulated data. The data acquisition and a pre-analysis with the application of the calibration values for the experimental and the simulation data is done within the AcquRoot framework. The final evaluation, calculation, and interpretation of the results was done with OSCAR. PLUTO was used as an Monte-Carlo event generator and these events were then simulated with the A2 Geant simulation. The A2 simulation is used to understand the properties of the experimental setup and further interpretation of the experimental data by also simulating the background reactions.

4.1 AcquRoot

AcquRoot is a C++ object-oriented software package based on the CERN ROOT framework [89]. It is used for the data acquisition (AcquDAQ), data analysis (AcquRoot), and the generation of Monte Carlo (MC) events (AcquMC) for the A2 collaboration experiments [90]. For the generation of Monte Carlo events, a PLUTO event generator was used instead of the event generator AcquMC. The data acquisition during the experiment was done with AcquDAQ, which generates binary output files. The binary output files of the experimental data and the simulation created by A2 Geant can be decoded and analysed with the AcquRoot framework. It provides the ability to analyse both the experimental and simulated data with the individual features and physical properties of all the available detectors. The experimental and simulated data are analysed in two different analysis steps: in the first analysis step, the calibration values from the calibration framework CaLib are applied and a pre-event selection is done, which reduces the data set size and in the second step, the pre-sorted data and simulations are analysed with the OSCAR framework to get the final results.

4.2 PLUTO

PLUTO [91] is a Monte-Carlo event generator, which was developed by the HADES Collaboration for hadronic and heavy ion reactions from pion production threshold

to intermediate energies of a few GeV per nucleon. It is written in C++ and is based on ROOT and allows an easy generation of particles with the appropriate physical properties. The individual particles of the simulated reactions are defined in single reactions chains and based on the final state and according to the decay products. Given a specific set of reaction chains, the particle tracks, as Lorentz vectors, are generated. These Lorentz vectors can be generated by the use of different angular distribution models. The needed physical processes, the different decay modes, and the physical properties of the particles are included in an internal database. The possible interactions of these events with the detector material and the generation of secondary particles can then be simulated with the A2 Geant simulation.

4.3 A2 Geant Simulation

For the MC simulation, a A2 Geant simulation package [92] based on Geant4 [93] [94], which was developed at CERN, was used. Geant4 is a C++ toolkit that uses the simulated geometry of a detector and is able to track the passage of a particles through matter.
For the simulations of this work, the entire A2 experimental detector setup containing all detector features and the target was implemented. Geant4 can calculate the possible interactions of ionizing radiation with matter and decay processes, as well as the individual detector responses. The standard package simulates an energy range of 1 keV and upwards and contains all possible interaction process for this energy range [95]. The most common possible interaction processes are the interactions with the target material and the detector material, which produces secondary particles. These include ionization processes, Compton scattering, other multiple scattering processes, photoelectric effects etc. Based on these hadronic and electromagnetic interactions, the particles lose their energy until they are detected by the detector system. Because the detectors are implemented with marked volumes, the simulation delivers the deposited energy and hit times in the detector system. By comparing the total simulated particles and those detected in the detector setup, the detection efficiency of the system can be determined. The detection efficiency is important for the calculation of the cross section, which will be discussed in Section 8.6. The A2 simulation also offers the possibility to simulate the background reactions of the experimental data. Thus, the individual background reactions can be understood in detail and the experimental data can be better interpreted.

4.4 OSCAR

The OSCAR (Simplifies Coding and Analyzing with ROOT) library is a C++ collection of applications and utility classes implemented by D. Werthmüller [78]. These applications and utility classes include:

- A2: base classes for particle reconstruction used in the pre-sort analysis
- analysis: main classes for data analysis
- MC: contains classes for the Monte Carlo event generator
- utils: helper classes for loading, output, and data storage classes
- math: collection of functions and fitting classes
- graph: can be used to create graphs

The graph library has not been used to create the histograms contained in this thesis and instead *jraph* [96] has been used.

4.5 CaLib

CaLib (Calibration Library) is a ROOT-based collection of classes for the calibration of the experimental data of $A2$ experiments. The calibration program was mainly developed by Dr. D. Werthmüller [78].
The calibration of the measured experimental data is necessary since the measured signals of the detector components depend on the actual given conditions of the measurement such as the temperature, the humidity in the air, the supplementation of the used voltage, and on the chosen beamtime settings, e.g. threshold values. These conditions have influence on the detection of the different detector components and thus the response of the identical signals can be different. However, for the evaluation of the measured experimental data, the electronic signals have to be correctly converted into physical quantities and thus, the obtained signals of the detectors have to be calibrated. The calibration has to be time and energy dependent for every detector included in the experimental setup. The time and energy calibration is done for the different detector modules and starts with initial values and is then iteratively improved by several calibration procedures. The final calibrated values are then written into the database and applied before the pre-analysis. Detailed

information about every energy and time dependent calibration of the different detector components are shown in Chapter 6.

5 Event Reconstruction

In this chapter, the methods of the event reconstruction for all the detectors will be discussed. For each detector, different reconstruction algorithms are needed to interpret the measured events. Due to the detector properties, the information of a single particle can be spread over multiple detector crystals. For example, a photon hitting a scintillator produces an electromagnetic shower, which spreads over various detector crystals in the Crystal Ball. For the event reconstruction, all hits in the detector setup have to be combined to clusters and evaluated by a corresponding cluster algorithm of the detectors. Using these cluster algorithms allows for the necessary information such as energy, time, position, and charge of the particle to be determined. The individual cluster algorithms of the detectors for the event reconstruction are discussed in the following sections.

5.1 Tagger

The energy of the bremsstrahlung photons are reconstructed by the photon tagger, as explained in Section 2.2.3. The scattered electrons of the bremsstrahlung process are deflected by the magnetic field and then the momentum of the detected electron is analysed by the photon tagger. The energy of the bremsstrahlung photons can then be calculated by the known initial energy of the electrons and the measured energy of the scattered electrons.
It is essential that the bremsstrahlung photon energy can be properly reconstructed from the bremsstrahlung scattered electrons. For the acceptance of an electron hit in the tagger, a coincident signal has to be detected in two adjacent tagger scintillators. This is important to make sure that only legitimate electron hits are considered and not noise. Since the degree of deflection and the detecting element depends on the applied magnetic field and the energy of the electron beam, a calibration is essential. The magnetic field itself plays an important role for the calibration of the tagger. The uniform magnetic field of the tagger was determined by several measurements [65]. The assignment of the individual tagger elements to the electron beam energy was done by scanning the single tagger elements with a very low electron beam intensity. These measurements have shown that the beam energy from MAMI can be measured up to an uncertainty of 140 keV [65] [59]. The photon tagger is then calibrated based on the electron beam energy, the average value of the magnetic flux density,

and the uniform magnetic field map as a reference. Through this calibration, each tagger element corresponds to a specific bremsstrahlung electron energy range and with the information of the electron beam energy, the energy of the bremsstrahlung photon can be determined using Equation (2.4).

5.2 Crystal Ball

For the particle reconstruction of the Crystal Ball, a cluster algorithm is used based on the detector geometry. The detector is made up of triangularly shaped detector elements. Given this detector element shape, a normal NaI crystal has 12 adjoining crystals and a corner crystal has only 11 adjoining ones, as seen in Fig. 5.1.

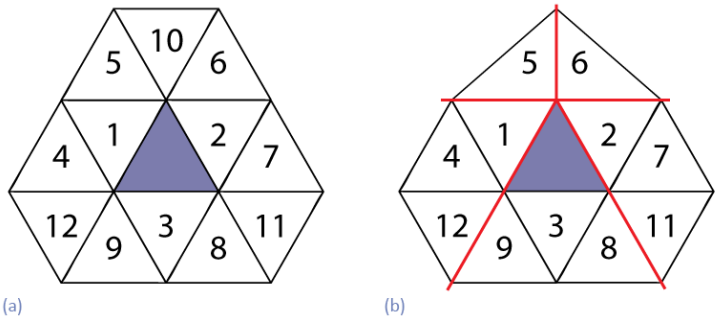

Figure 5.1.: The Crystal Ball detector element and the adjoining crystals for (a) a central crystal and (b) for a corner crystal. Figure taken from [34].

In the Crystal Ball detector, the deposited energy from a particle hit is up to 98% deposited in the hit and the adjoining crystals [70]. For the cluster algorithm, the crystal with the largest deposited energy is assigned as central crystal, and due to the production of an electromagnetic shower when a particle hits the detector, the adjoining crystal with their detected energy are composed to a cluster. Thus, a cluster consists of a maximum of 13 crystals. For the reconstruction of the location of all events, the crystals are ordered by their energy E_i . The crystals with the highest energies correspond to the central crystals of an event and when the adjoining crystals have an energy over a threshold of around 2 MeV, their energy is added to the cluster sum. If a crystal can be assigned to an event, it is removed from the list, so that the elements cannot contribute to other clusters. Thus, the cluster energy $E_{cluster}$ is the sum of all crystal energies E_i, which belong to the cluster by:

$$E^{CB}_{cluster} = \sum_{i=1}^{n} E_i. \tag{5.1}$$

The Crystal Ball is limited to detect only 12 distinct clusters and only the clusters with a total energy over 20 MeV are used for the event reconstruction. The energy threshold of 20 MeV for each cluster is used in order to reduce split-off effects. Such

split-off effects occur, for example, when a secondary photon escapes the cluster and creates an additional artificial cluster.
The cluster position $\vec{x}$ of an event can be calculated by an energy weighting of the individual crystal positions $\vec{X}_i$ by:

$$\vec{x}^{CB}_{cluster} = \frac{\sum_{i=1}^{n} \sqrt{E_i} \cdot \vec{x}_i}{\sum_{i=1}^{n} \sqrt{E_i}}. \tag{5.2}$$

5.2.1 Charged Particle Tracks

For the determination of the particle charge, the hit clusters of the Crystal Ball are compared with the hits in the PID elements and/or the MWPC. For the reconstruction of the charged particle by the PID, only hits with an azimuthal angle of $\Delta\phi < 15°$ between the CB cluster and a PID hit element are accepted. The PID itself only accepts a hit if the signal is above a 350 keV threshold to avoid false positives caused by noise. The hits are weighted according to the polar angle [97]:

$$E^{PID} = E^{PID}_{element} \cdot \sin\left(\theta^{CB}_{cluster}\right). \tag{5.3}$$

The PID determines the azimuthal angle of charged particles, but has no polar angle information. This missing polar angle information could lead to mismatching PID to Crystal Ball events. The MWPC covers the same azimuthal and polar angles as the Crystal Ball, thus, the charged particle can be identified with a higher precision for both angles. The minimum difference in the azimuthal angle $\Delta\phi$ and the polar angle $\Delta\theta$ between the Crystal Ball cluster and MWPC hit was determined by considering the electromagnetic background. Only the hits with very narrow angle ranges of $\Delta\theta < 10°$ and $\Delta\Phi < 10°$ between the CB and MWPCs, respectively were determined as charged particles to reject the electromagnetic background.

5.3 TAPS

The cluster algorithm for the TAPS detector works in the same way as the Crystal Ball detector. The deposited energy of the hits with an energy higher than the threshold of about $3 - 5$ MeV are registered. The TAPS element with the highest deposited energy is again defined as the cluster centre and the adjacent elements with high enough deposited energy are also added to the cluster. In contrast to the Crystal Ball algorithm, all geometrically connected TAPS elements with a deposited energy above a threshold of 20 MeV are combined to a cluster. Thus, the cluster is not limited by hits in the adjacent elements, but all hits are added until no more hits are found in

the adjacent elements. The cluster energy $E_{cluster}^{TAPS}$ is determined by the sum over all iteratively determined element energies E_i:

$$E_{cluster}^{TAPS} = \sum_{i=1}^{n} E_i, \tag{5.4}$$

wherein the maximum number of clusters n is limited to eight. The position of the event is determined by the weighted sum over all positions of the elements of the crystal by:

$$\vec{x}_{cluster}^{TAPS} = \frac{\sum_{i=1}^{n} w_i \vec{x}_i}{\sum_{i=1}^{n} w_i}, \tag{5.5}$$

with a weight w_0, which is based on the deposited energies in the element E_i [98]:

$$w_i = max\left\{0, \left[w_0 + ln\frac{E_i}{E_{cluster}^{TAPS}}\right]\right\} \text{with } w_0 = 0.5MeV. \tag{5.6}$$

The constant w_0 was determined by simulations [99].
Since the TAPS detector system is a flat detector which covers only the forward angle region, the particle travels a certain distance until it hits the detector and produces an electromagnetic shower. For that reason, a polar angle dependent correction on the hit position for the photons has to be performed, as shown in Fig. 5.2.

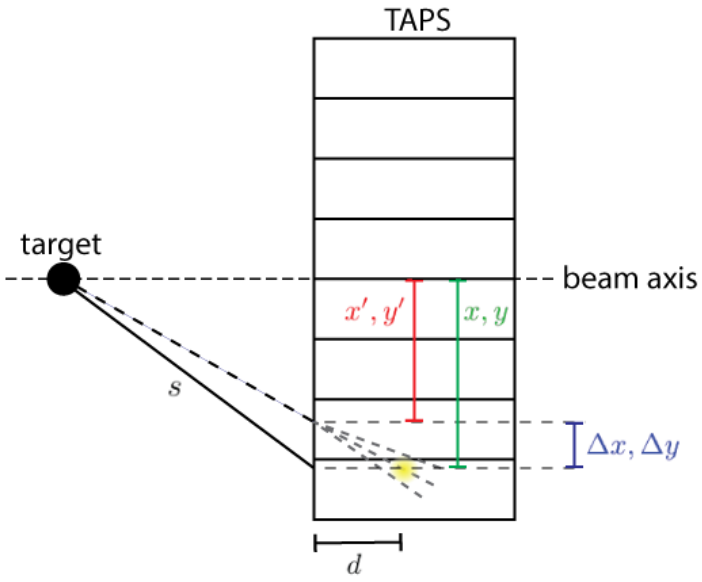

Figure 5.2.: Schematic representation of the impact of the long distance between the target and a hit in the TAPS detector. Figure taken from [100].

The shower depth d depends on the characteristics of the BaF_2 crystals and is given by [98]:

$$d = X_0 \cdot \left(log \left[\frac{E_{cluster}}{E_C} \right] + 1.2 \right) \tag{5.7}$$
$$\text{with} \quad X_0 = 2.05\,\text{cm} \quad \text{and} \quad E_C = 12.7\,\text{cm},$$

where X_0 is the radiation length and E_C is the critical energy. The initial hit position (x, y) has to be corrected by a distance s, which leads to a shift of Δx and Δy of the correct position (x', y'). This correction is done with the following equation [98]:

$$x' = x - x \left(\frac{s}{d} + 1 \right)^{-1} \tag{5.8}$$

$$y' = y - y \left(\frac{s}{d} + 1 \right)^{-1}. \tag{5.9}$$

On the basis of the flight path of a charged particle, it is possible that the charged particle passes the TAPS element and not its corresponding veto element, but a neighbouring one. This is often the case for TAPS elements in the outer rings, where the small angle deviations have more influence on the flight path. Hence, for a correct charge particle reconstruction, all detected TAPS clusters are checked for coincidences with hits in the veto detectors in front of the TAPS element and with the neighbouring veto detectors. If a coincidence is found, the particle is marked as a charged particle. For the vetos, a threshold of $150 - 300$ keV was used to prevent false positives that might be caused by noise.

6 Calibration

In the experiment, the analog signals of the time and energy of the detected particles were stored by Time-to-Digital Converters (TDC) and Analog-to-Digital Converters (ADC) as digital values. To convert the measured digital information in the ADCs and TDCs into physical values, a detector-dependent calibration is necessary. The respective conversion factors of the individual digital values of the ADCs and TDCs are determined by means of the calibration. Since each crystal has its own time and temperature dependence due to its electronics, the calibration factors are determined for each detector module and for different run sets. In the Sections 6.1 and 6.2 the extraction of the energy and time information for every detector will be discussed.

6.1 Energy Calibration

The deposited energy of the particles in the scintillating material of the crystals produces light, which is amplified by the corresponding PMTs or photodiodes and then converted in the ADCs. Thus, the energy information of the different particles is stored as a digital value. Since the produced digital signal c of the ADCs is in first approximation linearly dependent on the deposited energy E of the particles, the following condition applies [78]:

$$E = g \cdot (c - p)\,, \tag{6.1}$$

where g is the conversion gain and p is the pedestal position. When no energy is deposited in a detector crystal, the digital pedestal value is registered in the corresponding ACD. In the energy calibration procedure, the correct pedestal and gain values for each detector crystal have to be defined.

6.1.1 Crystal Ball

In order to correctly calibrate the energy information in the Crystal Ball, two energy calibrations were performed for the low and the high energy range. The low energy range calibration was done with a ^{241}Am/^{9}Be source before the data acquisition. In contrast to the calibration of the low-energy range, the calibration of the high-

energy range was made on the basis of the measured data. Both necessary energy calibrations for the Crystal Ball are described in the following section.

Energy Calibration in the Low Energy Range

As mentioned before, for the low-energy calibration of the Crystal Ball a ^{241}Am/^{9}Be source was used, which emits monochromatic photons with an energy of 4.439 MeV [97]. The Americium in the source decays according to [101]:

$$^{241}_{95}Am \rightarrow ^{237}_{93}Np + \alpha. \tag{6.2}$$

The alpha particles are then captured by the ^{9}Be nuclei leading to excited ^{12}C* nuclei. These excited ^{12}C* nuclei then decay back into the ground state by the following different reactions [101]:

$$\alpha + ^{9}Be \rightarrow ^{13}C^{*} \rightarrow \begin{cases} ^{12}C^{*} + n \\ ^{8}Be + \alpha + n \\ 3\alpha + n. \end{cases} \tag{6.3}$$

For the low-energy calibration of the Crystal Ball, the photons with an energy of 4.438 MeV from the dominant decay of the excited ^{12}C* nuclei into the ground state were used. In the calibration, the conversion gain of all photomultipliers are then adjusted so that, the response of each crystal to the 4.438 MeV photons results in approximately the same position in the ADC spectrum for all Crystal Ball detector elements. An example from a previous calibration of the A2 experiment is shown in Fig.6.1 (a).

Energy Calibration in the High Energy Range

For the calibration in the high energy range the $\gamma p \rightarrow p\pi^{0}$ reaction was used. For this, the invariant mass of the π^{0} mesons were reconstructed from the two decay photons in the Crystal Ball and then compared to the nominal π^{0} mass. For the reconstruction of the invariant mass of the π^{0} mesons, two decay photons were accepted with either one or no proton. The invariant mass of the π^{0} mesons was then reconstructed by the two decay photons in the Crystal Ball according to:

$$\begin{aligned} m_{\gamma_1\gamma_2} &= \sqrt{(p_{\gamma_1} + p_{\gamma_2})^2} && (6.4) \\ &= \sqrt{(E_{\gamma_1} + E_{\gamma_2})^2 - (\vec{p}_{\gamma_1} + \vec{p}_{\gamma_2})^2} \\ &= \sqrt{2E_{\gamma_1}E_{\gamma_2} \cdot (1 - \cos(\phi_{\gamma_1\gamma_2}))}, && (6.5) \end{aligned}$$

where $\vec{p}_{\gamma_1}$ and $\vec{p}_{\gamma_2}$ are the photon momenta, E_{γ_1} and E_{γ_2} are the photon energies, and $\phi_{\gamma_1\gamma_2}$ is the opening angle between the two photons. In the high energy range calibration procedure the gain g is then so determined, that the calculated invariant π^0 meson mass agrees with the nominal pion mass of $m_{\pi^0} = 134.9766$ MeV [15] according to [78]:

$$m_{\gamma_1\gamma_2} \stackrel{!}{=} m_{\pi^0}. \tag{6.6}$$

For this purpose, the calculated invariant mass of the pion was plotted against the central element of the cluster. Before the energy calibration the calculated invariant mass peak is not aligned to the nominal mass and the position of the calculated invariant mass peak $m_{\gamma_1\gamma_2}$ has to be determined. This was done, by fitting the invariant mass spectra with a Gaussian function and a polynomial to determine the signal and the background contribution. An example of this calibration process is shown in Fig. 6.1 (b).

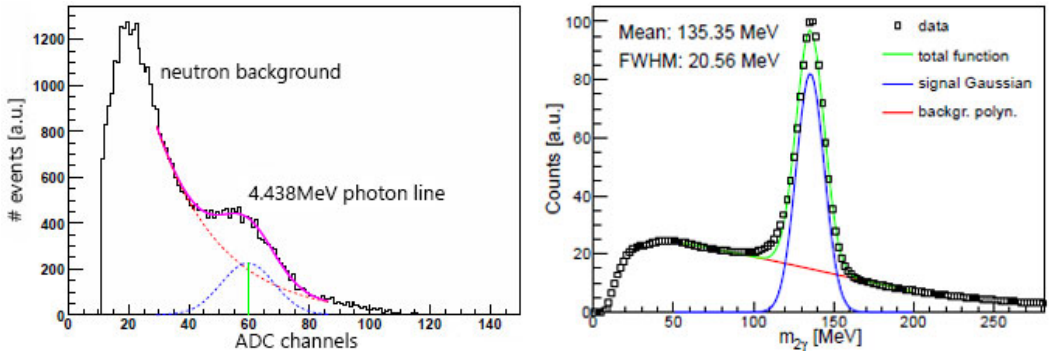

Figure 6.1.: (a) ADC signal from a ^{241}Am/^{9}Be source for one Crystal Ball crystal (black). The neutron background was determined by an exponential fit (red) and the signal of the 4.438 MeV photons was determined by a Gaussian distribution (blue), whereby the mean position of the Gaussian is shown by the green vertical line. The magenta line represents the sum of the signal and the background contribution. Figure taken from [97]. (b) Invariant mass distribution of two decay photons in the Crystal Ball after calibration of the data points (black). The signal was fitted with a Gaussian function (green) and the background with a polynomial (blue). The mean position of the Gaussian is indicated by the black vertical line. The sum of the signal and the background is shown in red. Figure taken from [78].

In the calibration procedure, the invariant mass peak is then shifted to the nominal pion mass by calculating a new gain g, according to the following condition [78]:

$$g = g_0 \cdot \frac{m^2_{\pi^0}}{m^2_{\gamma_1\gamma_2}}, \tag{6.7}$$

The new gain g cannot be calibrated in a single step because the deposited photon energy is not localized in a single cluster but spread over neighbouring elements. Therefore, an iterative procedure is needed. However, after this iteration process, only the invariant mass $m_{\gamma\gamma}$ of the pion is aligned to its nominal mass for each

crystal. A further calibration point can be constructed with the invariant mass of the η-meson. Due to the higher energy decay photons of the $\eta \to 2\gamma$ decay compared to the photons from the pion decay, the invariant mass peak of the η is shifted towards a higher energy as the nominal η mass of $m_\eta = 547.862$ MeV [15]. Therefore, a second order correction was applied to the quadratic function form of the deposited energy E [78]:

$$E' = a \cdot E + b \cdot E^2, \tag{6.8}$$

where E' is the corrected energy and the variables a and b are defined such that the invariant masses of the π^0 and η meson are shifted to the correct position.

6.1.2 TAPS

As with the energy calibration of the Crystal Ball, a calibration of the hardware thresholds of the individual BaF_2 crystals of the TAPS detector were first done before the data acquisition. In order to achieve a very precise energy calibration of the TAPS detector, the long and the short gate was then calibrated in the offline analysis. These calibration procedures are now discussed in more detail below.

Cosmic Calibration

The hardware threshold of the individual BaF_2 crystals of the TAPS detector were calibrated before and after the experiment by measuring the cosmic background radiation. The cosmic background radiation can be used for the calibration since the crystals of the TAPS detector are horizontally arranged and the deposition of the ionizing muons from the cosmic radiation is the same for each BaF_2 crystal [101]. This cosmic calibration has the advantage that it can be carried out at any time and does not require a radioactive source. For the determination of the hardware threshold, the very well-known energy position of the minimal ionising muons of the cosmic background radiation was measured. The energy loss $-dE/dx$ of the ionising muons in the BaF_2 crystal per path length x is given by the Bethe-Bloch equation [102]:

$$-\frac{dE}{dx} = \frac{4\pi n z^2}{m_e c^2 \beta^2} \cdot \left(\frac{e^2}{4\pi\epsilon_0}\right)^2 \cdot \left[ln\left(\frac{2m_e c^2 \beta^2}{I \cdot (1-\beta^2)}\right) - \beta^2\right], \tag{6.9}$$

where $\beta = v/c$ is the velocity of the particle v in units of the speed of light, E is the energy of the particle, $z \cdot e$ is the charge of the particle, ϵ_0 is the vacuum permittivity, n the electron density of the material, m_e is the rest mass of the electron, and I is the average ionisation potential of the material. For the BaF_2 crystals, the

minimum deposited energy of the muons is approximately 37.7 MeV for each crystal according to the crystal thickness of 5.9 cm [103]. Since all BaF_2 crystals of the TAPS are horizontally arranged, as mentioned before, the deposited energy in each ADC spectrum is identical, as shown in Fig. 6.2. In the ADC spectrum of each BaF_2

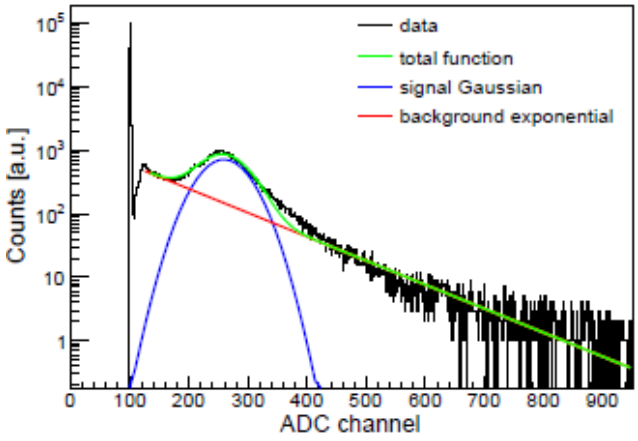

Figure 6.2.: Raw energy spectra of a cosmic background radiation measurement from one BaF_2 crystal. Shown is the obtained signal form the crystal (back), the linear fit function for the determination of the exponential background (red), the Gaussian fit for the determination of the signal (blue) and the total fit function (green). The pedestal peak corresponds to approximately 100 ADC channels. Figure taken from [78].

crystal the pedestal position at 0 MeV and the minimum ionising muons at 37.7 MeV could be determined. The pedestal position at 0 MeV from Equation (6.1), can be defined directly by the left high peak in the ADC spectra. The calibration gain was then determined by fitting the signal of the minimum ionisation muon peak with a Gaussian distribution (blue) and the corresponding background with an exponential fit function (red).

Long Gate Calibration

In the offline analysis, the long gate calibration of the TAPS detector was done by the use of the raw ADC spectra of the measured data runs [78]. For the calibration of the long gate the same calibration procedure with the invariant mass is used as for the energy calibration of the Crystal Ball. Therefore, the long gate was calibrated by calculating the invariant mass $m_{\gamma\gamma}$ of a decay photon in the Crystal Ball and a decay photon in the TAPS and determining the shift to the correct position of the nominal pion mass m_{π^0}. Since the TAPS can only detect the photons within an angle less than $21°$, the statistic of the π^0 mesons, with two decay photons in TAPS is not sufficient for the calibration. Therefore, the gain pedestal calibration requires one decay photon in the Crystal Ball and thus the energy calibration of the Crystal Ball.

Short Gate Calibration

After the calibration of the energies of the long gate, the energies of the short gate were calibrated. The short gate calibration was performed on the PSA spectra by plotting the PSA-radius r_{PSA} versus the PSA-angle ϕ, whereby the PSA-radius r_{PSA} and the PSA-angle ϕ have the following dependence to the short and long gate energies [78]:

$$r_{PSA} = \sqrt{E_l^2 + E_s^2} \tag{6.10}$$

$$\phi = \arctan\frac{E_s}{E_l}, \tag{6.11}$$

where E_l and E_s are the energies of the long gate and short gate, respectively. The ϕ_{PSA} position of the photon band was determined by fitting a Gaussian distribution to the projected photon band of the PSA spectra. This was done for two r_{PSA}-intervals at low PSA-radii of approximately 0 MeV $< r_{PSA} <$ 50 MeV and high PSA-radii of approximately 500 MeV $< r_{PSA} <$ 600 MeV. With the obtained two values of the PSA-angles and the mean PSA-radii the new values of the pedestal and gain were calculated so that the photon band after calibration is at a PSA-angle of 45 degrees. A typical PSA spectrum is shown in Fig. 6.3.

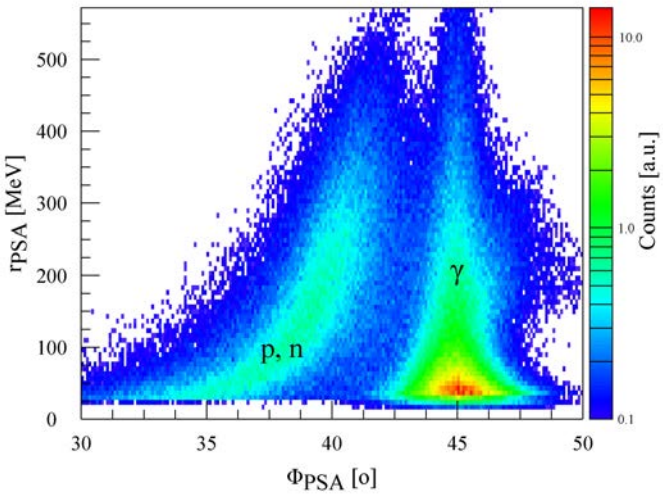

Figure 6.3.: TAPS PSA spectrum of the liquid hydrogen data April 2009: The photon band lies at a PSA angle of 45 degrees and the nucleon band lies at lower PSA angles. The nucleon band has a bent shape because the deposited energy of the nucleons depends on their initial energy and velocity.

Since the nucleons produce a smaller scintillation signal in the TAPS short gate the nucleon band lies at lower PSA angles. After the calibration, the photon band lies

at a PSA angle of 45 degrees and can be clearly separated from the curved nucleon band which is situated at lower PSA angles.

6.1.3 PID

For the PID energy calibration the method described in the PhD thesis of T. Jude [104] was used. In this method, the pedestal and conversion gain values are corrected so that the deposited energy of a proton agrees with the simulated values. The energies deposited in the PID were plotted against the energy deposited in the Crystal Ball. The energy dependent position of the protons was then determined by fitting the proton band in the ΔE versus E spectra with a Gaussian distribution. The obtained values of the mean proton position were then plotted against the MC simulation results and fitted with a linear function. The pedestal and gain values were then derived from the y-intercept and the slope of the linear fit function.

6.1.4 Veto

For the Veto energy calibration, the pedestal position was determined from the raw ADC spectra of the measured runs. Like with the gain calibration of the PID, the ΔE versus E spectra were used and the position of the proton band was shifted to the correct position determined by a MC simulation. For the ΔE versus E the energy in the vetoes was plotted against the energy in the BaF_2 crystals.

6.2 Time Calibration

In the experiment, the detector hit times were channel dependent recorded with time to digital converters (TDCs). Single time signals and multiple time signals can be recorded by the use of Single-Hit-TDCs or by Multi-Hit-TDCs. The relation between the time t and the different TCD channels c is given by [97]:

$$t = g \cdot (c - o)\,, \tag{6.12}$$

where g is a gain factor and o is a freely chosen offset value. The time signal T can be calculated by subtracting the trigger time t_{trig} from the real time t of the detector according to [97]:

$$T = t - t_{trig} \tag{6.13}$$

The inaccurate reference signal from the trigger timing, which is formed by many, non-aligned signals (jitter), could thus be eliminated by the subtraction of a reference time T_2 from the detector time signal T_1 according to [97]:

$$T_1 - T_2 = (t_1 - t_{trig}) - (t_2 - t_{trig}) = t_1 - t_2, \tag{6.14}$$

where t_1 and t_2 are the times of two different detector modules.

6.2.1 Crystal Ball

For a correct time calibration of the Crystal Ball detector, a time walk correction has to be carried out in addition to the calibration of the time signals. A time walk calibration of the NaI(TI) crystals is necessary, since in the low-energy range the crystals are strongly dependent on the deposited energy, the amplitude of the signal. All the necessary time calibration steps to achieve a precise time calibration for the Crystal Ball will be explained in this section.

Time Signal Calibration

Since the time signals in the Crystal Ball are stored by CATCH TDCs with a fixed conversion gain of 0.117 ns per channel only the offset of each NaI(TI) crystals has to be determined. For the first time calibration of the Crystal Ball, the time differences between all cluster hit combinations in the Crystal Ball were calculated depending on the central elements. For this calculation of the time differences only neutral clusters were selected to reduce background contributions. The new individual offset o_i' of each crystal was determined by fitting the time difference distributions of every detector element i by a Gaussian function according to [78]:

$$o_i' = o_i + \frac{\bar{m}_i}{g_i}, \tag{6.15}$$

whereby o_i is the old offset, $\bar{m}_i$ is the mean time, and g_i is the gain of every channel. This calibration was done iteratively until the mean values of all time peaks were aligned to zero.

Time Walk Calibration

Since the signals in the NaI(TI) crystals have a slow rise time and leading edge discriminators (LEDs) are used for the thresholds, the time signals have a strong energy dependence. For the maximization of the time resolution of the Crystal Ball

this time walk effect had to be corrected. For the time walk calibration only events from the π^0-production were used. The events from the $\pi^0 \rightarrow 2\gamma$ reaction were selected by applying an invariant mass cut and a missing mass cut. For the time correction, the spectra of the CB time relative to the tagger time in dependence of the deposited energy of every NaI(TI) crystal, as shown in Fig. 6.4, were fitted with the following function [78]:

$$t\,(E) = a + \frac{b}{(E+c)^d}, \tag{6.16}$$

where E is the deposited energy in the NaI(TI) crystals, and $a, b, ..., d$ are the fit parameters.

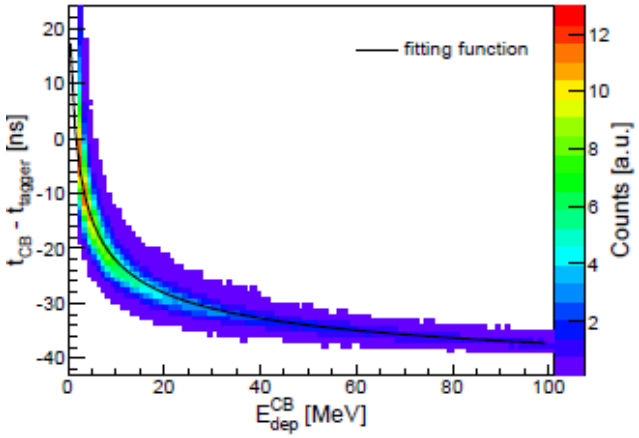

Figure 6.4.: An example of CB-Tagger time versus the deposited energy in the NaI(TI) crystals, fitted with the function of Equation 6.17 from a previous A2 experiment using a liquid hydrogen target. Figure taken from [78]

The fit parameters were individually determined for all detector elements of the Crystal Ball, as shown in Fig. 6.4. The Crystal Ball time t was then corrected by the individual determined fit parameters for every NaI(TI) crystal according to [78]:

$$t_{corr} = t - t\,(E)\,. \tag{6.17}$$

Since the time difference to the tagger was used as a reference, the corrected times t' are automatically aligned around zero. In order to improve the resolution a further final rise time calibration was done. For this purpose, an additional offset parameter a (as defined in Equation 6.16) was determined so that the coincidence time was aligned to zero after the time walk calibration.

6.2.2 TAPS

The fast risetime of the BaF_2 crystals and the long distance of approximately 1.5 m from the target to the TAPS detector make the TAPS detector very suitable for

a Time-of-Flight (TOF) analysis. Therefore, a good time calibration is required for the TAPS detector. In a first step of the TAPS time calibration the TDC gains were calibrated and in a second step the TDC offsets were calibrated. For the TAPS detector, a time walk correction is not necessary, since, in contrast to the LED's, the time signals come from the CFD (constant fraction discriminators) and thus the walk time is already eliminated in the hardware.

TDC Gain Calibration

The TDC conversion gains are usually time calibrated before the experiment. This was done by delaying the common stop signal of all TAPS detectors by inserting different cables with known length and delay times of 10 ns [78]. For the determination of the different delay times of the TAPS elements two measurements were done. In a first step, the exact delay times of the inserted cables were measured using a signal generator and an oscilloscope. In a second step, a TAPS alone measurement was performed to measure the position of the pedestal pulser signal for an increased pedestal pulser frequency. The correct position of the pedestal pulser signal is then determined by fitting the signal peak with a Gaussian function. The differences of the delays are plotted versus the differences of the pulser position for every BaF_2 element and linear fitted. The gain is then extracted by the slope of these linear fit functions.

TDC Offset Calibration

The time offsets for the BaF_2 and $PbWO_4$ elements of the TAPS detector were calibrated after the experiment by using the same calibration procedure as for the time prealignment of the Crystal Ball [78]. Therefore, the time difference of all combinations of neutral particles in TAPS were plotted against the central element of the cluster and fitted with a Gaussian distribution. The new offsets were calculated by Equation (6.15). The final offset can then be iteratively found by repeating this procedure until all peaks are aligned to zero.

6.2.3 Tagger

For the Tagger time measurement CATCH TDCS with a fixed conversion gain per channel were used. Because of the fixed gains, a calibration of only the TDC offsets is necessary. For this calibration, the time difference of a hit in the tagger and all neutral clusters in TAPS for each tagger channel were plotted in a spectrum [78].

Since the tagger time calibration depends on the TAPS time, the TAPS time should be calibrated first. The tagger channel timings are independent and therefore the coincidence peak position has to be determined only once. The new offsets were then calculated by using Equation (6.15).

6.2.4 PID and Veto

For the analysis in this work the PID and Veto times were not used. However, to align the relative timing of the individual detector elements a rough calibration was done by aligning the relative coincidence peaks of the individual detectors to zero.

7 Event Selection

The event selection is based on the cluster information of all the involved detectors in the system. Therefore, a calibration of every cluster has to be made to obtain the correct energy, time, and space information for the reconstruction of the particles. The reconstruction of the neutral $\pi^0\pi^0$ photoproduction events based on the cluster information and the identification of the charged particle, the recoil proton, is explained in the following sections. Furthermore, the different analysis steps for the reconstruction of the reaction and the necessary kinematical cuts for the rejection of the background contributions will also be discussed.

7.1 Event Classes

For the photoproduction from free protons, the following reaction was analysed:

$$\gamma p \longrightarrow \pi^0\pi^0 p. \tag{7.1}$$

This reaction has been analysed for the exclusive case with the detection of the proton as the recoil nucleon and for the dominant decay channel of π^0 [15]:

$$\pi^0 \rightarrow 2\gamma \text{ with a branching ratio of } 98.823 \pm 0.034. \tag{7.2}$$

All other π^0 decay modes were neglected because of their low probability. Due to the analysed decay mode of the π^0-meson, events from the $2\pi^0 \rightarrow 2\gamma 2\gamma$ decay must be separated from the following reactions:

$$\gamma p \longrightarrow \eta\,(\rightarrow 2\gamma)\,\pi^0 p \tag{7.3}$$

$$\gamma p \longrightarrow \eta\,(\rightarrow 6\gamma)\,p. \tag{7.4}$$

These reactions are caused by the incorrect interpretation and reconstruction of the different photons to the two neutral π^0-mesons, such as when a photon or more are mistaken for the reconstruction of π^0 meson. This wrong reconstruction cannot be completely prevented and for the understanding of their contributions in the reaction, the background reactions were simulated.
For the event selection of the reaction, the reconstructed clusters are first divided into neutral and charged particles according to the criteria in Chapter 5. Appropriate to

the number of charged and neutral particles of the analysed reaction, the events were then selected or rejected. For the exclusive analysis of the double π^0 photoproduction of the proton, one charged cluster and four neutral clusters were required.

7.2 Reconstruction of Double π^0

The double π^0 mesons were reconstructed from the identification of the four decay photons out of all the detected particles in the detector. Since the π^0-meson is a neutral particle, only the classified neutral cluster was used for the χ^2 method for the identification. To obtain a better energy resolution, the reconstructed π^0-mesons were corrected with the nominal mass of the π^0-meson.

7.2.1 Identification of the π^0-Decay Photons

The four-vector $(E_{2\pi^0}, \vec{p}_{2\pi^0})$ of two π^0-mesons consists of the four-vectors of the four decay photons $2\pi^0 \rightarrow 2\gamma 2\gamma$ and is defined the energy and momentum conservation as:

$$\begin{pmatrix} E_{2\pi^0} \\ \vec{p}_{2\pi^0} \end{pmatrix} = \sum_{i=1}^{2} \begin{pmatrix} E_{\pi_i^0} \\ \vec{p}_{\pi_i^0} \end{pmatrix} = \sum_{i=1}^{4} \begin{pmatrix} E_{\gamma_i} \\ \vec{p}_{\gamma_i} \end{pmatrix}, \tag{7.5}$$

where $\left(E_{\pi_i^0}, \vec{p}_{\pi_i^0}\right)$ and $(E_{\gamma_i}, \vec{p}_{\gamma_i})$ are the four-vectors of the pions and the corresponding decay photons, respectively. A direct detection of the π^0 meson is not possible due to the fast decay time of the π^0 meson with $\tau = (8.52 \pm 0.18) \times 10^{-17} s$ into 2γ [15]. Therefore, the π^0 events must be reconstructed from their decay products of 4γ, which can be detected by the calorimeter. Since the decay photons are indistinguishable, the corresponding decay photons of a double π^0 event were identified by a χ^2-test. Based on the χ^2-test, the best combination, the two "true" photons of each π^0-meson decay, can be determined. For this, the χ^2 was calculated with the following equation:

$$\chi^2_{ijkl} = \left(\frac{m_{\gamma_i\gamma_j} - m_{\pi^0}}{\Delta m_{\gamma_i\gamma_j}}\right)^2 + \left(\frac{m_{\gamma_k\gamma_l} - m_{\pi^0}}{\Delta m_{\gamma_k\gamma_l}}\right)^2, \tag{7.6}$$
$$\text{with} \quad i,j,k,l = 1,2,3,4 \quad \text{and} \quad i \neq j \neq k \neq l$$

where the indices i, j, k, l stand for the different decay photons, $m_{\gamma_i\gamma_j}$ and $m_{\gamma_k\gamma_l}$ are any initial combinations of photons pairs $\gamma_i\gamma_j$ and $\gamma_k\gamma_l$ of neutral clusters for the first and the second π^0 event, respectively, $\Delta m_{\gamma_i\gamma_j}$ and $\Delta m_{\gamma_k\gamma_l}$ are the corresponding errors of the invariant masses, respectively, and m_{π^0} is the nominal mass of $\pi^0 = 134.9766$ MeV [15]. For the reconstruction of the two pions, all

permutations of the neutral pion pairs are calculated to find the best combination of the photon pairs for which the χ^2-value is minimal. The photon pair combination for the smallest χ^2 were then assigned to the two π^0-mesons. The errors $\Delta m_{\gamma_i\gamma_j}$ and $\Delta m_{\gamma_k\gamma_l}$ depend on the errors given by the neutral clusters as the deposited energy ΔE and the azimuthal $\Delta\phi$ and polar $\Delta\theta$ angles of the four detected photons.

7.2.2 χ^2-Distribution and Confidence Level

The quality of the reconstructed double π^0 events can be verified by the distribution of the χ^2 values of the best photon pairs. For k independent degrees of freedom and normally distributed random variables x_i, the χ^2 values can be calculated by the following equation:

$$\chi^2 = \frac{\sum_{i=0}^{k} (x_i - e_i)^2}{\sigma_i^2}, \tag{7.7}$$

where σ_i is the standard deviation of the expectation values e_i. The corresponding probability density function (pdf) can be defined by a Gamma function $\Gamma(k/2)$ [105] as

$$f(\chi^2, k) = \frac{(\chi^2)^{k/2-1} \cdot e^{-\chi^2/2}}{2^{k/2}\Gamma(k/2)}. \tag{7.8}$$

Therefore, the calculated χ^2 values of the best photon combination are distributed according to a χ_k^2 distribution with $k = 2$ degrees of freedom corresponding to the photon decay of $2\pi^0 \to 4\gamma$. In Fig. 7.1 (a), the normalised χ^2 distributions of the double π^0-reconstruction of the data (solid line) and simulation (dashed line) are shown compared to a sampled χ_2^2 distribution (dotted line). If the background contribution is rejected by the necessary cuts of the analysis, then the data and the simulation are in agreement. Before the cuts were applied, a difference was visible between the simulation and the data, which is caused by the background in the data. The confidence level $W(\chi^2)$ provides another verification of the combination of the photons by the χ^2 method. For this, the probability of a random ζ^2 variable, which has a $f(\chi^2, k)$ distribution, is smaller or equal to a given χ^2- value [105]:

$$W\left(\chi^2\right) = P\left(\zeta^2 \leq \chi_i^2\right). \tag{7.9}$$

The χ^2-values correspond to the confidence levels and for large χ^2-values, the confidence level is small and for small χ^2-values, the confidence level is high. The confidence level distribution of the data (solid line) and simulation (dashed line) are shown in Fig. 7.1 (b). If for the reconstruction of the double π^0 events, the correct photon pairs are combined by the χ^2 method, the χ^2 values are small and the confidence level is flatly distributed. For wrong combinations of the photon pairs

caused by background events, the χ^2 values are high, which results in a non-flat distribution of the confidence level. After the background contribution are rejected by cuts, the wrong combination of the photon pairs by the background events can be prevented in the data and thus, the data and the simulation are in a good agreement. The flat distribution of the confidence level and the agreement between the data and simulation show that with the χ^2 method, the correct combination of the photon pairs are used for the reconstruction of the double π^0 events.

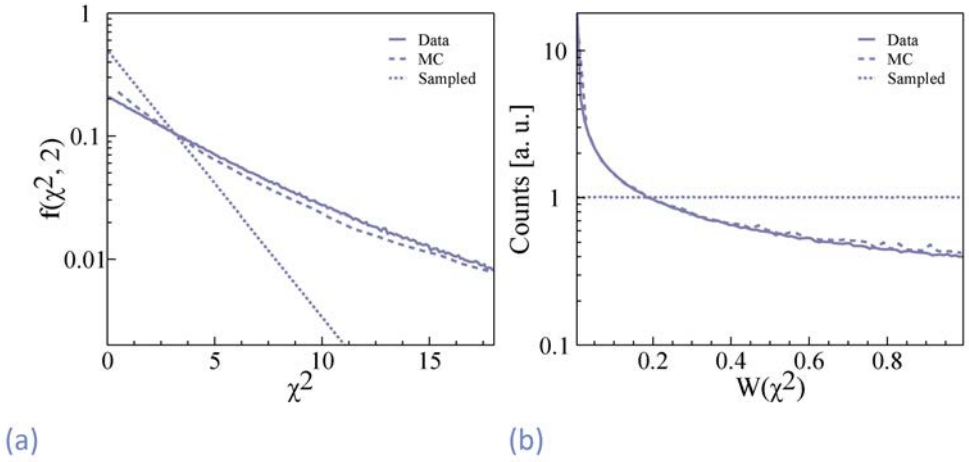

Figure 7.1.: (a) Data (solid line), simulation (dashed line) and sampled (dotted line) χ^2_2 distribution and (b) corresponding confidence level. The distributions are all normalised.

7.2.3 Correction of the π^0-Meson Energy

The invariant mass peaks of both π^0 mesons are located at the energy position of 135 MeV due to the energy calibration of all the detectors using the decay photons of π^0 and η-mesons. However, the invariant mass peaks have finite widths and are approximately normally distributed around the correct nominal mass. Due to this normal distribution of most events, the events in the peak centre have a correct nominal mass and the events with larger deviations from the peak centre deviate more and more from the correct nominal mass. These deviations from the nominal mass m_{π^0} can be corrected event-by-event [100].
The decay photon energy correction is then calculated based on the nominal mass m_{π^0} by:

$$E'_{\gamma_1,\gamma_2} = \frac{m_{\pi^0}}{m_{\gamma_1\gamma_2}} E_{\gamma_1,\gamma_2} \tag{7.10}$$

$$E'_{\gamma_3,\gamma_4} = \frac{m_{\pi^0}}{m_{\gamma_3\gamma_4}} E_{\gamma_3,\gamma_4}, \tag{7.11}$$

and $m_{\gamma_1\gamma_2}$ and $m_{\gamma_3\gamma_4}$ are the measured invariant masses and $E_{\gamma_1\gamma_2}$, $E_{\gamma_3\gamma_4}$ are the photon energies of the first and the second π^0-meson, respectively.
The correction of the two π^0-meson energy is applied after the invariant mass analysis to improve the resolution for the missing mass spectra.

7.3 Time Cuts

Timing information is important for three different reasons. The experiment involves a coincidence between the scattered electron in the tagger focal-plane detector and reaction products detected in the calorimeter. Furthermore, random background from abundant electromagnetic interactions in the production target can contribute to the hits detected in the calorimeter. Finally, time-of-flight information contributes to the identification of particle types.

7.3.1 Coincidence Cuts

Coincidence cuts were used to ensure that the detected photons in the detectors originate from the same reaction. The coincidence time between two photon hits in the Crystal Ball and TAPS detector is shown in Fig. 7.2.

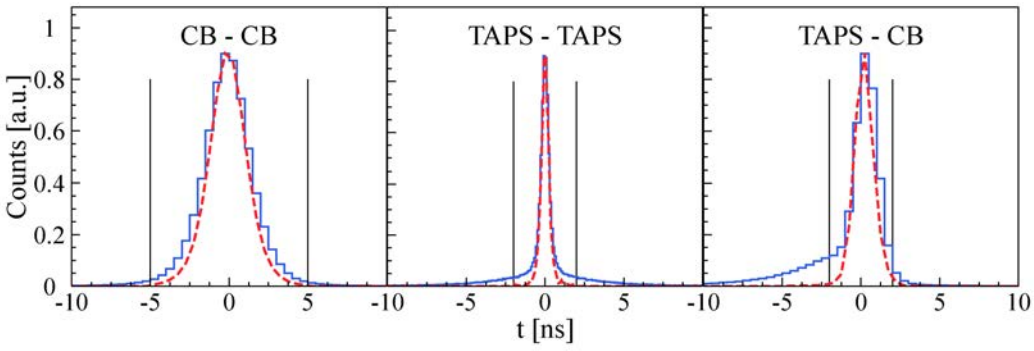

Figure 7.2.: Coincidence time between two photons after the χ^2 method (blue line) and after all analysis cuts are applied (red dashed line). The coincidence time cut positions are indicated by the black vertical lines. The time distribution from left to right denote the time differences from two photons in the Crystal Ball, two photons in TAPS, and one photon in Crystal Ball and one in TAPS.

The coincidence time is shown after the identification of the decay photons of the mesons by the χ^2-test (blue line) and after all cuts were applied (red dashed line). The width of the coincidence peaks come from the different time resolution of the Crystal Ball and TAPS detector. The time resolution of the TAPS detector is better than for the Crystal Ball. Therefore, the width of the coincidence peak of the TAPS-TAPS is narrow, for the CB-CB quite wide, and for the CB-TAPS medium. The

trail on the left side of the TAPS-CB coincidence time peak after the identification of the mesons by the χ^2-test (blue line) occurs due to neutrons falsely assigned to photons. However, these falsely assigned photons are eliminated by the application of the kinematical cuts (mainly by the missing mass cut), which can be seen in the coincidence spectra with the applied cuts (red line). The combination of the χ^2-analysis and the additional cuts removes almost completely these falsely assigned clusters. The applied time cuts for the analysis were chosen relatively wide in order to not remove any real events.

7.3.2 Random Background Subtraction

The Glasgow Tagger Photon Spectrometer is used to determine the energy of the photon from a momentum analysis of the bremsstrahlung electron, as discussed in Section 2.2.3. The tagger registers all bremsstrahlung electron hits during a specified tagger time window. Due to the high intensity of the electron beam during the coincidence window several electrons will produce bremsstrahlung photons. Due to the small hadronic cross-section, not all of the produced bremsstrahlung photons trigger a reaction in the target. Therefore, all scattered electrons that are associated to a photon that interacted in the target are detected in the tagger, but also the additional electrons which produced bremsstrahlung photons that did not induce a reaction in the target. These additional detected scattered electrons are random electrons which cannot be removed by an event-event correction.
The true coincidence electrons which are correlated to the photons that trigger the events can be determined by a statistical subtraction of the uncorrelated background electrons in the tagger-calorimeter coincidence time spectra. For the calorimeter time, the hit times of the decay photons in the Crystal Ball and TAPS were averaged to obtain a better resolution. The tagger-calorimeter coincidence time spectra for the Crystal Ball and TAPS are shown in Fig. 7.3. The background of the uncorrelated electron hits is random and distributed flatly in the coincidence time spectra. Therefore, a sideband subtraction can be used to determine the uncorrelated electron hits (green) and the correlated electron hits (red) in the prompt signal. For the sideband subtraction, the random background distribution is determined using two background windows (blue) next to the coincidence peak. The distribution of the true coincidences in the prompt peak can then be calculated by the subtraction of the normalised random background distribution obtained by these intervals. The random background subtraction was done for the coincidence time between the tagger and a hit in the Crystal Ball or in TAPS, whereby the prompt intervals were determined separately for both timings. To obtain a correct subtraction of the random background hits, the events in the analysis were weighted. The events in the

prompt interval were weighted with $w_p = 1$ and the random events were weighted proportional to their relative time intervals with:

$$w_r = -\frac{\Delta t_p}{\Delta t_{r1} + \Delta t_{r2}}, \tag{7.12}$$

where Δt_{r1} and Δt_{r2} are the widths of the two background intervals, respectively, and Δt_p is the width of the prompt interval. The number of correlated events N_t can then be calculated with the following formula:

$$N_t = N_p + \sum_{i=1}^{N_r} w_r^i = N_p + w_r N_r, \tag{7.13}$$

where N_p is the number of prompt events, N_r is the number of random events, and w_r is the corresponding weighting factor. The statistical error ΔN_t is the square root of the prompt events and the weighted random events and can be calculated by the following formula:

$$\Delta N_t = \sqrt{N_p^2 + w_r^2 N_r^2}. \tag{7.14}$$

The statistical error can be improved by a better determination of the random background distribution by using larger intervals which minimize the weight factor w_r.

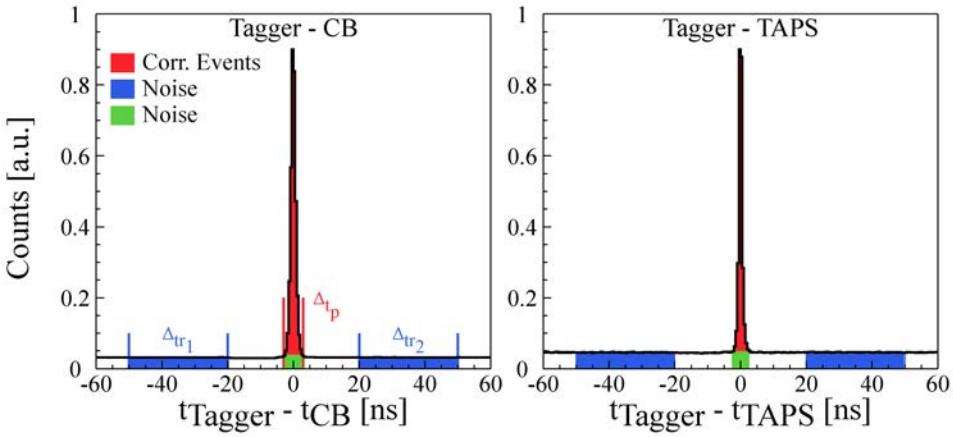

Figure 7.3.: Coincidence times between the tagger and a hit in the Crystal Ball (left) and in TAPS (right). For the determination of the correlated (red) events in the prompt window, the random background events in the prompt window (green) were subtracted and the random background contribution was defined in the random windows (blue).

7.4 Analysis Cuts

For the reaction $\gamma p \to \pi^0\pi^0 p$, exactly four neutral hits and one charged hit were selected. The reaction was analysed for a polarised butanol target for the measurement of the polarisation observables F and T. Since only the unbound hydrogen protons in the butanol target can be polarised, as explained in Section 3.3, the reaction was additionally measured with a liquid hydrogen and a carbon target. For the determination of the free polarisable hydrogen contribution and the unpolarisable carbon contribution in the butanol target, the liquid hydrogen target and the carbon target was measured under almost the same conditions as the butanol target. The polarisation observables F and T can be extracted by two different ways, which eliminate the unpolarised carbon background contribution. As it can be seen in the definition of the polarisation observables, Equations (1.33) and (1.34), in the numerator of the asymmetry there is no unpolarised carbon background and in the denominator, the unpolarised carbon can either be subtracted (which makes a carbon measurement necessary) or the unpolarised hydrogen cross-section can be used (for which a hydrogen measurement is necessary). An overview of the used butanol, hydrogen, and carbon beamtimes can be found in Section 2.5.
In the following sections, the different analysis cuts for the identification of the two neutral pions from their two-photon decays and the recoil proton is explained in detail. In the first sections, the identification of the recoil proton by the pulse-shape analysis (PSA), time of flight (TOF), and ΔE -E analysis is discussed. Then the kinematic analysis such as the invariant mass cut, the coplanarity cut, and the missing mass cut will be discussed. The invariant mass analysis is used to remove the small background contribution of either combinatorial background from the true double π^0 events or from the $\eta\pi^0$ photoproduction after the identification of the two-decay photons by the χ^2 method. The kinematic cuts are used for the identification of the double π^0 reaction of free proton and to remove the background from the existing background reaction channels ($\gamma p \to \eta(\to 2\gamma)\pi^0 p$ and $\gamma p \to \eta(\to 6\gamma)p$), whereby the background channel contribution occurring from the wrong event selection are mainly removed by the missing mass analysis. The incorrect identification of the particles can occur due to inefficiencies of the charged particle detectors and thus a false detection of the neutral and charge particles or because of combinatorial errors in the χ^2-test.
For the analysis, the different analysis cuts were mostly determined from the liquid hydrogen data, and then the same cut positions were used for the polarised butanol data. This was done to ensure that only the free polarisable hydrogen protons of the butanol target are used in the analysis for the calculation of the polarisation observables and no hydrogen background reactions are included in the analysis. For the determination of the liquid hydrogen analysis cuts, the $\gamma p \to \pi^0\pi^0 p$ reaction and the background reactions ($\gamma p \to \eta(\to 2\gamma)\pi^0 p$ and $\gamma p \to \eta(\to 6\gamma)p$) were simulated

and fit to the experimental liquid hydrogen data. For the simulation, the same experimental setup were used as for the measured liquid hydrogen data. The missing mass cuts were then chosen so that these background channel reactions are safely cut away. For the visualisation of the free polarisable hydrogen contribution and the unpolarised carbon contribution of the butanol, the kinematical analysis of the invariant mass cut, coplanarity cut, and the missing mass cut are shown with these contributions. Therefore, the counts of the different analysis spectra were absolutely normalised by the photon flux, the detector efficiency, and the nucleus normalisation of the corresponding data. For the analysis of the butanol data, two different analysis methods were used: the butanol data from June 2010 and the hydrogen data were analysed with the Crystal Ball including the PID and TAPS detector, and for the butanol data from April 2011, the MWPCs were used instead of the PID. For a correct determination of the unpolarised background, the carbon was analysed with both methods.

7.4.1 Pulse Shape Analysis

The nucleons can be distinguished from the photons in TAPS by a Pulse Shape Analysis (PSA). Through this distinction, a clear separation between the nucleons and photons can be achieved by the PSA cuts and a correct identification of the nucleons and photons in the analysis is possible. After calibration, the photon band lies at a PSA angle of $45°$. The nucleons produce a smaller scintillation signal in the TAPS short gate and the nucleon band lies at lower PSA angles. The nucleon band has a bent shape because the produced scintillation signal depends on the initial energy of the nucleons and their velocity. Slower nucleons deposit more energy in TAPS crystals than fast nucleons.
The PSA cut is applied after the identification of the decay photons of the two π^0 events by the χ^2-test. For the PSA cut, the PSA angle is plotted against the PSA radius and the cut position was then determined by a Gaussian fit of the projections of the photon band. The PSA cuts can only be determined and applied on the data because the scintillation light components of the BaF_2 crystals were not simulated. Since the data must be analysed in the same way as the simulation, non-stringent PSA cuts of $\pm 3\sigma$ were chosen to ensure that only the marginal background and no real events are discarded. In the region between 85 and 380 MeV, no PSA spectra cut has been applied, to make sure that no real high-energetic protons, which can be located in this region at large PSA angles, are cut away. The nucleons were cut away with a PSA radius larger than 380 MeV or smaller than 85 MeV when they are located closer than 3σ to the photon band. The PSA spectra for the $2\pi^0 \rightarrow 2\gamma 2\gamma$ decay and the recoil nucleon without (top row) and with (bottom row) analysis cuts is shown in Fig. 7.4. The PSA cut positions are indicated by the black dashed lines.

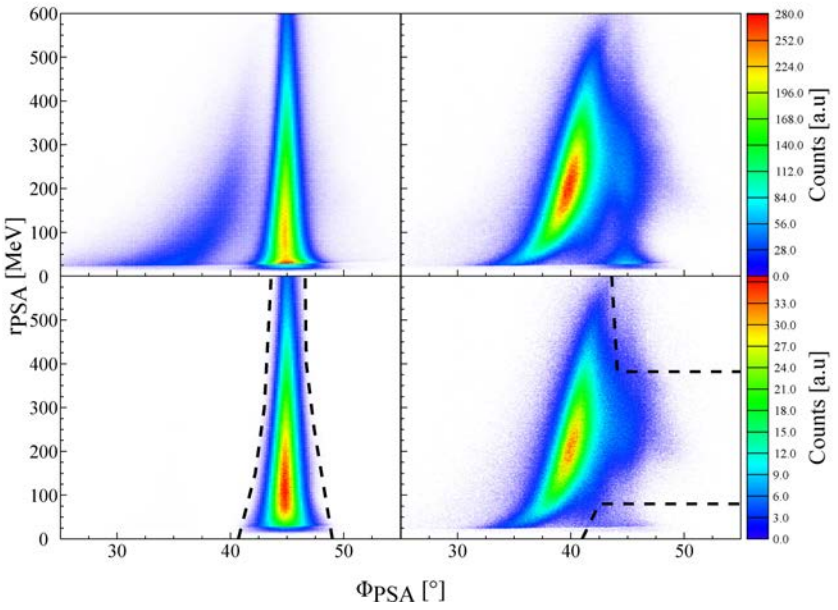

Figure 7.4.: Pulse Shape analysis spectra for the $2\pi^0 \rightarrow 4\gamma$ decay (left) and the recoil proton (right). In the top row, the PSA spectra without the analysis cuts are shown and in the bottom row the PSA spectra are shown with the analysis cuts. The PSA cuts are indicated by the black dashed lines.

7.4.2 Time of Flight

The time of flight (TOF) of a particle depends on the mass of the particle. Lighter particles have a shorter time of flight than heavier particles with the same kinetic energy. For the time of flight analysis, this effect is used to distinguish between the particles with the same kinetic energy and different masses. The main difference between the photons and heavy particles can be distinguished. To achieve a good time resolution for the time of flight measurement, the flight path of the particles and the distance from the target to the detector must be sufficiently large. Due to the large distance from the target to the TAPS detector, approximately 1.5 m, the time of flight measurement was performed for the detected particles in the TAPS detector.

For the comparison of the time of flight of the detected particles, the different flight paths lengths were normalised to 1 m. The time of flight in $[ns/m]$ can be calculated by:

$$t_{TOF} = \frac{\Delta t}{s} + \frac{1}{c}\,[ns/m], \tag{7.15}$$

where Δt is the time difference for a hit in TAPS and the photon tagger and s is the normalised flight paths of the detected particles. The photon tagger was used instead of the Crystal Ball because of the better time resolution. For the normalisation of the photon flight time, a factor of $1/c$ was introduced to compensate for the previous

calibration, which aligns the photon times to zero.
For the TOF spectra, the deposited energy in TAPS was plotted versus the calculated time of flight t_{TOF}. The difference of the TOF of the photons and the nucleons can be clearly seen in the TOF spectra, shown in Fig. 7.5.

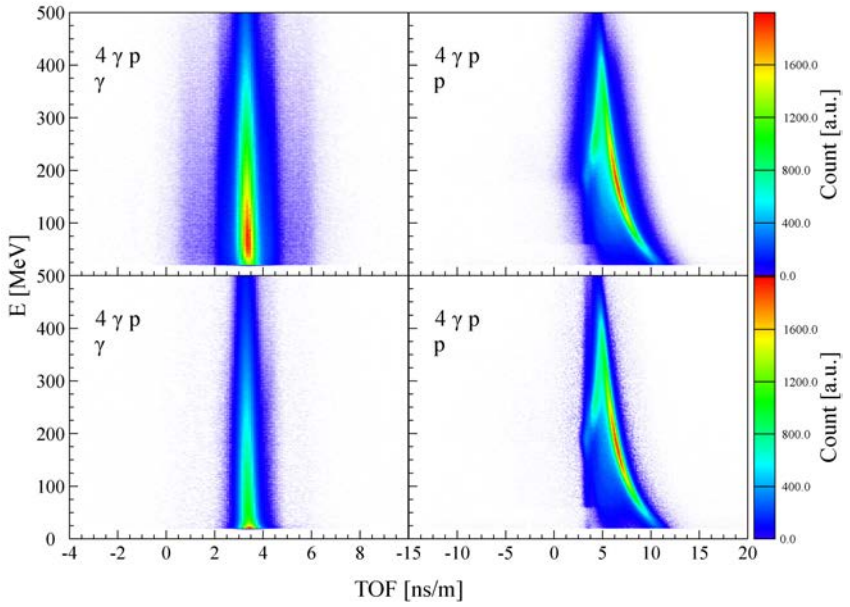

Figure 7.5.: The Time of flight (TOF) versus energy plot for TAPS for the photons (left side) and the protons (right side). The TOF versus energy plot are shown without (top row) and with (bottom row) applied analysis cuts.

The TOF versus energy plot are shown without (top row) and with (bottom row) applied analysis cuts, even with the cut of the PSA. The TOF for the photons is independent from the energy and therefore, the photon band is located around 3.3 ns. For the nucleons, the TOF depends on the energy and the resulting velocity. Slow nucleons have low energies and thus a long TOF in contrast to fast nucleons with high energies and a short TOF. Through this energy dependence, the nucleon band in the TOF spectra has a distinctively bent shape, whereby the descending branch around 5 [ns/m] in the nucleon TOF spectra comes through punch-through states.

7.4.3 ΔE versus E

The identification of the charged particles by the PID or the TAPS detector can be checked by the ΔE versus E plot. The charged particles are identified by the PID or the vetoes of the TAPS detector and are then measured in the corresponding calorimeter, the Crystal Ball and the TAPS detector, respectively. For the ΔE versus E spectra, the differential energy loss ΔE in the charged particle detectors, the PID or the vetoes of the TAPS detector versus the residual deposited energy E in the corresponding calorimeter, Crystal Ball or TAPS detector, is shown in Fig. 7.6. The

ΔE versus E for the Crystal Ball and TAPS detector are shown without (top row) and with (bottom row) applied analysis cuts, including the PSA cut.

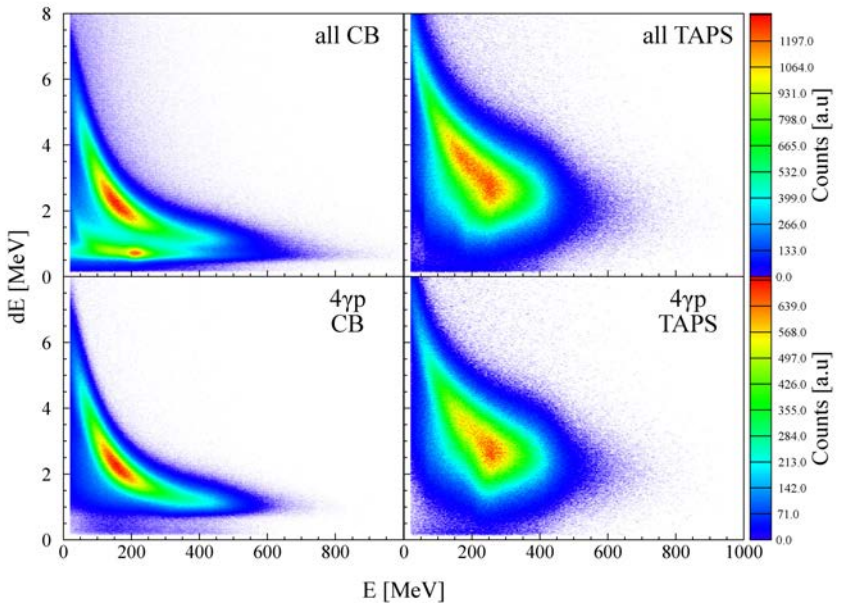

Figure 7.6.: ΔE versus E for the Crystal Ball (left side) and TAPS (right side). The ΔE versus E for the Crystal Ball and TAPS detector are shown without (top row) and with (bottom row) applied analysis cuts.

For charged particles which do not deposit their full residual energy in the calorimeter, the ΔE versus E method will not work correctly. For protons, the deposited energy in the charged particle detectors is proportional to the total energy of the proton and depends on the velocity of the proton. A slower proton deposits more energy in the crystals compared to a fast proton. Thus, the proton band has a curved structure. The deposited energy for charged pions and electrons is roughly constant at $1 - 2$ MeV. Protons up to 425 MeV and charged pions up to 250 MeV can be stopped by the Crystal Ball. In the ΔE versus E spectra of the differential energy loss ΔE measured in the PID and the energy E measured in the Crystal Ball, the distinct bands of the different particle types can be seen. After all cuts, which were discussed in the previous sections were applied, it can be seen that the proton as the charged particle was correctly identified by the event selection of the reaction. To ensure that no charged particle other than the proton is considered in the analysis, a proton band cut was made in the ΔE versus E spectra of the PID and Crystal Ball detector. This additional check for the event selection was only possible for the analysis using the PID.

7.4.4 Invariant Mass Cut

After the identification of the two neutral π^0 mesons from their two-photon decay by the χ^2 minimization method and the application of all previous kinematic cuts, an invariant mass analysis was done. For the invariant mass analysis, the two-dimensional invariant-mass distribution of the "best" combination of four photons to two π^0 mesons was first considered. The two-dimensional invariant mass spectra after the cuts on the detector time coincidence and the random tagger background subtraction were applied, the "best" photon pair combination for which the χ^2 has the minimum is shown in Fig. 7.7.

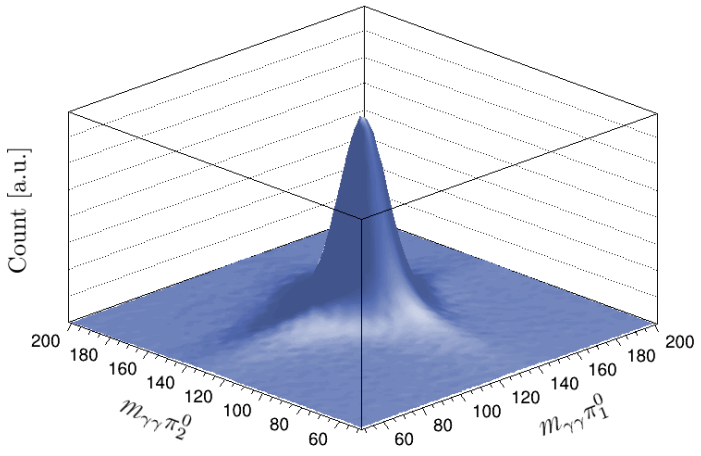

Figure 7.7.: Two-dimensional invariant-mass distribution of the "best" combination of four photons to two π^0 mesons by the χ^2 method.

The small background structure below the prominent peak from the $\pi^0\pi^0$ photoproduction was subtracted by a side-band analysis. This small background consists of either combinatorial background from the χ^2 method or from the $\eta\pi^0$ photoproduction, as indicated by the two small shoulders. The combinatorial background occur through the wrong combinations of the photon pairs from the true double π^0 events due to the small pion mass and the almost equal four neutral cluster hits. The side-band-analysis was done identically for the Monte Carlo simulations because of the combinatorial background of the true double π^0 events, which also contributes to the simulation. However, the analysis results with and without the side-band-analysis were identical after the application of all cuts within the statistical errors, which indicates that the different analysis cuts remove these background events.

For the determination of the invariant mass cuts, projections were made for one of the two pions for selected energy and angular bins. As the pions were randomized and the spectra for both pions are identical within statistical fluctuations, the invariant mass cut position can be determined for both pions at one pion. The invariant

mass of each π^0 meson was calculated by the four-vectors of the two decay photons resulting from the χ^2-test, where the four momenta $\vec{p}_{\pi_1^0}$, and $\vec{p}_{\pi_2^0}$ were reconstructed by the corresponding photon pairs γ_1, γ_2, and γ_3, γ_4, respectively, as:

$$\vec{p}_{\pi_1^0} = \vec{p}_{\gamma_1} + \vec{p}_{\gamma_2} \tag{7.16}$$

$$\vec{p}_{\pi_2^0} = \vec{p}_{\gamma_3} + \vec{p}_{\gamma_4}. \tag{7.17}$$

The invariant mass of each π^0 meson is then given by:

$$m_{\pi_1^0} = \sqrt{E_{\pi_1^0}^2 - \vec{p}_{\pi_1^0}^2} = \sqrt{\left(\sum_{i=1}^{2} E_{\gamma_i}\right)^2 - \left(\sum_{i=1}^{2} \vec{p}_{\gamma_i}\right)^2} \tag{7.18}$$

$$m_{\pi_2^0} = \sqrt{E_{\pi_2^0}^2 - \vec{p}_{\pi_2^0}^2} = \sqrt{\left(\sum_{j=1}^{2} E_{\gamma_j}\right)^2 - \left(\sum_{j=1}^{2} \vec{p}_{\gamma_j}\right)^2}, \tag{7.19}$$

where $E_{\pi_1^0}$, $E_{\pi_2^0}$ and E_{γ_i}, E_{γ_j} and $\vec{p}_{\pi_1^0}$, $\vec{p}_{\pi_2^0}$ and $\vec{p}_{\gamma_i}$, $\vec{p}_{\gamma_j}$ are the energy and the momenta of each π^0 meson and the corresponding decay photon pair.

The invariant mass analysis of the two decay photons of the π^0 meson was first done for the hydrogen data. For the determination of the cut positions of the invariant mass spectra for the different energy ranges and $cos\theta$ angles, the $\gamma p \to \pi^0\pi^0 p$ reaction as well as the background channel reactions ($\gamma p \to \eta(\to 2\gamma)\pi^0 p$ and $\gamma p \to \eta(\to 6\gamma)p$) were simulated. For the simulation the same experimental setup with the condition of the liquid hydrogen data was used. The simulated liquid hydrogen signal and the signals of the background channel reactions were then fit to the liquid hydrogen data. The ratio between the liquid hydrogen signal and the background reactions was calculated using the missing mass spectra, where the background contribution does not lie under the signal and can be fit, as shown in Fig. 7.12. However, the main background contribution is occurring from the $\gamma p \to \eta(\to 2\gamma)\pi^0 p$ reaction. The energy dependent invariant mass spectra from the hydrogen data are shown in Fig. 7.8. It can be seen that the hydrogen data (dark blue) agrees with the sum (black) of the simulated signal (light blue) and the simulated background (magenta), which indicates that the identification of the reaction and background channel contribution is understood. For the determination of the mean value and the widths of the signal contribution of the invariant mass peak, the line shape of the fit results were fit with a Gaussian distribution. An invariant mass cut of $\pm 3\sigma$ was chosen for each energy and $cos\theta$ angle. The simulation is consistent with the data and therefore, the same invariant mass cuts were applied to both.

The same invariant mass cut of $\pm 3\sigma$ was used for the butanol data. For the visualization of the free polarisable hydrogen protons and the unpolarised carbon background in the butanol data, the liquid hydrogen and carbon contribution were added in the

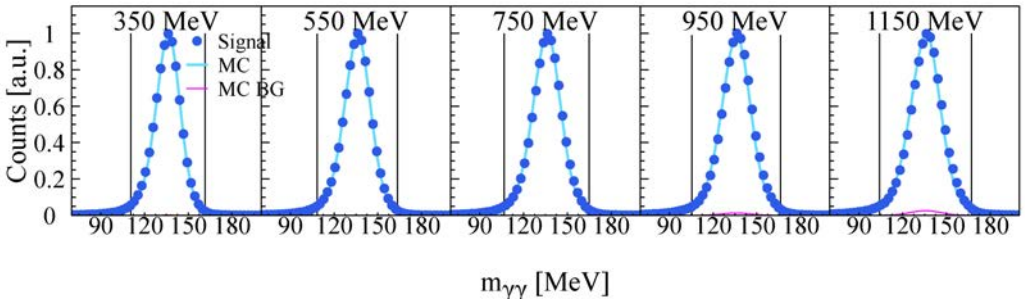

Figure 7.8.: The invariant mass spectra for the liquid hydrogen target for five bins of incident photon energy E_γ. The invariant mass distribution of the liquid hydrogen data are shown by the dark blue points and the results of the corresponding fit simulations are shown by the light blue line. The magenta line indicates the fit simulation results of the background channel reactions $\gamma p \to \eta(\to 2\gamma)\pi^0 p$, $\gamma p \to \eta(\to 6\gamma)p$. The dashed black vertical lines indicated the $\pm 3\sigma$ cut positions.

invariant mass spectra. Therefore, the counts of the invariant mass spectra $N_{m_{\gamma\gamma},B}$ of the butanol data were absolutely normalized by:

$$\frac{N_{m_{\gamma\gamma},B}}{N_\gamma^B \epsilon_H n_p^B}, \tag{7.20}$$

where N_γ^B is the photon flux of the butanol data, ϵ_H is the detector efficiency of the hydrogen contribution of the butanol, and n_p^B is the target surface density of the hydrogen protons inside the butanol target. More detailed information about the photon flux is given in Section 8.4, detector efficiency in Section 8.6, and the target surface density in Section 8.3. The contribution of the free polarisable hydrogen protons of the butanol can be obtained by the absolute normalisation of the counts of the invariant mass spectra $N_{m_{\gamma\gamma},H}$ of the hydrogen data by:

$$\frac{N_{m_{\gamma\gamma},H}}{N_\gamma^H \epsilon_H n_T^H}, \tag{7.21}$$

where N_γ^H is the photon flux of the liquid hydrogen data, ϵ_H is the detector efficiency and n_t^H is the target surface density of the liquid hydrogen data. The unpolarised carbon contribution of the butanol data was obtained by the absolute normalisation of the counts of the invariant mass spectra $N_{m_{\gamma\gamma},C}$ of the carbon data by:

$$\frac{N_{m_{\gamma\gamma},C}}{N_\gamma^C \epsilon_H n_T^C} \cdot \frac{n_{CO} + n_{He}}{n_T^B}, \tag{7.22}$$

where N_γ^C is the photon flux of the carbon data, ϵ_H is the detector efficiency of the liquid hydrogen contribution of the butanol target because it can be assumed that the carbon in the butanol target has the same detector efficiency that the hydrogen contribution inside the butanol target has, n_T^C is the target surface density and the scaling factor $(n_{CO} + n_{He})/n_T^B$ (see Section 8.3.3) is used to normalise the carbon

nuclei of the carbon data to the carbon nuclei in the butanol target under the consideration of the contributions from the liquid He coolant.

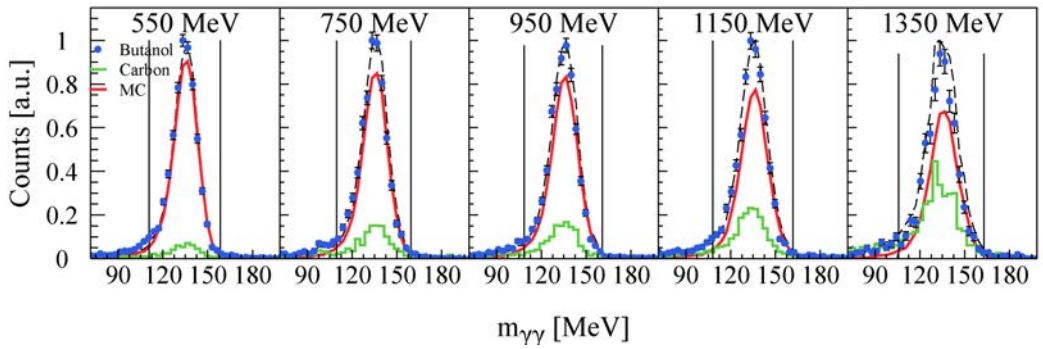

(a) Invariant mass spectra for the butanol data June 2010 as a function of the incident beam energy from 450 up to 1450 MeV.

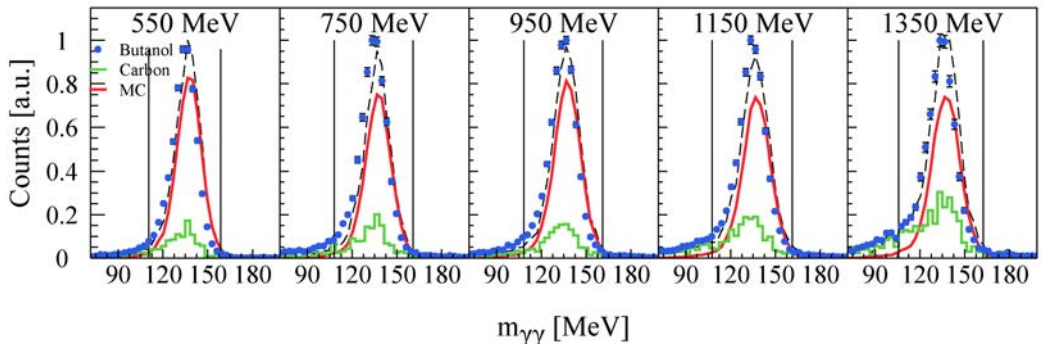

(b) Invariant mass spectra for the butanol data April 2011 as a function of the incident beam energy from 450 up to 1450 MeV.

Figure 7.9.: The relative normalised invariant mass spectra for the butanol data, June 2010 (top row) and April 2011 (bottom row), for five bins of the incident photon energy E_γ. The invariant mass distribution of the butanol data are shown by the (blue) points. The relative normalised carbon and hydrogen contribution is shown by the green, and the (red) line, respectively. The sum of the carbon and hydrogen contribution is shown by the black line. The dashed black lines indicate the $\pm 3\sigma$ cut position, which were first determined on the liquid hydrogen data.

However, the measured liquid hydrogen data cannot be used for the sum representation of the invariant mass spectra of the hydrogen and carbon contribution. Since the liquid hydrogen target was 10 cm, which was larger than the butanol target of 2 cm, the peaks of these data have different widths. Therefore, the liquid hydrogen contribution of the butanol target was simulated with the same experimental conditions as the butanol data. For the invariant mass spectra, the simulated liquid hydrogen contribution was absolutely normalised with the liquid hydrogen data and used instead (the yields were determined by the measured data but the shape by the simulation). The energy dependent invariant mass spectra for the butanol data with the two different analysis methods for the detection and identification of the charged particle (the proton), with PID and TAPS or with MWPC and TAPS, are shown in

Fig. 7.9 (a) and Fig. 7.9 (b). In the invariant mass spectra, the sum (black) of the hydrogen contribution (red) and the carbon contribution (green) corresponds to the butanol data (blue) by the relative normalisation (the y-axis shows the counts in [a.u.]). The invariant mass cut positions are indicated by the black vertical lines. In contrast to the dominant carbon background, the hydrogen background is negligible in the shown invariant mass spectra.

7.4.5 Coplanarity Cut

In the center-of-momentum (cm) frame, the two-pion system and the recoil nucleon are emitted coplanarly due to momentum conservation. The difference between the azimuthal angle of the three-momentum vector of the nucleon and the sum of the momentum vectors of the two pions must be $180°$ in the cm frame:

$$\Delta\phi = \begin{cases} \phi_{\pi\pi} - \phi_p, & \text{if } \phi_{\pi\pi} - \phi_p \geq 0, \\ 2\pi - |\phi_{\pi\pi} - \phi_p|, & \text{if } \phi_{\pi\pi} - \phi_p \leq 0 \end{cases}, \tag{7.23}$$

where ϕ_p is the azimuthal angle difference between the recoil proton and $\phi_{\pi\pi}$ is the azimuthal angle of the π^0-meson vector. For the coplanarity cut, the recoil proton has to be detected and identified as a charged particle in the detector setup. As with the invariant mass cut, the coplanarity cut was first determined for the hydrogen data and then the same cut position was applied for the butanol data. The coplanarity cut was determined on the coplanarity spectra for different energies and $\cos(\theta)$ angles. An energy dependent coplanarity spectra for the hydrogen data is shown in Fig. 7.10.

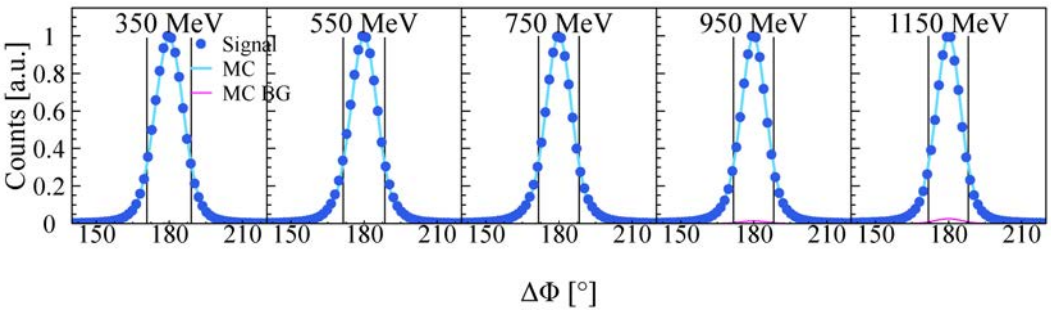

Figure 7.10.: The normalised coplanarity spectrum for the liquid hydrogen target for five bins of the incident photon energy E_γ. The angular difference $\Delta\phi$ between the recoil proton and the double π^0 mesons for the liquid hydrogen data are shown by the dark blue points and the results of the corresponding fit simulations are shown by the light blue line. The magenta line indicates the simulation fit results of the background reactions ($\gamma p \to \eta(\to 2\gamma)\pi^0 p$ and $\gamma p \to \eta(\to 6\gamma)p$). The dashed vertical lines indicate the $\pm 1.5\sigma$ cut positions.

For the determination of the cut positions of the coplanarity spectra for the different energy ranges and $cos\theta$ angles, the $\gamma p \to \pi^0\pi^0 p$ reaction as well as the background

channel reactions ($\gamma p \to \eta\,(2\gamma)\,\pi^0 p$ and $\gamma p \to \eta\,(6\gamma)\,p$) were simulated. The simulated liquid hydrogen signal (light blue) and the signals of the background channel reactions (magenta) were then fit to the liquid hydrogen data (dark blue), whereby the ratio of the liquid hydrogen signal and background channel contributions were determined from the missing mass spectra. In the missing mass spectra, the channel background contribution lies next to the missing mass peak and can be determined and seen in the liquid hydrogen missing mass spectra in Fig. 7.12. However, the main background contribution is occurring from the $\gamma p \to \eta(\to 2\gamma)\pi^0 p$ reaction. The mean value and the width of the signal contribution of the coplanarity peak for different energies and $\cos\theta$ angles were determined by fitting the line shape of the simulated fit result combined with a Gaussian distribution. For further analysis, a coplanarity cut of $\pm 1.5\sigma$ was used.

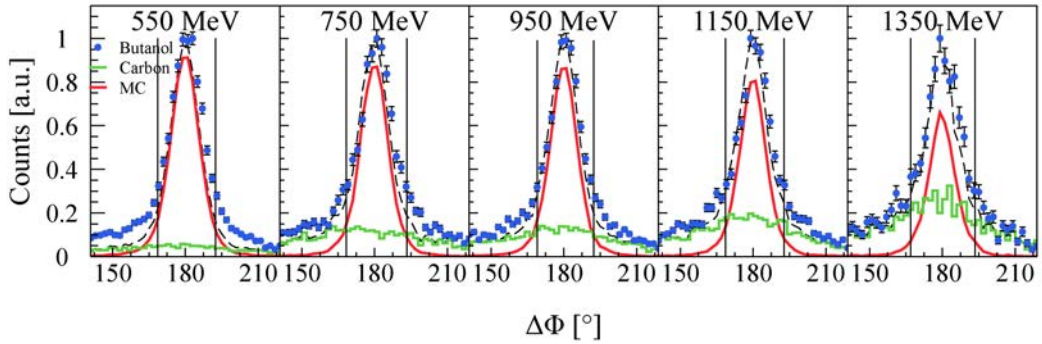

(a) Coplanarity spectra for the butanol data (June 2010) as a function of the incident beam energy from 450 up to 1450 MeV.

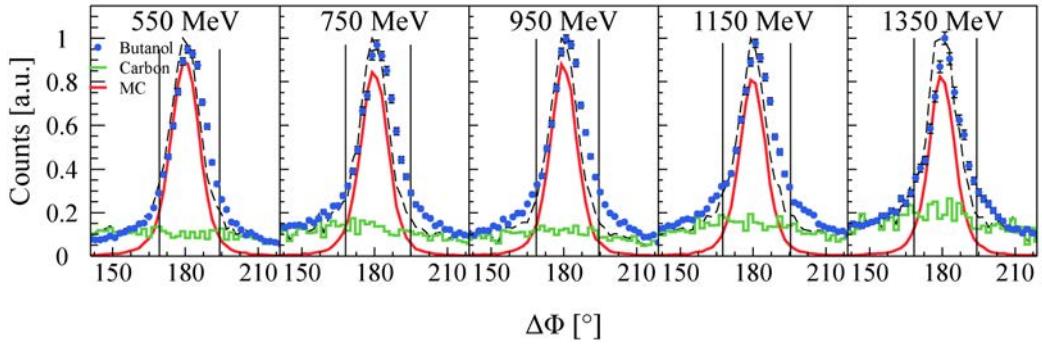

(b) Coplanarity spectra for the butanol data (April 2011) as a function of the incident beam energy from 450 up to 1450 MeV.

Figure 7.11.: The relative normalised coplanarity spectrum for the butanol data, June 2011 (top row) and April 2011 (bottom row), for five bins of the incident photon energy E_γ. The angular difference $\Delta\phi$ between the recoil proton and the double π^0 mesons for the butanol data are shown by the (blue) points. The relative normalised carbon and hydrogen contribution are shown by the green and red line, respectively. The sum of the carbon contribution and the hydrogen contribution is indicated by the black line and the dashed black lines indicate the $\pm 1.5\sigma$ cut position defined on the liquid hydrogen data.

For the butanol data, the same coplanarity cut of $\pm 1.5\sigma$ for different energies and

$cos\theta$ angles were used. For the visualization of the polarisable unbound hydrogen protons and the unpolarisable carbon background in the butanol, the liquid hydrogen and carbon contribution are added in the coplanarity spectra. Therefore, the energy dependent counts of the coplanarity cut spectra from the butanol $N_{\Delta\phi,B}$, liquid hydrogen $N_{\Delta\phi,H}$, and carbon $N_{\Delta\phi,C}$ are absolutely normalised as it was done for the invariant mass analysis. The counts of the coplanarity spectra of the butanol data $N_{\Delta\phi,B}$ are absolutely normalised by the photon flux of the butanol data, the detector efficiency of the hydrogen contribution of the butanol data, and the target surface density for the protons of the hydrogen contribution inside the butanol target, according to Equation (7.20). For the determination of the liquid hydrogen contribution of the butanol target the counts of the liquid hydrogen data $N_{\Delta\phi,H}$ of the coplanarity spectra were absolutely normalised by using Equation (7.21). The unpolarised carbon contribution of the butanol target was determined by the absolute normalisation of the carbon data and using a scaling factor $(n_{CO}+n_{He}/n_T^B)$ (see Section 8.3.3), which scales the carbon nuclei of the carbon data to the carbon nuclei inside the butanol target including effects from the He cooling. Thus, the carbon counts of the coplanarity spectra $N_{\Delta\phi,C}$ were normalised by Equation (7.22). For the sum representation of the coplanarity spectra, the hydrogen contribution of the butanol target was again simulated with the same experimental conditions as the butanol target because of the different target sizes of the butanol target of 2 cm and liquid hydrogen target of 10 cm, as mentioned before. The simulated liquid hydrogen contribution was then normalised by the measured liquid hydrogen data and used instead. The energy dependent relative normalised coplanarity spectra for both butanol data, analysed with the PID and TAPS or with the MWPC and TAPS for the recoil proton, detection and identification, are shown in Fig. 7.11 (a) and (b), respectively. The butanol data (blue) and the sum (black) of the hydrogen contribution (red) and the carbon contribution (green) agree by the relative normalisation (since the counts are shown in [a.u.]) for both analysis methods. The cut positions of $\pm 1.5\sigma$ are indicated by the black vertical lines. In the coplanarity spectra of the butanol data, the liquid hydrogen background is very small in contrast to the carbon background and not shown.

7.4.6 Missing Mass Cut

On the basis of the missing mass cut, the identified final state particles, the double π^0 events and the possible recoil proton, can be checked and more background can be rejected. For the missing mass cut, the recoil proton is treated as an undetected particle of the $\pi^0\pi^0 p$ reaction and this mass is defined as the missing mass m_x of the reaction and only the reconstruction of the double π^0 events is required. The missing mass m_x of the recoil proton can be calculated from the four-momenta of

initial state particles $p_i^{is} = (E^{is}, \vec{p}_i^{is})$ and the final state particles $p_j^{fs} = \left(E^{fs}, \vec{p}_j^{fs}\right)$ of the reaction and is given by:

$$m_x = \sqrt{\left(\sum_i p_i^{is} - \sum_j p_j^{fs}\right)^2} = \sqrt{\left(\sum_i E_i^{is} - \sum_j E_j^{fs}\right)^2 - \left(\sum_i \vec{p}_i^{is} - \sum_j \vec{p}_j^{fs}\right)^2}. \tag{7.24}$$

The missing mass of the initial state proton for the $\pi^0\pi^0$ photoproduction from the free proton can then be calculated by:

$$m_x = \sqrt{\left(E_\gamma + m_p - E_{\pi_1^0} - E_{\pi_2^0}\right)^2 - \left(\vec{p}_\gamma - \vec{p}_{\pi_1^0} - \vec{p}_{\pi_2^0}\right)^2}, \tag{7.25}$$

where E_γ and $\vec{p}_\gamma$ are the energy and momentum of the incident photon beam, respectively, and $E_{\pi_1^0}$, and $E_{\pi_2^0}$ and $\vec{p}_{\pi_1^0}$, and $\vec{p}_{\pi_2^0}$ are the energy and momentum of the two π^0 mesons, and m_p is the proton mass. For this work, the proton mass m_p was subtracted from the missing mass m_x:

$$\Delta m = m_x - m_p, \tag{7.26}$$

so that the missing mass peak is located at zero and not around the proton mass. The energy dependent missing mass spectra of the liquid hydrogen data is shown in Fig. 7.12.

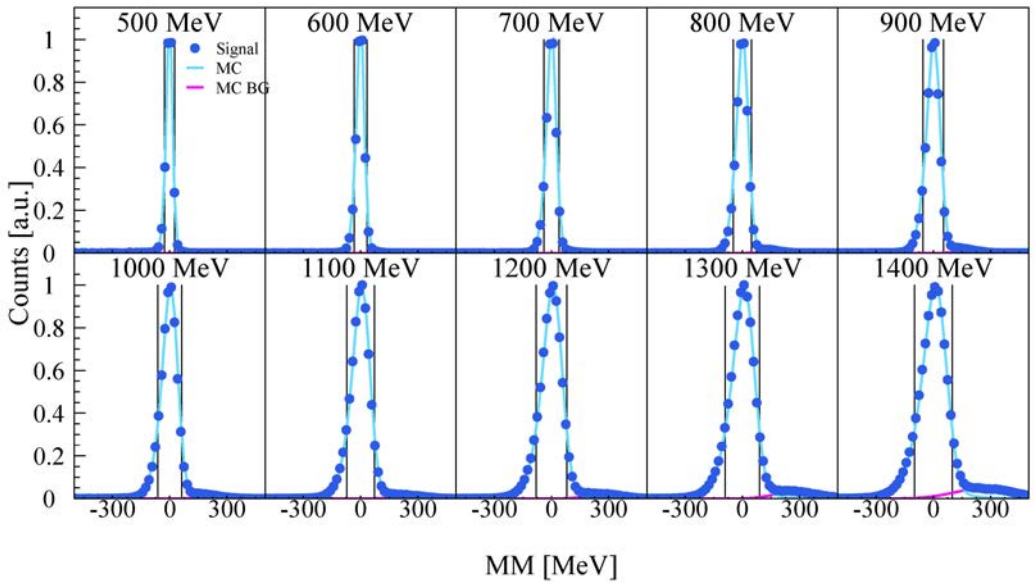

Figure 7.12.: The normalised missing mass spectra for the liquid hydrogen target for ten bins of the incident photon energy E_γ. The missing mass distribution of the liquid hydrogen data is shown by the dark blue points and the results of the corresponding fit simulation are shown by the light blue line. The magenta line indicates the fit simulation results of the background channel reactions $\gamma p \to \eta(\to 2\gamma)\pi^0 p$ and $\gamma p \to \eta(\to 6\gamma)p$. The dashed vertical lines indicate the $\pm 1.5\sigma$ cut positions.

For the determination of missing mass cut of the liquid hydrogen data, the signal of the liquid hydrogen of the reaction $\gamma p \to \pi^0\pi^0 p$ and the corresponding background channel contribution ($\gamma p \to \eta(\to 2\gamma)\pi^0 p$ and $\gamma p \to \eta(\to 6\gamma)$) were simulated and fit to the measured liquid hydrogen data. Therefore, the simulations were done with the same experimental conditions as the measured liquid hydrogen data. The ratio of the signal and the background channel contribution was calculated in the missing mass spectra, where the background channel contribution can be determined by the peak right to the missing mass peak. The main background contribution is occurring from the $\gamma p \to \eta(\to 2\gamma)\pi^0 p$ reaction. For the determination of the width and the mean values of the missing mass peak, the line shape of the fit results were fit with a Gaussian distribution. A missing mass cut of $\pm 1.5\sigma$ was chosen for different energy ranges and $cos\theta$ angles to reject all the background channel reactions, which is located on the right side of the missing mass peak. The background reaction channels increased for higher energies corresponding to their thresholds. The missing mass cut positions are indicated by the black vertical lines. The same missing mass cuts of $\pm 1.5\sigma$ for the different energy ranges and $cos\theta$ angles were used for the butanol data to ensure that the hydrogen background channel contribution is rejected in the butanol data. The missing mass spectra as a function of the incident photon beam energy $E_\gamma = 450 - 1450$ MeV of the butanol for both analysis methods of the detection and identification of the recoil proton, with the PID and TAPS for June 2010 and MWPC and TAPS for April 2011, are shown in Figs. 7.13 and 7.14, respectively. In Figs. 7.13 and 7.14, the $cos\theta$ angle dependent missing mass spectra for the butanol data (June 2010 and April 2011) are shown. For the determination of the liquid hydrogen and carbon contribution of the butanol target, the shown missing mass spectra were absolutely normalised. Therefore, the counts of the missing mass spectra $N_{\Delta M,B}$ of the butanol data were absolutely normalised by the photon flux of the butanol data, the detector efficiency of the hydrogen contribution of the butanol data, and the target surface density of the protons of the hydrogen contribution according to Equation (7.20). The polarisable unbound hydrogen contribution of the butanol target was determined by the absolute normalisation of the missing mass counts of the liquid hydrogen $N_{\Delta M,H}$ corresponding to Equation (7.21). For the determination of the unpolarised carbon contribution of the butanol data the carbon counts of the missing mass spectra $N_{\Delta M,C}$ were absolute normalised corresponding to Equation (7.22), whereby an additional scaling factor was used to scale the carbon nuclei to the carbon nuclei inside the butanol target under the cooling process.

However, for the sum representation of the missing mass spectra, the measured liquid hydrogen data cannot be used because of the larger target size of 10 cm in contrast to the butanol target size of 2 cm, which leads to a different broadening of the missing mass peaks. Therefore, the hydrogen contribution of the butanol target was simulated under the same experimental conditions as the measured butanol target. In the missing mass spectra, the simulated hydrogen contribution was then

absolutely normalised by the measured liquid hydrogen data and used instead. In the missing mass spectra, it can be seen that the butanol (blue) agree with the sum (black) of the liquid hydrogen contribution (red) and the carbon contribution (green). The missing mass cut positions are indicated by the black vertical lines. The hydrogen background channel contribution from the $\gamma p \rightarrow \eta(\rightarrow 2\gamma)\pi^0 p$ and $\gamma p \rightarrow \eta(\rightarrow 6\gamma)p$ reactions compared to the carbon background is negligible and is not shown in the missing mass spectra, but is rejected by the missing mass cut, which were defined from the hydrogen data. The missing mass spectra of only the hydrogen contribution of the butanol data (June 2010 and April 2011) are shown in Section 9.4 in Figs. 8.1 and 8.2. For the butanol analysis with the MWPC, more background is created by the poorer identification of the charged particles since the MWPC has a worse efficiency for the detection of the charged particles than the PID, as explained in Section 8.6.

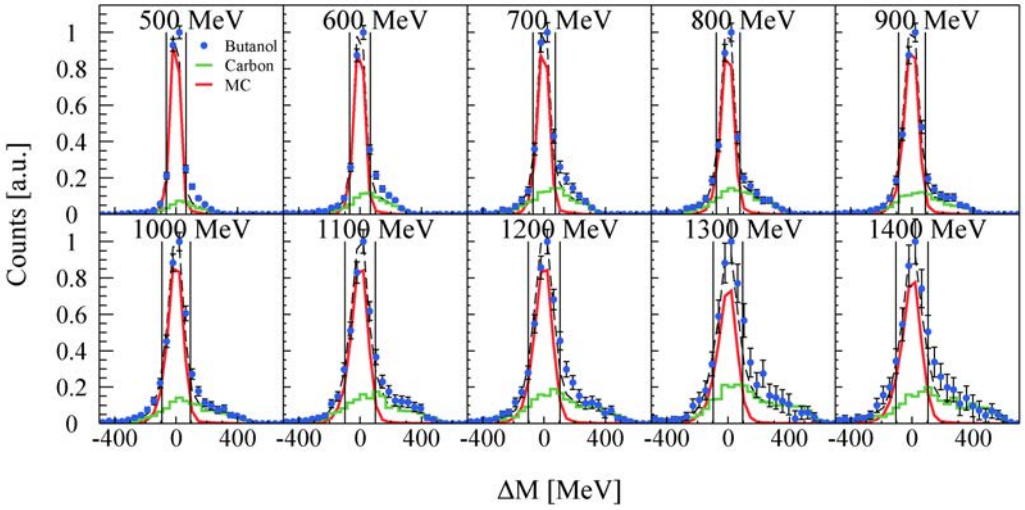

(a) Missing mass spectra for the butanol data (June 2010) as a function of the incident beam energy from 450 up to 1450 MeV.

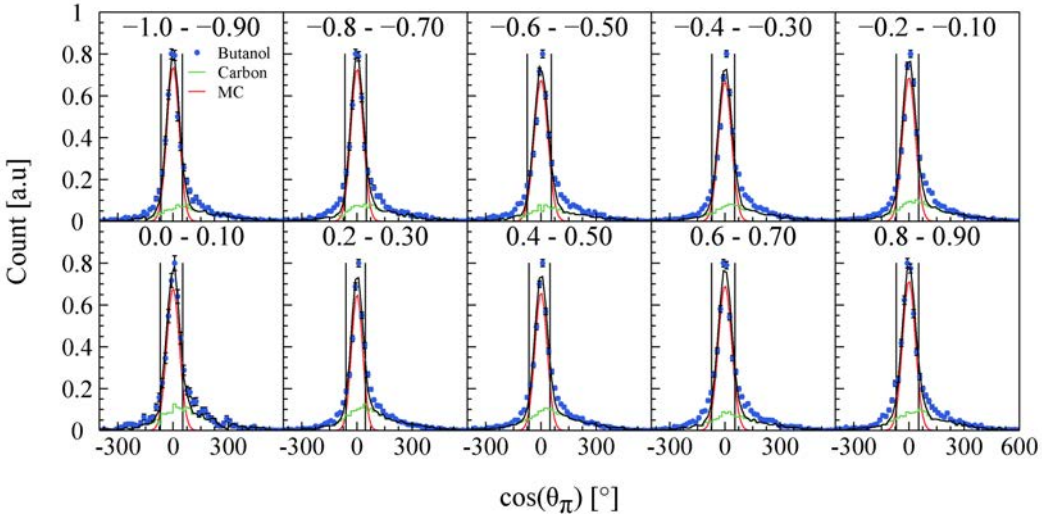

(b) Missing mass spectra for the butanol data (June 2010) as a function of ten different $cos\theta$ angle.

Figure 7.13.: The relative normalised missing mass spectra for the butanol data (June 2010) in (a) for ten energy bins of the incident photon beam energy $E_\gamma = 450 - 1450$ MeV and in (b) for ten $cos\theta$ angle bins. The relative normalised $cos\theta$ angle dependent missing mass distribution of the butanol data is shown by the blue points. The relative normalised carbon and hydrogen contribution are shown by the green line and red line, respectively. The sum of the carbon and hydrogen contribution is shown by the black line. The black vertical lines indicate the missing mass cut position of $\pm 1.5\sigma$.

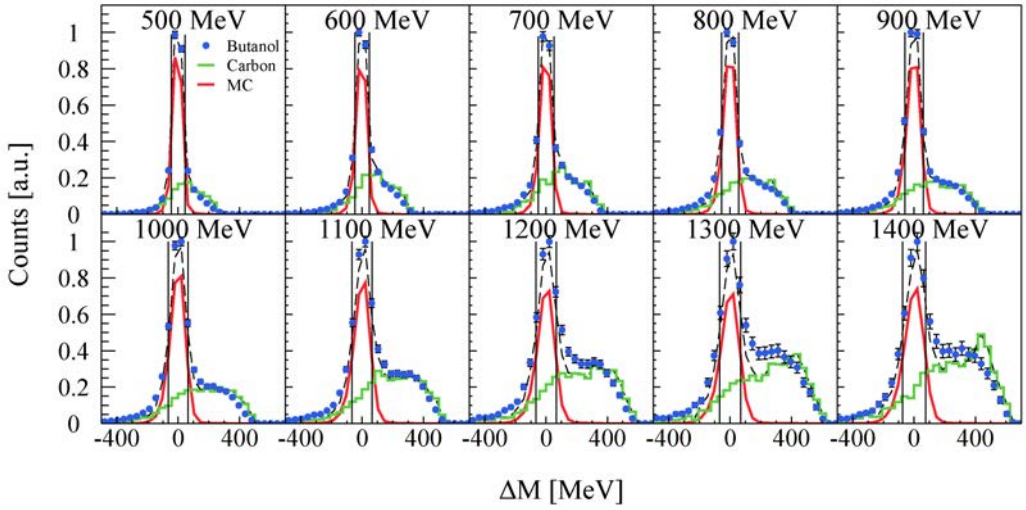

(a) Missing mass spectra for the butanol data (April 2011) as a function of the incident beam energy from 450 up to 1450 MeV.

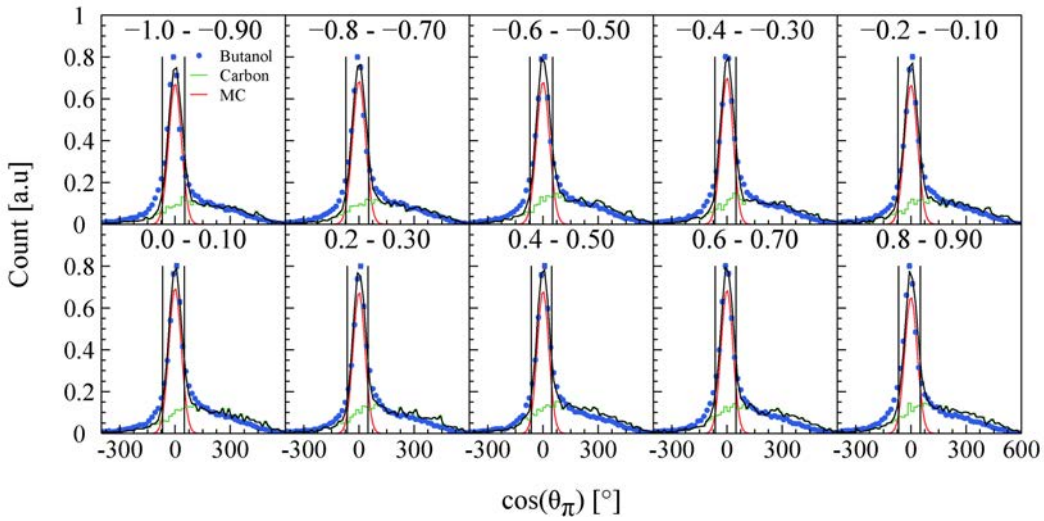

(b) Missing mass spectra for the butanol data (April 2011) as a function of ten different $cos\theta$ angle.

Figure 7.14.: The relative normalised missing mass spectra for the butanol data (April 2011) in (a) for ten energy bins of the incident photon beam energy $E_\gamma = 450 - 1450$ MeV and in (b) for ten $cos\theta$ angle bins. The relative normalised $cos\theta$ angle dependent missing mass distribution of the butanol data is shown by the blue points. The relative normalised carbon and hydrogen contribution are shown by the green line and red line, respectively. The sum of the carbon and hydrogen contribution is shown by the black line. The black vertical lines indicate the missing mass cut position of $\pm 1.5\sigma$.

8 Cross Sections

In this chapter, the extraction of the unpolarised total cross section of the double π^0 photoproduction from free proton will be discussed. The events for the cross section were determined through selected kinematical cuts, as explained in Section 7.4. In the following sections, the formalism to normalise the detected events of the $\gamma p \to \pi^0\pi^0 p$ reaction by the photon flux, the detector efficiency, the target surface density, the branching ratio of the π^0 meson decay mode of $\pi^0 \to 2\gamma$, and the solid angle of the experiment, will be explained in detail.

As mentioned before in Section 7.4, the polarisation observables F and T can be calculated by two different ways to remove the unpolarised carbon background, which occurs in the denominator of the asymmetries. In the carbon subtraction method, the unpolarised carbon contribution in the denominator of the asymmetries is subtracted from the butanol. This requires an additional carbon target measurement under similar experimental conditions as the measurement of the butanol target. For the carbon subtraction, the butanol and the carbon data were absolutely normalised and the carbon nuclei of the carbon target are scaled to the carbon nuclei inside the butanol target. Hence, the number of nuclei of the carbon and oxygen have to be normalised to the number on the butanol target under the consideration of the cooling process with the $^3He -^4 He$ mixture. Hence, the unpolarised total cross section of the hydrogen contribution of the butanol was measured to check the absolute normalisation of the butanol data and simultaneously, the one of the carbon data, as well as the nuclei normalisation. The unpolarised total cross section of the hydrogen contribution of the butanol was measured for both butanol data to check both analysis methods of the detection and identification of the charged particle. The recoil proton was identified with the PID and TAPS for the June 2010 data and with the MWPC and TAPS for the April 2011. For the determination of the unpolarised carbon contribution, the carbon data was analysed with both methods. The nuclei normalisation and the corresponding target surface densities of the used butanol and carbon data will be discussed in Sections 8.3.2 and 8.3.3. The other method for the extraction of the polarisation observables is the hydrogen normalisation method, where in the denominator of the asymmetries the unpolarised liquid hydrogen cross section is used. This method requires an additional measurement of a liquid hydrogen data and the extraction of the unpolarised total cross section. The extraction of the unpolarised total liquid hydrogen cross section including all the normalisation variables such as the photon flux, the detector efficiency, the target

surface density, and the branching ratio, will be discussed in the following sections. For the interpretation of the total cross section results, the sources of the systematic uncertainties as well as the errors of the systematic uncertainties will be discussed in Section 8.7.

8.1 Extraction of Cross Sections

The unpolarised differential cross section as a function of the incident photon energy E_γ and $cos\theta^*_{2\pi^0}$, the cosine of the polar angle of the double π^0 meson in the cm frame, can be calculated by [78]:

$$\left.\frac{d\sigma}{d\Omega}\right|_{unpol}(E_\gamma, cos\theta^*_{2\pi^0}) = \frac{N\left(E_\gamma, cos\theta^*_{2\pi^0}\right)}{N_\gamma\left(E_\gamma\right)\cdot\epsilon_{det}\left(E_\gamma, cos\theta^*_{2\pi^0}\right)\cdot n_T\cdot(\Gamma_i/\Gamma)^2\cdot\Delta\Omega}, \quad (8.1)$$

where the following nomenclature for the variables was used:

E_γ	incident photon energy
$N\left(E_\gamma, cos\theta^*_{2\pi^0}\right)$	E_γ and $\cos\theta^*_{2\pi^0}$ angle dependent number of detected events
$N_\gamma\left(E_\gamma\right)$	incoming photon flux
$\epsilon_{det}\left(E_\gamma\right)$	detection efficiency
n_T	target surface density $[barn^{-1}]$
Γ_i/Γ	branching ratio of π^0 meson [15]
	$\pi^0 \rightarrow 2\gamma : (98.823 \pm 0.034)$
$\Delta\Omega$	solid angle of the $cos\theta^*_{2\pi^0}$ bin in [sr].

In this work, the unpolarised total cross section of the liquid hydrogen data and the unpolarised total cross section of the hydrogen contribution of the butanol data was measured for an incident photon beam of 450 up to 1450 MeV. The extraction of the energy and $\cos\theta^*_{2\pi^0}$ angle dependent number of detected events, the yields from the missing mass distributions, is explained in detail in Section 9.4. More information about the determination of the photon flux and the target surface density of the used butanol, liquid hydrogen, and carbon data can be found in Sections 8.4 and 8.3.

8.2 Extraction of the Yields

The reaction yields for the calculation of the total cross section of the liquid hydrogen and the total cross section of the hydrogen contribution of the butanol data were extracted from the missing mass distribution. Therefore, the missing mass histograms were filled as a function of the incident photon energy E_γ from 450 up to 1450 MeV, using the available statistics. For the calculation of the total cross section of the

hydrogen and total cross section of the hydrogen contribution of the butanol, the same number of energy and $cos\theta_{2\pi^0}$ bins were chosen to compare the results. The number of bins was determined from the butanol data, which has poorer statistics than the hydrogen data. For the calculation of the cross sections, 64 energy bins and only one $cos\theta_{2\pi^0}$ bin was used.

For the hydrogen data, the cuts described in Section 7.4 were used to reject all the background of the contamination channels and the yields were extracted by integrating the missing mass spectra in the range of the missing mass cuts for the corresponding energy range. For the butanol data, the cuts reject most of the carbon background and all the hydrogen background of the contamination channels, but not the carbon background within the missing mass spectra. Therefore, the missing mass spectra of the butanol with the hydrogen and carbon contribution were normalised absolutely based on the nucleon normalisation, photon flux, and detector efficiency, as shown in Figs. 7.13 and 7.14. Through the absolute normalisation, the carbon background contribution can be determined and subtracted from the missing mass spectra. The yields of the hydrogen contribution of the butanol can be extracted by integrating these missing mass spectra in the range of the missing mass cuts for the corresponding energy range. The energy dependent missing mass spectra of the hydrogen contribution, which were used to extract the yields, are shown in Figs. 8.1 and 8.2. It can be seen, that the resulting hydrogen contribution corresponds to the simulated hydrogen signals and the carbon background contribution was correctly subtracted from the butanol for both analysis methods.

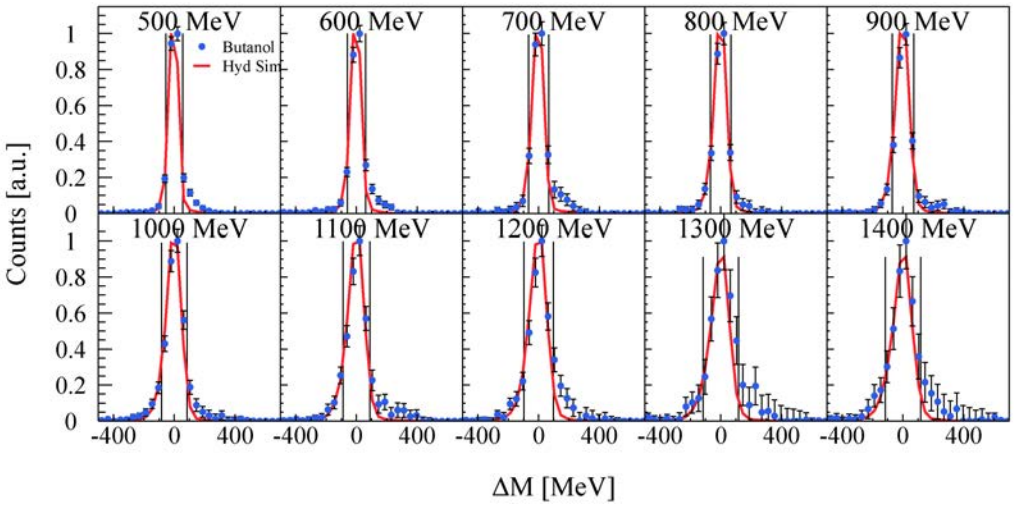

Figure 8.1.: The hydrogen contribution of the butanol data (June 2010) after the subtraction of the carbon contribution for ten bins of the incident photon beam energy $E_\gamma = 450 - 1450$ MeV. The blue points describe the hydrogen contribution of the butanol after the carbon subtraction. The simulated hydrogen contribution of the butanol is shown by the red line. The used missing mass cuts of $\pm 1.5\sigma$ are indicated by the black vertical lines.

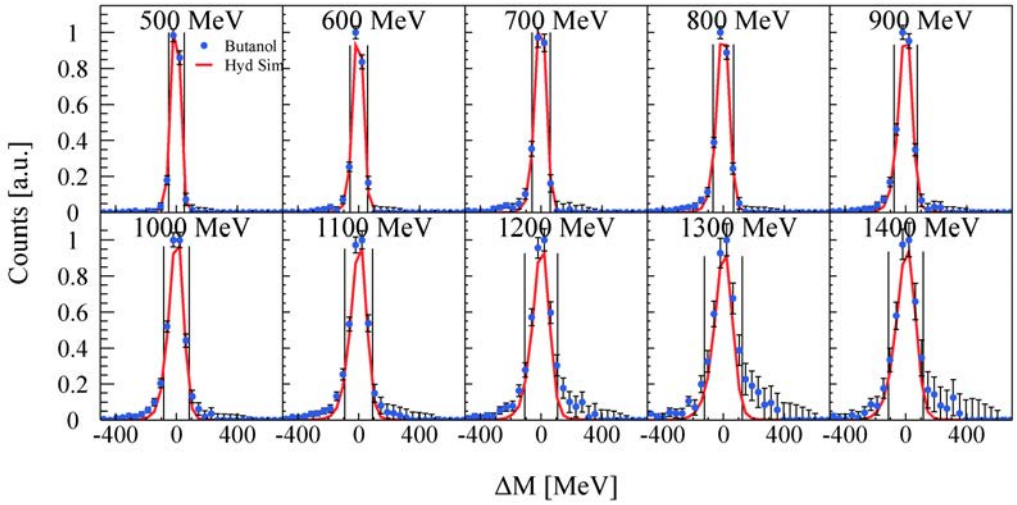

Figure 8.2.: The hydrogen contribution of the butanol data (April 2011) after the subtraction of the carbon contribution for ten bins of the incident photon beam energy E_γ. The blue points describe the hydrogen contribution of the butanol after the carbon subtraction. The simulated hydrogen contribution of the butanol is shown by the red line. The used missing mass cuts of $\pm 1.5\sigma$ are indicated by the black vertical lines.

8.3 Nucleon Normalisation

The target surface density, which is equal to the number of protons per barn (barn=10^{-24}cm^2) for the cross section of the hydrogen, can be easily calculated. As illustrated in Fig. 8.3, the Butanol molecule has the chemical formula $C_4H_{10}0$, whereby only the unbound hydrogen protons can be polarised and the carbon and oxygen nuclei are unpolarised background contribution. For the calculation of the cross section of the hydrogen contribution of the butanol, the polarisable protons per barn for the hydrogen contribution and the unpolarised carbon background contribution of the entire target must be known. The dilution of carbon and oxygen nuclei and thus, their number of protons per barn of the butanol including the contribution from the He coolant, is discussed in the following sections.

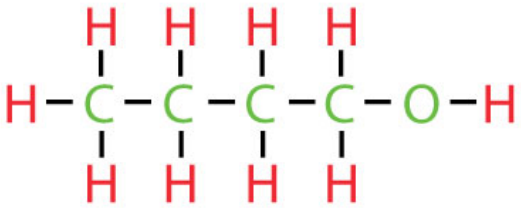

Figure 8.3.: Structural formula for the Butanol molecule $C_4H_{10}0$. The polarised protons of the hydrogen are indicated by the red H, the unpolarised carbon and oxygen nuclei are indicated in green.

8.3.1 Nucleon Normalisation of the Hydrogen

For the liquid hydrogen data, the target surface density n_T^H, which gives the number of protons per barn, can be calculated by:

$$n_T^H = \frac{N_A \cdot \rho_H \cdot l}{M_{mol}} = 0.421\,\mathrm{b}^{-1}, \tag{8.2}$$

where the following nomenclature is used for the different variables:

N_A	Avogadro's constant: 6.02214×10^{23} mol^{-1}
ρ_H	density of liquid hydrogen: 0.070548 g/cm^3 at 1080 mbar
l	target length: (10.0 ± 0.1) cm
M_{mol}	molar mass of atomic hydrogen: 1.00794 g/mol.

The cross section of the liquid hydrogen data σ_H can then be calculated by using Equation (8.1) as:

$$\sigma_H = \frac{N_H}{N_\gamma^H \epsilon_H n_T^H (\Gamma_i/\Gamma)^2}, \tag{8.3}$$

where N_H is the number of detected events which were extracted from the missing mass spectra of the hydrogen data with all applied cuts to reject all the background events, as explained in Section 9.4, N_γ^H is the incoming photon flux of the liquid hydrogen data measurement, ϵ_H is the detector efficiency of the hydrogen data, which was determined by a Monte Carlo simulation with the same detector setup settings (see Section 8.6), and Γ_i/Γ is the branching ratio of $\pi^0 \to 2\gamma : (98.823 \pm 0.034)$ [15].

8.3.2 Nucleon Normalisation of the Butanol

Since the butanol target was filled with butanol beads, the target volume was not completely covered by butanol. Hence, for the calculation of the target surface density of the butanol n_T^B, the filling factor f of the butanol breads must be considered:

$$n_T^B = \frac{N_A \cdot \rho_B \cdot f \cdot l}{M_{mol}^B} = 0.09163\,\mathrm{b}^{-1}, \tag{8.4}$$

where the following nomenclature is used for the different variables:

N_A	Avogadro's constant: 6.02214×10^{23} mol^{-1}
ρ_B	density of butanol: 0.94 g/cm^3 at 1080 mbar
f	filling factor of the target: 0.6
l	target length: (2.0 ± 0.02) cm
M_{mol}	molar mass of atomic butanol: 74.1216 g/mol.

For the calculation of the total cross section of the hydrogen contribution of the butanol, the target surface density of the hydrogen protons inside the butanol target has to be determined. Hence, the number of protons per barn of the hydrogen contribution of the entire butanol target is multiplied by the number of hydrogen nuclei per butanol molecule by:

$$n_p^B = 10 \cdot n_T^B = 0.09163\,\mathrm{b}^{-1}. \tag{8.5}$$

The cross section of the hydrogen contribution of the butanol target $\sigma_{B'}$ can then be calculated using Equation (8.1):

$$\sigma_{B'} = \frac{N_{B'}}{N_\gamma^B \epsilon_H n_p^B (\Gamma_i/\Gamma)^2}, \tag{8.6}$$

where $N_{B'} = N_B - N_C$ is the detected events of the hydrogen contribution of the butanol data, which were extracted by the carbon background subtraction of the normalized missing mass spectra and all applied cuts, as explained in Section 9.4. N_γ^B is the energy dependent incoming number of photons of the butanol measurement, ϵ_H is the detector efficiency of the hydrogen signal of the butanol, which was simulated with Monte Carlo simulations and with the same experimental condition as the data, n_p^B is the target surface density of the protons per barn of the hydrogen contribution calculated with Equations (8.4) and (8.5) and Γ_i/Γ is the branching ratio of $\pi^0 \to 2\gamma : (98.823 \pm 0.034)$ [15]. More information about the determination of the photon flux of the corresponding butanol data and the detector efficiency can be found in Sections 8.4 and 8.6.

8.3.3 Nucleon Normalisation of the Carbon

The target surface density for the carbon data n_T^C can be calculated by:

$$n_T^C = \frac{N_A \cdot \rho_C \cdot l}{M_{mol}^C} = 0.056586\,\mathrm{b}^{-1}, \tag{8.7}$$

with the following nomenclature for the variables:

N_A	Avogadro's constant: 6.02214×10^{23} mol^{-1}
ρ_C	density of carbon: 0.57 g/cm^3
l	target length: (1.98 ± 0.02) cm
M_{mol}	molar mass of atomic carbon: 12.011 g/mol.

The number of carbon and oxygen nuclei in one butanol molecule, under the assumption that the cross section scales with $A^{2/3}$ [106], can be calculated with the molar mass of carbon $M_C = 12.011$ g/mol and oxygen $M_C = 12.011$ g/mol by:

$$K_{CO} = 4 + (M_O/M_C)^{2/3}. \tag{8.8}$$

The number of carbon and oxygen nuclei in the butanol target is then given by the number of butanol molecules multiplied by the carbon and oxygen nuclei with:

$$n_{CO} = K_B \cdot K_{CO}. \tag{8.9}$$

For the cooling process, the butanol beads in the target were surrounded by a ^3He $-^4$ He mixture. Therefore, the number of helium nuclei in the ^3He $-^4$ He mixture also has to be taken into account for the absolute nucleon normalisation. The number of helium nuclei n_{He} depends on the helium density $\rho_{He} = 0.14$ g/cm^3 and on the size of the end gaps L_{end} of the butanol target and can be calculated by:

$$n_{He} = K_{He} \frac{\rho_{He} \cdot [(1-f)L_B + L_{end}] \cdot N_A}{M^{He}_{mol}}, \tag{8.10}$$

where for the helium molecules K_{He}, the helium molar mass is $M_{He} = 3.016$ g/mol and can be approximated with the carbon molar mass M_C [107] by:

$$K_{He} = (M_{He}/M_C)^{2/3}. \tag{8.11}$$

The scaling factor for the carbon cross section σ_C is then given by:

$$\frac{n_{CO} + n_{He}}{n^B_T} = 0.6424. \tag{8.12}$$

The cross section of the carbon contribution of the butanol data can then be calculated using Equation (8.1) and the scaling factor from Equation (8.12) by:

$$\sigma_C = \frac{N_C}{N^C_\gamma \epsilon_H n^C_T (\Gamma_i/\Gamma)^2} \cdot \frac{n_{CO} + n_{He}}{n^B_T}, \tag{8.13}$$

where N_C is the detected events of the carbon data extracted by the missing mass spectra of the carbon, N^C_γ is the incoming photon flux of the carbon measurement, ϵ_H is the detector efficiency of the simulated hydrogen signal of the butanol (the carbon background contribution inside the butanol has the same detector efficiency),

n_T^c is the target surface density of the protons per barn of the carbon contribution of the butanol data, and Γ_i/Γ is the branching ratio of $\pi^0 \rightarrow 2\gamma : (98.823 \pm 0.034)$ [15].

8.4 Photon Flux Normalisation

For the normalisation of the cross sections the number of incoming photons, the photon flux on the target must be known. Therefore, the photon flux N_γ was calculated by the number of electrons N_{e^-} detected in the different tagger channels and multiplied by the tagging efficiency ϵ_{tagg}:

$$N_\gamma = N_{e^-} \cdot \epsilon_{tagg}. \tag{8.14}$$

The tagging efficiency ϵ_{tagg} is determined by tagging efficiency measurements at certain times during data taking. The electron flux N_{e^-} is measured constantly during the experiment by counting the scaler modules of the discriminated signals from each tagger channel. Due to the different data acquisition systems of the tagger and the rest of the detector setup, the measured electron flux in the tagger must be corrected. Since the electrons in the tagger were counted without the consideration of the readout time and the time when the event information was collected in the detector setup, the counted electrons have to be corrected by the live times of the tagger Γ_{tagg} and the total live time Γ_{tot} of the detector setup. The number of electrons $N_{e^-}^{'}$ can then be calculated by the different live times by:

$$N_{e^-}^{'} = N_{e^-} \cdot \frac{\Gamma_{tot}}{\Gamma_{tagg}}, \tag{8.15}$$

whereby the total live time of the detectors was around $\Gamma_{tot} \approx 44\%$ and the live time of the tagger was around $\Gamma_{tagg} \approx 60\%$. The tagger channel distribution of the electrons is shown in the top row of Fig. 8.4. The number of electrons per tagger channel has an inverse energy dependence given by the bremsstrahlung's process in the radiator. Therefore, the high tagger channels correspond to a high bremsstrahlung electron energy and a low bremsstrahlung photon energy and vice versa. The tagger channels without counts were broken elements and were removed from the analysis.

The incident photon flux upon the target cannot be directly inferred from the measured electron flux in the target due to the collimation of the bremsstrahlung photon beam. Hence, tagger efficiency measurements must be done to determine the electron flux based on the photon flux on the target. For the tagger efficiency measurement, very low beam intensities and a lead glass detector are used to measure the number of photons, which reach the target. The lead glass detector has an efficiency of roughly 100% for low energy beam intensities and a size of 20 cm $\times$

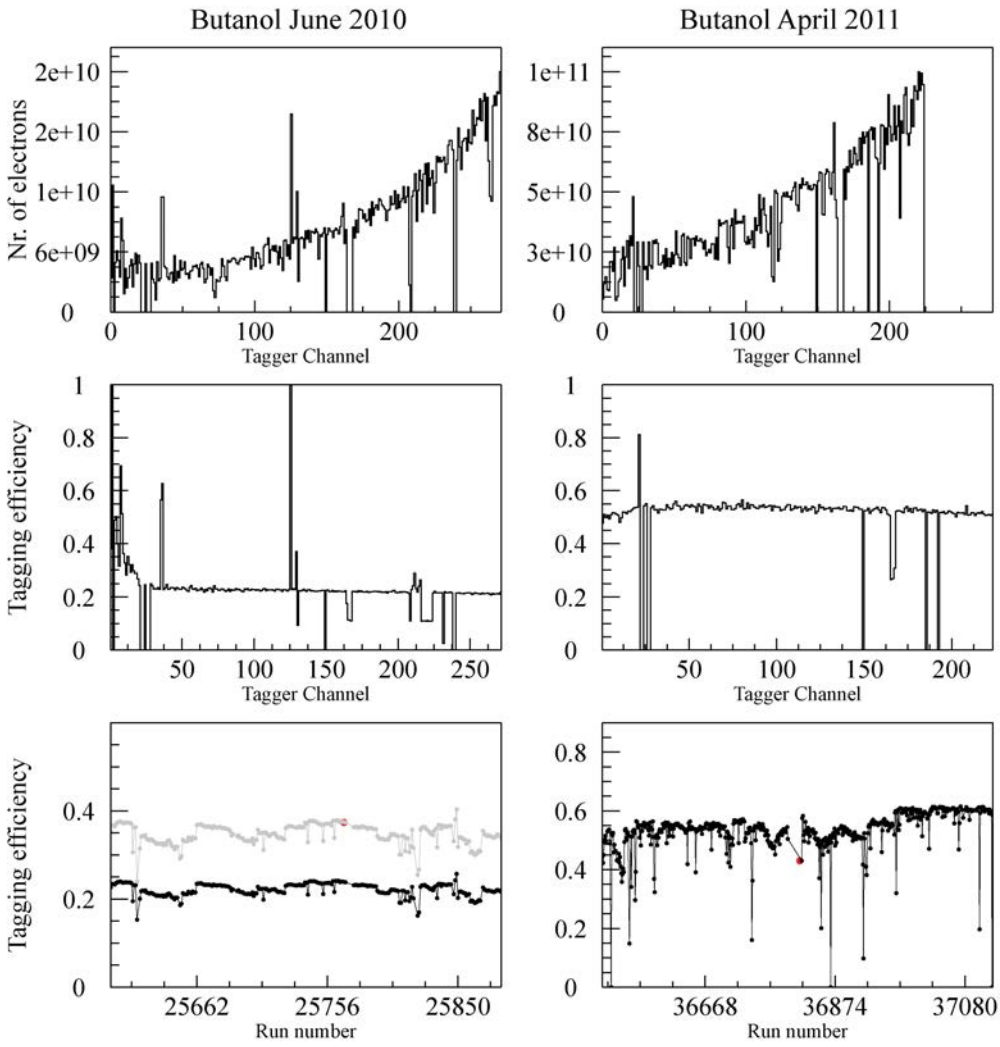

Figure 8.4.: In the top row, the tagging efficiency of the butanol data June 2010 (left) and butanol data April 2011 (right) is shown. In the middle row, the tagging efficiency per channel is shown. In the bottom row, the time dependent tagger efficiency per run determined by the ionization chamber (P2) (left) and the number of detected $\eta + X$ events (right) is shown, whereby the red points indicate the tagger efficiency measurements. The measured tagging efficiency shown by the grey line has to be scaled by a factor of 1.52 to the black line because of incorrect inhibited scalers.

20 cm $\times$ 20 cm and is placed in the beam line, 15 m behind the radiator. Because of the low beam intensities, background hits caused by cosmic rays and nuclear decays due to activated material are also measured by the tagger efficiency measurement. For the determination and the subtraction of these background hits, a measurement without beam was taken before and after each tagger efficiency measurement. The measured efficiency values ϵ_{tagg} can be directly applied to the normal production runs with higher intensities because the difference due to the beam intensities can be neglected. For a time-dependent tagging efficiency measurement, the photon

flux during the experiment must be determined since the beam position and quality of beam change over time and hence, so does the tagger efficiency. The time dependence of the photon flux was determined by measuring the counts of the photon beam by an ionization chamber $(P2)$ whose counts are proportional to the photon flux.
However, the ionization chamber did not work properly during the measurement of the April 2011 butanol data and August 2011 carbon data and so the time dependence per run was determined by counting the number of detected $\eta + X$ (inclusive eta production) events. The average tagging efficiency of the j tagger efficiency measurement over all tagger channels N_c can be calculated by:

$$\langle \epsilon_j \rangle = \frac{1}{N_c} \sum_{i=1}^{N_c} \epsilon_i, \tag{8.16}$$

where ϵ_i is the tagging efficiency for each tagger channel i. To obtain the time dependent photon flux the $\eta + X$ counts from each run N_r were scaled to the average tagging efficiency values as defined in Equation (8.16) to obtain the time dependent photon flux. The tagging efficiency for each production run r and tagger channel i can then be calculated by the following formula:

$$\epsilon_r^i = \frac{\langle \epsilon_i \rangle}{\sum_{j=1}^{N_c} \langle \epsilon_j \rangle} \cdot \langle N_r \rangle, \tag{8.17}$$

where ϵ_i is defined as:

$$\langle \epsilon_i \rangle = \frac{1}{N_m} \sum_{j=1}^{N_m} \epsilon_i. \tag{8.18}$$

The tagging efficiencies of the June 2010 and April 2011 butanol data are shown in Fig. 8.4. The middle row of Fig. 8.4 shows the tagging efficiency per channel and the bottom row shows the tagger efficiency measurement scaled to the tagger efficiency measurements.
For the butanol beamtimes, two different collimator diameters were used. For the June 2010 beam time, a collimator of 2 mm was used and for the April 2011 beam time, a collimator with 2.5 mm was used, which results in a x^2 higher tagger efficiency measurement through the 50% larger opening (in area). The tagger efficiency measurement for the June 2010 data shown by the grey line in the bottom row on the left side, has to be scaled by 1.52 to the black line because of an issue with the inhibited scalers during the tagging efficiency measurement, which caused wrong live time values.

8.5 Empty Target Subtraction

For the calculation of the cross section, only the events due to reactions in the target material are considered. The events generated in the material of the target container, which mainly consists of carbon nuclei, lead to a background contribution in the measurement, which must be subtracted. Therefore, the contribution of the target container background of the liquid hydrogen data April 2009 has to be determined. In contrast to the butanol data from June 2010 and April 2011, the target container background cancels out in the calculation of the unpolarised total cross section of the hydrogen contribution as well as in polarisation observables due to the subtraction of the carbon contribution.

For the determination of the target container background contribution of the liquid hydrogen data April 2009, the resulting carbon cross section was measured with production runs using an empty target container. The empty target runs were then analysed similarly as the normal data by using the same analysis cuts. The empty target cross section as a function of the incident beam energy E_γ was then obtained by the absolute normalisation of the yields. For the removal of the empty target contribution from the filled liquid hydrogen target, a normalised ratio was calculated between the filled and empty target and used to scale down the filled target cross section. The relative empty target contribution percentage to the total hydrogen cross section is shown in Fig. 8.5. At lower energies, a significant increase can be seen in the empty target cross section. This increase is due to the Fermi motion of the carbon nuclei in the target container and is strongly increased in comparison to the liquid hydrogen (proton) cross section.

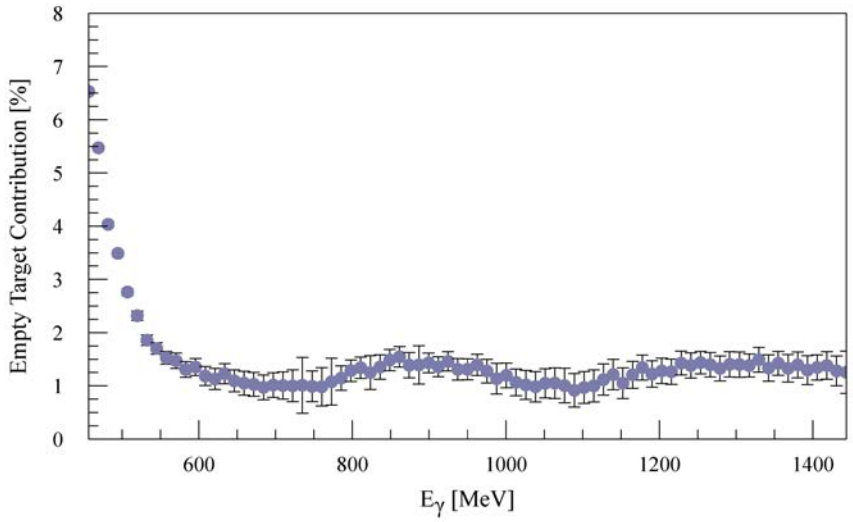

Figure 8.5.: The incident photon beam energy E_γ dependence empty target contribution of the liquid hydrogen data.

8.6 Detection Efficiency Correction

The detection efficiency correction for the total normalisation of the cross section was determined using the Geant software package A2, as explained in Section 4.3. The reaction $\gamma + p \rightarrow \pi^0\pi^0 p$ was generated by the Pluto event generator and the interactions with the same experimental setup as the data was then simulated by the Geant software. For the detection efficiency correction of the liquid hydrogen cross section in the Geant 4 simulation, the same hydrogen target with the corresponding target container was used. For the cross section of the hydrogen contribution of the butanol, the detection efficiency correction of the hydrogen contribution was determined by simulations of the hydrogen contribution inside the butanol target. Both reactions were simulated in phase space. For the simulation, a beam spot with a diameter of 1.3 cm was used, which can lead to random reactions inside the entire target volume.
For the determination of a detection efficiency correction, the simulated data must correspond to the experimental data. Therefore, the same malfunctioning detector elements were removed for the event selections and the same trigger thresholds were used as were used for the experimental data. The selected events of the reaction were then analysed by the same analysis, applying the same cuts as in the experimental data.
The detection efficiency can be calculated by the number of detected events N_{det} and generated events N_{gen} of the simulated double π^0 reaction by:

$$\epsilon\left(E, \cos\theta^*_{2\pi^0}\right) = \frac{N_{det}\left(E_{det}, \cos\left(\theta^*_{2\pi^0,det}\right)\right)}{N_{gen}\left(E_{gen}, \cos\left(\theta^*_{2\pi^0,gen}\right)\right)}, \tag{8.19}$$

where E is the incoming photon beam energy and $cos\left(\theta^*_{2\pi^0}\right)$ is the $2\pi^0$ meson polar angle in the centre-of mass frame.

8.6.1 Software Trigger

To determine the detection efficiency of the measured reaction, the same experimental conditions of the trigger must be applied to the simulation events. The Crystal Ball energy sum trigger checks the total sum of the analogue signals above a certain energy threshold of all NaI(TI) crystals. The energy sum of the experimental and simulated data can be determined by the analogue signals of the de-calibrated energies of all NaI(TI) crystals [108][109]. Since only uncalibrated signals can enter into the analog hardware energy sum, only uncalibrated signals can be used in the analysis for the determination of the energy sum. The use of the calibration constants could lead to an over or underestimation of the analog signals of each

NaI(TI) crystal. The energy sum has to be determined reaction dependent, since the relative contribution of all the NaI(TI) crystals depends on the energy and angular distribution of the two π^0 meson.
The Crystal Ball photon energy sum E_{sum} spectra for the butanol April 2011 data and the corresponding simulation are shown in Fig. 8.6. All analysis cuts were applied to the spectra. The spectrum from the experimental data (red) was normalised to the simulation (blue) in the intervals between 480 and 650 MeV, where the energy sum has a negligible influence. The ratio of the experimental and simulation data is shown in Fig. 8.6. Events with lower energies are suppressed by the hardware trigger in the experimental data compared to the simulated data. For the reproduction of the experimental software trigger, the simulated events were weighted with a factor $f_{MC} < 1$, which was determined from the ratio histogram. The simulation events were only weighted in the region up to $E_{sum} \sim 480$ MeV, where the software trigger has an influence.

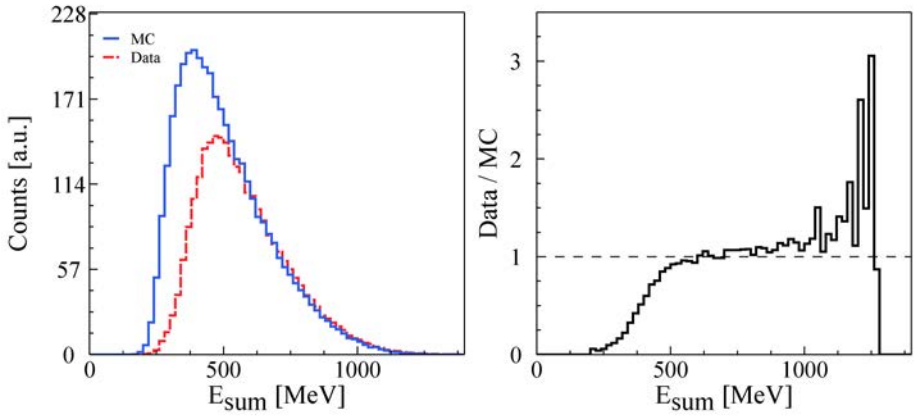

Figure 8.6.: The Crystal Ball sum for the MC simulation (blue) and the April 2011 data (red) is shown on the left side. For the determination of the software trigger for the simulation, the data were normalised to the simulation between [480-650] MeV for the $2\pi^0 \rightarrow 4\gamma$. The ratio of the data/MC is shown on the right.

8.6.2 Nucleon Detection Efficiency Correction

The simulation of nucleon interactions with material of the implemented experimental setup depends strongly on the energy and on the used physics model. Hence, inconsistencies between experimental and simulation data, which occur through geometrical deviations of the implemented setup to the experimental setup or inefficiencies of the charged particle detectors (PID and vetoes), have an influence on the nucleon detection efficiency. The differences in the nucleon detection efficiency of the data and simulation are corrected by applying a nucleon detection efficiency

correction to the simulation to ensure that the simulated data is consistent with the experimental data.
For the determination of the nucleon efficiency of the double π^0 reaction, liquid hydrogen data was used because the hydrogen only consists of protons. The difference between the exclusive and inclusive analysis is that the detection of the proton is not required in the inclusive analysis. Therefore, the undetected nucleon must be a proton. For the exclusive analysis, the proton has to be detected in coincidence with the double π^0 meson. The proton efficiency can then be determined by comparing the inclusive and exclusive analysis and the simulation by:

$$N\left(\gamma p \to \pi^0\pi^0 p\right)$$
$$N\left(\gamma p \to \pi^0\pi^0 X\right).$$

Since the PID and veto thresholds influence the proton detection efficiency, the software threshold of all data sets were set to a maximum to avoid effects from different thresholds. For the background reaction and reaction identification for both analyses, a coplanarity and a missing mass cut were applied.
The nucleon detection efficiency for experimental and simulation data can then be calculated by the ratio of the number of exclusive and inclusive events depending on the proton polar angle in the laboratory frame θ_p and on the proton kinetic energy T_p by:

$$\epsilon_p\left(T_p, \theta_p\right) = \frac{N\left(\gamma p \to \pi^0\pi^0 p\right)}{N\left(\gamma p \to \pi^0\pi^0 p\right) + N\left(\gamma p \to \pi^0\pi^0 X\right)}. \tag{8.20}$$

Since the recoil proton was not always detected, the polar angle and kinetic energy of the recoil proton were calculated from kinematics. The correction factor for the simulation can then be calculated by the ratio of the extracted nucleon efficiency of the simulation ϵ_p^{MC} and experimental data ϵ_p^{data} by:

$$f_p^{corr}\left(T_p, \theta_p\right) = \frac{\epsilon_p^{MC}\left(T_p, \theta_p\right)}{\epsilon_p^{data}\left(T_p, \theta_p\right)} \tag{8.21}$$

The correction factor f_p^{corr} was then applied by weighting every simulation event with $1/f_p^{corr}\left(T_p, \theta_p\right)$ for the corresponding kinetic energies T_p and polar angles θ_p.
The nucleon detection efficiency correction factor f_p^{corr} for the different kinetic energies T_p and polar angles θ_p is shown in Fig. 8.7. It can be seen that the proton detection efficiency between the data and simulation are different. For some kinetic energies T_p and polar angles θ_p, the proton efficiency is over or underestimated, which is then corrected by nucleon efficiency values larger or smaller than one. In the forward angular range of the Crystal Ball $\theta_p < 25°$ and TAPS $\theta_p < 20°$, the proton efficiency is overestimated for low kinetic energies. This overestimation of the proton detection efficiency comes from different materials and differences in the

geometry. Specifically, the transition of the Crystal Ball and TAPS $(15° < \theta_p < 25°)$ is difficult to implement in the simulation and only small geometrical deviations have strong influences on the proton efficiency [78].

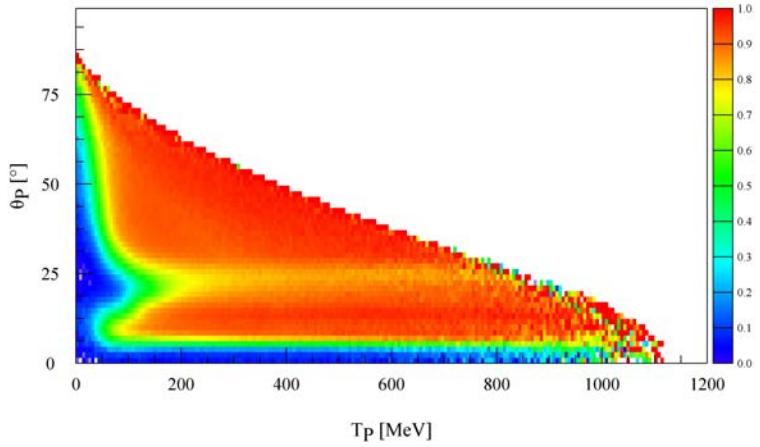

Figure 8.7.: Proton detection efficiency correction f^{corr} as a function of the kinetic energy T_p for the proton and the reconstructed polar angle θ_p of the recoil proton in the lab frame.

The proton detection efficiency correction could only be calculated and applied to the simulation where the proton was identified with the PID and the vetoes because no hydrogen data is available in the same energy range as the butanol data with working MWPCs. Therefore, no nucleon detection efficiency correction could be calculated for the butanol April 2011 data analysed with the MWPCs and applied to the corresponding simulation.

8.6.3 Charged Particle Detection Efficiency Correction

In the liquid hydrogen April 2009 data used, the PID and veto detectors did not work correctly and therefore some protons were mistakenly identified as neutrons. The fact that some of the protons have been mistakenly identified as neutrons, is evident in the comparison of the measured inclusive and exclusive cross section of this data. This comparison shows a significant discrepancy of about 10%. However, it could not be found out, why the charged particle detectors were not always identifying the protons as protons and therefore the experimental conditions could not be correctly simulated. For that reason, the simulation used overestimated the charge particle detection efficiency. To correct this overestimation of the simulation a charged particle detection efficiency correction was calculated.
For the determination of the charged particle efficiency, the inclusive and exclusive analysis of the experimental date and simulation were analysed with and without

the PID and veto detectors. For the inclusive analysis, the following event selection of the neutral (n) and charged (c) particles were used [110]:

with PID and Veto:	$5n \,\&\, 0c$	without PID and Veto:	$5n$
	$4n \,\&\, 1c$		$4n$
	$4n \,\&\, 0c$		

and for the exclusive analysis the following event selection of neutral (n) and charged (c) particles were used [110]:

with PID and Veto:	$5n \,\&\, 0c$	without PID and Veto:	$5n$
	$4n \,\&\, 1c.$		

The individual nucleon detection efficiencies for the data and simulation can then be calculated for the inclusive and exclusive analysis with and without the use of the charged particle detectors. For the calculation, the events from the analysis with the PID and veto detectors are denoted with w and with wo when the information of the charged particle detectors were or were not used, respectively. The number of events in the clusters is denoted by H for hit or NH for no hit, whereby H is used for detected events in five clusters and NH for detected events in four clusters. The nucleon detection efficiency can then be calculated for both analyses with and without the use of the charge particle detectors by [110]:

$$\epsilon^{w}_{MC} = \frac{H^{w}_{MC}}{NH^{w}_{MC} + H^{w}_{MC}} \quad \epsilon^{wo}_{MC} = \frac{H^{wo}_{MC}}{NH^{wo}_{MC} + H^{wo}_{MC}} \tag{8.22}$$

$$\epsilon^{w}_{data} = \frac{H^{w}_{data}}{NH^{w}_{data} + H^{w}_{data}} \quad \epsilon^{wo}_{data} = \frac{H^{wo}_{data}}{NH^{wo}_{data} + H^{wo}_{data}}. \tag{8.23}$$

For the determination of the charged particle efficiency, the ratio of the nucleon efficiency with and without the detection of the charged particle for the data and the simulation must be considered [110]:

$$\zeta_{data} = \frac{\epsilon^{w}_{data}}{\epsilon^{wo}_{data}} \quad \zeta_{MC} = \frac{\epsilon^{w}_{MC}}{\epsilon^{wo}_{MC}}. \tag{8.24}$$

For the correction of the misidentified protons of the liquid hydrogen data of the exclusive analysis where the detection of the proton is necessary, the ratio between the nucleon efficiency with and without the detection of the proton was considered. For the liquid hydrogen data, the double π^0 photoproduction can only occur on the proton, regardless of whether it is detected or not and the misidentified protons that were mistakenly detected as neutral particles can be determined. A charged particle

detection efficiency correction can then be calculated by the ratio of the calculated nucleon efficiencies of the data and simulation for both analysis by [110]:

$$\zeta^{CPI} = \frac{\zeta_{MC}}{\zeta_{data}} = \frac{\epsilon^{w}_{MC}}{\epsilon^{wo}_{MC}} \cdot \frac{\epsilon^{wo}_{data}}{\epsilon^{w}_{data}} = \eta^{w} \cdot \frac{1}{\eta^{wo}}. \tag{8.25}$$

The correction factor ζ^{CPI} depends on the proton kinetic energy T_p, polar angle θ_p, and on the azimuthal angle θ_p in the lab frame. For the charged particle detection efficiency correction, the simulation events were then weighted with this correction factor ζ^{CPI} corresponding to their proton kinetic energy T_p, polar angle θ_p, and azimuthal angle θ_p.

Since this liquid hydrogen data was used to calculate the nucleon detection efficiency, i.e. for this data and the butanol June 2010 data, the influence of the charged particle detection that was not working, must be checked. In the definition of the charged particle detection efficiency (Equation (8.20)), it can be seen that the determination of the charged particle detection efficiency is based on the nucleon efficiency for the analysis with the charged particle detectors. Therefore, the correction factor for the simulation can be factorized by the nucleon detection efficiency η^{w} as defined in Equation (8.20) and the correction of the charge particle detection efficiency η^{wo} defined by Equation (8.25) by [110]:

$$\zeta^{CPI} = \frac{\epsilon^{w}_{MC}}{\epsilon^{wo}_{MC}} \cdot \frac{\epsilon^{wo}_{data}}{\epsilon^{w}_{data}} = \frac{\epsilon^{w}_{MC}}{\epsilon^{w}_{data}} \cdot \frac{1}{\frac{\epsilon^{wo}_{MC}}{\epsilon^{wo}_{data}}} \tag{8.26}$$

$$= \eta^{w}\left(T_p, \theta_p\right) \cdot \frac{1}{\eta^{wo}\left(T_p, \theta_p, \phi_p\right)} \tag{8.27}$$

$$= \underbrace{\frac{\epsilon^{w}_{MC}\left(T_p, \theta_p\right)}{\epsilon^{w}_{data}\left(T_p, \theta_p\right)}}_{\text{std. nucl. eff. corr.}} \cdot \underbrace{\frac{1}{\frac{\epsilon^{wo}_{MC}(T_p, \theta_p, \phi_p)}{\epsilon^{wo}_{data}(T_p, \theta_p, \phi_p)}}}_{\text{add. nucl. eff. corr.}} . \tag{8.28}$$

For the comparison of the standard nucleon detection efficiency with the nucleon detection efficiency extracted from the charged particle detection efficiency, the azimuthal angle of the proton ϕ_p was integrated. The standard nucleon detection efficiency correction obtained over the charged particle detection efficiency is shown in Fig. 8.8 on the left side. It can be seen that the standard nucleon detection efficiency, as discussed in Section 8.6.2, is in a good agreement with the nucleon detection efficiency extracted from the charged particle detection efficiency and can be used for the nucleon detection efficiency. The additional nucleon detection efficiency correction of the charged particle detection efficiency correction is shown in Fig. 8.8 in the middle. The charged particle detection efficiency correction, the product of the standard and additional nucleon detection efficiency correction is shown in Fig. 8.8 on the right side.

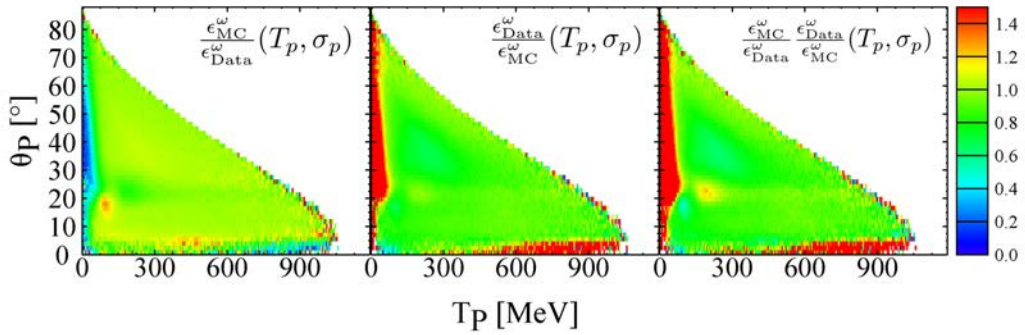

Figure 8.8.: Left side: Nucleon detection efficiency correction as a function of the kinetic energy T_p and the reconstructed polar angle θ_p of the recoil proton in the lab frame. Middle: Charged particle correction as a function of the kinetic energy T_p and the reconstructed polar angle θ_p of the recoil proton in the lab frame. Right side: Full charged particle detector efficiency including the nucleon detection efficiency and the charged particle detection efficiency as a function of the kinetic energy T_p and the reconstructed polar angle θ_p of the recoil proton in the lab frame.

8.6.4 Correction of the Gap between the Crystal Ball and TAPS

The gap between the Crystal Ball and TAPS detector reduces the detection efficiency [110]. The detector efficiency within the gap is not consistent with the experimental data and leads to an overestimation of the angle dependent cross section. The effect of the drop in the efficiency can be seen in the differential cross section for the exclusive analysis for the proton polar angle in the laboratory frame of $18° < \theta_p < 24°$, which corresponds to the angular range of the gap between the Crystal Ball and TAPS. The differential cross section of the double π^0 photoproduction on the proton for the liquid hydrogen data for this energy range is shown in Fig. 8.9 by the filled circles. The region of the gap is indicated by the black vertical lines. For the correction, the points in the peak position were removed and the remaining points were fit with a second degree polynomial. The events in the sensitive region of the gap between the two detectors of the simulation are then weighted by the ratio of the cross section value and the corresponding value of the fit function. By this weighting in the simulation, the reduced detection efficiency of the gap between the Crystal Ball and TAPS can be corrected. The result of the corrected differential cross section of the liquid hydrogen can be seen in Fig. 8.9 by the dashed line. Since the detection efficiency is reduced for all data in the gap region, the determined correction factor was also applied to the corresponding butanol and carbon data.

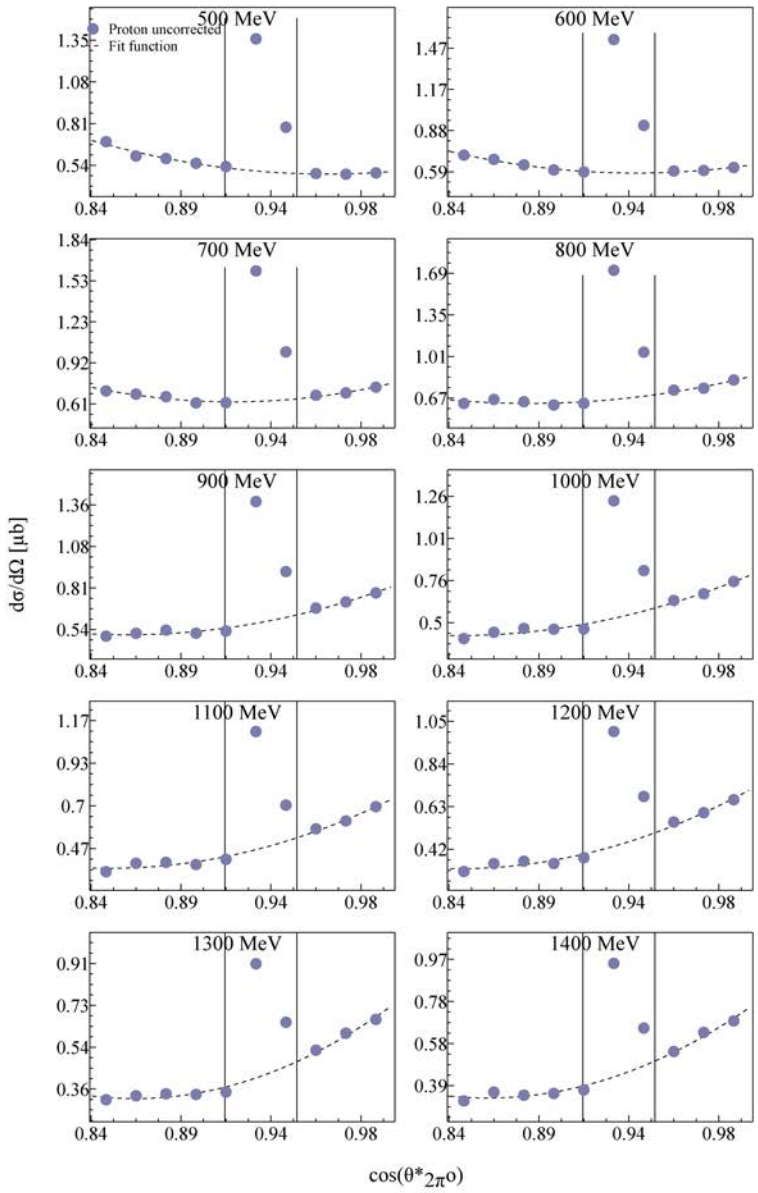

Figure 8.9.: Correction of the gap between the Crystal Ball and TAPS detector for the double π^0 photoproduction for the liquid hydrogen data (April 2009). The uncorrected differential cross section as a function of the proton polar angle in the lab frame are shown by the purple points. The corrected fit function is shown by the black dashed line and the fit of the uncorrected purple points is shown by the black line. The region of the Crystal Ball and TAPS detector is shown by the black vertical lines.

8.6.5 Final Detection Efficiency

For the determination of the detection efficiencies of the hydrogen and butanol data, all cuts, the software trigger, and necessary detection efficiency correction, i.e. nucleon detection efficiency, the correction of the gap between the Crystal Ball and TAPS, and the charged particle detection efficiency for the liquid hydrogen data, were applied to the detected events of the simulation. The detection efficiency was then calculated by dividing simulated detected events by simulated generated events, corresponding to Equation (8.19). For the detection efficiency, the same number of energy bins for the incident photon energy E_γ and number of $\cos\theta^*_{2\pi^0}$ bins were used as in the experimental data, 64 energy bins and one $\cos\theta^*_{2\pi^0}$ bin.
The detection efficiency as a function of the incident photon beam energy from 450 up to 1450 MeV of the liquid hydrogen and of the butanol data are shown in Fig. 8.10.

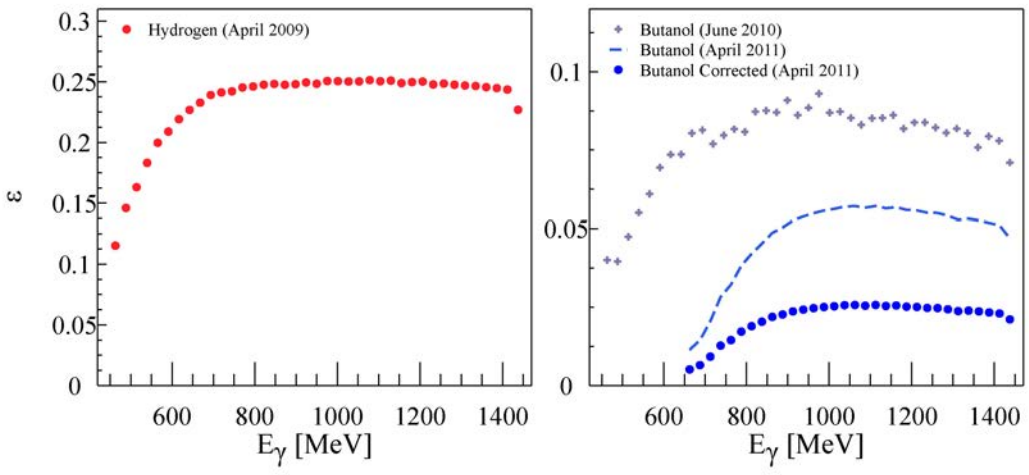

Figure 8.10.: Detection efficiencies for the unpolarised total cross section of the incident beam energy $E_\gamma = 450-1450$ MeV. Left hand side: detection efficiency of the liquid hydrogen data. Right hand side: detection efficiency of the butanol data (June 2010) indicated by the purple cross, uncorrected and corrected detection efficiency of the butanol data (April 2011) indicated by the dashed blue line and blue points, respectively.

The liquid hydrogen data has a much higher detection efficiency than the butanol data, which results from the better detection efficiency of the charged particle detectors. For the June 2010 butanol data, one PID element was broken and could not be used and for the April 2011, only one MWPC and the vetoes could be used for the charged particle detection. For the butanol data (April 2011), problems with the gas mixture of the MWPCs occurred, which reduced the detector efficiency, as explained in Section 2.4.4. Since it was impossible to simulate the resulting inefficiencies of the identification and detection of the charged particles occurring

through the MWPC gas mixture, the detector efficiency must be scaled so that the absolute normalization of the total cross section is correct.

8.7 Systematic Uncertainties

For the interpretation of the measured cross section results, the systematic uncertainties must be considered. Therefore, the sources of the systematic uncertainties must be determined and the corresponding errors must be estimated. In the following sections, the determination of the sources and the corresponding estimated systematic uncertainties are discussed. In the end of this section, a summary of all systematic uncertainties is given.

8.7.1 Sources of the Systematic Uncertainties

The systematic uncertainties of the cross section can be separated into two groups. The first group of systematic uncertainties are caused by measurements such as the target surface, the decay branching ratio, and the photon flux. These uncertainties are energy and angle dependent. The second group of systematic uncertainties are channel dependent such as the analysis cuts, the Crystal Ball energy sum trigger, and the nucleon efficiency correction. These uncertainties are energy E_γ and angle $\cos\left(\theta^*_{2\pi^0}\right)$ dependent and therefore, the uncertainties must also be determined for the different energies and angles.

Target Surface Density

The systematic uncertainty of the target surface density arises in uncertainties in the determination of the target length and the target density, which has a pressure and temperature dependence. For the hydrogen data, the target surface density uncertainty was estimated to be around 3%. The systematic uncertainty of the butanol target was estimated to be around 3%.

π^0 Decay Branching Ratio

The systematic uncertainty of the decay branching ratio for the $\pi^0 \to 2\gamma$ is 0.034% of 98.823% [15].

Photon Flux

The systematic uncertainty of the photon flux depends mainly on the measurement of the tagging efficiency. For the hydrogen data, the time dependent tagging efficiency was determined by the P2/tagger ratio using the absolute tagging efficiency measurements. The systematic uncertainty of the tagging efficiency measurement was then determined by scaling the P2/tagger ratio of the minimum value to the maximum value of the tagger efficiency measurements. By this, a systematic uncertainty of the photon flux of approximately 2.5% was estimated.
For the butanol data, only one tagger efficiency measurement was taken during the beam time. Hence, the systematic uncertainty could not be determined by scaling the P2 tagger ratio (June 2010) or the $\eta + X$ count rate (April 2011) to the maximum or minimum values of the tagging efficiencies measurements. For that reason, the systematic uncertainty of the photon flux was estimated to be around 5%.

Analysis Cuts

The determination of the analysis cuts has a significant influence on the event selection and thus, the cross section result. If the analysis cuts are chosen too loose, more background contribution contaminates the analysis of the desired reaction. On the other hand, if the analysis cuts are chosen to be too strict, then signal events can be cut away. For the determination of the systematic uncertainty of the analysis cuts, the difference of loose and strict cuts on the cross section result must be known. Therefore, the cut position of the invariant mass cut, coplanarity cut, and missing mass cut were varied by a value of $\pm 3\%$. The systematic uncertainty was then determined by the influence of the differences of the two analyses with loose and strict cuts on the final cross section result.

Empty Target Subtraction

As mentioned in Section 8.5, the empty target subtraction is only necessary for the hydrogen cross section. For the calculation of the cross section of the hydrogen contribution of the butanol, the carbon was subtracted from the butanol data and thus, the target container contribution, which is the same for both data. For the hydrogen data, the empty target contribution was estimated to approximately half of the relative empty target contribution, due to the low statistics of the empty target runs. Thus, the uncertainty for the empty target subtraction was assumed to be 2.5%.

CB Energy Sum Trigger

The CB energy sum trigger has a strong influence on the detection efficiency where the simulation events were corrected corresponding to the Crystal Ball energies of the data, as explained in Section 8.6.1. Since the simulated events were only weighted for Crystal Ball energy sums below 350 MeV to achieve the same software conditions in the data and simulation, the systematic uncertainty only has be determined for this energy range. For the determination of the systematic uncertainty, the cross section was calculated by two analyses, one with the applied Crystal Ball energy sum trigger and a second with a fixed cut at $E_{CB} > 350$ MeV. The systematic uncertainty was then calculated by the deviation of the two cross sections and is about $2 - 3\%$ depending on the energy.

Nucleon Detection Efficiency

For the exclusive analysis, the simulation must be corrected by a nucleon detection efficiency, which was determined on the hydrogen data, as explained in Section 8.6.2. For the determination of the systematic uncertainty of the nucleon efficiency, the cross section was calculated inclusively (without requiring the recoil proton to be detected) and exclusively (with the detection of the recoil proton) without applying the nucleon detection efficiency. Since both analysis methods should give the same result, the systematic uncertainty of the nucleon efficiency can be calculated by the difference of these cross sections.

8.7.2 Combined Systematic Uncertainties

For the measurement of the total cross section, the systematic uncertainties caused by the measurement of the individual systematic uncertainties such as the target surface density $\Delta\sigma_{t.s.d}$, the branching ratio $\Delta\sigma_{b.r}$, the photon flux $\Delta\sigma_f$, and the empty target $\Delta\sigma_{e.t}$ are independent and can be added quadratically by:

$$\Delta\sigma_{tot} = \sqrt{\Delta\sigma^2_{t.s.d.} + \Delta\sigma^2_{b.r} + \Delta\sigma^2_f + \Delta\sigma^2_{e.t}}. \tag{8.29}$$

The channel dependent systematic uncertainties such as the analysis cuts $\Delta\sigma_{cuts}$, the Crystal Ball energy sum $\Delta\sigma_{CBS}$, and the nucleon efficiency $\Delta\sigma_{n.e}$ are independent and added quadratically corresponding to their energy and $\cos\left(\theta^*_{2\pi^0}\right)$ values by:

$$\Delta\sigma\left(E_\gamma, \cos\left(\theta^*_{2\Pi^0}\right)\right) = \sqrt{\Delta\sigma^2_{cuts} + \Delta\sigma^2_{CBE} + \Delta\sigma^2_{n.e}}. \tag{8.30}$$

The total systematic uncertainties of the total cross section are the sum of the individual systematic uncertainties of the measurement given by Equation (8.29) and the channel dependent systematic uncertainties given by Equation (8.30). The relative incident energy E_γ dependent systematic uncertainties for the different cross sections can be seen in Fig. 8.11. The red points correspond to the cross section of the hydrogen data and the purple cross and blue points correspond to the cross section of the hydrogen contribution of the butanol data (June 2010 and April 2011).

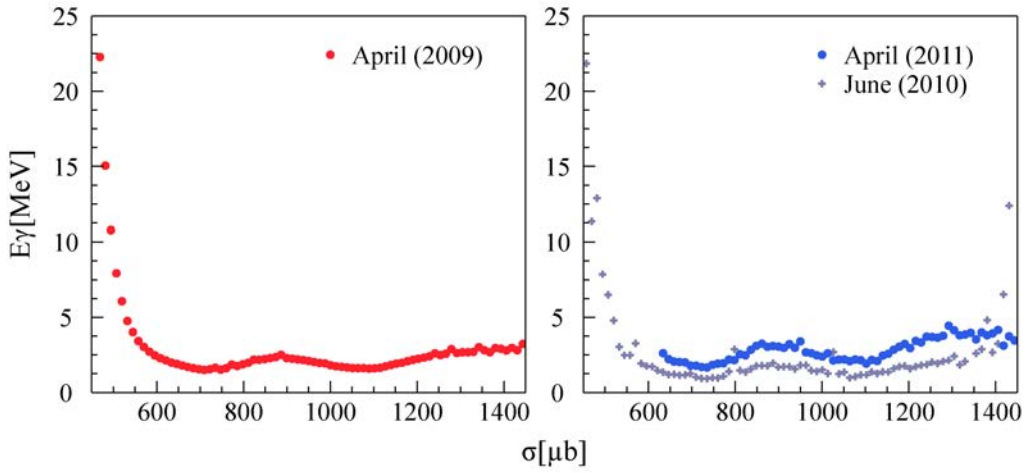

Figure 8.11.: Total systematic uncertainties of the total cross section for the incident beam energy E_γ. Left hand side: liquid hydrogen data. Right hand side: butanol data. June 2010 and April 2011 are indicated by the purple cross and blue points, respectively.

9 Polarisation Observables

In this chapter, the extraction of the polarisation observables F and T of the double π^0 photoproduction from free proton will be discussed. The formalism to determine the polarised cross sections of the butanol, leading to the polarisation observables F and T will be explained in Section 9.1. The events for the polarised differential cross section were determined through the selected cuts and the absolute normalisation, as discussed in Section 7.4. The polarisation observables F and T were measured with a frozen spin butanol target, which has the advantage that only the unbound protons of the hydrogen contribution can be polarised and quasifree reactions on the oxygen and carbon nuclei lead to unpolarised background contributions. The polarisation observables from the azimuthal distribution of double π^0 mesons and the recoil proton can be calculated by two different methods, which eliminate the unpolarised carbon background in the denominator of the asymmetries. In the carbon subtraction method, the unpolarised carbon contribution in the denominator of the asymmetries is subtracted from the butanol. The other method for the extraction of the polarisation observables is the hydrogen normalisation method, where in the denominator of the asymmetries the unpolarised liquid hydrogen cross section is used. These methods, the carbon subtraction method and the absolute normalisation method, will be explained in detail in Section 9.5. In the end of this chapter, the sources and the determination of the systematic uncertainties will be discussed.

9.1 Polarisations Observables F and T

The general formalism for photoproduction of two pseudo-scalar mesons and the corresponding formulas for the different polarisation observables were presented in [36]. The differential polarised cross section for an incident circularly polarised photon beam and transversally polarised target nucleons can be simplified to the following form:

$$\left.\frac{d\sigma}{d\Omega}\right|_{pol} = \left.\frac{d\sigma_0}{d\Omega}\right|_{unpol} \{1 + \frac{1}{\sqrt{2}}[1 + P_{circ}P_x F\cos(\phi) + P_y T\sin(\phi)]\}, \tag{9.1}$$

where the unpolarised differential cross section is denoted as $d\sigma_0$, and F and T are the polarisation observables, and P_{circ} is the degree of photon circular polarisation

of the incident photon beam. The degree of nucleon polarisation P_T for the x and y direction is defined by:

$$P_x = P_T \cdot \cos(\phi) \tag{9.2}$$

$$P_y = P_T \cdot \sin(\phi)\,. \tag{9.3}$$

The ϕ angle depends on the direction of the polarisation of the nucleon target spin. For the measurement of the polarisation observables, the photon beam was circularly polarised with positive and negative helicity, as explained in Section 3.2, and the target nucleons were polarised such that the direction of the spin protons were vertically up or down, as explained in Section 3.3. Therefore, four polarisation cross sections can be defined for the different photon beam polarisation and nucleon target spin polarisation:

$$d\sigma^{+\uparrow}(\phi) = a(\phi)N_\gamma^{+\uparrow}\left(1 + P_{circ}P_x F\cos(\phi) + P_y T\sin(\phi)\right) \tag{9.4}$$

$$d\sigma^{+\downarrow}(\phi) = a(\phi)N_\gamma^{+\downarrow}\left(1 - P_{circ}P_x F\cos(\phi) - P_y T\sin(\phi)\right) \tag{9.5}$$

$$d\sigma^{-\uparrow}(\phi) = a(\phi)N_\gamma^{-\uparrow}\left(1 - P_{circ}P_x F\cos(\phi) + P_y T\sin(\phi)\right) \tag{9.6}$$

$$d\sigma^{-\downarrow}(\phi) = a(\phi)N^{-\downarrow}\left(1 + P_{circ}P_x F\cos(\phi) - P_y T\sin(\phi)\right), \tag{9.7}$$

where $\pm$ denote the helicity state of the incident photon beam and $\uparrow$, $\downarrow$ is the direction of the nucleon target spin vertically up or down. By considering only the nucleon target polarisation, two polarised cross sections can be defined by:

$$d\sigma^{\uparrow}(\phi) = a(\phi)N_\gamma^{\uparrow}\left(1 + P_y T\sin(\phi)\right) \tag{9.8}$$

$$d\sigma^{\downarrow}(\phi) = a(\phi)N_\gamma^{\downarrow}\left(1 + P_y T\sin(\phi)\right). \tag{9.9}$$

The polarised cross section depends on the azimuthal angle acceptance $a(\phi)$ measured with the Crystal Ball. The Crystal Ball acceptance $a(\phi)$ is independent of the photon beam polarisation and the nucleon target spin polarisation and is the same for each defined polarised differential cross section. The photon flux N_γ depends on the corresponding beam-target polarisation setting of the polarised cross section. However, for the measurement, the events for the different beam-target polarisation settings should be equal. For the different photon fluxes, the following conditions apply $N_\gamma^{+} = N_\gamma^{-}$ and $N_\gamma^{\uparrow} = N_\gamma^{\downarrow}$. Therefore, the Crystal Ball acceptance $a(\phi)$ and the corresponding photon fluxes N_γ can be removed for the asymmetries, which allows the extraction of the polarisation observables F and T according to:

$$A_F(\phi) = \frac{d\sigma^{+}(\phi) - d\sigma^{-}(\phi)}{d\sigma^{+}(\phi) + d\sigma^{-}(\phi)} \tag{9.10}$$

$$A_T(\phi) = \frac{d\sigma^{\uparrow}(\phi) - d\sigma^{\downarrow}(\phi)}{d\sigma^{\uparrow}(\phi) + d\sigma^{\downarrow}(\phi)}, \tag{9.11}$$

where A_F and A_T, are the asymmetry of the polarisation observable F and T, respectively. The beam target asymmetry can then be derived by applying the equations of the polarised cross sections Equations (9.5) and (9.7) into Equation (9.10). The beam target asymmetry depends on the circularly photon polarisation and on the nucleon polarisation and is given by:

$$\frac{d\sigma^{+}(\phi) - d\sigma^{-}(\phi)}{d\sigma^{+}(\phi) + d\sigma^{-}(\phi)} = \frac{P_{circ} P_T F \cos(\phi)}{1 + P_T T \sin(\phi)}. \tag{9.12}$$

The target asymmetry can be derived by applying Equations (9.8) and (9.9) into Equation (9.11). Therefore, the target asymmetry depends only on the nucleon target spin polarisation corresponding to:

$$\frac{d\sigma^{\uparrow}(\phi) - d\sigma^{\downarrow}(\phi)}{d\sigma^{\uparrow}(\phi) + d\sigma^{\downarrow}(\phi)} = P_T T \sin(\phi). \tag{9.13}$$

The double polarisation observable F can be derived from the beam asymmetry (Equation (9.12)), since the polarisation observable T is 0 in the beam asymmetry for normalised target spin up and down with the same number of events. Thus, the double polarisation observable F is defined by the circular photon beam polarisation and the transversal nucleon polarisation according to:

$$F \cos(\phi) = \frac{1}{P_T P_{circ}} \frac{d\sigma^{+}(\phi) - d\sigma^{-}(\phi)}{d\sigma^{+}(\phi) + d\sigma^{-}(\phi)}. \tag{9.14}$$

The polarisation observable T depends only on the transversal target polarisation and can be derived from the target asymmetry (Equation (9.13)) by:

$$T \sin(\phi) = \frac{1}{P_T} \frac{d\sigma^{\uparrow}(\phi) - d\sigma^{\downarrow}(\phi)}{d\sigma^{\uparrow}(\phi) + d\sigma^{\downarrow}(\phi)}. \tag{9.15}$$

9.2 Extraction of the Polarisation Observable F

The double polarisation observable F can be extracted by using Equation (9.14) based on the asymmetry as seen in Equation (9.10). For the calculation of the double polarisation observable F, the differential cross sections $d\sigma^{+}(\phi)$ and $d\sigma^{-}(\phi)$ have to be defined corresponding to the circular photon beam polarisation with positive and negative helicity and the nucleon target spin polarisation, vertically up or down. Since F is a double polarisation observable, the definition depends on both polarisations values according to:

$$d\sigma^{+}(\phi) = d\sigma^{+\uparrow}(\phi) + d\sigma^{-\downarrow}(\phi) \tag{9.16}$$

$$d\sigma^{-}(\phi) = d\sigma^{+\downarrow}(\phi) + d\sigma^{-\uparrow}(\phi), \tag{9.17}$$

where $\pm$ denote the helicity state of the incident photon beam and $\uparrow, \downarrow$ is the direction of the nucleon target spin vertically up or down. The double polarisation observable F is defined by Equation (9.14) and can then be written with the definitions given in Equation (9.17) as:

$$\frac{d\sigma^{+}(\phi) - d\sigma^{-}(\phi)}{d\sigma^{+}(\phi) + d\sigma^{-}(\phi)} = \frac{\left(d\sigma^{+\uparrow}(\phi) + d\sigma^{-\downarrow}(\phi)\right) - \left(d\sigma^{+\uparrow}(\phi) + d\sigma^{-\uparrow}(\phi)\right)}{d\sigma^{+\uparrow}(\phi) + d\sigma^{-\downarrow}(\phi) + d\sigma^{+\uparrow}(\phi) + d\sigma^{-\uparrow}(\phi)}. \tag{9.18}$$

The numerator can then be calculated in the following way:

$$\begin{aligned} &\left(d\sigma^{+\uparrow}(\phi) + d\sigma^{-\downarrow}(\phi)\right) - \left(d\sigma^{+\uparrow}(\phi) + d\sigma^{-\uparrow}(\phi)\right) \\ &= d\sigma_0\{(1 + P_T T\sin(\phi) + P_{circ}P_T F\cos(\phi) + 1 - P_T T\sin(\phi) + P_{circ}P_T F\cos(\phi) \\ &\quad - 1 + P_T T\sin(\phi) + P_{circ}P_T F\cos(\phi) - 1 - P_T T\sin(\phi) + P_{circ}P_T F\cos(\phi)\} \\ &= 4P_{circ}P_T F\cos(\phi)\cdot d\sigma_0(\phi), \end{aligned} \tag{9.19}$$

and the denominator can be calculated in the following way:

$$\begin{aligned} &\left(d\sigma^{+\uparrow}(\phi) + d\sigma^{-\downarrow}(\phi)\right) + \left(d\sigma^{+\uparrow}(\phi) + d\sigma^{-\uparrow}(\phi)\right) \\ &= d\sigma_0\{(1 + P_T T\sin(\phi) + P_{circ}P_T F\cos(\phi) + 1 - P_T T\sin(\phi) + P_{circ}P_T F\cos(\phi) \\ &\quad + 1 - P_T T\sin(\phi) - P_{circ}P_T F\cos(\phi) + 1 + P_T T\sin(\phi) - P_{circ}P_T F\cos(\phi)\} \\ &= 4d\sigma_0(\phi). \end{aligned} \tag{9.20}$$

By these definitions of the polarised differential cross section $d\sigma^{+}(\phi), d\sigma^{-}(\phi)$ given in Equation (9.18), only the numerator depends on the polarisation degree of the photon beam and the nucleon target spin and the denominator is given by unpolarised differential cross section $d\sigma_0(\phi)$. Thus, the double polarisation observable F can be extracted as:

$$\frac{d\sigma^{+}(\phi) - d\sigma^{-}(\phi)}{d\sigma^{+}(\phi) + d\sigma^{-}(\phi)} = \frac{4P_{circ}P_T F\cos(\phi)\cdot d\sigma_0}{4d\sigma_0(\phi)} \tag{9.21}$$

$$\Rightarrow\ F\cos(\phi) = \frac{1}{P_T P_{circ}}\frac{d\sigma^{+}(\phi) - d\sigma^{-}(\phi)}{d\sigma^{+}(\phi) + d\sigma^{-}(\phi)}. \tag{9.22}$$

Alternatively, the double polarisation observable F can also be calculated by different ϕ angles between the double π^0 mesons and the recoil nucleon in the numerator by:

$$F\cos(\phi) = \frac{1}{P_{circ}P_T}\frac{\left(d\sigma^{+\uparrow}(\phi) + d\sigma^{+\downarrow}(\pi-\phi)\right) - \left(d\sigma^{-\uparrow}(\phi) + d\sigma^{-\downarrow}(\pi-\phi)\right)}{d\sigma^{+\uparrow}(\phi) + d\sigma^{+\downarrow}(\phi) + d\sigma^{-\uparrow}(\phi) + d\sigma^{-\downarrow}(\phi)}. \tag{9.23}$$

The double polarisation observable F was calculated for both ϕ definitions given by Equations (9.22) and(9.23). Both methods are shown in Appendix A.4.

9.3 Extraction of the Polarisation Observable T

The polarisation observable T, also known as target asymmetry, depends only on the nucleon polarisation and can be calculated by Equation (9.15). Since only one measurement was done for the extraction of the polarisation observable F and T, the photon beam polarisation has to be considered for the definitions of the differential cross section $d\sigma^{\uparrow}(\phi)$ and $d\sigma^{\downarrow}(\phi)$. However, for the helicity dependent differential cross section it can be assumed that, the sum of both differential cross section with positive $d\sigma^{+}$ and negative helicity $d\sigma^{-}$ is equal to the unpolarised differential cross section $d\sigma^{0} = d\sigma^{+}(\phi) + d\sigma^{-}(\phi)$. The differential cross section for the calculation of the polarisation observable T can then be defined according to:

$$d\sigma^{\uparrow}(\phi) = d\sigma^{+\uparrow}(\phi) + d\sigma^{-\uparrow}(\phi) \tag{9.24}$$

$$d\sigma^{\downarrow}(\phi) = d\sigma^{+\downarrow}(\phi) + d\sigma^{-\downarrow}(\phi). \tag{9.25}$$

The polarisation observable T is defined by Equation (9.15) and can then be written with the definitions given in Equation (9.25) as:

$$\frac{d\sigma^{\uparrow}(\phi) - d\sigma^{\downarrow}(\phi)}{d\sigma^{\uparrow}(\phi) + d\sigma^{\downarrow}(\phi)} = \frac{\left(d\sigma^{+\uparrow}(\phi) + d\sigma^{-\uparrow}(\phi)\right) - \left(d\sigma^{+\uparrow}(\phi) + d\sigma^{-\downarrow}(\phi)\right)}{d\sigma^{+\uparrow}(\phi) + d\sigma^{-\uparrow}(\phi) + d\sigma^{+\uparrow}(\phi) + d\sigma^{-\downarrow}(\phi)}. \tag{9.26}$$

The numerator can then be calculated in the following way by:

$$\begin{aligned}
&\left(d\sigma^{+\uparrow}(\phi) + d\sigma^{-\uparrow}(\phi)\right) - \left(d\sigma^{+\downarrow}(\phi) + d\sigma^{-\uparrow}(\phi)\right) \qquad (9.27)\\
&= d\sigma_0\{(1 + P_T T\sin(\phi) + P_{circ}P_T F\cos(\phi) + 1 + P_T T\sin(\phi) - P_{circ}P_T F\cos(\phi)\\
&\quad - 1 - P_T T\sin(\phi) + P_{circ}P_T F\cos(\phi) - 1 + P_T T\sin(\phi) - P_{circ}P_T F\cos(\phi))\}\\
&= 4TP_T\sin(\phi)d\sigma_0(\phi)
\end{aligned}$$

and for the denominator applies:

$$\begin{aligned}
&\left(d\sigma^{+\uparrow}(\phi) + d\sigma^{-\uparrow}(\phi)\right) + \left(d\sigma^{+\downarrow}(\phi) + d\sigma^{-\uparrow}(\phi)\right) \qquad (9.28)\\
&= d\sigma_0\{(1 + P_T T\sin(\phi) + P_{circ}P_T F\cos(\phi) + 1 + P_T T\sin(\phi) - P_{circ}P_T F\cos(\phi)\\
&\quad + 1 - P_T T\sin(\phi) - P_{circ}P_T F\cos(\phi) + 1 - P_T T\sin(\phi) + P_{circ}P_T F\cos(\phi))\}\\
&= 4d\sigma_0(\phi).
\end{aligned}$$

By these definitions of the differential cross sections $d\sigma^{\uparrow}(\phi)$, $d\sigma^{\downarrow}(\phi)$ given in Equation (9.25), the photon beam polarisation cancels out and the numerator depends only on the nucleon polarisation. The denominator is again given by the unpolarised

cross section $d\sigma_0(\phi)$. Thus, the polarisation observable T can be extracted through these definitions by:

$$\begin{aligned}\frac{d\sigma^{\uparrow}(\phi) - d\sigma^{\downarrow}(\phi)}{d\sigma^{\uparrow}(\phi) + d\sigma^{\downarrow}(\phi)} &= \frac{4TP_T \sin(\phi) \cdot d\sigma_0}{4d\sigma_0(\phi)} \\ &= TP_T \sin(\phi)\end{aligned} \tag{9.29}$$

$$\Rightarrow T\sin(\phi) = \frac{1}{P_T}\frac{d\sigma^{\uparrow}(\phi) - d\sigma^{\downarrow}(\phi)}{d\sigma^{\uparrow}(\phi) + d\sigma^{\downarrow}(\phi)}. \tag{9.30}$$

9.4 Extraction of the Yields

In this work, the polarisation observables F and T were extracted for four different representations: for the $cos\theta_{\pi^0}$ of the pions, for the $cos\theta_p$ of the recoil proton, for the invariant mass of the two π^0 pions, and the invariant mass of π^0 pions combined with the recoil proton. The ϕ angle definitions in the centre-of-momentum (cm) system for the extraction of the polarisation observables F and T are shown in Fig. 9.1.

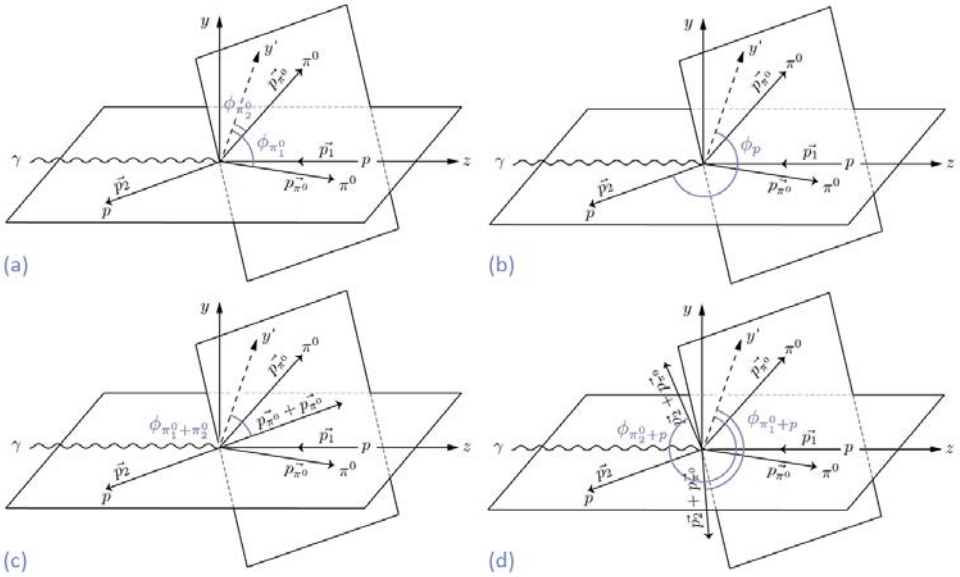

Figure 9.1.: Representation of the coordinate system used in the centre-of-momentum (cm) and the different azimuthal ϕ angles between the π^0 mesons and the recoil proton to the target spin indicated by the y' axis. (a) The $\phi_{1,2}$ angles between the two π^0 mesons depending on the direction of the target spin. (b) The ϕ_p angle between the recoil proton and the target spin. (c) The $\phi_{\pi^0_1+\pi^0_2}$ angle of the meson vector depending on the direction of the target spin. (d) The $\phi_{\pi^0_{1,2}+p}$ angle of each $\pi^0_{1,2}$ meson and the proton depending on the direction of the target spin.

For both polarisation observables F and T, each of the four different representations of the $cos\theta$ angles or the invariant masses, are dependent on the incident photon beam energy E_γ and their corresponding ϕ angle. For the $\phi_{1,2}$ angles, in the $cos\theta_{\pi^0}$ representation, the azimuthal angle from each single pion to the direction of the target polarisation is used, as shown in the Fig. 9.1 (a). In this representation, the azimuthal angle of the pions are used separately to extract more information from $\gamma + p \rightarrow \pi^0\pi^0 p$ reaction, since the use of the combined vector $\pi^0_1 + \pi^0_2$ would have the same information as the $-cos\theta_p$. The ϕ_p angle for the $cos\theta_p$ representation is the azimuthal angle from the recoil proton to the direction of the target polarisation, as shown in Fig. 9.1 (b). For the invariant mass of the two pions representation, the ϕ angle is defined as the azimuthal angle from the meson vector $\pi^0_1 + \pi^0_2$ to the target spin, as seen in Fig. 9.1 (c). For the representation of each pion combined with the recoil proton, the azimuthal $\phi_{\pi^0_{1,2}+p}$ angle is defined between the combined vectors of each pion and the recoil proton $\pi^0_{1,2} + p$ to the target polarisation, as shown in Fig. 9.1. As with the $cos\theta_{\pi^0}$ representation both pions combined with the recoil proton are recorded separately to obtain more information from the reaction. Due to the available statistics for all yields the incident photon beam energy E_γ from 450 up to 1450 MeV is split into 10 energy ranges, the ϕ angles and the representation each into 8 ranges. For the polarisation observables in the representation of the invariant masses, the range of the invariant mass spectra is extended for higher energies.
For the calculation of the polarisation observables F and T using the carbon subtraction method and the hydrogen normalisation method, explained in detail in Section 9.5.1, the yields were extracted from the polarised butanol, the unpolarised carbon and liquid hydrogen data. Before the yields were extracted all the necessary cuts, introduced in Section 7.4, were applied to reject hydrogen background channel contribution. Finally, the yields of the differential cross sections for the polarisation observables were extracted by integrating the different spectra in the range of the cuts.

9.5 Methods

As mentioned in Section 2.5, the measurement of the polarisation observables F and T requires a circularly polarised photon beam and transversally polarised target nucleons. The photon polarisation for the butanol data (June 2010 and April 2011) was given via the helicity transfer of a longitudinally polarised electron beam with an energy of 1557 MeV and a polarisation degree of around 80%, as explained in Section 3.2. The unbound hydrogen protons were polarised by the DNP method, as explained in Section 3.3. Based on this method, a target polarisation of approximately $P_T = 80\%$ could be reached. However, the use of a butanol target has the disadvantage that only the free hydrogen protons can be polarised and unpolarised

background contributions occur from quasi-free reactions on the bound and not polarisable carbon and oxygen nuclei. Due to the definitions of the asymmetries of the polarisation observables F and T, the unpolarised carbon background channels cancel out in the numerator of the asymmetries, but remain in the denominator of the asymmetries. For the extraction of the polarisation observables, two different methods exist to remove the unpolarised carbon contribution in the denominator of the asymmetries: the carbon subtraction method and the hydrogen normalisation method. These two methods will be explained in detail in the following sections.

9.5.1 Carbon Subtraction Method

In the carbon subtraction method, the remaining carbon contribution in the denominator of the asymmetries of the polarisation observables is subtracted by the unpolarised differential carbon cross section. Hence, an additional measurement of a carbon target under almost the same experimental conditions as the butanol target was required. For the carbon subtraction, the number of carbon and oxygen nuclei has to be normalised to the carbon nuclei inside the butanol target under the consideration of the cooling process of the frozen-spin butanol target with a ^3He $-^4$ He mixture, as explained in Section 8.3.3. In the following sections, the carbon subtraction method for the polarisation observables F and T will be discussed.

Polarisation Observable F

As mentioned in Section 9.2, the double polarisation observable F is defined for a circularly polarised photon beam and a transversally polarised target and can be calculated by:

$$F\cos(\phi) = \frac{1}{P_T P_{circ}} \frac{d\sigma_B^+(\phi) - d\sigma_B^-(\phi)}{d\sigma_B^+(\phi) + d\sigma_B^-(\phi)} = \frac{1}{P_T P_{circ}} \frac{d\sigma_{diff}(\phi)}{d\sigma_{sum}(\phi)}, \tag{9.31}$$

where P_{circ} and P_T are the polarisation degree of the photon beam and the hydrogen target protons, respectively, and $d\sigma_B^+(\phi)$ and $d\sigma_B^-(\phi)$ are the polarised differential cross sections of the butanol depending on the circularly polarised photon beam and transversally polarised target protons, as defined in Equation (9.17). Hence, the nominator is defined by the difference of the differential polarised cross section of the butanol and the denominator is defined by the sum of the differential polarised cross sections.
Since the differential cross section of the butanol consists of the differential cross

section of the hydrogen and the carbon and oxygen contribution, the following condition applies for the numerator:

$$d\sigma_B^+(\phi) - d\sigma_B^-(\phi) = d\sigma_H^+(\phi) + d\sigma_{CO}(\phi) - d\sigma_H^-(\phi) - d\sigma_{CO}(\phi) \tag{9.32}$$

$$= d\sigma_H^+(\phi) - d\sigma_H^-(\phi) = \sigma_{diff}(\phi), \tag{9.33}$$

where $d\sigma_H^+(\phi)$ and $d\sigma_H^-(\phi)$ are the differential cross sections of the hydrogen contribution of the butanol for the defined beam and target polarisation and $d\sigma_{CO}(\phi)$ is the unpolarised differential cross section of the carbon and oxygen contribution of the butanol. The numerator is defined by the difference of the polarised differential cross section for the defined photon beam and target polarisation and the differential cross section of the unpolarised carbon background cancels out. In contrast to the denominator, where the differential cross section of the carbon and oxygen are added and remain:

$$d\sigma_B^+(\phi) + d\sigma_B^-(\phi) = d\sigma_H^+(\phi) + d\sigma_{CO}(\phi) + d\sigma_H^-(\phi) + d\sigma_{CO}(\phi) \tag{9.34}$$

$$= d\sigma_H^+(\phi) - d\sigma_H^-(\phi) + 2 \cdot d\sigma_C(\phi). \tag{9.35}$$

To extract the double polarisation observable F, the existing oxygen and carbon background contribution in the denominator must be removed. As mentioned in Section 8.3, a carbon cross section was measured under almost the same experimental conditions ad the butanol target to subtract the unpolarised carbon contribution in the denominator according to:

$$F\cos(\theta) = \frac{1}{P_T P_{circ}} \frac{d\sigma_B^+(\phi) - d\sigma_B^-(\phi)}{d\sigma_B^+(\phi) + d\sigma_B^-(\phi) - 2 \cdot d\sigma_C(\phi) \cdot \frac{n_{CO}+n_{HE}}{n_T^B}}, \tag{9.36}$$

where the scaling factor $n_T/(n_{CO}+n_{HE})$ is used to scale the number of carbon and oxygen nuclei to the number of carbon nuclei inside the butanol target under the consideration of the cooling process, as explained in Section 8.3.3.
The double polarisation observable F yields the following expression by the normalization parameters of the differential cross section, as explained in Section 8.1 by:

$$F\cos(\phi) = \frac{1}{P_T P_{circ}} \frac{\frac{N_B^+}{N_{\gamma,B}^+ \epsilon_B^+ n_p^B} - \frac{N_B^-}{N_{\gamma,B}^- \epsilon_B^- n_p^B}}{\frac{N_B^+}{N_{\gamma,B}^+ \epsilon_B^+ n_p^B} + \frac{N_B^-}{N_{\gamma,B}^- \epsilon_B^- n_p^B} - 2 \cdot \frac{N_C}{N_{\gamma,C} \epsilon_B n_T^C} \cdot \frac{n_{CO}+n_{HE}}{n_T^B}}, \tag{9.37}$$

where N_B^+, N_B^- are the yields of the butanol target with the defined polarisation of the circularly polarised photon beam and transversally polarised target protons and N_C are the yields of the carbon target, which are then normalized by the corresponding photon flux $N_{\gamma,B}^{\pm}$ for the butanol data and $N_{\gamma,C}$ for the carbon data, $\epsilon_B^{\pm}$ is the detector efficiency of the butanol, and n_p^B and n_T^C are the target surface

densities of the butanol and carbon, respectively, as introduced in Section 8.3. Since it can be assumed that the unpolarised carbon background inside the butanol target has the same detector efficiency as the butanol, the detector efficiency from the butanol was used for the carbon cross section. The branching ratio is the same for all differential cross sections and can be neglected.

Polarisation Observable T

The polarisation observable T depends only on the nucleon polarisation, as mentioned in Section 9.3, and can be calculated by:

$$T \sin(\phi) = \frac{1}{P_T} \frac{d\sigma_B^{\uparrow}(\phi) - d\sigma_B^{\downarrow}(\phi)}{d\sigma_B^{\uparrow}(\phi) + d\sigma_B^{\downarrow}(\phi)} = \frac{1}{P_T} \frac{d\sigma_{diff}(\phi)}{d\sigma_{sum}(\phi)}, \tag{9.38}$$

where P_T is the degree of nucleon polarization and $d\sigma_B^{\uparrow}(\phi)$ and $d\sigma_B^{\downarrow}(\phi)$ are the polarised differential cross sections of the butanol with proton target polarisation up and down, respectively. Hence, the numerator is defined by the difference of differential polarised cross sections of the butanol and the denominator is defined by the sum of the differential polarised cross section.
The numerator can also be written in the representation of the differential cross section of the hydrogen and background contribution of oxygen and carbon as:

$$\begin{aligned} d\sigma_B^{\uparrow}(\phi) - d\sigma_B^{\downarrow}(\phi) &= d\sigma_H^{\uparrow}(\phi) + d\sigma_{CO}(\phi) - d\sigma_H^{\downarrow}(\phi) - d\sigma_{CO}(\phi) && (9.39) \\ &= d\sigma_H^{\uparrow}(\phi) - d\sigma_H^{\downarrow}(\phi) = d\sigma_{diff}(\phi), && (9.40) \end{aligned}$$

where $d\sigma_H^{\uparrow}(\phi)$ and $d\sigma_H^{\downarrow}(\phi)$ are the differential cross sections of the hydrogen contribution of the butanol with proton target polarisation of spin-up and spin-down, respectively, and $d\sigma_{CO}(\phi)$ is the unpolarised differential cross section of the oxygen and carbon contribution of the butanol. Thus, the numerator is defined by the differences of the nucleon polarisation with spin up and spin down and the differential cross section of the background contributions cancels out. For the denominator, the differential cross sections of the carbon and oxygen are added:

$$\begin{aligned} d\sigma_B^{\uparrow}(\phi) + d\sigma_B^{\downarrow}(\phi) &= d\sigma_H^{\uparrow}(\phi) + d\sigma_{CO}(\phi) + d\sigma_H^{\downarrow}(\phi) + d\sigma_{CO}(\phi) && (9.41) \\ &= d\sigma_H^{\uparrow}(\phi) + d\sigma_H^{\downarrow}(\phi) + 2 \cdot d\sigma_{CO}(\phi). && (9.42) \end{aligned}$$

For the extraction of the polarisation observable T, the remaining oxygen and carbon background contribution in the denominator must to be removed. As mentioned in Section 9.5.1, the carbon background can again be subtracted by the measured unpolarised carbon cross sections under the same experimental conditions as for the

butanol data. Thus, the polarisation observable T with the carbon subtraction can be written as:

$$T\sin(\phi) = \frac{1}{P_T}\frac{d\sigma_B^{\uparrow}(\phi) - d\sigma_B^{\downarrow}(\phi)}{d\sigma_B^{\uparrow}(\phi) + \cdot d\sigma_B^{\downarrow}(\phi) - 2\cdot d\sigma_{CO}(\phi)\cdot\frac{n_{CO}+n_{HE}}{n_T^B}}, \tag{9.43}$$

where the scaling factor for the nuclei $(n_{co}+n_{He})/n_T^B$ is used to scale the number of carbon and oxygen nuclei to the number of hydrogen nuclei inside the butanol target under the consideration of the cooling process of the frozen-spin butanol target, as explained in Section 8.3.3. The polarisation observable T can then be written by using the yields and the corresponding normalization parameters according to:

$$T\sin(\phi) = \frac{1}{P_T}\frac{\frac{N_B^{\uparrow}}{N_{\gamma,B}^{\uparrow}\epsilon^{\uparrow}n_p^B} - \frac{N_B^{\downarrow}}{N_{\gamma,B}^{\downarrow}\epsilon^{\downarrow}n_p^B}}{\frac{N_B^{\uparrow}}{N_{\gamma,B}^{\uparrow}\epsilon^{\uparrow}n_p^B} + \frac{N_B^{\downarrow}}{N_{\gamma,B}^{\downarrow}\epsilon^{\downarrow}n_p^B} - 2\cdot\frac{N_C}{N_{\gamma,C}\epsilon_B n_T^C}\cdot\frac{n_{CO}+n_{HE}}{n_T^B}}, \tag{9.44}$$

where $N_B^{\uparrow}$ and $N_B^{\downarrow}$ are the yields of the butanol target with proton spin up and down, respectively, and N_C is the yield of the carbon target, which are then normalized by the corresponding photon flux $N_{\gamma}^{\uparrow,\downarrow}$ for the butanol data and $N_{\gamma,C}$ for the carbon data, $\epsilon_B^{\uparrow,\downarrow}$ is the detector efficiency of the butanol, and n_p^B and n_T^C are the target surface densities of the butanol and carbon, respectively, as introduced in Section 8.3. For the detector efficiency, the butanol efficiency was again used for the carbon since the carbon contribution inside the butanol target was considered. The branching ratio can again be neglected since it depends only on the reaction and is the same for all differential cross sections.

9.5.2 Hydrogen Normalisation Method

In the hydrogen normalisation method, the unpolarised differential cross section of the liquid hydrogen data is used in the denominator of the asymmetries for the calculation of the polarisation observables F and T. This has the advantage that no carbon has to be subtracted in the denominator of the asymmetries. However, an additional measurement of a liquid hydrogen data under almost the same experimental conditions as the butanol target is required. In the following sections, the hydrogen normalisation method for the polarisation observables F and T will be discussed.

Polarisation Observable F

As mentioned in Section 9.5.1, the numerator of the double polarisation observable F is given by the difference of the photon beam polarisation and the proton target polarisation. Thus, the unpolarised cross section of the liquid hydrogen, which applies to $d\sigma_H(\phi) = d\sigma_H^+(\phi) + d\sigma_H^-(\phi)$, can be used to normalise the polarisation observable F according to:

$$F\cos(\phi) = \frac{1}{P_T P_{circ}} \frac{d\sigma_B^+(\phi) - d\sigma_B^-(\phi)}{d\sigma_H(\phi)} = \frac{1}{P_T P_{circ}} \frac{d\sigma_{diff}(\phi)}{d\sigma_H(\phi)}, \tag{9.45}$$

where P_{circ} and P_T are the polarisation degree of photon beam and the target proton spin, respectively, $d\sigma_B^{\pm}(\phi)$ is the differential cross section of the polarised butanol with the defined photon beam and proton target polarisation, and $d\sigma_H(\phi)$ is the unpolarised differential cross section of the liquid hydrogen data.
This method has the advantage that the unpolarised carbon background contribution cancels out in the numerator of the asymmetry and the denominator of the asymmetry is given by the unpolarised liquid hydrogen cross section. Therefore, a carbon background subtraction is not necessary. Since the butanol and the liquid hydrogen data were measured under different experimental conditions by using different target sizes, the differential cross section has to be normalised by the photon flux, the detector efficiency, and the target surface densities. The double polarisation observable F can be written by using the yields and the corresponding normalisation parameters as:

$$F\cos(\phi) = \frac{1}{P_T P_{circ}} \frac{\frac{N_B^+}{N_{\gamma,B}^+ \epsilon_B^+ n_p^B} + \frac{N_B^-}{N_{\gamma,B}^- \epsilon_B^- n_p^B}}{\frac{N_H}{N_{\gamma,H} \epsilon_H n_T^H}}, \tag{9.46}$$

where N_B^+ and N_B^- are the yields of the polarised butanol data depending on the defined circularly photon beam polarisation and proton target polarisation, N_H is the yield of the unpolarised liquid hydrogen data, $N_{\gamma,B}^{\pm}$ and $N_{\gamma,H}$ are the corresponding photon fluxes of the butanol and hydrogen data, $\epsilon_B^{\pm}$, ϵ_H are the detector efficiencies of the butanol and the hydrogen, and n_p^B, n_T^H are the target surface surfaces densities of the hydrogen protons of the butanol target and the liquid hydrogen target, as explained in Section 8.3.3.

Polarisation Observable T

As mentioned in Section 9.5.1, the numerator of the polarisation observable T is given by the difference of the transversally polarised target proton spin, vertically up or down. Since for the unpolarised liquid hydrogen cross section, the following

condition applied $d\sigma_H(\phi) = d\sigma^{\uparrow}(\phi) + d\sigma^{\downarrow}(\phi)$, the asymmetry of the polarisation observable T can be normalised according to:

$$T \sin(\phi) = \frac{1}{P_T} \frac{d\sigma_B^{\uparrow}(\phi) - d\sigma_B^{\downarrow}(\phi)}{d\sigma_H(\phi)} = \frac{1}{P_T} \frac{d\sigma_{diff}(\phi)}{d\sigma_H(\phi)}, \tag{9.47}$$

where P_T is the degree of nucleon polarisation, $d\sigma_B^{\uparrow}(\phi)$ and $d\sigma_B^{\downarrow}(\phi)$ are the differential cross section with proton target spin-up and spin-down, respectively, and $d\sigma_H(\phi)$ is the unpolarised liquid hydrogen cross section.
Since the carbon contribution cancels out in the numerator and the denominator is given by the hydrogen cross section, a carbon subtraction is not required. However, the butanol and the liquid hydrogen data were measured with different target sizes, the frozen-spin butanol target has a length of 2 cm and the liquid hydrogen target has a length of 10 cm. Due to the different measurements of the butanol and hydrogen data, the differential cross section had to be normalised by the photon flux, the detector efficiency, and the target surface density. Thus, the polarisation observable T can be written by the use of the yields and the normalization parameters as:

$$T \sin(\phi) = \frac{1}{P_T} \frac{\frac{N_B^{\uparrow}}{N_{\gamma,B}^{\uparrow} \epsilon_B^{\uparrow} n_p^B} + \frac{N_B^{\downarrow}}{N_{\gamma,B}^{\downarrow} \epsilon_B^{\downarrow} n_p^B}}{\frac{N_H}{N_{\gamma,H} \epsilon_H n_T^H}}, \tag{9.48}$$

where $N_B^{\uparrow}$ and $N_B^{\downarrow}$ are the yields of the polarised butanol with target spin-up and spin-down, respectively, N_H is the yield of the unpolarised liquid hydrogen, $N_{\gamma,B}^{\uparrow,\downarrow}$ and $N_{\gamma,H}$ are the corresponding photon fluxes of the butanol and hydrogen data, respectively, $\epsilon_B^{\uparrow,\downarrow}$ and ϵ_H are the detector efficiencies of the butanol and of the liquid hydrogen, respectively, and n_p^B and n_T^H are the target surface densities of the hydrogen protons of the butanol target and the liquid hydrogen target, introduced in Section 8.3.3.

9.6 Detector Efficiency Correction

For the extraction of the polarisation observable T, the polarised differential cross section of the butanol data as well as the unpolarised differential cross section of the liquid hydrogen and the carbon data must be detector efficiency corrected. This has to be done so that the asymmetry of the detector setup is not included into the measurement results. For the double polarisation observable F, the detector efficiency can be neglected since the asymmetry of the detector system cancels out in the extraction of this observable.
For the detector efficiency correction of the polarisation observable T, the same Geant4 simulation was used as for the total cross section, but for the corresponding yields of the observable. For the unpolarised differential cross section of the liquid

hydrogen, the hydrogen simulation with the same experimental setup as in the measured liquid hydrogen data was used. For the butanol and the carbon differential cross sections, only the hydrogen contribution of the butanol target was simulated with the same experimental setup of the corresponding butanol data. Since in the butanol target only the unbound protons of the hydrogen contribution of the butanol can be polarised, as explained in Section 3.3, and the unpolarised contribution of the carbon and oxygen of the butanol is rejected by the hydrogen normalisation method or the carbon subtraction method. For the unpolarised differential cross section of the carbon, the same detector efficiency as for the butanol is used under the assumption that the carbon contribution of the butanol target has the same efficiency as the butanol.

For the calculation of the detection efficiency correction, the generated and detected simulated events have to be divided corresponding to Equation (8.19). The detection efficiency correction was then calculated for the same energy E_γ, invariant masses of the pions, and the recoil proton and $\cos\theta_{2\pi^0}$ and ϕ angles as the yields, which were used for the calculation of the polarisation observables. The simulation was corrected by the software thresholds, as explained in Section 8.6.1 and the charged particle detection efficiency correction for the hydrogen, as explained in Section 8.6.3 was applied. All other corrections such as the nucleon detection efficiency, explained in Section 8.6.2 and the gap correction between the Crystal Ball and TAPS, can be neglected because they cancel out in the calculation of the polarisation observable T. The detector efficiency for the differential cross sections of the April 2011 butanol data and also for the carbon data for the different $cos\theta_{\pi^0}$ bins as a function of the photon beam energy and ϕ_{π^0} angle of each pion to the direction of the target spin, is shown in Fig. 9.2.

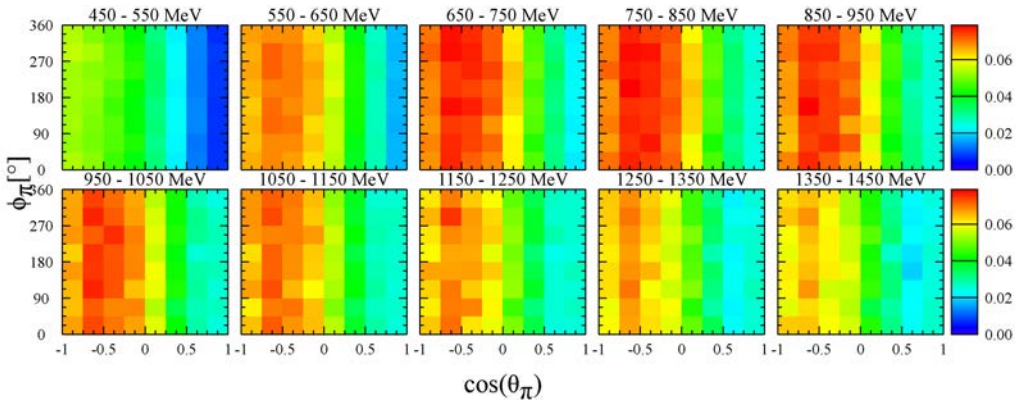

Figure 9.2.: Detector efficiency correction for the April 2011 butanol data for the different $cos\theta_{\pi^0}$ as a function of the photon beam energy and the ϕ_{π^0} angle of each pion to the direction of the target spin.

However, the experimental data can only be corrected for the detector efficiency when the experimental and simulation data are consistent. For the June 2010 butanol data, some angle dependent problems occurred from the charged particle detector,

the PID, which could not be identified and could not be solved by simulating the same problem. Through these inconsistencies in the identification and detection of the recoil proton, the detector efficiency correction was over or underestimated in some angle ranges. Hence, the polarisation observable T for the June 2010 data cannot be correctly determined and this data was discarded for the extraction of the polarisation observable T.

9.7 Fits

For the extraction of the polarisation observables F and T, the asymmetries A_F and A_T of the observables defined by Equations (9.10) and (9.11) are fit with the corresponding functions from Equations (9.14) and (9.15). In the following sections, the measured asymmetry results of the double polarisation observable F for the butanol data (June 2010 and April 2011) and the polarisation observable T for the butanol data (April 2011) with the corresponding fit functions are shown.

9.7.1 Fits of the Double Polarisation Observable F

For the extraction of the double polarisation observable F, the asymmetry A_F, given by Equation (9.10), has to be fit with a cosine function. The asymmetry A_F as a function of the photon beam energy from 650 up to 750 MeV and $\cos\theta_{\pi^0} = -0.325$ is shown in Fig. 9.3.

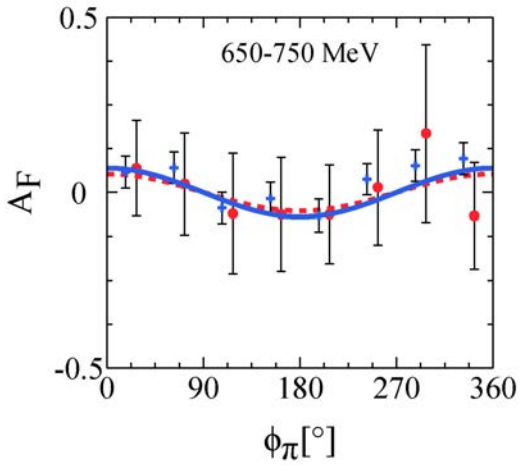

Figure 9.3.: Target asymmetry A_F of the double polarisation observable F for the carbon subtraction method for the incident photon beam energy range of 650 up to 750 MeV and $cos\theta_{\pi^0} = -0.325$. The red points and the blue cross show the asymmetry results of the butanol June 2010 and April 2011 data (shifted by $\pm 2.5\%$) with the corresponding fit function.

The red points and the blue cross are the measurement results of the asymmetry A_F of the June 2010 and April 2011 data, respectively. The fit of the cosine function has the same coloring as the corresponding butanol data. The double polarisation observable F is then given by the amplitude of the cosine fit for the corresponding $cos\theta_{\pi^0}$ angle and energy range of 650 up to 750 MeV. All the measured asymmetry results A_F of the double polarisation observable F with the corresponding fit functions are shown in Appendix A.2.

9.7.2 Fits of the Polarisation Observable T

The polarisation observable T is extracted by fitting the asymmetry A_T, given by Equation (9.11), with a cosine function. However, the asymmetry A_T could only be correctly calculated for the April 2011 butanol data, due to the detection efficiency correction problems with the charged particle detector, the PID, for the June 2010 butanol data, as explained in Section 9.6. The asymmetry A_T of the polarisation observable T as a function of the photon beam energy from 650 up to 750 MeV and $\cos\theta_{\pi^0} = -0.125$ is shown in Fig. 9.4.

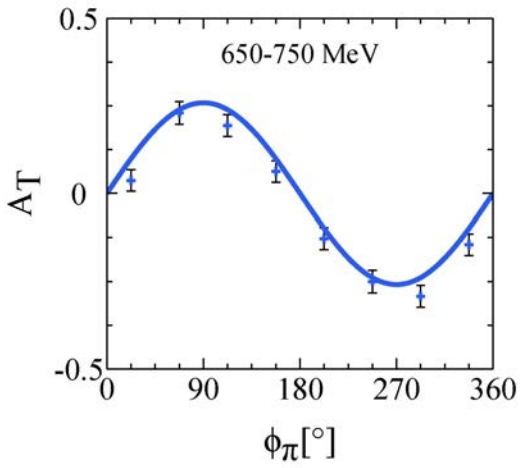

Figure 9.4.: Target asymmetry A_T of the polarisation observable T for the carbon subtraction method for the incident photon beam energy range of 650 up to 750 MeV and $cos\theta_{\pi^0} = -0.125$. The asymmetry A_T for the butanol April 2011 data with the corresponding fit function is shown.

The blue points are the measured results of the asymmetry A_T of the butanol April 2011 data. The blue line shows the fit result of the sine function. The polarisation observable T is then given by the amplitude of the sine fit. All the measured asymmetry results A_T of the polarisation observable T with the corresponding fit functions are shown in Appendix A.3.

9.8 Systematic Uncertainties

For the evaluation of the measured polarisation observable results, the systematic uncertainties have to be determined. Since for the calculation of the polarisation observables F and T, the polarised differential cross section of the butanol and the unpolarised differential cross section of the hydrogen were used, the systematic uncertainties caused by these measurements must be considered. However, for the determination of the polarisation observables by the carbon subtraction method and the hydrogen normalisation method, most of the systematic uncertainties, such as the uncertainties coming from the branching ratio and analysis cuts, cancel out since they appear in the numerator and denominator of the asymmetries. Hence, only the systematic uncertainties, which do not cancel out, such as the uncertainties coming from the carbon subtraction or the hydrogen normalisation of the polarised and unpolarised differential cross section have to be considered. In contrast to the unpolarised differential cross sections of the carbon and the liquid hydrogen, the systematic uncertainties of the polarisation values have to be considered for the polarised differential cross sections of the butanol. Since the necessary systematic uncertainties for the measurement of the unpolarised total cross section and thus, for the unpolarised differential cross section, were discussed in Section 8.7, only the additional systematic uncertainties coming from the measurement of the photon beam polarisation and the target polarisation will be discussed in the following Sections.

Photon Polarisation

The photon polarisation was determined by the Mott measurement, which measures the electron beam polarisation, as mentioned in Section 3.1.1. Therefore, the systematic uncertainties of the photon polarisation are given by the Mott measurement [34]:

-1.1%	due to the bending of the electron beam of around 3.1° before the A2 hall
-2.2%	due to the fact that not all electrons could be polarized longitudinally and some electrons have a transverse polarisation
-1.0%	from the Mott measurement itself according to the finite thickness of the Mott radiator
-0.2%	statistical errors.

The total relative systematic uncertainty of the electron polarisation by the Mott measurement is then about 2.7%

Target Polarisation

The systematic uncertainties of the target polarisation from the NMR measurement for the June 2010 June data (left) and for the April 2011 data (right) are shown in Fig. 9.5.

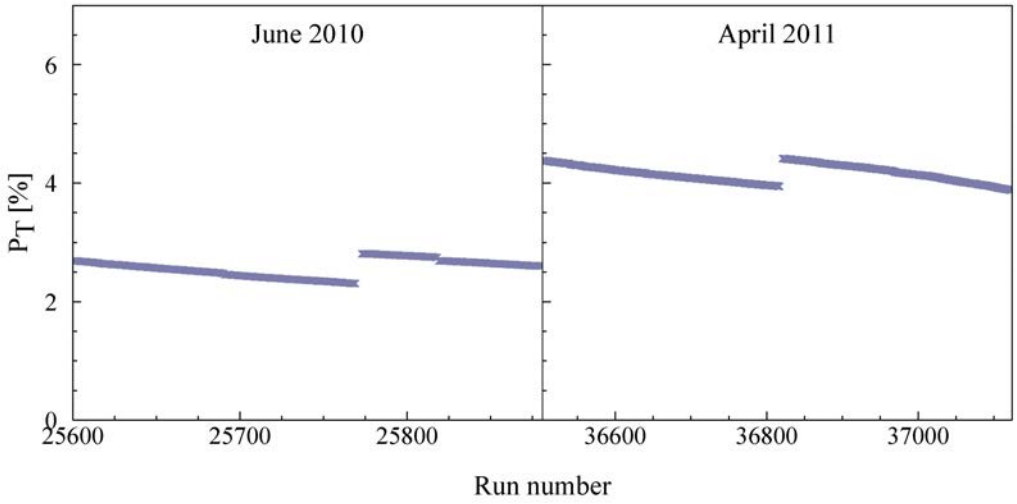

Figure 9.5.: Target polarisation errors for the butanol data June 2010 (left) and butanol data April 2011 (right).

9.8.1 Combined Systematic Uncertainties

As mentioned in Section 9.8, most of the systematic uncertainties cancel out in the calculation of the polarisation observables F and T. For the double polarisation observable F, only the systematic uncertainties of the target surface density $\Delta\sigma_{t.s.d}$, and the photon flux $\Delta\sigma_f$ have to be considered for the unpolarised differential cross section of the carbon and the liquid hydrogen. For the polarised differential cross section of the butanol, the systematic uncertainties of the photon beam polarisation $\Delta\sigma_{b.p}$ and target polarisation $\Delta\sigma_{t.p}$ have to be considered additionally. Since the individual systematic uncertainties are independent, the overall systematic uncertainty for the double polarisation observable F is then given by summing all of the systematic uncertainties quadratically according to:

$$\Delta\sigma_{F,tot} = \sqrt{\Delta\sigma_{t.s.d}^2 + \Delta\sigma_f^2 + \Delta\sigma_{b.p}^2 + \Delta\sigma_{t.p}^2}. \tag{9.49}$$

For the measurement of the polarisation observable T, the sum of systematic uncertainties depend on the same systematic uncertainties as for the double polarisation observable F. However, the polarised butanol differential cross sections for the polarisation observable T are independent of the photon beam polarisation and thus, the systematic uncertainty of the photon beam polarisation can be neglected.

Therefore, the overall systematic uncertainty for the polarisation observable T is given by:

$$\Delta\sigma_{T,tot} = \sqrt{\Delta\sigma_{t.s.d}^2 + \Delta\sigma_f^2 + \Delta\sigma_{t.p}^2}. \tag{9.50}$$

9.9 Merging of the Datasets

The polarisation observables F and T were extracted for each butanol data set to ensure that both measurements with different analysis methods have the same result. Since the results of the polarisation observable have no systematic deviations, the datasets could be merged.
For the merging of the two datasets, the average $\langle x \rangle$ was calculated from the data points x_i and weighted by the statistical uncertainties according to:

$$\langle x \rangle = \frac{\sum_{i=1}^{2} \frac{x_i}{(\Delta x_i)^2}}{\sum_{i=1}^{2} \frac{1}{(\Delta x_1)^2}} \quad \Delta\langle x \rangle = \frac{1}{\sqrt{\sum_{i=1}^{2} \frac{1}{(\Delta x_i)^2}}}, \tag{9.51}$$

where $x_1 \pm \Delta x_1$ and $x_2 \pm \Delta x_2$ are the data points of the polarisation observables F and T for the butanol June 2010 data and the butanol April 2011 data, respectively. The statistical errors Δx are given by the standard error propagation.

10 Results and Discussion

In this chapter, the final results of the unpolarised total cross section and the polarisation observables F and T of the double π^0 reaction from free proton will be discussed. In Section 10.1, the results of the unpolarised total cross section of the liquid hydrogen data and the unpolarised cross section of the hydrogen contribution of the butanol data will be presented. The results of both unpolarised total cross sections were extracted from an exclusive analysis, which requires the detection of the recoil proton as a function of the incident photon energy E_γ from 450 up to 1450 MeV. The unpolarised total hydrogen cross section was measured for the hydrogen normalisation method of the polarisation observables F and T, as explained in Section 9.5.2. The unpolarised total cross section of the hydrogen contribution of the butanol data was measured to check the absolute normalisation of both analysis methods of the butanol and carbon data. In Sections 10.2.1 and 10.2.2, the results of the polarisation observables F and T are presented for the carbon subtraction method and the hydrogen normalisation method, as explained in Section 9.5. The incident photon beam energy dependent results for the polarisation observables F and T for the double π^0 mesons, the recoil proton and the invariant masses, as introduced in Section 9.1, are presented. The results were compared with the theoretical predictions of the MAID isobar model [41] and the BnGa coupled channel wave analysis model [111][112]. For the interpretation of the results, the systematic uncertainties were indicated as lines with the same colouring as the corresponding measurement method, the carbon subtraction method or the hydrogen normalisation method. A conclusion of all the obtained results in this work will be given at the end of this chapter.

10.1 Cross Sections

In the following section, the results of the unpolarised cross section of the liquid hydrogen data and the unpolarised total cross section of the hydrogen contribution of the butanol data will be presented. Both total cross sections were extracted from the missing mass spectra after the removal of the background channel events by the applied cuts. For the total cross section of the hydrogen contribution of the butanol data, the carbon contribution was additionally subtracted from the absolute normalized missing mass spectra. The unpolarised total cross sections were extracted

from the exclusive double π^0 reaction as a function of the incident beam energy E_γ.

10.1.1 Liquid Hydrogen Cross Section

In this section, the unpolarised total cross section of the liquid hydrogen data for the double π^0 photoproduction of the free proton as a function of the incident beam energy $E_\gamma = 450 - 1450$ MeV is presented. The liquid hydrogen data were analysed for the exclusive case where the detection of the recoil proton is in coincidence with the double π^0 mesons. The result of the unpolarised total cross section of the liquid hydrogen for the $\gamma p \to \pi^0\pi^0 p$ reaction of the free proton is shown in Fig. 10.1 by the blue crosses.

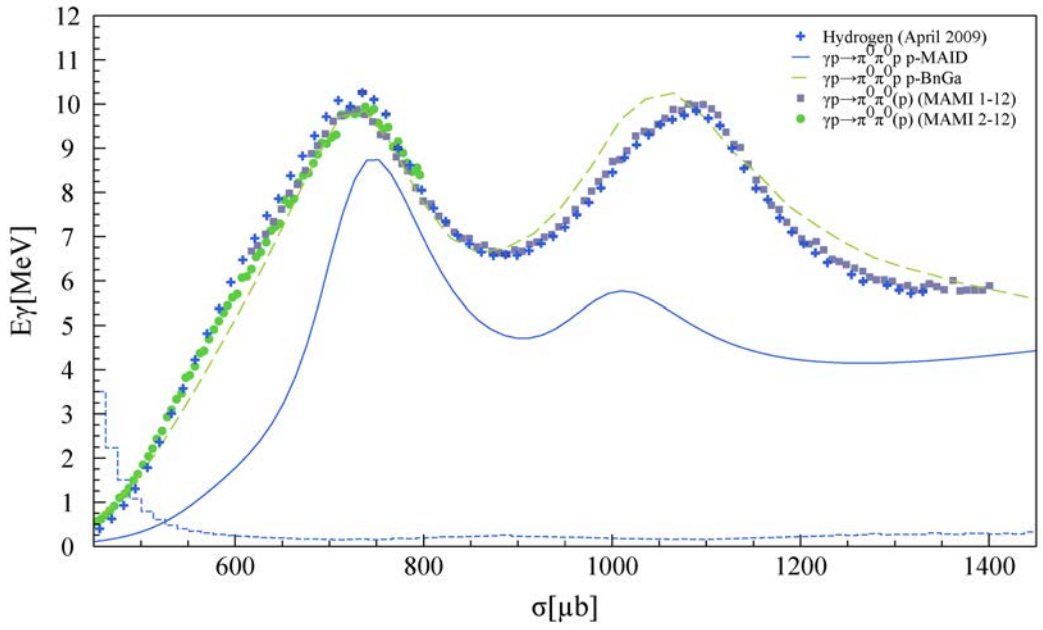

Figure 10.1.: Total cross section for the $\gamma p \to \pi^0\pi^0 p$ of the free proton target as a function of the incident beam energy E_γ. The presented results of the unpolarised total cross section for the double π^0 mesons detected in coincidence with the recoil proton are shown by the blue cross. The previous inclusive results of the double π^0 photoproduction are shown by the full purple squares MAMI1-12 [52] and the full green points MAMI2-12 [55]. The systematic error is indicated by the line at the bottom of the histogram. The solid blue line and the dashed green line are the results of the theoretical MAID model [41] and the BnGa model [111], respectively.

The unpolarised total cross section of the liquid hydrogen was measured to check the analysis and the absolute normalisation of this data since it was used for the calculation of several correction factors and also for the butanol data as the determination

of the nucleon detection efficiency (see Section 8.6.2) and for the correction of the gap between the Crystal Ball and TAPS detectors (see Section8.6.4). Additionally, the unpolarised cross section was used for the calculation of the polarisation observables F and T by the hydrogen normalisation method.
The results of the unpolarised total cross section of the hydrogen have good agreement to previously measured results from MAMI1-12 [52] and MAMI2-12 [55], denoted by the full green points and the full purple squares, respectively. These results correspond to inclusive measurement results of the double π^0 photoproduction of a liquid hydrogen data without the requirement of the coincidence of the detected recoil proton. The agreement between the previous inclusive measurements and the exclusive measurement of this work show that the detection and identification of the charged particle is correct. Hence, the problem with the poorly working charged particle detectors, the PID and the TAPS detector, could be corrected by the charged particle detection efficiency correction applied to the simulation (see Section 8.6.3). The systematic uncertainties are indicated by the line at the bottom of the histogram. The comparison of the total cross section result with the theoretical models shows that the resonance contribution and the helicity couplings are not well understood for this reaction. The predictions of the MAID isobar model [41] (solid blue line) do not agree with the measured data. The prediction of the BnGa coupled channel partial wave analysis [111] has a better agreement to the measured data since the model is based on fits to previously measured ELSA data.

10.1.2 Cross Section of the Hydrogen Contribution of the Butanol

The unpolarised total cross section for the $\gamma p \to \pi^0\pi^0 p$ reaction was also measured for the hydrogen contribution of the butanol data. For the comparison of both unpolarised total cross sections to each other, the total cross section of the hydrogen contribution of the butanol data was also measured by an exclusive analysis where the detection of the recoil proton in coincidence with the double π^0 mesons was required.
The result of the unpolarised total cross section of the hydrogen contribution of the butanol as a function of the incident photon beam energy from 450 up to 1450 MeV is shown in Fig. 10.2. The blue cross and the red triangles correspond to the exclusive analysis of the butanol data where the recoil proton was detected by the PID and veto detectors (June 2010) and the MWPCs and veto detectors (April 2011), respectively. For the determination of the hydrogen contribution of the butanol, the carbon data was subtracted in the absolutely normalised missing mass spectra, as explained in Section 9.4. For the determination of the hydrogen contribution by the carbon subtraction, the carbon data was analysed in the same way as the butanol data for the recoil proton detection, once with the PID and veto detectors and once

with the MWPCs and veto detectors. Therefore, the statistical error bars indicate the statistical errors of the butanol data and simultaneously the statistical error which arises through the subtraction of the carbon data under the consideration of the statistical errors of the carbon data itself. The result of the unpolarised cross section of the hydrogen contribution of the butanol shows that both analysis methods of the detection and identification of the recoil proton with the PID and veto detectors and with the MWPCs and veto detectors and the corresponding absolute normalisation of this data is correct like the carbon data. It can also be concluded that the nuclei normalisation of the carbon and oxygen nuclei of the carbon data to the whole butanol target under the consideration of the cooling process is correctly determined. Additionally, the present results for both butanol data (red triangles and blue cross) show also a good agreement with the measured result of the unpolarised cross section of the liquid hydrogen obtained in this work (green points), as shown in Fig. 10.1 and agrees also with the previously measured data.

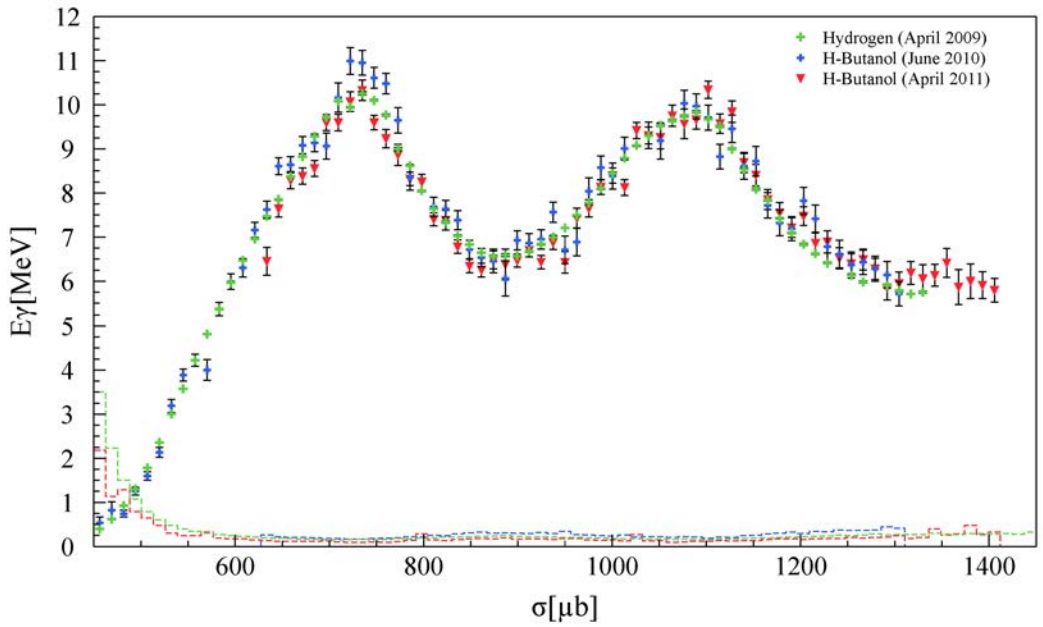

Figure 10.2.: Results of the total unpolarised cross section of the hydrogen contribution of the butanol are shown by the blue cross (June 2010) and red triangles (April 2011) for the butanol data, as a function of the incident beam energy E_γ. The total cross section of the liquid hydrogen data is shown by the green points (April 2009). The systematic errors are indicated by the same coloured lines as the corresponding measurement in the baseline of the histogram.

10.2 Polarisation Observables

In this section, the results of the polarisation observables F and T for the double π^0 photoproduction of free proton are presented. The polarisation observables were extracted with the carbon subtraction method and the hydrogen normalisation method, as explained in Sections 9.5.1 and 9.5.2. The formalism to determine the polarised differential cross section of the butanol and the unpolarised differential cross section of the liquid hydrogen and carbon data, leading to the polarisation observables was explained in detail in Section 9.1. Both polarisation observables were measured for four different representations: for the cosθ angle of each pion and also for the recoil proton and for the invariant mass of the two pions and also of each pion and the recoil proton as a function of the incident beam energy E_γ. For the extraction of the asymmetries of the polarisation observables for the different angle and invariant mass distribution, the azimuthal ϕ angle definitions, as explained in Section 9.4, were used. For the interpretation of the results, the total systematic uncertainties caused by the measurement or the reaction dependent once are shown by lines in the histogram, coloured corresponding to the measurement method. The results of the measured polarisation observables F and T were then compared with the predictions to the models, the MAID isobar model [41] and the BnGa coupled channel partial wave analysis [111] [112], as discussed in detail in Section 1.4.1.

10.2.1 Polarisation Observable F

In this section, the results of the double polarisation observable F for the different representations as a function of the incident photon beam energy range from 450 up to 1450 MeV are shown. The measured results for this polarisation observable for the carbon subtraction method and the hydrogen normalisation method are shown in Figs. 10.3 and 10.4 by the red points and blue crosses, respectively. Both methods, the carbon subtraction method and the hydrogen normalisation method, of the merged butanol data from June 2010 and April 2011 have a good agreement. Since different analysis methods were used for the identification and detection of the charged particle, the recoil proton, the agreement between the measured results of both analyses were first checked before the results were merged. Due to the problem with the charged particle detector, the PID in the April 2011 butanol data, the MWPCs and the veto detectors were used for the identification and detection of the recoil proton instead of the PID and veto detectors, as in the June 2010 butanol data. Since both analysis methods with the PID and the veto detectors or with the MWPCs and the veto detectors have the same result for the measured double polarisation observable F, it can be concluded that the identification and the detection of the recoil proton is correct for both analysis methods. The agreement between the

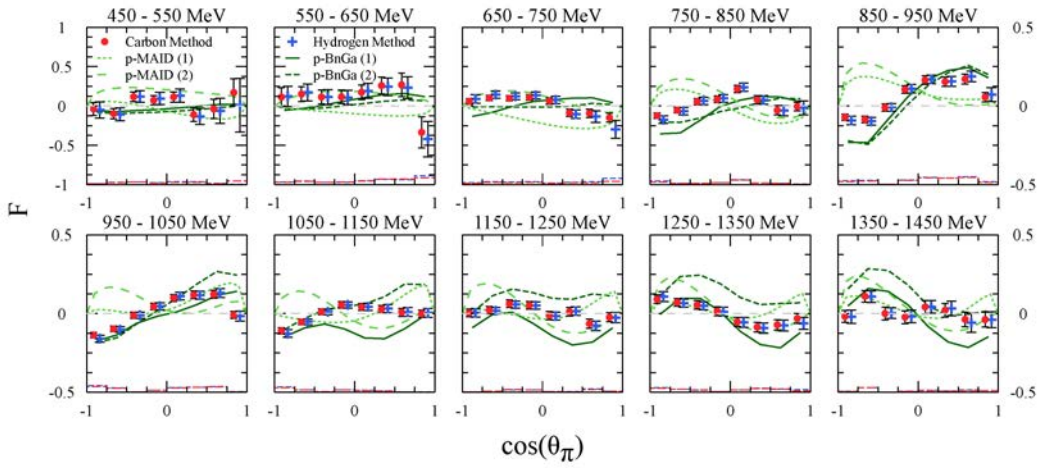

(a) Double polarisation observable F results for the cosθ_π representation of the two pions.

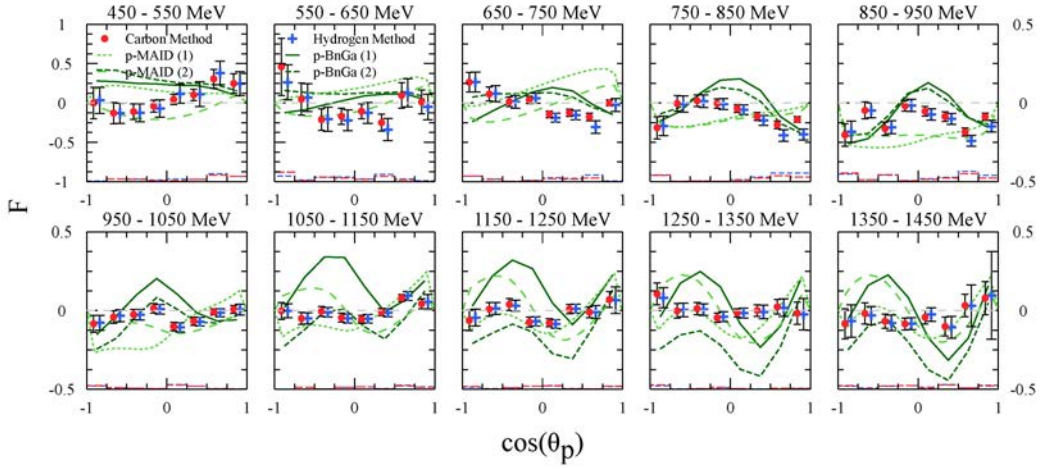

(b) Double polarisation observable F results for the cosθ representation of the recoil proton.

Figure 10.3.: Double polarisation observable F results for the cosθ representation of the two pions (a) and the recoil proton (b) as a function of the incident photon beam energy from 450 up to 1450 MeV. The results of the double polarisation observable F for the carbon subtraction method and the hydrogen normalisation method are shown by the red points and the blue cross (shifted by $\pm 2.5\%$), respectively. The systematic uncertainties are indicated by the same coloured line at the bottom of the histogram. The predictions of the isobar MAID model are shown by the pointed [41] and dashed light green [42] lines, whereby the dashed light green line containing additional smooth varying terms with $J < 3/2$ in the partial wave analysis. The theoretical predictions of BnGa with the main partial wave analysis fits are shown by the solid green line [111] and the partial wave analysis without the resonance $N(1900)3/2^+$ is shown by the dashed green lines [112].

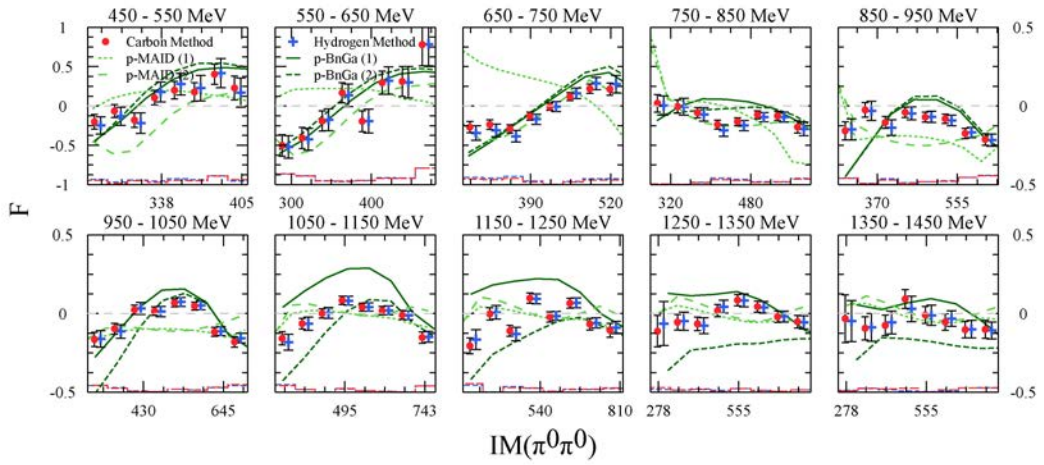

(a) Double polarisation observable F results for the invariant mass representation of the two π^0-mesons.

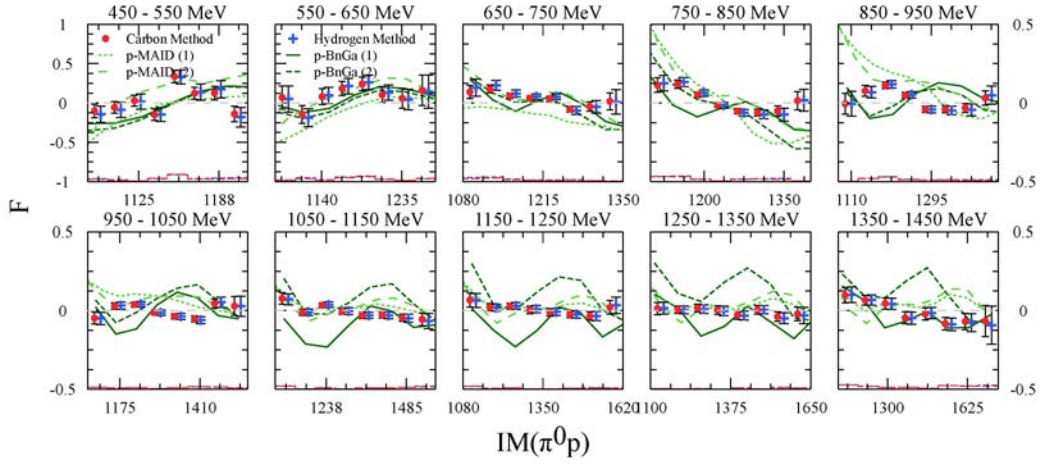

(b) Double polarisation observable F results for the invariant mass representation of each π^0-meson and the recoil proton.

Figure 10.4.: Double polarisation observable F results for the invariant mass of the two π^0-mesons (a) and each π^0-meson and the recoil proton (b) as a function of the incident beam energy from 450 up to 1450 MeV. The results of the double polarisation observable F for the carbon subtraction method and the hydrogen normalisation method are shown by the red points and blue cross (shifted by $\pm 2.5\%$), respectively. The systematic uncertainties are indicated by the same coloured line at the bottom of the histogram. The predictions of the isobar MAID model are shown by the pointed [41] and dashed light green [42] lines, whereby the dashed light green line containing additional smooth varying terms with $J < 3/2$ in the partial wave analysis. The theoretical predictions of BnGa with the main partial wave analysis fits are shown by the solid green line [111] and the partial wave analysis without the resonance $N(1900)3/2^+$ is shown by the dashed green lines [112].

individual measurement results for the butanol data for all representations of the double polarisation observables are shown in Appendix A.5. The systematic uncertainties of the measurements are denoted by the same coloured lines corresponding to the measurement methods in the different histograms. For the determination of the systematic uncertainties, the systematic error occurring through the measurement of the polarisation degree of the circularly polarised photon beam and the transversally polarised proton target spin (vertical up or down) have to be additionally considered in contrast to the unpolarised total cross section, as explained in Section 9.8.

Additionally, the measurement results were compared with another measurement, which uses only the cluster size of the Crystal Ball for the detection and the identification of the double π^0 mesons in coincidence with the recoil proton, as shown in Appendix A.5. The analysis results of V. L. Kashevarov [113] were determined by the carbon subtraction method and show a good agreement to the analysis results of this work. A satisfactory agreement between the measurement results of V. L. Kashevarov and the individual measurement results of the butanol data (June 2010 and April 2011) are also visible, as shown in Appendix A.5.

The predictions of the models are shown by the different green curves in Fig. 9.14. It can be seen that the agreement between the measured results and the predictions of the isobar MAID model [41] (pointed light green line) is rather poor in the region below the resonance $N(1520)$ with spin parity $J^P = 3/2^-$ [42]. However, the predictions of the isobar MAID model differ also from the measured results of the total cross sections in this energy range. Therefore, it is not surprising that the model predictions also deviate from the measured polarisation observables results. The dashed light green line denotes the predictions of the isobar MAID model [42] containing additional smoothly varying terms of $J < 3/2$ in the partial wave analysis. In the energy region up to 1 GeV and especially at the energies below the resonance $N(1520)$ with spin parity $J^P = 3/2^-$, the measured values are rather larger than the expected theoretical predictions of both MAID models. Altogether, it can be seen that the corrected isobar MAID model (dashed light green line) with a totally excluded or strongly suppressed resonance contribution of $N(1440)$ has a better agreement with the measured results, especially in the energy range of 1 up to 1.35 GeV. This shows that the resonance contribution of $N(1440)$ with spin parity $J^P = 1/2^+$ is overestimated in the uncorrected isobar MAID model shown by the dashed light green line. In general, the asymmetry is in the angular distributions generated by the interference of the positive spin parity states and the negative spin parity states. From the invariant mass distribution shown in Fig. 10.3 it can be concluded that in the energy region below $E_\gamma = 800$, MeV the main contribution of the double polarisation observable F occurs through the interference between the negative spin parity state $3/2^-$ and the positive spin parity states $1/2^+$ and $3/2^+$ [42]. The MAID models underestimate this positive and negative spin parity states in this energy ranges. However, it can be concluded that the contribution interference effects

for the double polarisation observable F are not fully understood. The theoretical predictions of the coupled BnGa partial wave analysis [112] (solid and dashed green line) show a better agreement with the measured results since the model is based on fits to previous measured ELSA data. The BnGa model [111] with the main partial wave analysis fits shown by the solid green line has a better agreement with the measured results than the BnGa model [112] with the partial wave analysis without the resonance contribution of $N(1900)$ with spin parity $J^P = 3/2^+$ shown by the dashed green line. This can especially be seen in the high energy ranges of 1.25 up to 1.45 GeV. Therefore, it can be concluded that the resonance contribution of $N(1990)3/2^+$ has an influence on the results of the double polarisation observable F for the double π^0 meson photoproduction in the energy ranges of $E_\gamma = 450 - 1450$ MeV and cannot be neglected in the underlying models.

10.2.2 Polarisation Observable T

For the extraction of the polarisation observable T, the differential cross section of the butanol data, as well as the differential cross section of the hydrogen and carbon data must be corrected for the detector efficiency so that the asymmetry of the detector setup is not included into the measurement results. In contrast to the double polarisation observable F where the detector efficiency correction can be neglected based on the definition of this observable, for the polarisation observable T it is necessary. The experimental data can only be corrected for the detector efficiency when the experimental setup is consistent with the simulation setup. For the June 2010 data, some angle dependent problems occurred through the charged particle detector PID, which could not be identified and could not be solved by simulating the same problem. Therefore, the data and the simulation has some angle dependent inconsistencies due to the poorly working PID and thus, the detector efficiency is over or underestimated in some angle ranges. This angle dependent inconsistency between the data and the simulation can especially be seen by the measured results of the polarisation observable T for only one proton target spin polarisation, vertically up or down, as shown in Appendix A.6. The resulting asymmetry contribution of the detector setup occurring through the wrong detector efficiency could obviously be seen for the June 2010 data by fitting the measured result of the polarisation observable T with a cosine function instead of a sine function, as shown in Appendix A.7. Due to these problems with the incorrect detector efficiency correction of the June 2010 data, the present polarisation observable T results were only shown from the April 2011 data.

For the April 2011 data analysed with the MWPC and the veto detectors for the charged particle detection, it could be seen that the detector efficiency is correct and no detector asymmetry is contributing to the result of the polarisation observable T, as shown in Appendix A.6 and A.7. The small deviations in the measured

results of the polarisation observables are attributed to angle dependent systematic uncertainties arising through the gas mixture in the MWPC. For the consideration of these systematic uncertainties, the average values of both results were used for the presented results of the polarisation observables in the following sections. The total systematic uncertainties are then defined by the difference of the obtained result with only one spin direction.

The results of the polarisation observable T for the carbon subtraction method and the hydrogen normalisation method as a function for the incident photon beam energy from 450 up to 1450 MeV are shown in Figs. 10.5 and 10.6, by the red points and blue cross, respectively. Both measured results of the carbon subtraction method and the hydrogen normalisation method are in good agreement. The measured results of the polarisation observable T were also compared with the measured results of V.L. Kashevarov [113]. The obtained results of V.L. Kashevarov were analysed over the cluster size of the Crystal Ball without the charged particle detectors for the detection and identification of the double π^0 mesons in coincidence with the recoil proton. The polarisation observable result T of this work, including only the neutral pions, show a good agreement with the obtained results of V.L. Kashevarov under the consideration of the systematic uncertainties, as shown in Appendix A.5. But the comparison between the measured results of this work and the results of V.L. Kashevarov including the recoil proton, have some visible deviations, especially in the backward angle direction and in the low energy ranges of 0.65 up to 1 GeV, as shown in Appendix A.5. As mentioned before, the total systematic uncertainties arise mainly from the angle dependent uncertainty of the detection efficiency of the gas mixture of the MWPC are given by the difference of the measured polarisation observable T for only one nucleon spin polarisation, vertically up or down. The systematic uncertainties are shown by the same coloured lines as the measurement results of both methods, the carbon subtraction method or the hydrogen normalisation method, in the histograms.

The predictions of the models are shown by the different green curves in Fig. 9.15. It can be seen that the agreement between the measured results and the predictions of the isobar MAID models pointed light green [41] and dashed light green [42] line are rather poor in the region below the resonance contribution of $N(1520)$ with spin parity $J^P = 3/2^-$. As mentioned before, the isobar MAID model [41] deviates from the total cross section and therefore, it is not surprising that the isobar model also deviates from the measured polarisation observable T result. The dashed light green line indicates the predictions of the isobar MAID model [42] containing additional smoothly varying terms of $J < 3/2$ in the partial wave analysis. This corrected isobar MAID model [42] with the totally excluded or strongly suppressed resonance contribution $N(1440)$ has a better agreement with the measured results than the general isobar MAID model [41]. It can be seen again that in the energy region up

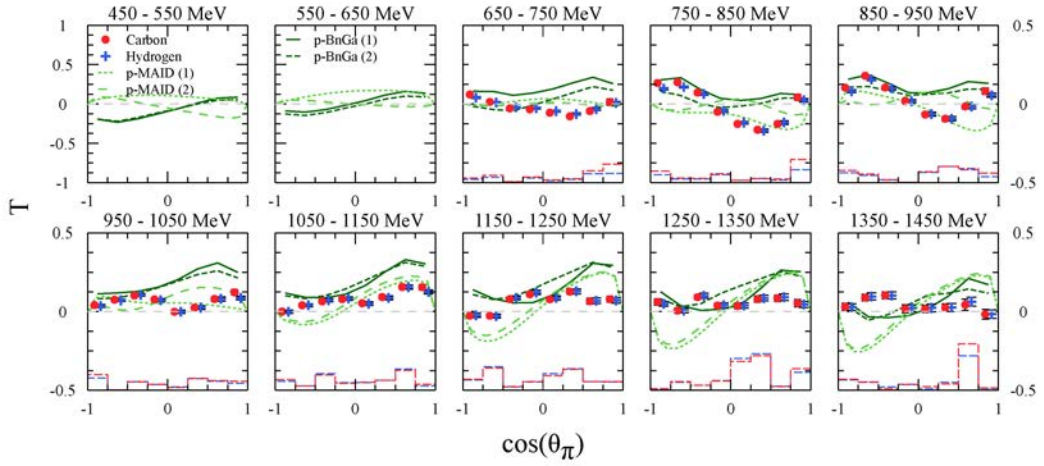

(a) Polarisation observable T results for the cosθ_π representation of the two pions.

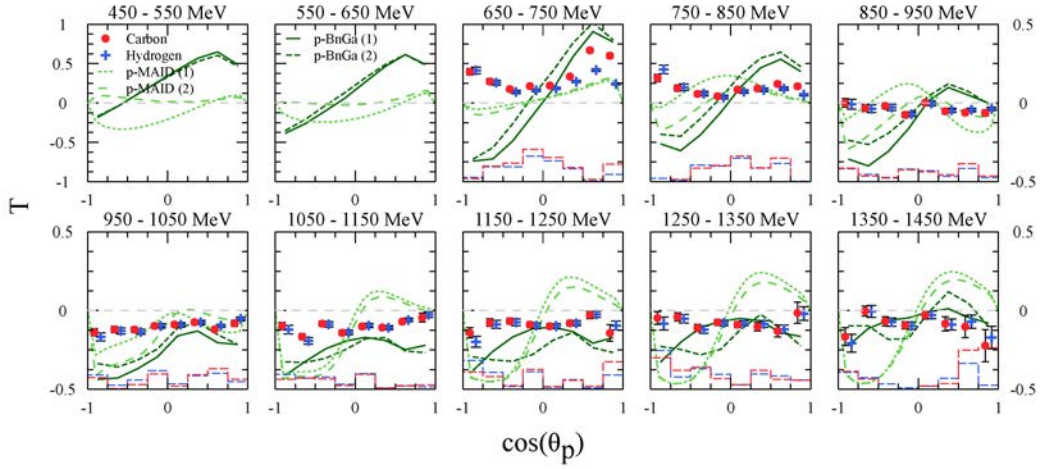

(b) Polarisation observable T results for the cosθ_p representation of the recoil proton.

Figure 10.5.: Polarisation observable T results for the cosθ representation of the two pions (a) and the recoil proton (b) as a function of the incident photon beam energy from 450 up to 1450 MeV. The results of the polarisation observable T for the carbon subtraction method and the hydrogen normalisation method are shown by the red points and the blue cross (shifted by $\pm 2.5\%$), respectively. The systematic uncertainties are indicated by the same coloured line at the bottom of the histogram. The predictions of the isobar MAID model are shown by the pointed [41] and dashed light green [42] lines, whereby the dashed light green line containing additional smooth varying terms with $J < 3/2$ in the partial wave analysis. The theoretical predictions of BnGa with the main partial wave analysis fits are shown by the solid green line [111] and the partial wave analysis without the resonance $N(1900)3/2^+$ is shown by the dashed green lines [112].

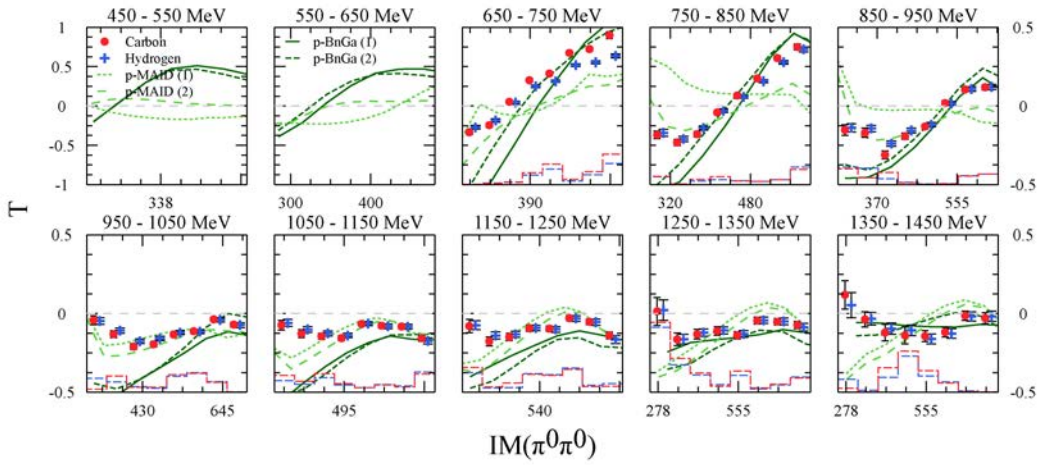

(a) Polarisation observable T results for the invariant mass representation of the two π^0-mesons.

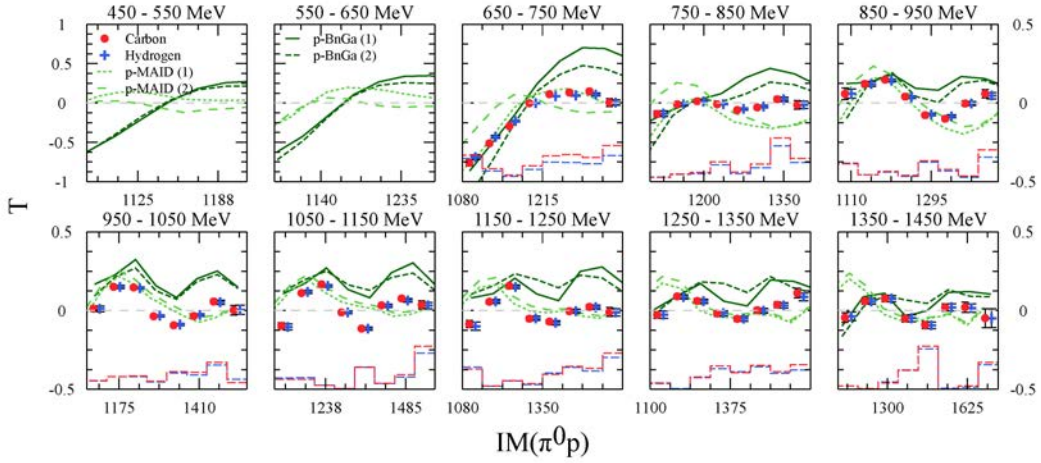

(b) Polarisation observable T results for the invariant mass representation of each π^0-meson and the recoil proton.

Figure 10.6.: Polarisation observable T results for the invariant mass of the two π^0-mesons (a) and each π^0-meson and the recoil proton (b) as a function of the incident beam energy from 450 up to 1450 MeV. The results of the polarisation observable T for the carbon subtraction method and the hydrogen normalisation method are shown by the red points and blue cross (shifted by 2.5%), respectively. The systematic uncertainties are indicated by the same coloured line at the bottom of the histogram. The predictions of the isobar MAID model are shown by the pointed [41] and dashed light green [42] lines, whereby the dashed light green line containing additional smooth varying terms with $J < 3/2$ in the partial wave analysis. The theoretical predictions of BnGa with the main partial wave analysis fits are shown by the solid green line [111] and the partial wave analysis without the resonance $N(1900)3/2^+$ is shown by the dashed green lines [112].

to 1 GeV, and especially at the energies below the resonances $N(1520)3/2^-$, the measured values are larger than the predictions of both MAID models. From the large deviations of the MAID models and the measured results, it can be concluded that the invariant mass distributions, shown in Fig. 10.6 below the energy range $E_\gamma = 800$ MeV appear through interferences between the negative spin parity state $3/2^-$ and the positive spin parity states of $1/2^+$ and $3/2^+$, which were underestimated in both models. However, the positive and negative spin parity states, which lead to interferences and thus contribute to the polarisation observable T are not yet completely determined for the $\gamma p \to \pi^0\pi^0 p$ reaction. Therefore, the models have some deviations with the measured results. The predictions of the BnGa partial wave analysis [111] are shown by the solid green and the dashed green lines, whereby for the dashed green line, the partial wave analysis without the resonance contribution of $N(1900)3/2^-$ is shown. The predictions of the BnGa coupled channel partial wave analysis models show a better agreement to the measured data for the polarisation observable in the $cos\theta$ representation of the pions since the model is based on fits to previous measured data. In contrast to the predictions of the BnGa partial wave analysis of the double polarisation observable F, no large derivation between the two BnGa models are visible. Therefore, it can be concluded that the contribution of the resonance $N(1900)3/2^-$ for the polarisation observable T has less influence.

10.3 Conclusions

In the present work, the experimental results of the total cross sections and of the polarisation observable F and T for the double π^0 reaction of the free proton obtained with a circularly polarised photon beam and transversally polarised target protons were presented. The measurements were performed at the MAMI tagged photon facility in Mainz, Germany using the Crystal Ball and the TAPS spectrometer and additionally the MWPCs for the charged particle tracking. The experimental results were measured for further studies of the partial wave content of the double pion photoproduction in the second and third resonance regions.

The experimental result of the unpolarised total cross section of the liquid hydrogen data compared to the model results show that the different resonance contributions of the double pion photoproduction are not fully understood, especially for the isobar model [41]. However, for the isobar MAID model, it could be shown by previous works [52] and [53] that the unpolarised cross section is dominated by three partial wave amplitudes $1/2^+$, $3/2^+$ and $3/2^-$ in the energy region of the second resonance and below [42]. The coupled channel partial wave analysis BnGa [111] has a better agreement to the measured data since the model is based on fits to previous measured ELSA data. The experimental results of the unpolarised cross section of the liquid hydrogen for the exclusive measurement of the double π^0

mesons in coincidence with the recoil proton compared to previous measurement [55] [52] show good agreement. Furthermore, it can be concluded that the recoil proton was correctly detected and identified since the previous experimental results were inclusively analysed without the recoil proton in coincidence with the double π^0 mesons. The agreement of the unpolarised total cross section of the liquid hydrogen data with the unpolarised total cross section of the hydrogen contribution of the butanol show that the absolute normalisation of the butanol data for both analysis methods for the identification and detection of the recoil proton (with the PID and veto detectors and with the MWPCs and veto detectors) is correct. Additionally, it can be concluded that the hydrogen contribution and the carbon contribution of the butanol were correctly determined, which is essential for the calculation of the polarisation observables F and T by the carbon subtraction method and the hydrogen normalisation method.

The experimental results of the double polarisation observable F for the carbon subtraction method and the hydrogen normalisation method show a good agreement as well as the individual measurement of the butanol data from June 2010 and April 2011 with the different identification and detection methods. The extracted double polarisation observables F were additionally compared to the measurement results from V. L. Kashevarov [113], which used the cluster size of the Crystal Ball for the identification and detection of the double π^0 mesons in coincidence with the recoil proton based on the same butanol data. An agreement between the measured results of this work and the result of V. L. Kashevarov [113] by the carbon subtraction method could be shown.

For the polarisation observable T, only the butanol data from April 2011 was used for the presented results. In contrast to the double polarisation observable F, the calculation of the polarisation observable T from the differential cross sections must be corrected for the detector efficiency to prevent contributions of the detector setup asymmetry in the results. For the June 2010 data, some angle dependent problems occurred through the charged particle detector (PID), which could not be well identified and therefore, not solved by simulating the identical experimental setup for the PID to obtain a correct detector efficiency. Also the problem with the PID could not be solved by a charged particle detection efficiency correction, which was used to solve the problem in the liquid hydrogen data, as shown in this work, since the butanol data contains carbon background, which contributes differently for the exclusive and inclusive analysis and therefore, led to an over or underestimated correction. However, calculating the charged particle detection efficiency correction for the exclusive and inclusive analysis by subtracting the carbon contribution led to the problem that the carbon statistics were not sufficient and therefore, the correction needed a lower sample rate, which was not good enough and led to over or underestimated corrections.

For the calculation of the polarisation observable T, the average of the polarisation observable T results with only one proton target spin polarisation, vertically spin

up or spin down, was used for the consideration of the angle dependent systematic uncertainties arising through the gas mixture of the MWPC. The present measured results of the polarisation observable T for the carbon subtraction method and the hydrogen normalisation method show a satisfactory agreement. The comparison of the obtained measured results with the measured results from V. L. Kashevarov show a good agreement under the consideration of the systematic uncertainties. Notice that for the polarisation observable T results, the recoil proton deviations in the backwards angle of the cosθ angles are visible.
Since the isobar models [41] do not reproduce the unpolarised total cross section of the $\gamma p \rightarrow \pi^0\pi^0 p$ reaction, the agreement between the measured polarisation observables and the predictions of the theoretical models are also rather poor, especially for the isobar model for the energies in the region below the resonance contribution of $N(1520)3/2^-$. For the corrected isobar model [42] with the total excluded or at least strongly suppressed resonance contribution of $N(1440)$, a better agreement with the measured results could be shown as with the uncorrected isobar model. However, for the MAID isobar model, it can be concluded that the comparison of the predictions of the model and the measured results are in a qualitative agreement, for which the photoproduction amplitude contains the resonance in the $3/2^-$ wave and the $1/2^+$ and $3/2^+$ resonances depend smoothly on the incident photon beam energy and generate mostly background contributions [42]. The predictions of the coupled channel BnGa partial wave analysis has a better agreement to the measured data since the model is based on fits to the previous measured ELSA data. In general, the BnGa partial wave analysis with the main fits [111] show a better agreement to the measured results as the BnGa partial wave analysis fits without the resonance contribution of $N(1900)3/2^-$ [112], especially for the double polarisation observable F, where the difference between these models are visible. Therefore, it can be concluded that this resonance contribution of $N(1900)3/2^-$ has a non-negligible influence on the polarisation observables F and T.

Appendix

A

A.1 Polarisation Observables

The polarised cross section for the single meson photoproduction including higher order terms is defined by [114]:

$$
\begin{aligned}
d\sigma^{B,T,R}\left(\vec{P}^{\gamma},\vec{P}^{T},\vec{P}^{R}\right) = \frac{1}{2}\{ & d\sigma_0[1 - P_L^{\gamma}P_y^T P_{y'}^R \cos(2\phi_\gamma)] \\
& + \hat{\Sigma}[-P_L^{\gamma} cos(2\phi) + P_\gamma^T P_{y'}^R] \\
& + \hat{T}[P_\gamma^T - P_L^{\gamma} P_{y'}^R cos(2\phi_\gamma)] \\
& + \hat{P}[P_{y'}^R - P_L^{\gamma} P_y^T cos(2\phi_\gamma)] \\
& + \hat{E}[-P_c^{\gamma} P_z^T + P_L^{\gamma} P_x^T P_{y'}^R sin(2\phi_\gamma)] \\
& + \hat{G}[P_L^{\gamma} P_z^T sin(2\phi) + P_c^{\gamma} P_x^T P_{y'}^R] \\
& + \hat{F}[P_c^{\gamma} P_x^T + P_L^{\gamma} P_z^T P_{y'}^R sin(\phi_\gamma)] \\
& + \hat{H}[P_L^{\gamma} P_x^T sin(2\phi) - P_c^{\gamma} P_z^T P_{y'}^R] \\
& + \hat{C}_{x'}[P_c^{\gamma} P_{x'}^R - P_L^{\gamma} P_y^T P_{z'}^R sin(2\phi_\gamma)] \\
& + \hat{C}_{z'}[P_c^{\gamma} P_{z'}^R + P_L^{\gamma} P_y^T P_{x'}^R sin(2\phi_\gamma)] \\
& + \hat{O}_{x'}[P_L^{\gamma} P_{x'}^R sin(2\phi) + P_c^{\gamma} P_y^T P_{z'}^R] \\
& + \hat{0}_{z'}[P_L^{\gamma} P_{z'}^R sin(2\phi) - P_c^{\gamma} P_y^T P_{x'}^R] \\
& + \hat{L}_{x'}[P_z^T P_{x'}^R + P_L^{\gamma} P_x^T P_{z'}^R cos(2\phi_\gamma)] \\
& + \hat{L}_{z'}[P_z^T P_{z'}^R - P_L^{\gamma} P_x^T P_{x'}^R cos(2\phi_\gamma)] \\
& + \hat{T}_{x'}[P_x^T P_{x'}^R - P_L^{\gamma} P_z^T P_{z'}^R cos(2\phi_\gamma)] \\
& + \hat{T}_{z'}[P_x^T P_{z'}^R + P_L^{\gamma} P_z^T P_{x'}^R cos(2\phi_\gamma)]\}
\end{aligned}
$$

A.2 Fits of the Polarisation Observable F

In this section, the extracted asymmetries A_F of the double polarisation observable F for the butanol data (June 2010 and April 2011) with the corresponding fit functions are shown. The double polarisation observable asymmetries A_F are shown for all the measured representations of the cosθ angle of the two pions or the recoil proton, as well as for the invariant mass for each pion or a pion and the recoil proton as a function of the incident photon beam energy from 450 MeV up to 1450 MeV. Since the measured results for the carbon subtraction method and the hydrogen normalisation method are in a good agreement, as shown in Section 10.2.1, only the measured results of the carbon subtraction method are shown.

A.2.1 Results of the Pions

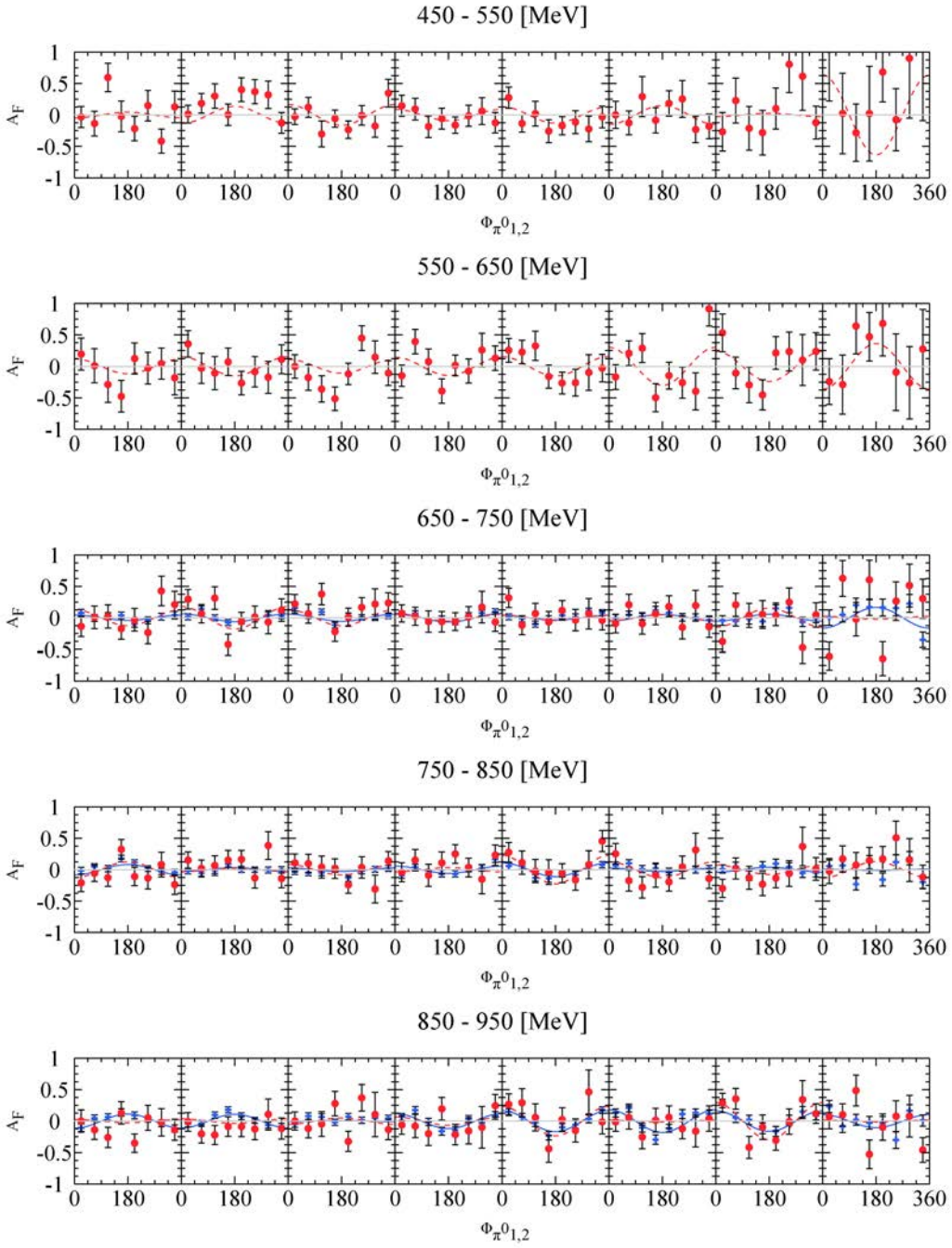

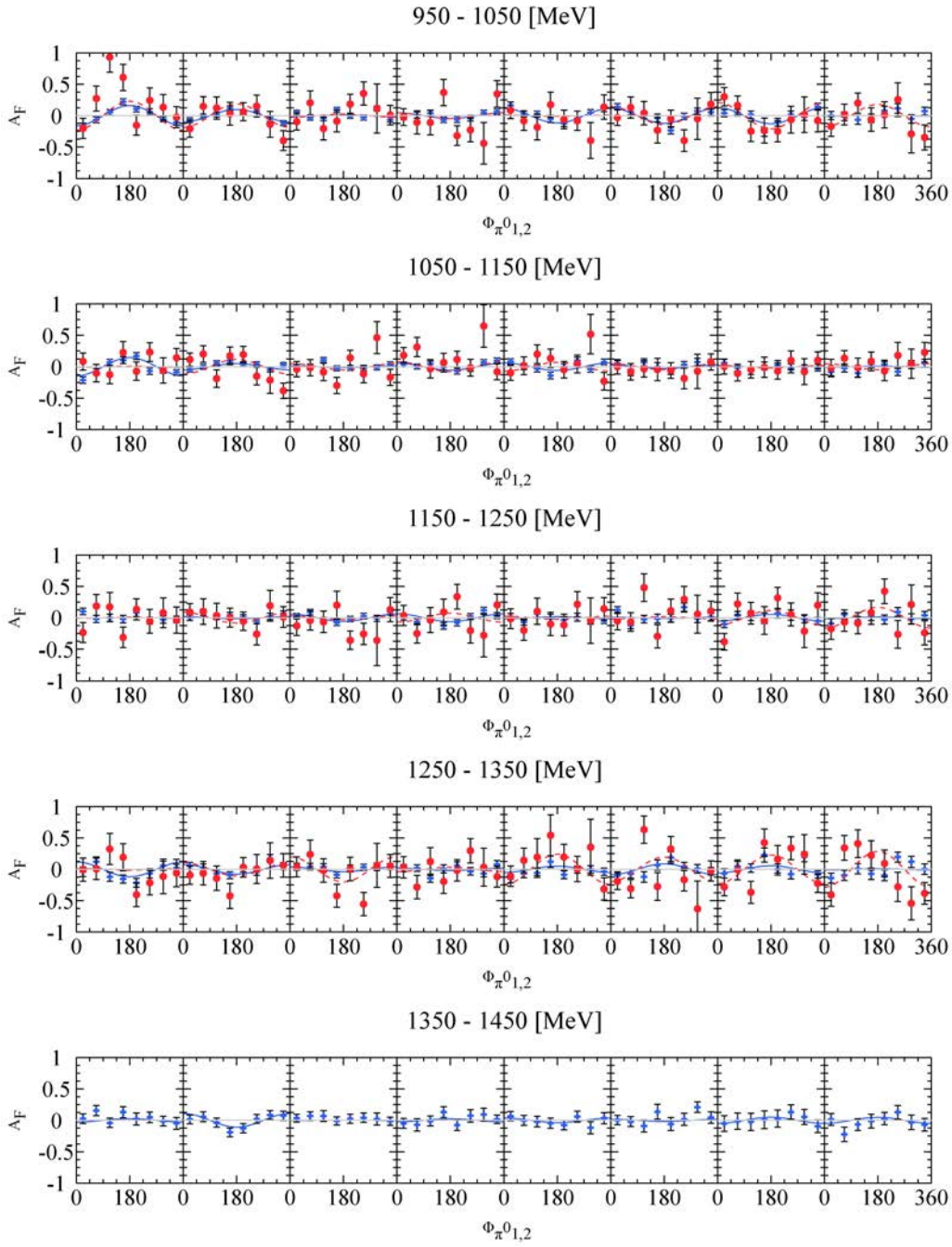

Figure A.1.: Asymmetry of the double polarisation observable F for the different $\phi_{\pi^0_{1,2}}$ angles between each π^0 meson and the direction of the target proton spin as a function of the incident beam energy from 450 up to 1450 MeV. The results of the asymmetry F for the hydrogen normalisation method are shown by the red points and the blue cross for the butanol data June 2010 and April 2011, respectively. The corresponding cosine fit for the extraction of the polarisation observable F are shown by the same colored lines.

A.2.2 Results of the Proton

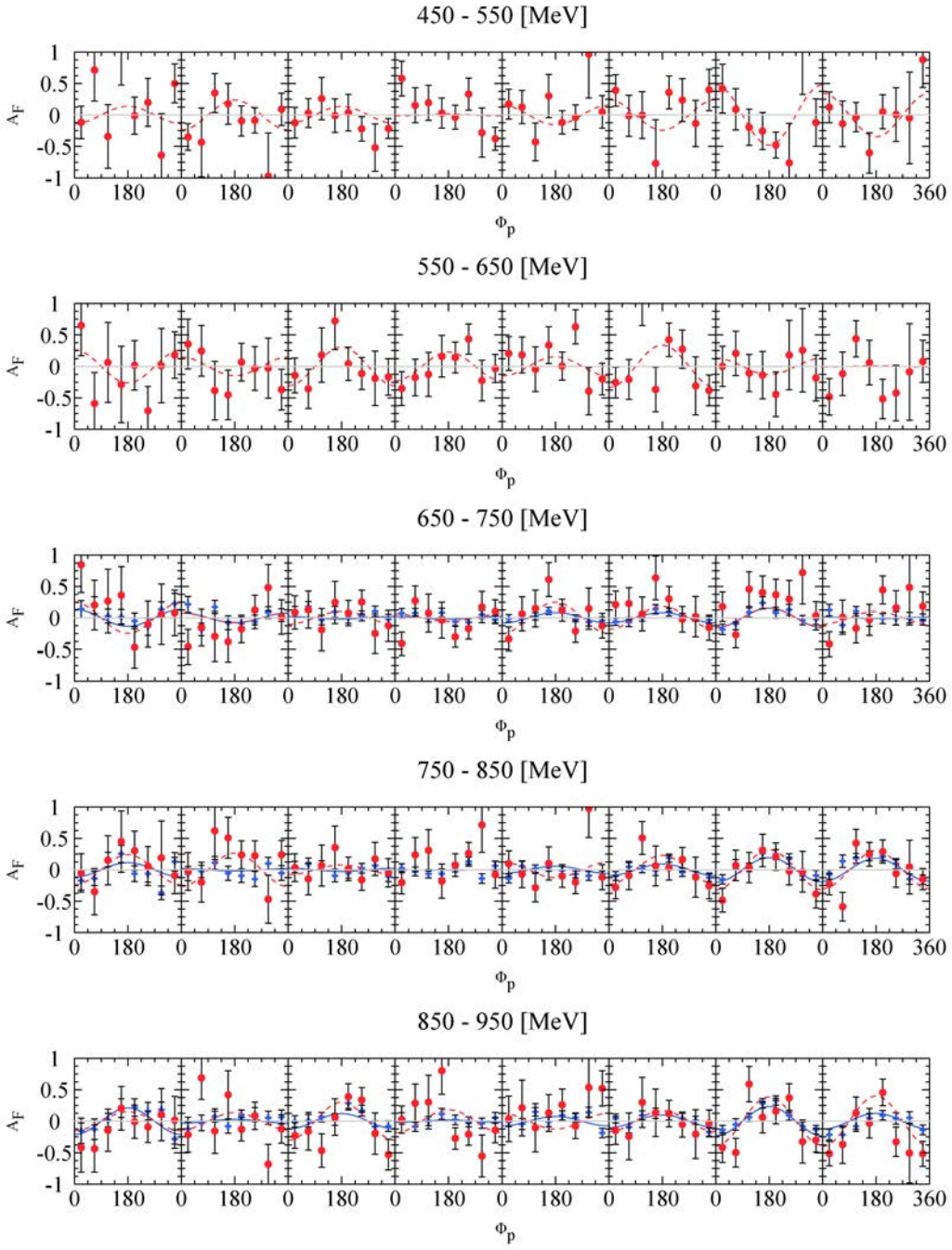

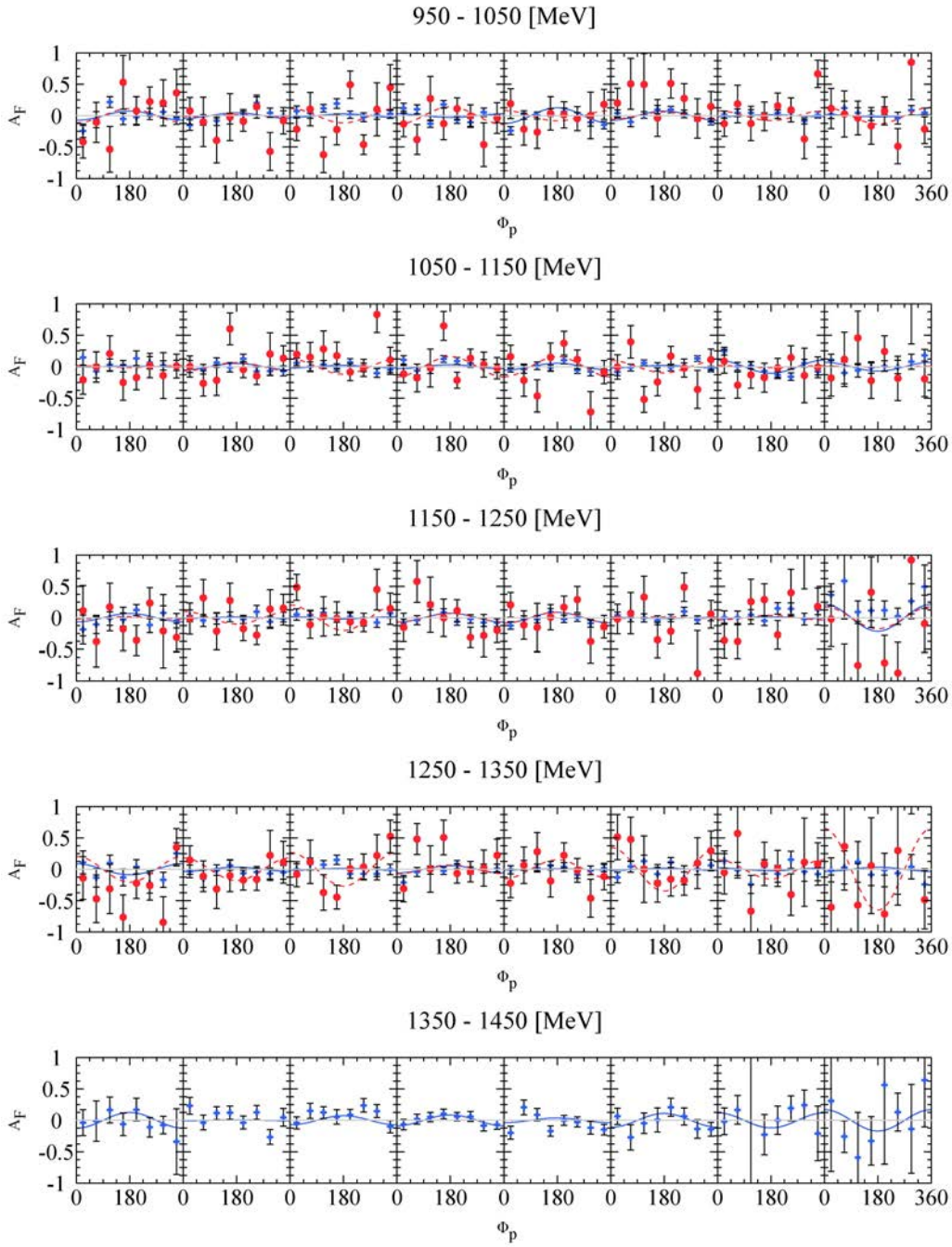

Figure A.2.: Asymmetry of the double polarisation observable F for the different ϕ_p angles between the recoil proton and the direction of the target proton spin as a function of the incident beam energy from 450 up to 1450 MeV. The results of the asymmetry F for the hydrogen normalisation method are shown by the red points and the blue cross for the butanol data June 2010 and April 2011, respectively. The same colored lines represent the corresponding cosine fit for the extraction of the polarisation observable F.

A.2.3 Results for the Invariant Mass of the Pions

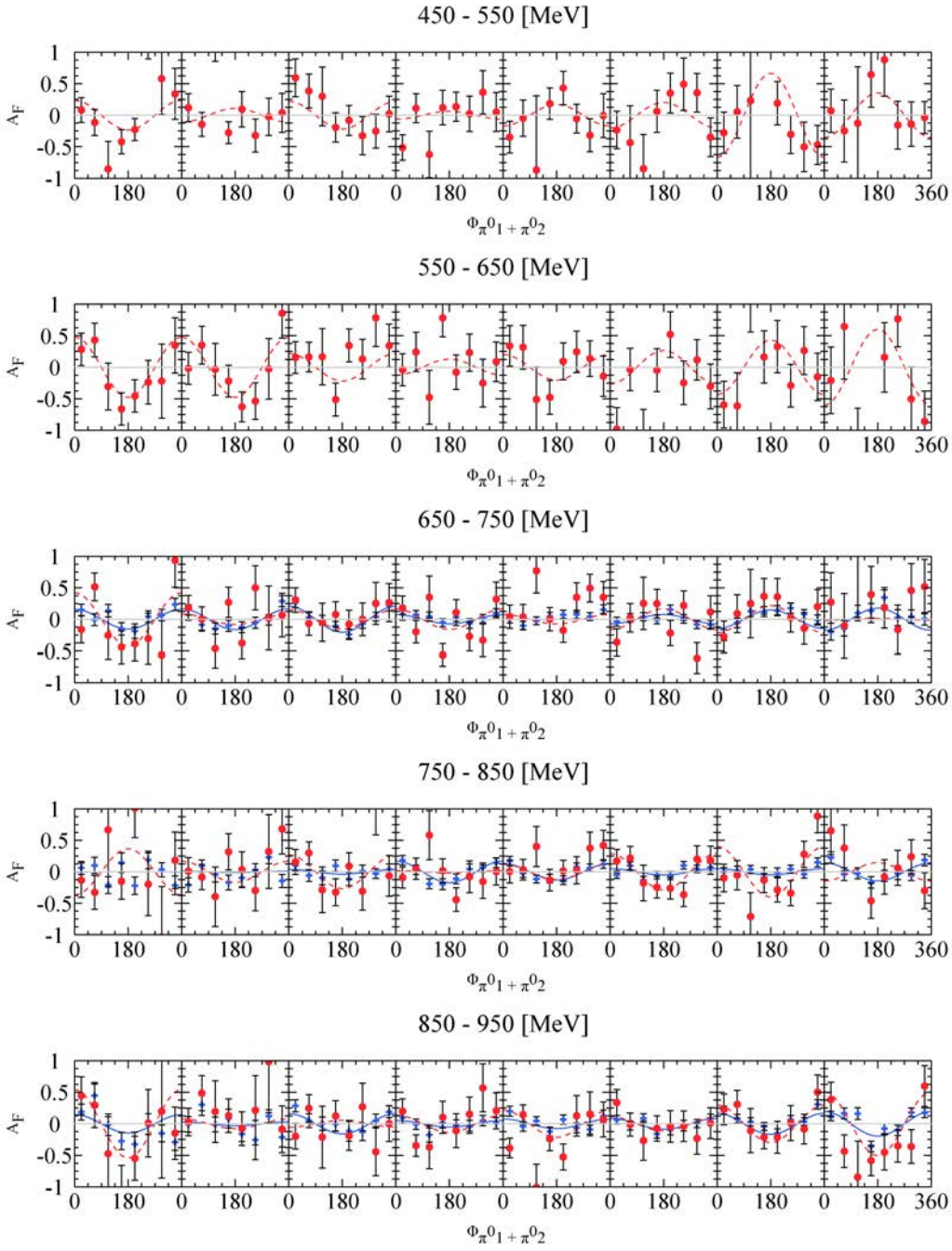

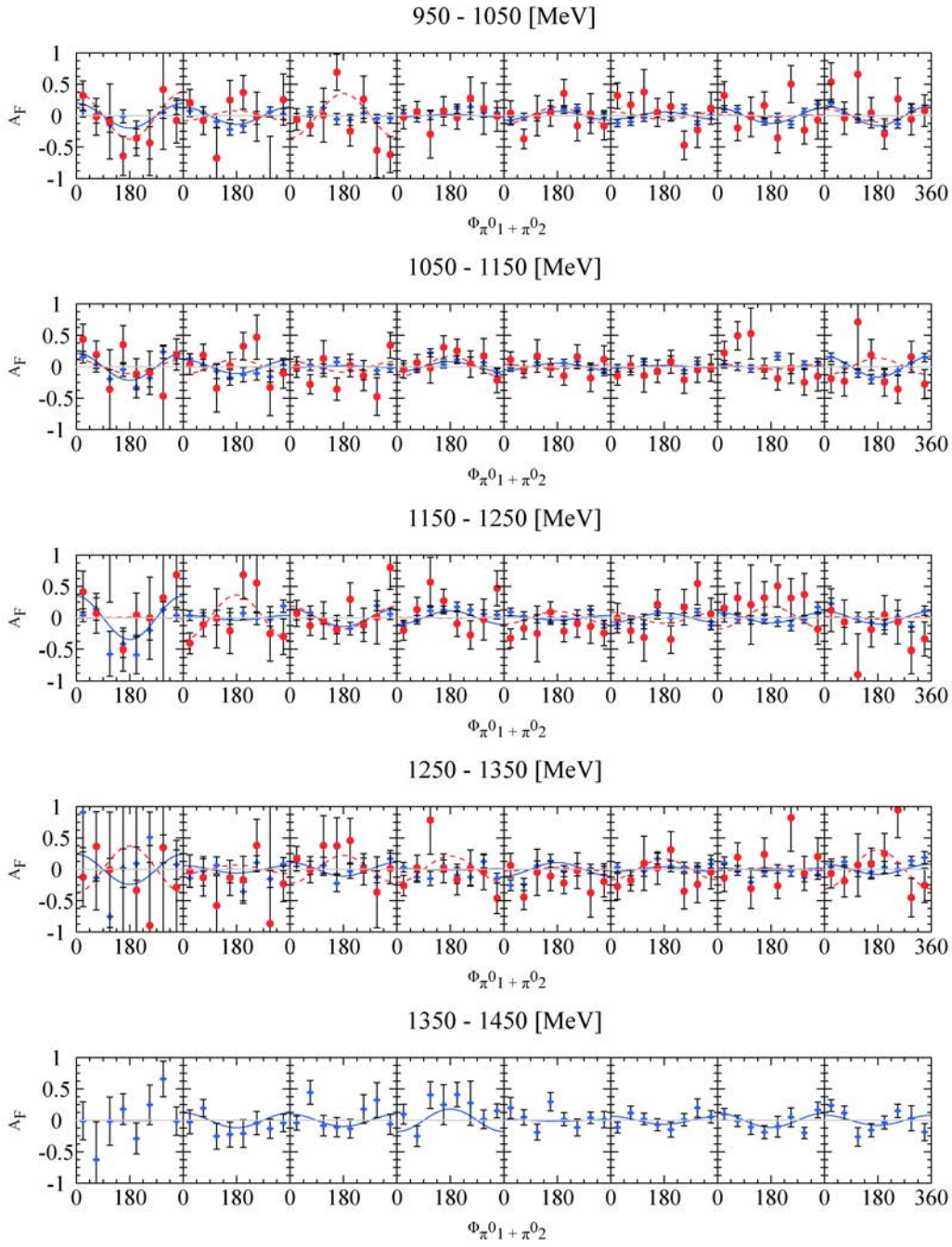

Figure A.3.: Incident photon beam energy $E_\gamma = 450 - 1450$ MeV dependent asymmetry of the double polarisation observable F for the different $\phi_{\pi^0_1+\pi^0_2}$ angles between the meson vector and the direction of the target proton spin. The results of the asymmetry F for the hydrogen normalisation method as shown by the red points and the blue cross for the butanol data June 2010 and April 2011, respectively. The corresponding cosine fit for the extraction of the polarisation observable F are shown by the same colored lines.

A.2.4 Results for the Invariant Mass of the Pions and the Proton

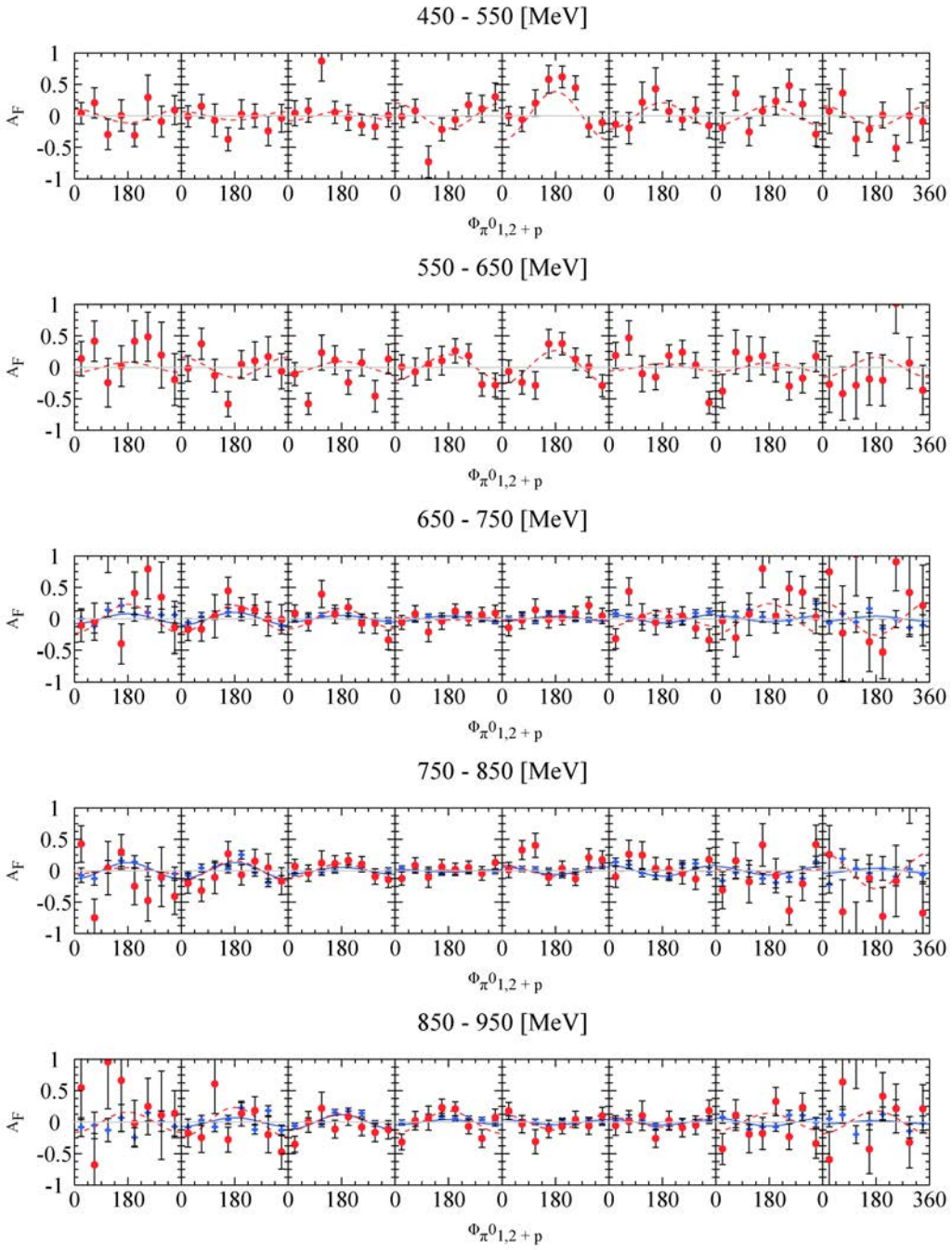

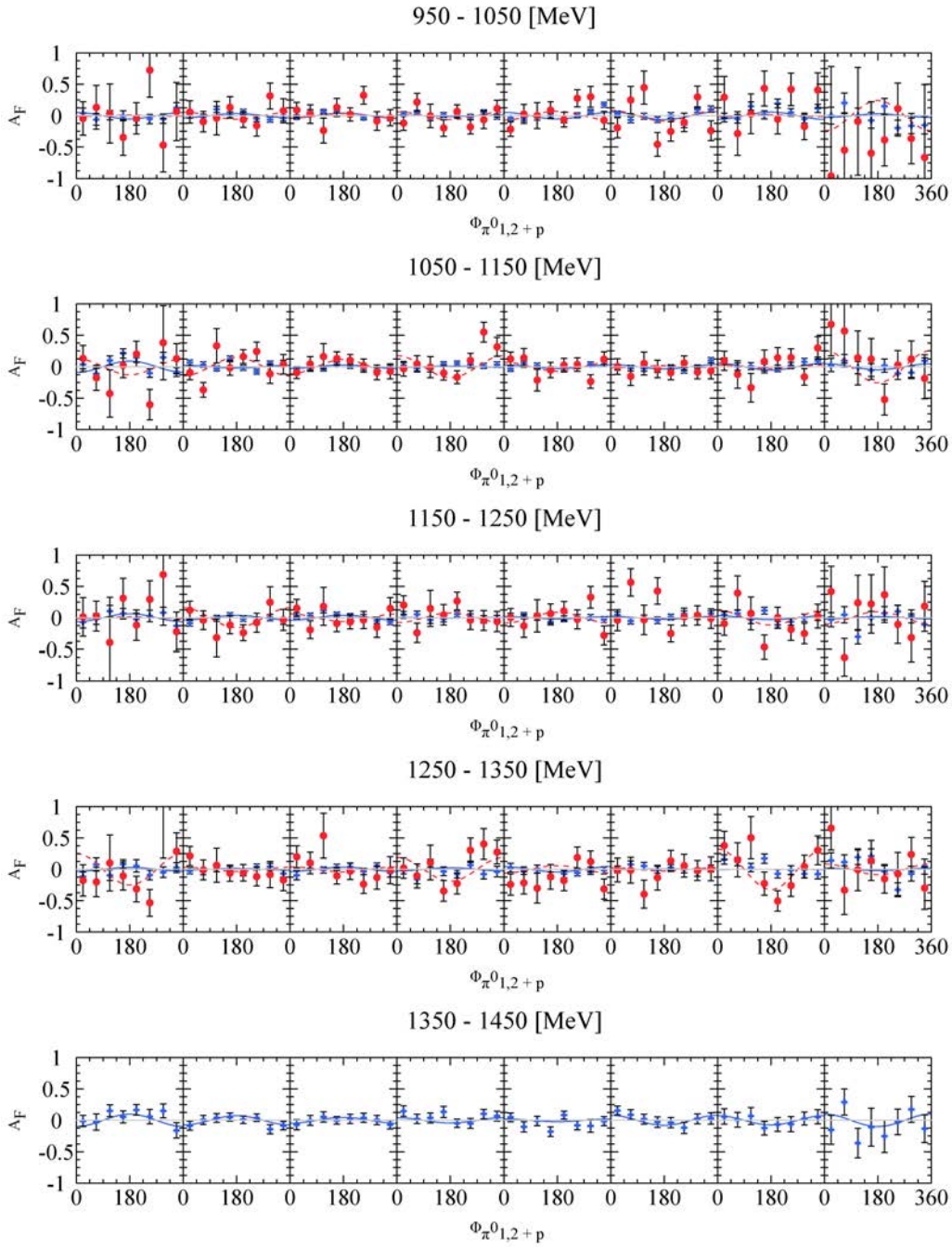

Figure A.4.: Incident photon beam energy $E_\gamma = 450 - 1450$ MeV dependent asymmetry of the double polarisation observable F for the different $\phi_{\pi^0_{1,2}+p}$ angles between each π^0 meson and the recoil proton vector and the direction of the target proton spin. The result of the asymmetry F for the hydrogen normalisation method as shown by the red points and the blue cross for the butanol data June 2010 and April 2011, respectively. The same colored lines represent the corresponding cosine fit for the extraction of the polarisation observable F.

A.3 Fits of the Polarisation Observable T

In this section, the extracted asymmetries A_T of the polarisation observable T for the butanol data (June 2010 and April 2011) with the corresponding fit functions are shown. The polarisation observable asymmetries A_T are shown for all the measured representations of the cosθ angles of the two pions or the recoil proton, as well as for the invariant mass for each pion or a pion and the recoil proton as a function of the incident photon beam energy from 450 MeV up to 1450 MeV. Since the measured results for the carbon subtraction method and the hydrogen normalisation method are in a good agreement, as shown in Section 10.2.2, only the measured results of the carbon subtraction method are shown.

A.3.1 Results of the Pions

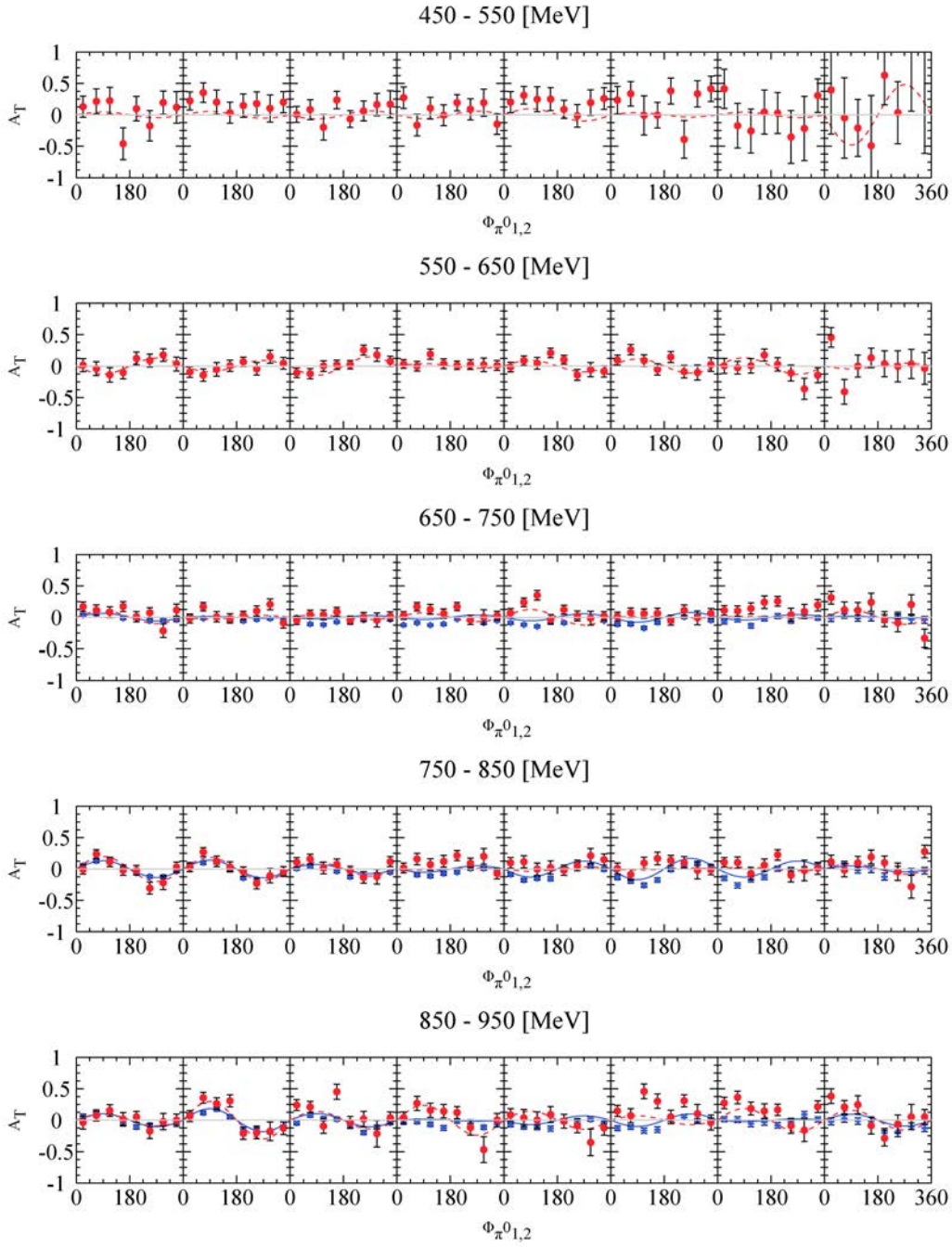

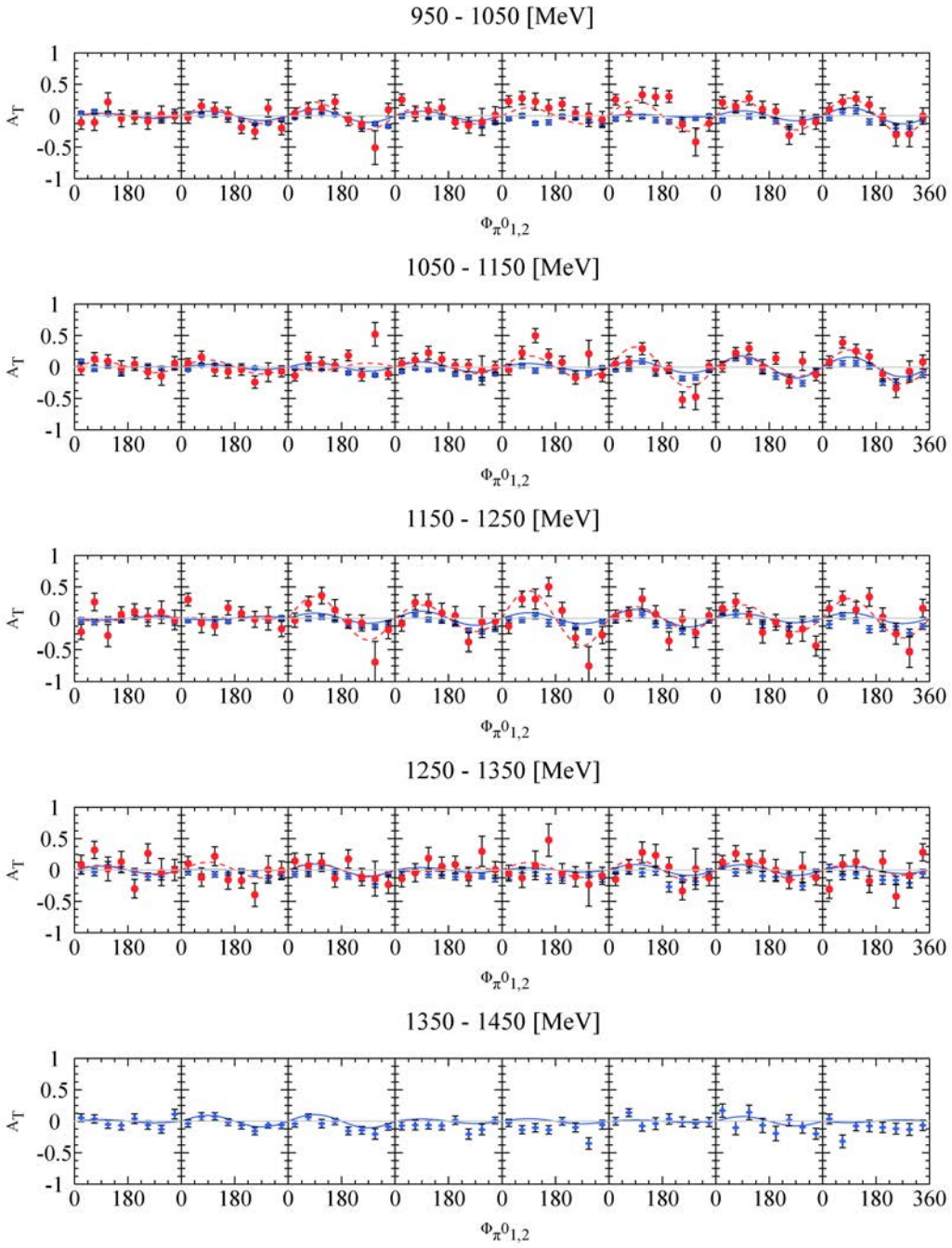

Figure A.5.: Asymmetry of the polarisation observable T for the different $\phi_{\pi^0_{1,2}}$ angles between each π^0 meson and the direction of the target proton spin as a function of the incident beam energy from 450 up to 1450 MeV. The results of the asymmetry T for the hydrogen normalisation method are shown by the red points and the blue cross for the butanol data June 2010 and April 2011, respectively. The corresponding sine fit for the extraction of the polarisation observable T are shown by the same colored lines.

A.3.2 Results of the Proton

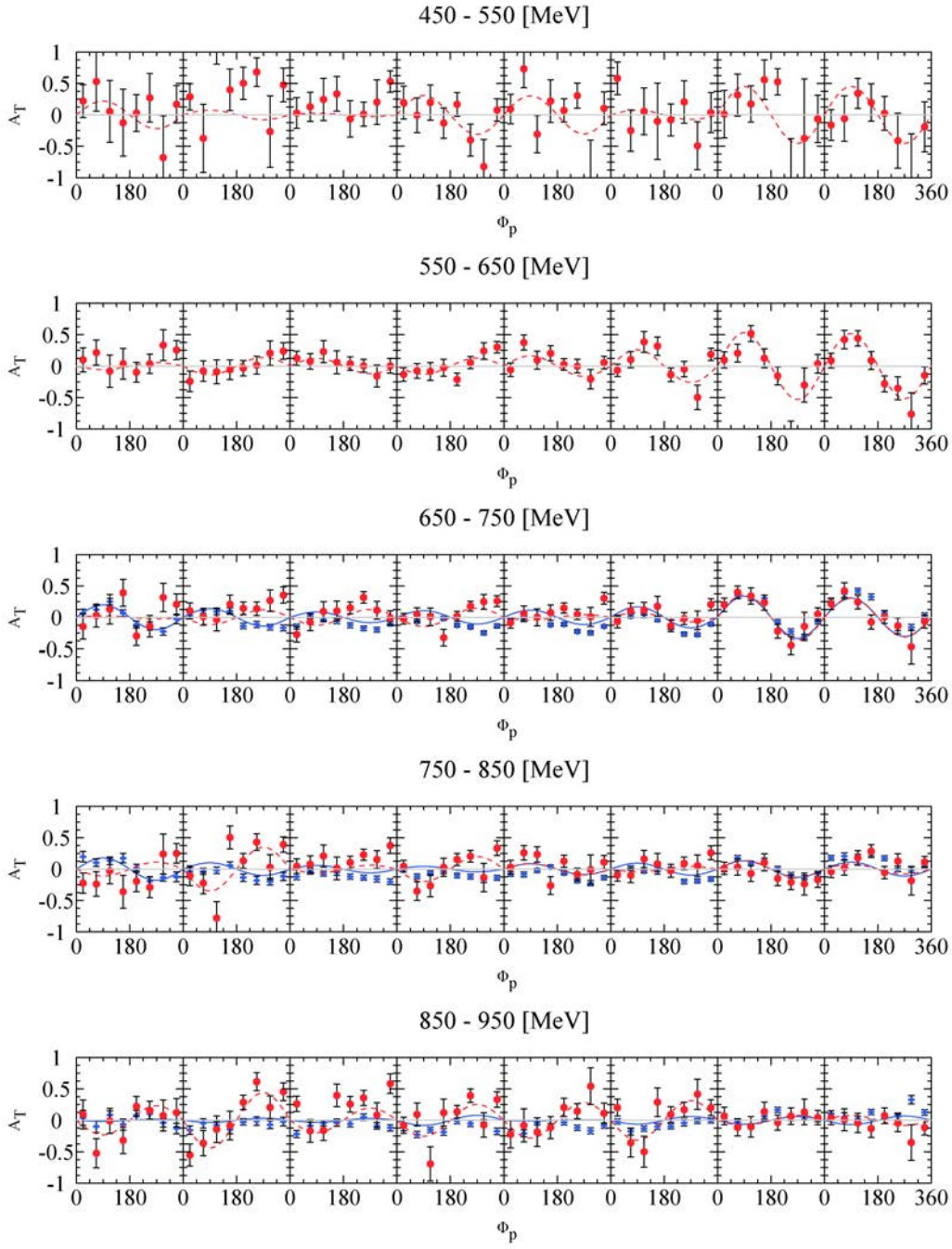

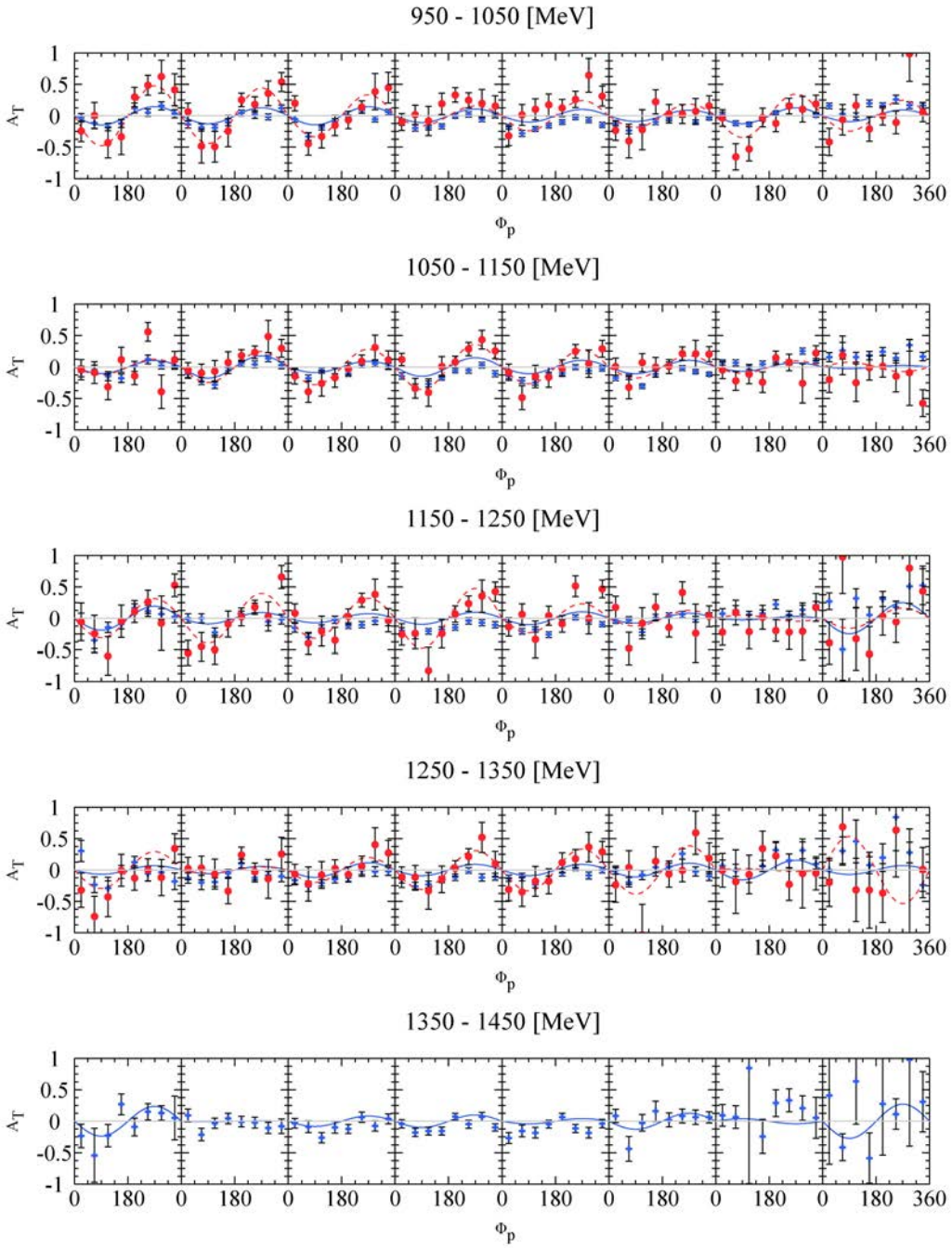

Figure A.6.: Asymmetry of the polarisation observable T for the different ϕ_p angles between the recoil proton and the direction of the target proton spin as a function of the incident beam energy from 450 up to 1450 MeV. The results of the asymmetry T for the hydrogen normalisation method are shown by the red points and the blue cross for the butanol data June 2010 and April 2011, respectively. The same colored lines represent the corresponding sine fit for the extraction of the polarisation observable T.

A.3.3 Results for the Invariant Mass of the Pions

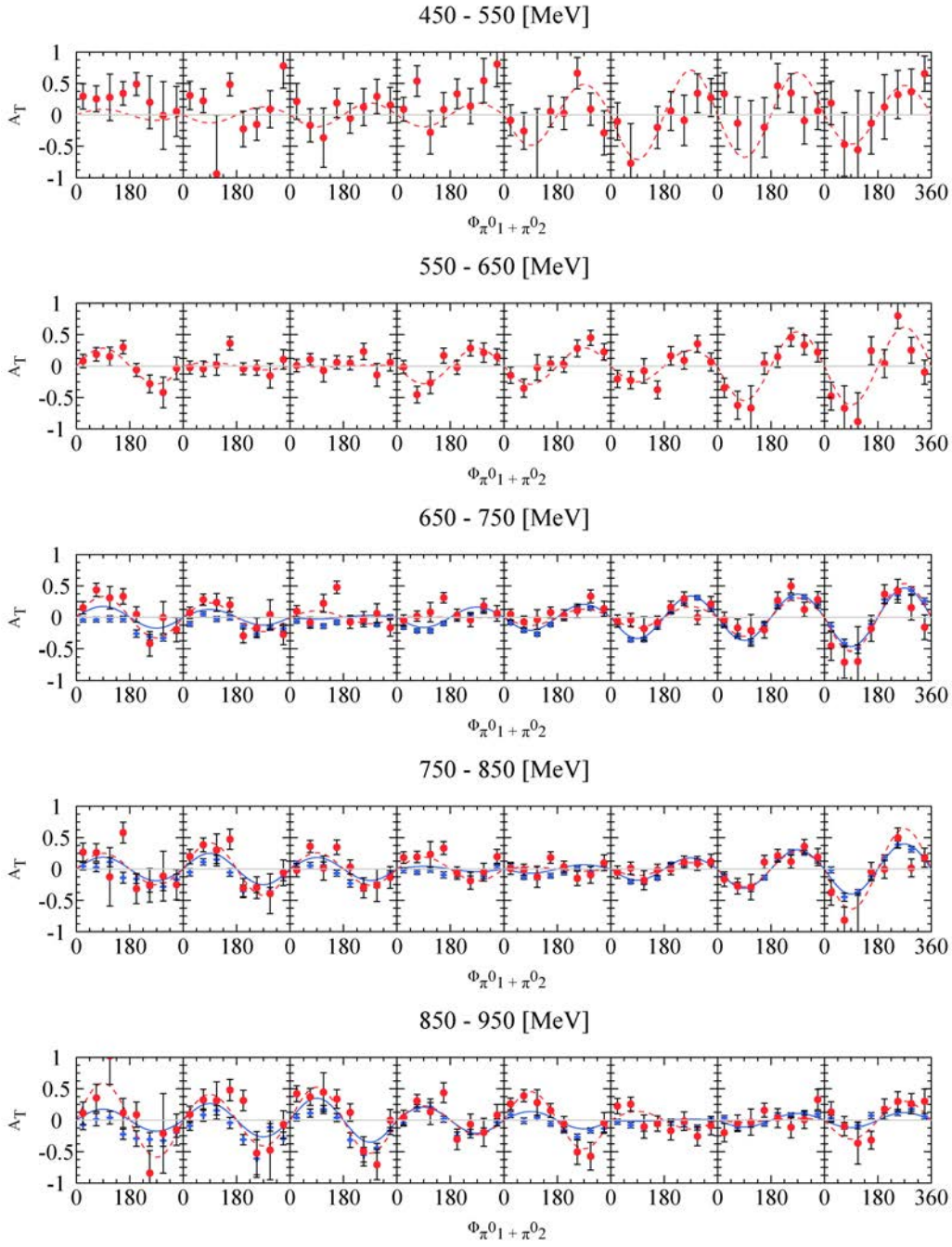

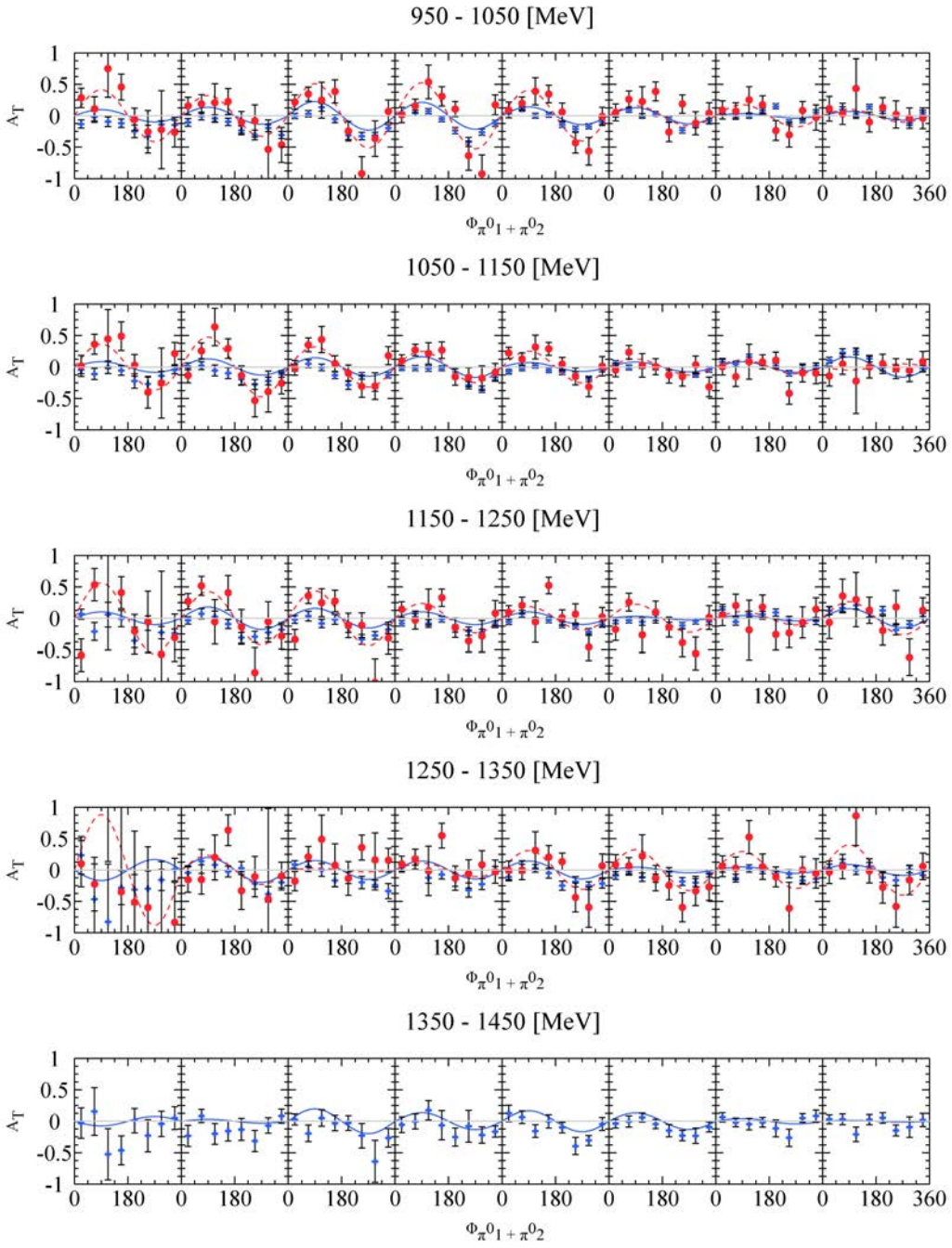

Figure A.7.: Incident photon beam energy $E_\gamma = 450 - 1450$ MeV dependent asymmetry of the polarisation observable T for the different $\phi_{\pi_1^0+\pi_2^0}$ angles between the meson vector and the direction of the target proton spin. The results of the asymmetry T for the hydrogen normalisation method as shown by the red points and the blue cross for the butanol data June 2010 and April 2011, respectively. The corresponding sine fit for the extraction of the polarisation observable T are shown by the same colored lines.

A.3.4 Results for the Invariant Mass of the Pions and the Proton

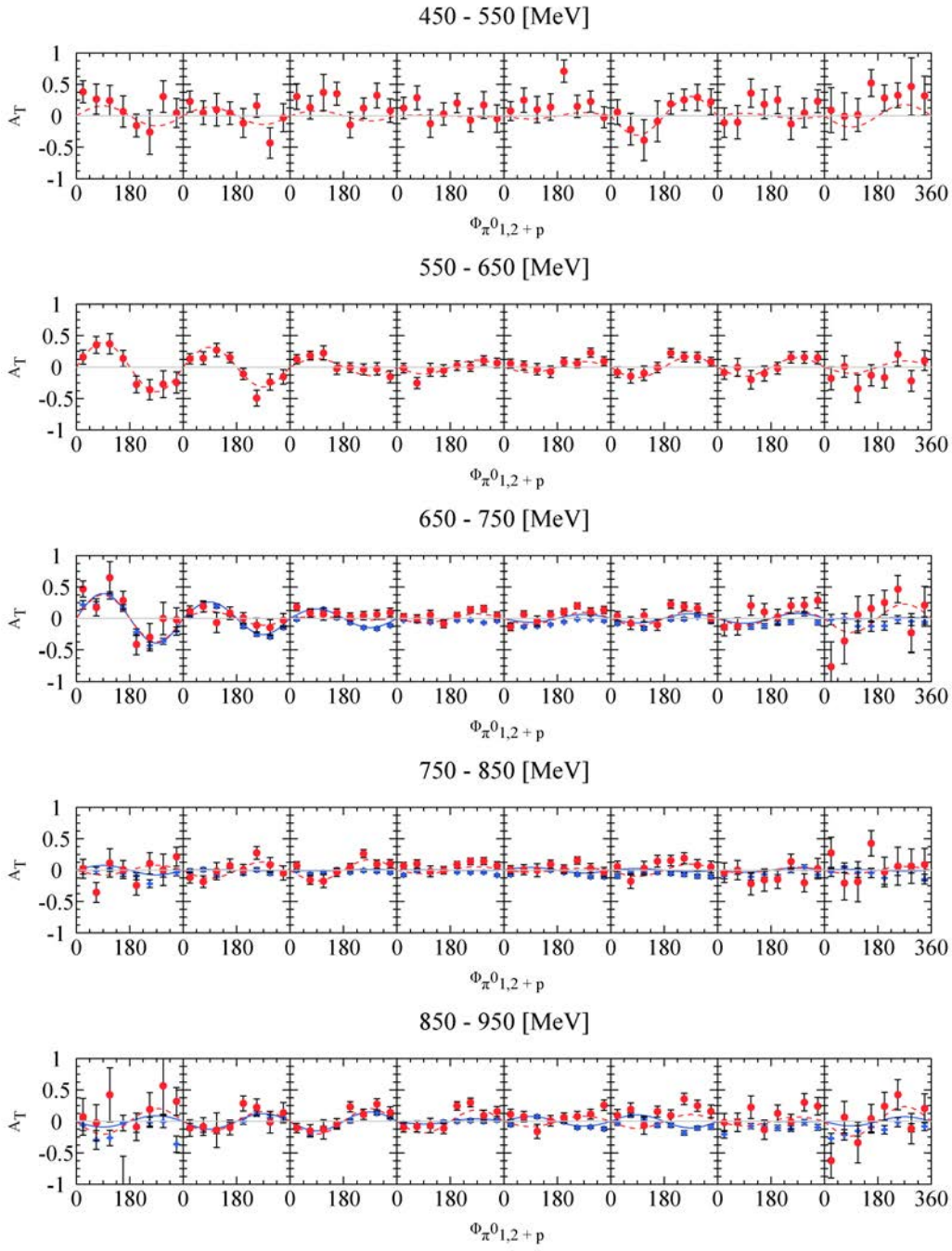

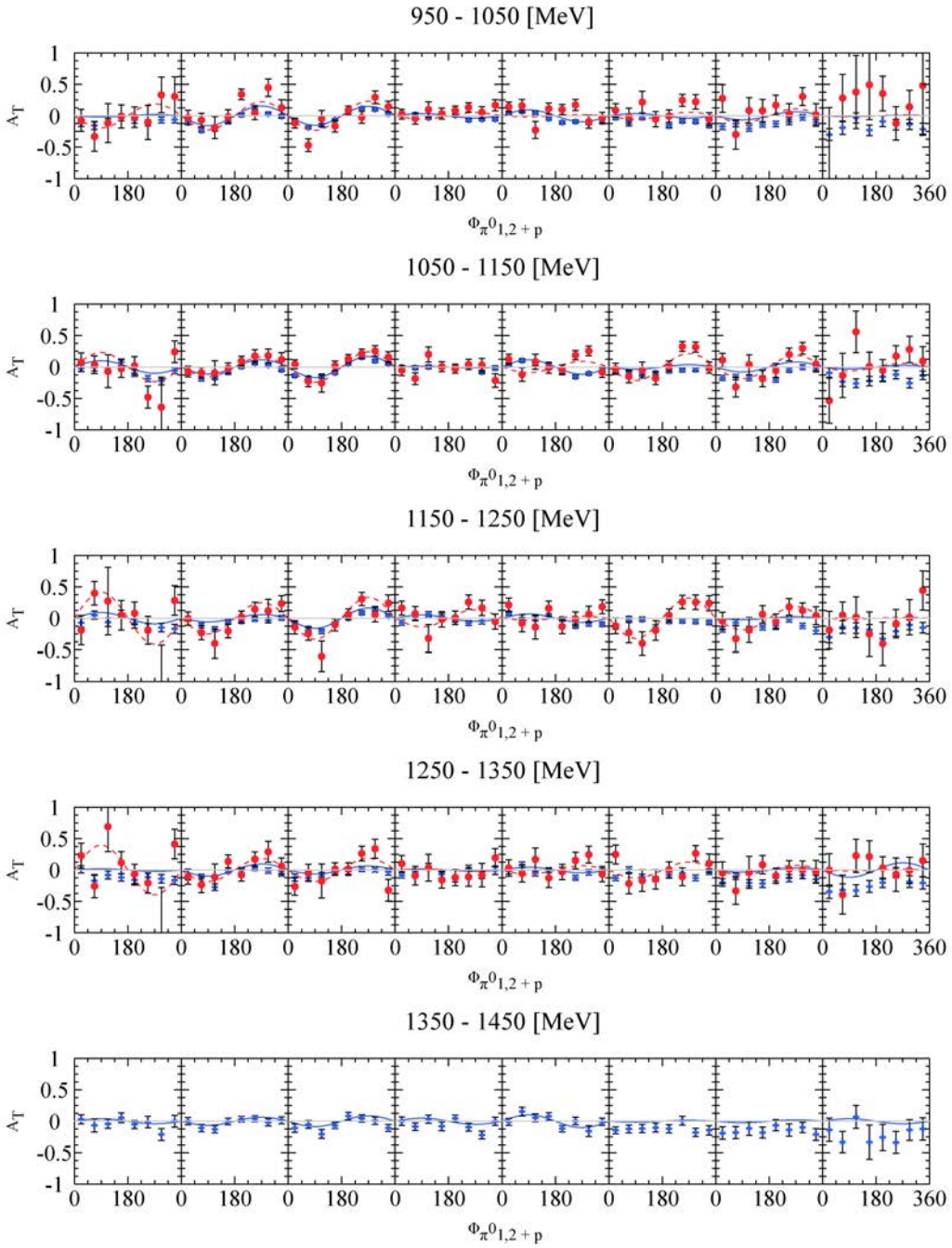

Figure A.8.: Incident photon beam energy $E_\gamma = 450 - 1450$ MeV dependent asymmetry of the polarisation observable T for the different $\phi_{\pi^0_{1,2}+p}$ angles between each π^0 meson and the recoil proton vector and the direction of the target proton spin. The result of the asymmetry T for the hydrogen normalisation method as shown by the red points and the blue cross for the butanol data June 2010 and April 2011, respectively. The same colored lines represent the corresponding sine fit for the extraction of the polarisation observable T.

A.4 Results for the Different Calculation Methods

In this section, the result for the double polarisation observable F for the extraction over the two possible angle definitions to the direction of the nucleon target spin, as explained in Section 9.2, are shown. The agreement between both calculation methods for the butanol data (June 2010 and April 2011), are shown in the following results.

A.4.1 Double Polarisation Observable F

Result of the Pions

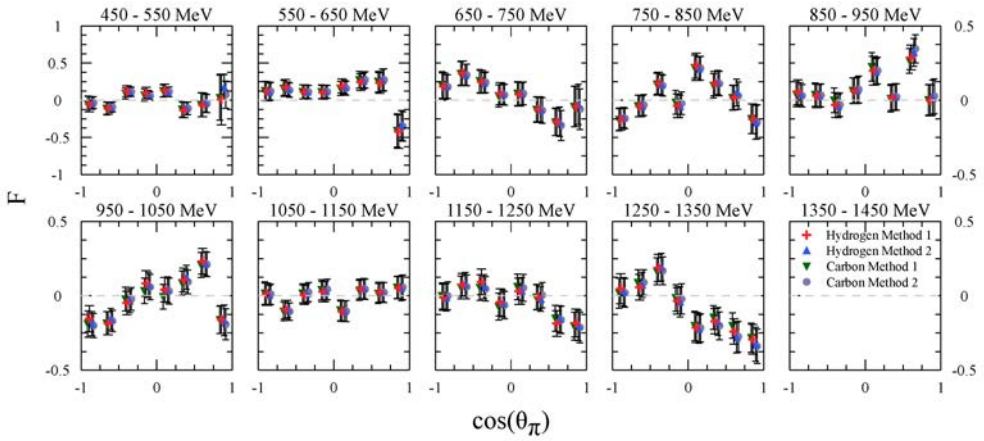

Figure A.9.: Results of the double polarisation observable F of the butanol June 2010 data for both calculation methods for the $cos\theta_{\pi^0}$ angle of each π^0 mesons as a function of the incident photon energy from 450 up to 1450 MeV. The results for the carbon subtraction method for both calculation methods are shown by the red cross and blue triangles (shifted by $\pm 2.5\%$), respectively. The hydrogen normalisation method results are shown by the green triangles and purple points (shifted by $\pm 2.5\%$).

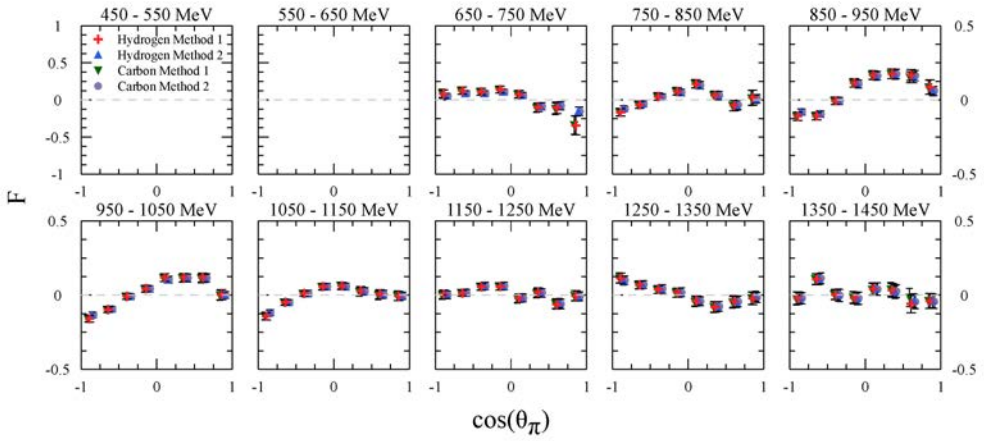

Figure A.10.: Results of the double polarisation observable F of the butanol April 2011 data for both calculation methods for the $cos\theta_{\pi^0}$ angle of each π^0 mesons as a function of the incident photon energy $E_\gamma = 450 - 1450$ MeV. The results for the carbon subtraction method for both calculation methods are shown by the red cross and blue triangles (shifted by $\pm 2.5\%$), respectively. The results of the hydrogen normalisation method are shown by the green triangles and purple points (shifted by $\pm 2.5\%$).

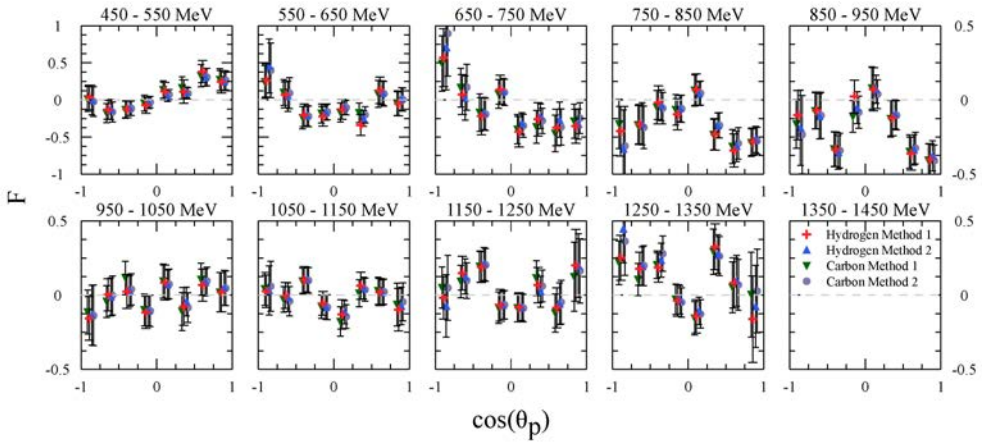

Figure A.11.: Results of the double polarisation observable F of the butanol June 2010 data for both calculation methods for the $cos\theta_p$ angle of the recoil proton as a function of the incident photon energy from 450 up to 1450 MeV. The results for the carbon subtraction method for both calculation methods are shown by the red cross and blue triangles (shifted by $\pm 2.5\%$), respectively. The hydrogen normalisation method results are shown by the green triangles and purple points (shifted by $\pm 2.5\%$).

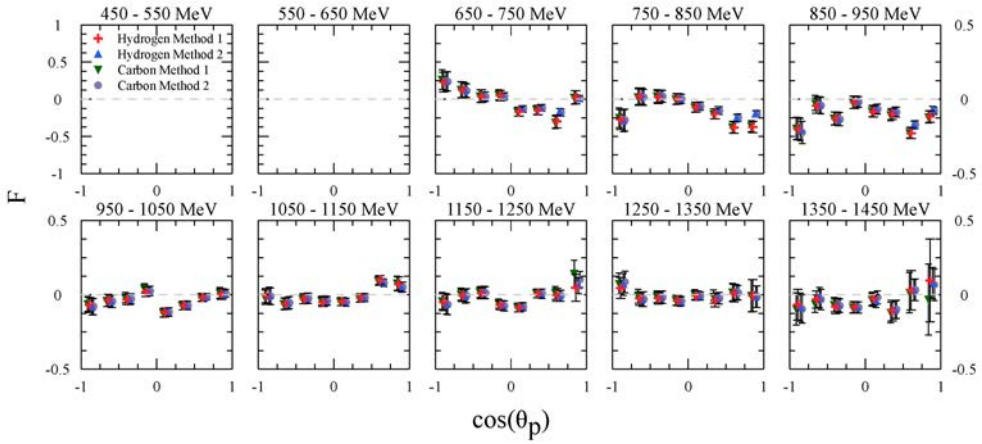

Figure A.12.: Results of the double polarisation observable F of the butanol April 2011 data for both calculation methods for the $cos\theta_p$ angle of the recoil proton as a function of the incident photon energy $E_\gamma = 450 - 1450$ MeV. The results for the carbon subtraction method for both calculation methods are shown by the red cross and blue triangles (shifted by $\pm 2.5\%$), respectively. The results of the hydrogen normalisation method are shown by the green triangles and purple points (shifted by $\pm 2.5\%$).

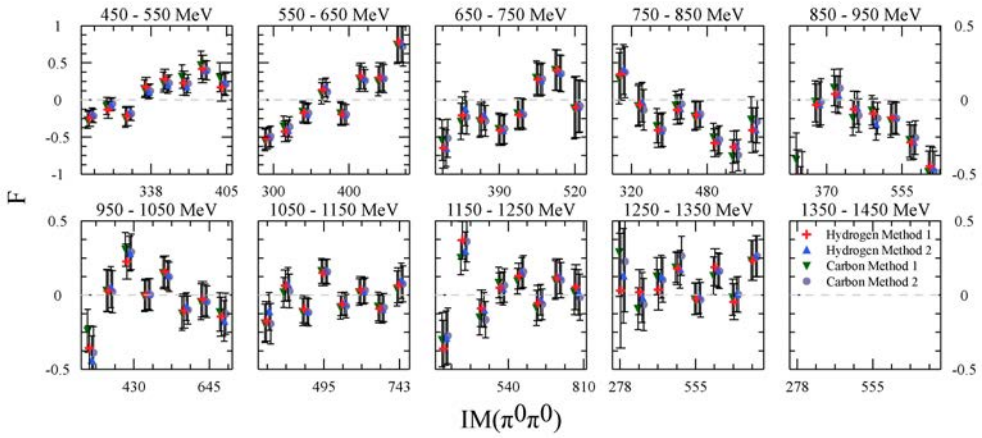

Figure A.13.: Results of the double polarisation observable F of the butanol June 2010 data for both calculation methods for the invariant mass of the double π^0 mesons as a function of the incident photon energy from 450 up to 1450 MeV. The results for the carbon subtraction method for both calculation methods are shown by the red cross and blue triangles (shifted by $\pm 2.5\%$), respectively. The hydrogen normalisation method results are shown by the green triangles and purple points (shifted by $\pm 2.5\%$).

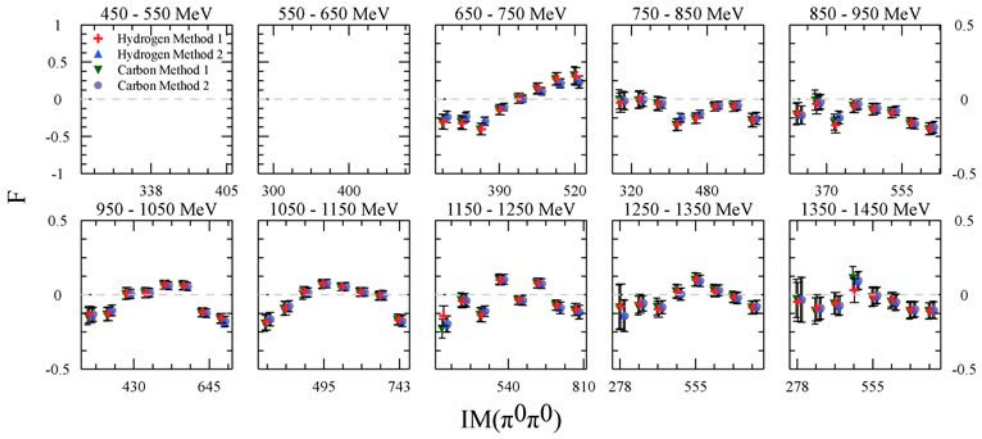

Figure A.14.: Results of the double polarisation observable F of the butanol April 2011 data for both calculation methods for the invariant mass of the double π^0 mesons as a function of the incident photon energy $E_\gamma = 450 - 1450$ MeV. The results for the carbon subtraction method for both calculation methods are shown by the red cross and blue triangles (shifted by $\pm 2.5\%$), respectively. The results of the hydrogen normalisation method are shown by the green triangles and purple points (shifted by $\pm 2.5\%$).

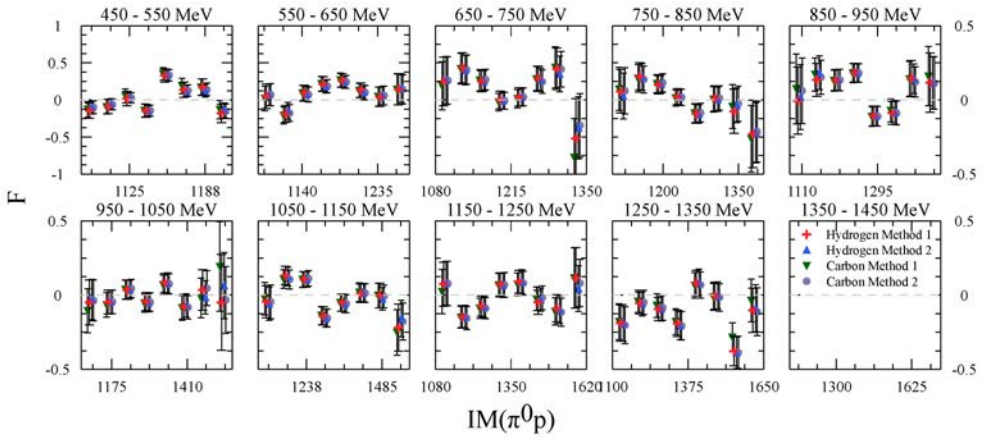

Figure A.15.: Results of the double polarisation observable F of the butanol June 2010 data for both calculation methods for the invariant mass of the each π^0 meson and a recoil proton as a function of the incident photon energy from 450 up to 1450 MeV. The results for the carbon subtraction method for both calculation methods are shown by the red cross and blue triangles (shifted by $\pm 2.5\%$), respectively. The hydrogen normalisation method results are shown by the green triangles and purple points (shifted by $\pm 2.5\%$).

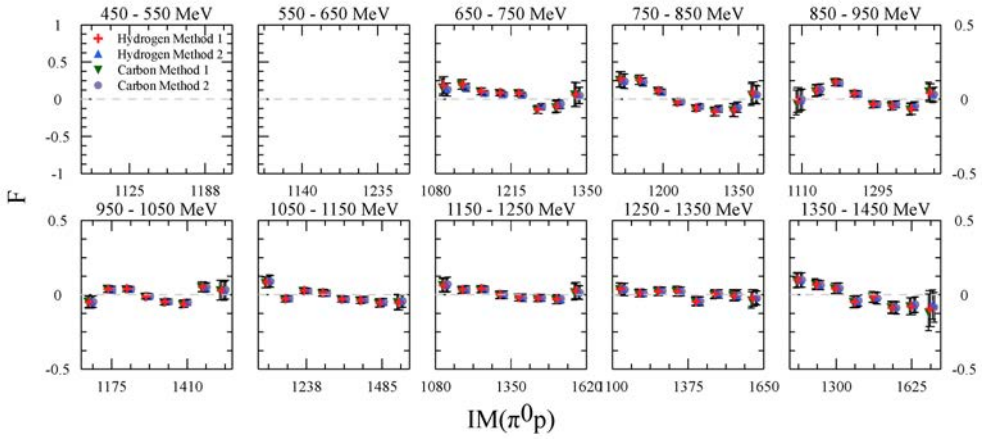

Figure A.16.: Results of the double polarisation observable F of the butanol April 2011 data for both calculation methods for the invariant mass of the double π^0 meson and the recoil proton as a function of the incident photon energy $E_\gamma = 450 - 1450$ MeV. The results for the carbon subtraction method for both calculation methods are shown by the red cross and blue triangles (shifted by $\pm 2.5\%$), respectively. The results of the hydrogen normalisation method are shown by the green triangles and purple points (shifted by $\pm 2.5\%$).

A.5 Comparison with another Measurement

In this section, the individual results of the polarisation observable F and T for the butanol data (June 2010 and April 2011), are shown. Additionally, the present polarisation observable results were compared with the measurement result of the carbon subtraction method by V. L. Kashevarov [113]. The results of V. L. Kasehvarov were obtained by a cluster size analysis of the Crystal Ball without the use of the charged particle detectors.

A.5.1 Double Polarisation Observable F

Results of the Pions

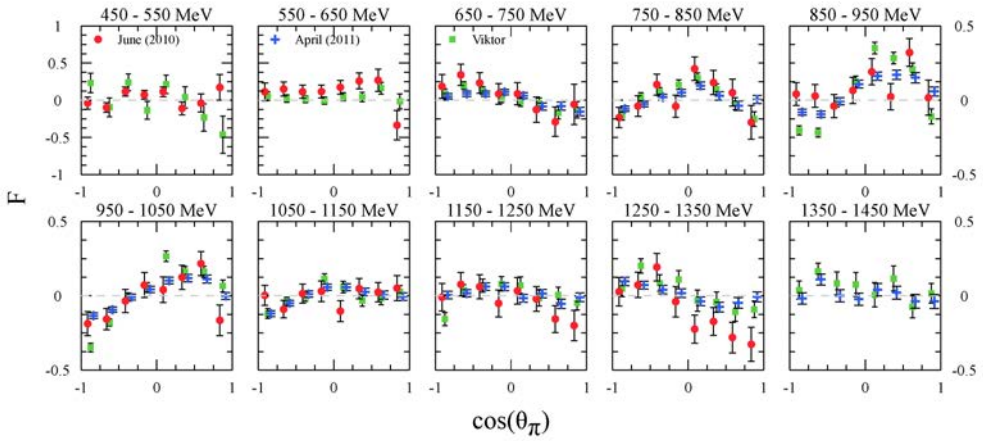

Figure A.17.: Results of the double polarisation observable F for the different $cos\theta_{\pi^0}$ angles of the double π^0 mesons as a function of the incident beam energy from 450 up to 1450 MeV. The measured results for the hydrogen normalisation method for the butanol data (June 2010 and April 2011) are shown by the red points and blue cross respectively (shifted by $\pm 2.5\%$). The green squares show the measured result of V. L. Kashevarov [113] by the carbon subtraction method analysed over the cluster size.

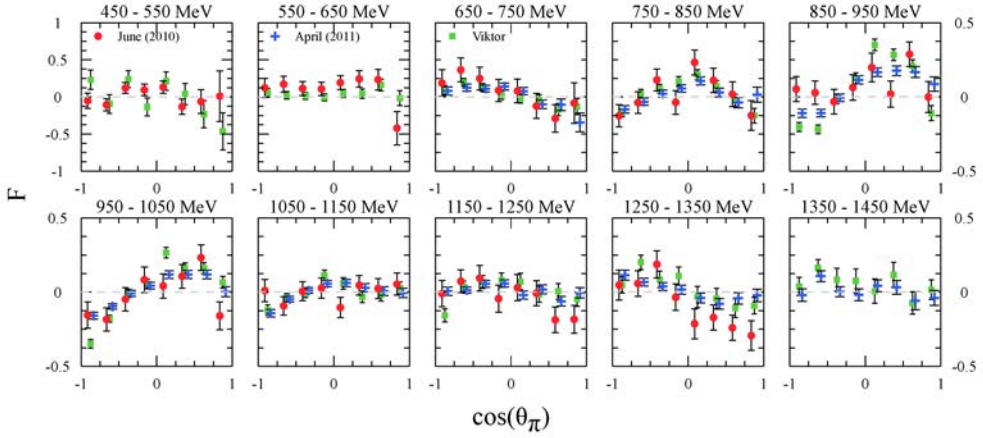

Figure A.18.: Results of the double polarisation observable F for the different $cos\theta_{\pi^0}$ angles of the double π^0 mesons as a function of the incident beam energy from 450 up to 1450 MeV. The measured results for the carbon subtraction method for the butanol data (June 2010 and April 2011) are shown by the red points and blue cross (shifted by $\pm 2.5\%$), respectively. The green squares show the measured result of V. L. Kahevarov [113] by the carbon subtraction method analysed over the cluster size.

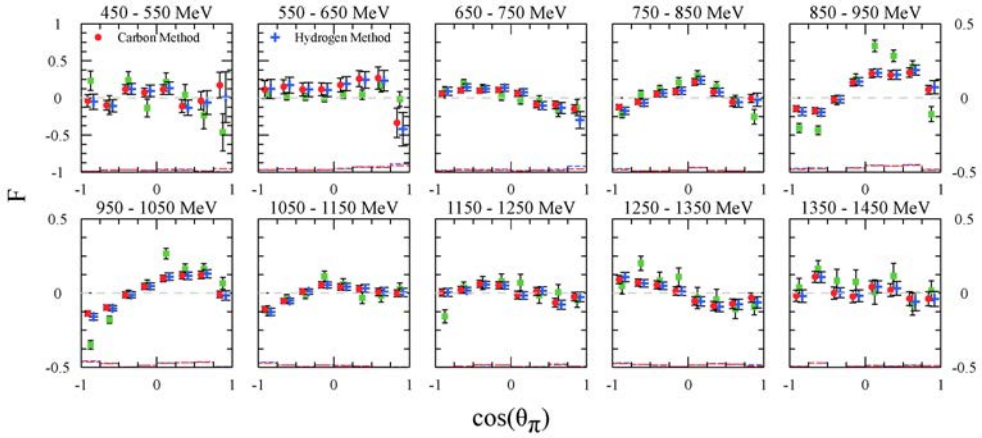

Figure A.19.: Merged results of the double polarisation observable F of both butanol data for the different $cos\theta_{\pi^0}$ angles of the double π^0 mesons as a function of the incident beam energy from 450 up to 1450 MeV. The double polarisation observable result F for the carbon subtraction method and the hydrogen normalisation method are shown by the red points and blue cross (shifted by $\pm 2.5\%$), respectively. For the comparison with the measured results of the cluster size analysis the results of V. L. Kashevarov [113] are shown by the green squares.

Results of the Proton

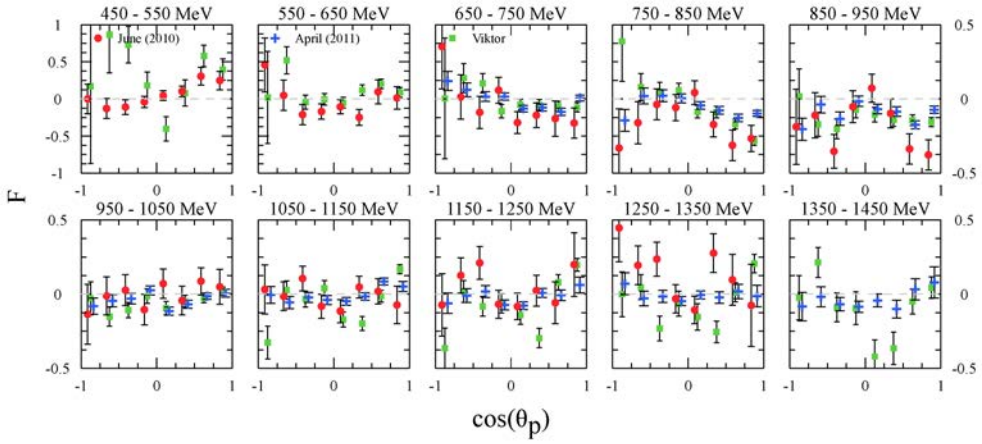

Figure A.20.: Results of the double polarisation observable F for the different $cos\theta_p$ angles of the recoil proton as a function of the incident beam energy from 450 up to 1450 MeV. The measured results for the hydrogen normalisation method for the butanol data (June 2010 and April 2011) are shown by the red points and blue cross (shifted by $\pm 2.5\%$), respectively. The green squares show the measured result of V. L. Kashevarov [113] by the carbon subtraction method analysed over the cluster size.

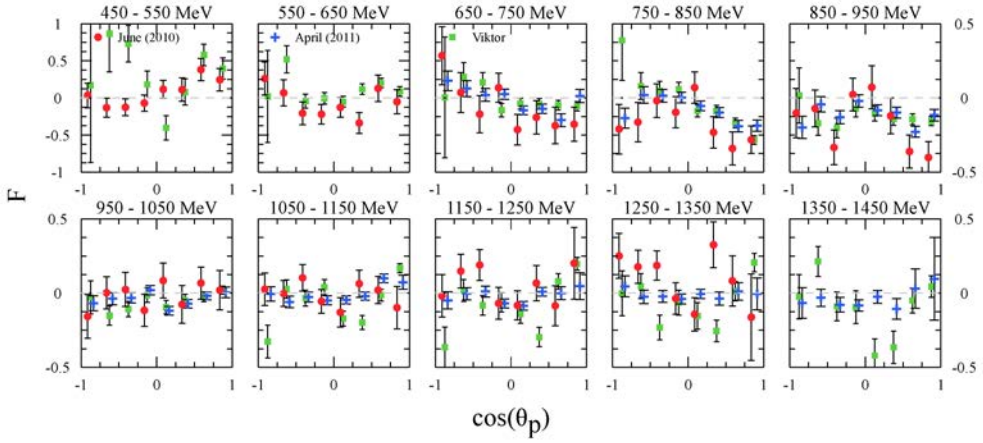

Figure A.21.: Results of the double polarisation observable F for the different $cos\theta_p$ angles of the recoil proton as a function of the incident beam energy from 450 up to 1450 MeV. The measured results for the carbon subtraction method for the butanol data (June 2010 and April 2011) are shown by the red points and blue cross (shifted by $\pm 2.5\%$), respectively. The green squares show the measured result of V. L. Kahevarov [113] by the carbon subtraction method analysed over the cluster size.

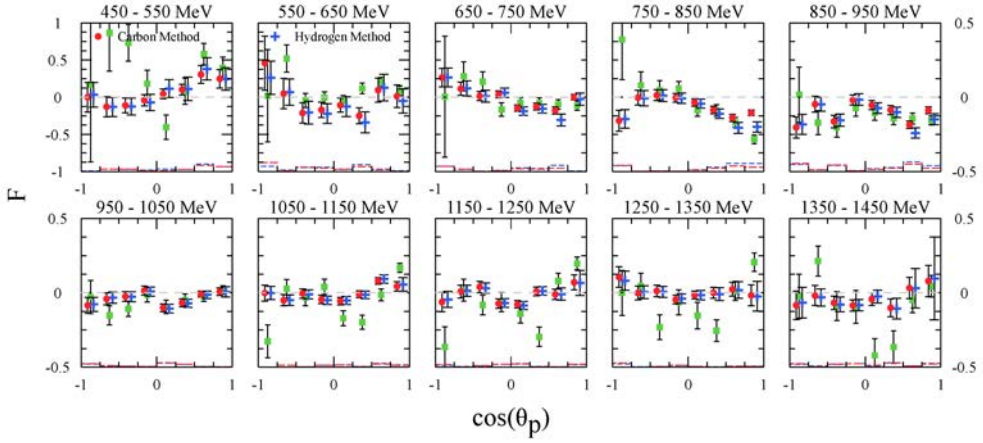

Figure A.22.: Merged results of the double polarisation observable F of both butanol data for the different $cos\theta_p$ angles of the recoil proton as a function of the incident beam energy from 450 up to 1450 MeV. The double polarisation observable result F for the carbon subtraction method and the hydrogen normalisation method are shown by the red points and blue cross (shifted by $\pm 2.5\%$), respectively. For the comparison with the measured results of the cluster size analysis the results of V. L. Kashevarov [113] are shown by the green squares.

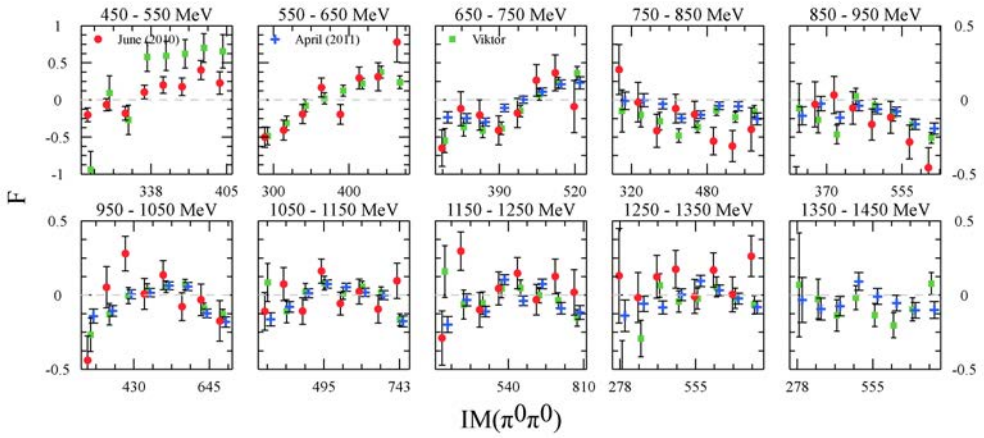

Figure A.23.: Results of the double polarisation observable F for the invariant mass of the double π^0 mesons a function of the incident beam energy from 450 up to 1450 MeV. The measured results for the hydrogen normalisation method for the butanol data (June 2010 and April 2011) are shown by the red points and blue cross (shifted by $\pm 2.5\%$), respectively. The green squares show the measured result of V. L. Kashevarov [113] by the carbon subtraction method analysed over the cluster size.

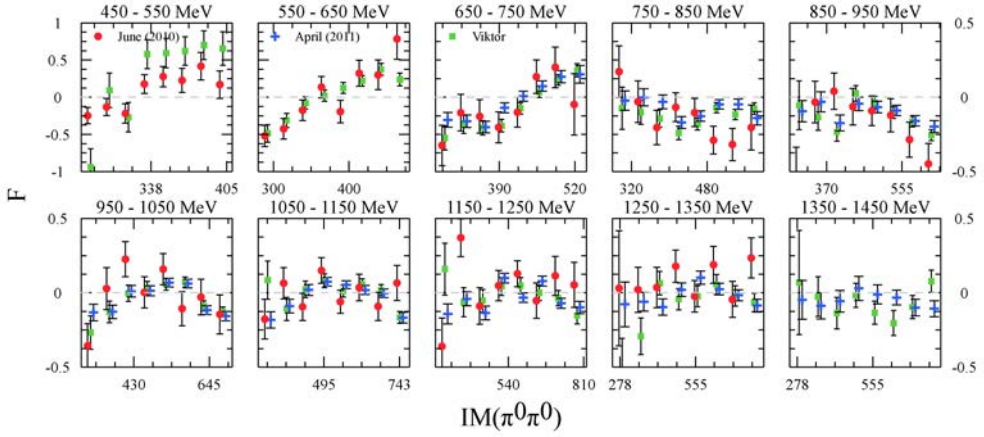

Figure A.24.: Results of the double polarisation observable F for the invariant mass of the double π^0 mesons as a function of the incident beam energy from 450 up to 1450 MeV. The measured results for the carbon subtraction method for the butanol data (June 2010 and April 2011) are shown by the red points and blue cross (shifted by $\pm 2.5\%$), respectively. The green squares show the measured result of V. L. Kahevarov [113] by the carbon subtraction method analysed over the cluster size.

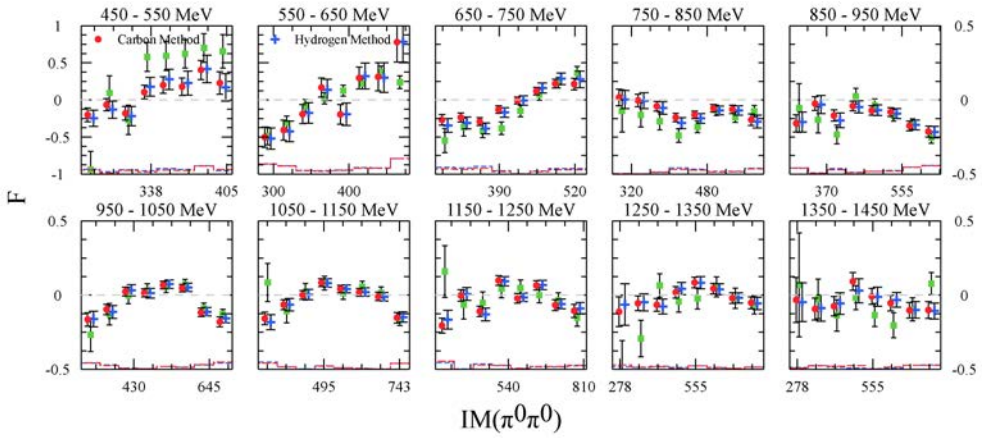

Figure A.25.: Merged results of the double polarisation observable F of both butanol data for the invariant mass of the double π^0 mesons as a function of the incident beam energy from 450 up to 1450 MeV. The double polarisation observable result F for the carbon subtraction method and the hydrogen normalisation method are shown by the red points and blue cross (shifted by $\pm 2.5\%$), respectively. For the comparison with the measured results of the cluster size analysis the results of V. L. Kashevarov [113] are shown by the green squares.

Results for the Invariant Mass of the Pions and the Proton

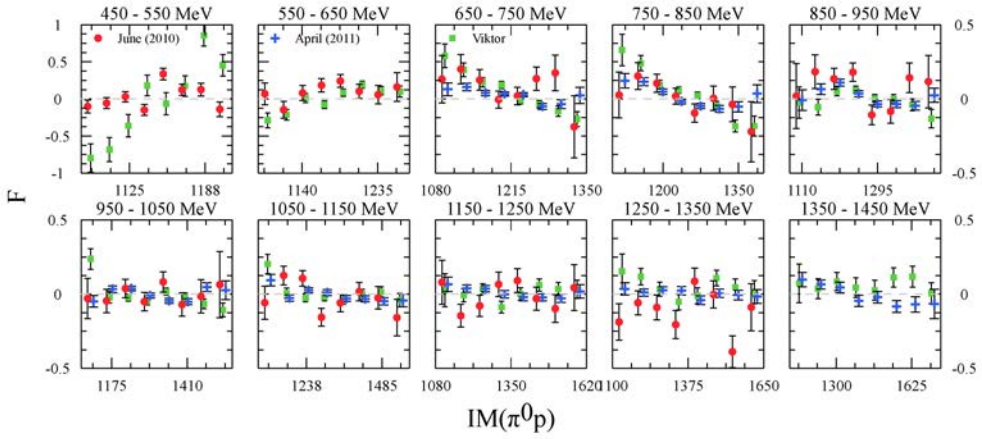

Figure A.26.: Results of the double polarisation observable F for the invariant mass of each π^0 meson and the recoil proton as a function of the incident beam energy from 450 up to 1450 MeV. The measured results for the hydrogen normalisation method for the butanol data (June 2010 and April 2011) are shown by the red points and blue cross (shifted by $\pm 2.5\%$), respectively. The green squares show the measured result of V. L. Kashevarov [113] by the carbon subtraction method analysed over the cluster size.

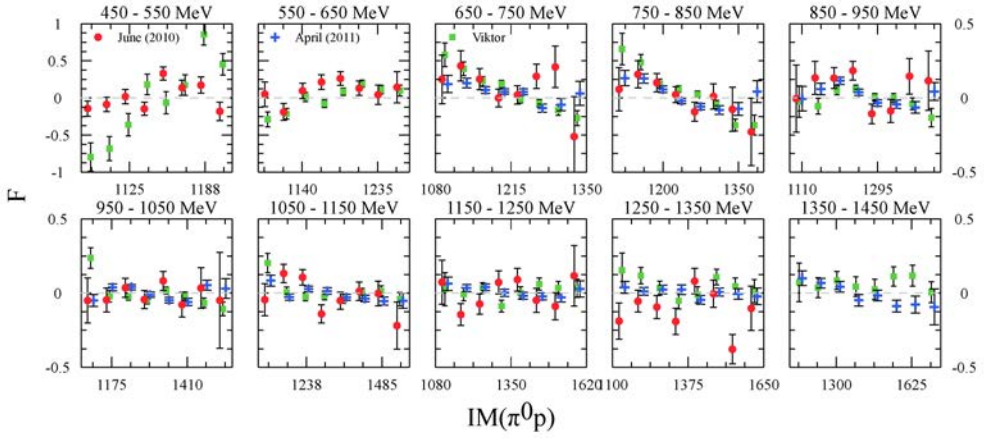

Figure A.27.: Results of the double polarisation observable F for the invariant mass of each π^0 meson and the recoil proton as a function of the incident beam energy from 450 up to 1450 MeV. The measured results for the carbon subtraction method for the butanol data (June 2010 and April 2011) are shown by the red points and blue cross (shifted by $\pm 2.5\%$), respectively. The green squares show the measured result of V. L. Kahevarov [113] by the carbon subtraction method analysed over the cluster size.

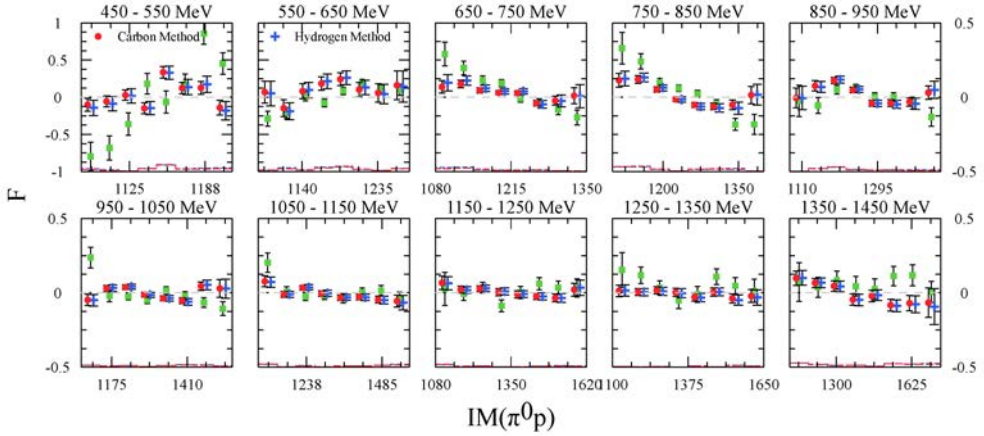

Figure A.28.: Merged results of the double polarisation observable F of both butanol data for the invariant mass of each π^0 meson and the recoil proton as a function of the incident beam energy from 450 up to 1450 MeV. The double polarisation observable result F for the carbon subtraction method and the hydrogen normalisation method are shown by the red points and blue cross (shifted by $\pm 2.5\%$), respectively. For the comparison with the measured results of the cluster size analysis the results of V. L. Kashevarov [113] are shown by the green squares.

A.5.2 Polarisation Observable T

Results of the Pions

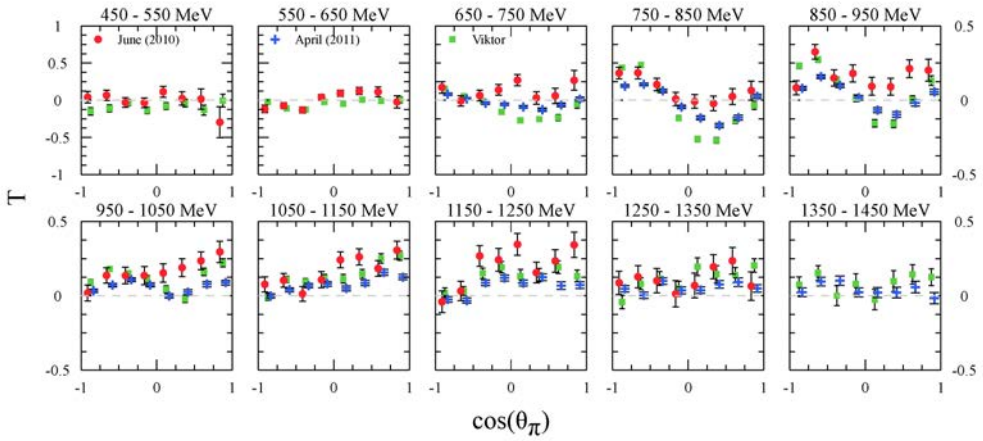

Figure A.29.: Results of the polarisation observable T for the different $cos\theta_{\pi^0}$ angles of the double π^0 mesons as a function of the incident beam energy from 450 up to 1450 MeV. The measured results for the hydrogen normalisation method for the butanol data (June 2010 and April 2011) are shown by the red points and blue cross (shifted by $\pm 2.5\%$), respectively. The green squares show the measured result of V. L. Kashevarov [113] by the carbon subtraction method analysed over the cluster size.

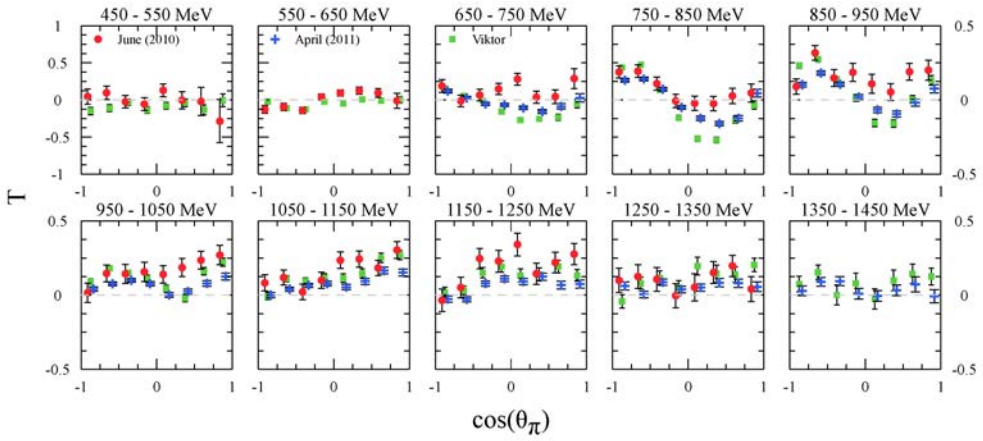

Figure A.30.: Results of the polarisation observable T for the different $cos\theta_{\pi^0}$ angles of the double π^0 mesons as a function of the incident beam energy from 450 up to 1450 MeV. The measured results for the carbon subtraction method for the butanol data (June 2010 and April 2011) are shown by the red points and blue cross (shifted by $\pm 2.5\%$), respectively. The green squares show the measured result of V. L. Kahevarov [113] by the carbon subtraction method analysed over the cluster size.

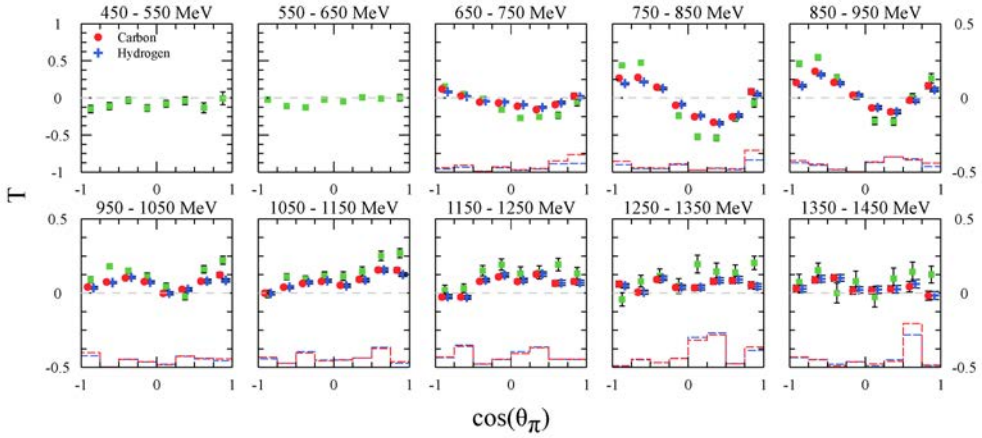

Figure A.31.: Results of the polarisation observable T of the butanol April 2011 data for the different $cos\theta_{\pi^0}$ angles of the double π^0 mesons as a function of the incident beam energy from 450 up to 1450 MeV. The double polarisation observable result T for the carbon subtraction method and the hydrogen normalisation method are shown by the red points and blue cross (shifted by $\pm 2.5\%$), respectively. For the comparison with the measured results of the cluster size analysis the results of V. L. Kashevarov [113] are shown by the green squares. The systematic uncertainties are indicated by the same colored lines like the measurement methods.

Results of the Proton

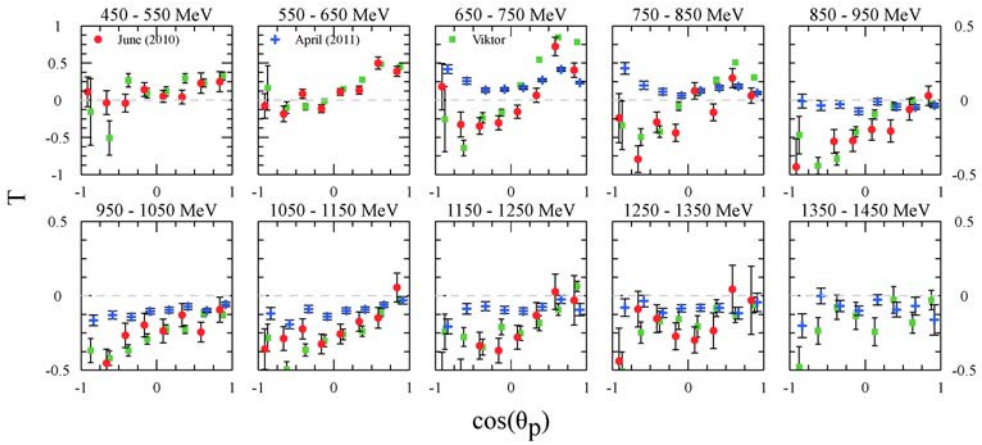

Figure A.32.: Results of the polarisation observable T for the different $cos\theta_p$ angles of the recoil proton as a function of the incident beam energy from 450 up to 1450 MeV. The measured results for the hydrogen normalisation method for the butanol data (June 2010 and April 2011) are shown by the red points and blue cross (shifted by $\pm 2.5\%$), respectively. The green squares show the measured result of V. L. Kashevarov [113] by the carbon subtraction method analysed over the cluster size.

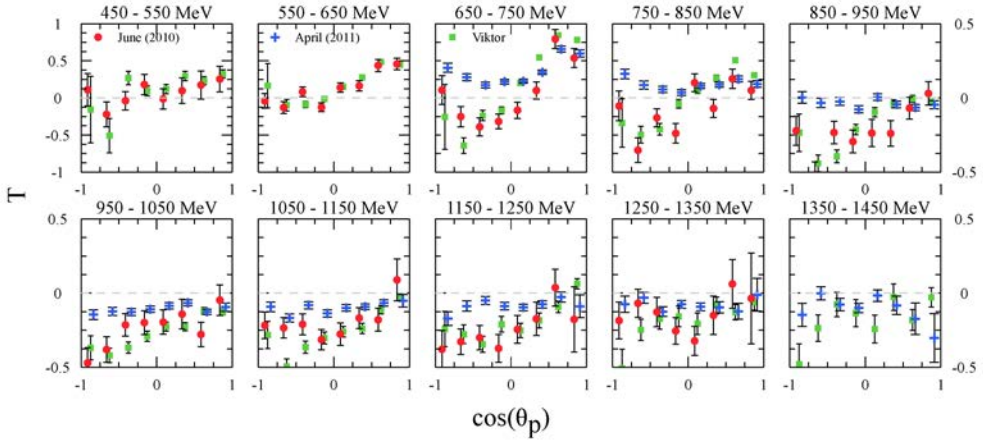

Figure A.33.: Results of the polarisation observable T for the different $cos\theta_p$ angles of the recoil proton as a function of the incident beam energy from 450 up to 1450 MeV. The measured results for the carbon subtraction method for the butanol data (June 2010 and April 2011) are shown by the red points and blue cross (shifted by $\pm 2.5\%$), respectively. The green squares show the measured result of V. L. Kahevarov [113] by the carbon subtraction method analysed over the cluster size.

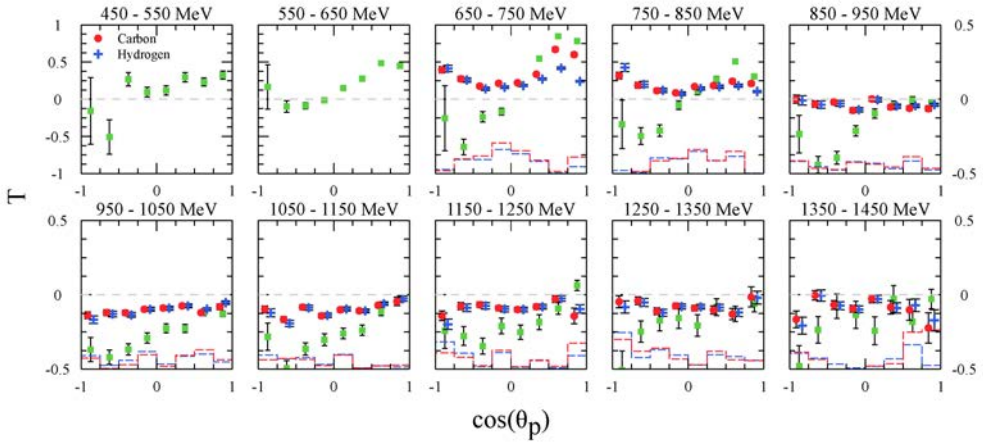

Figure A.34.: Results of the polarisation observable T of the butanol April 2011 data for the different $cos\theta_p$ angles of the recoil proton as a function of the incident beam energy from 450 up to 1450 MeV. The polarisation observable result T for the carbon subtraction method and the hydrogen normalisation method are shown by the red points and blue cross (shifted by $\pm 2.5\%$), respectively. For the comparison with the measured results of the cluster size analysis the results of V. L. Kashevarov [113] are shown by the green squares. The systematic uncertainties are indicated by the same colored lines like the measurement methods.

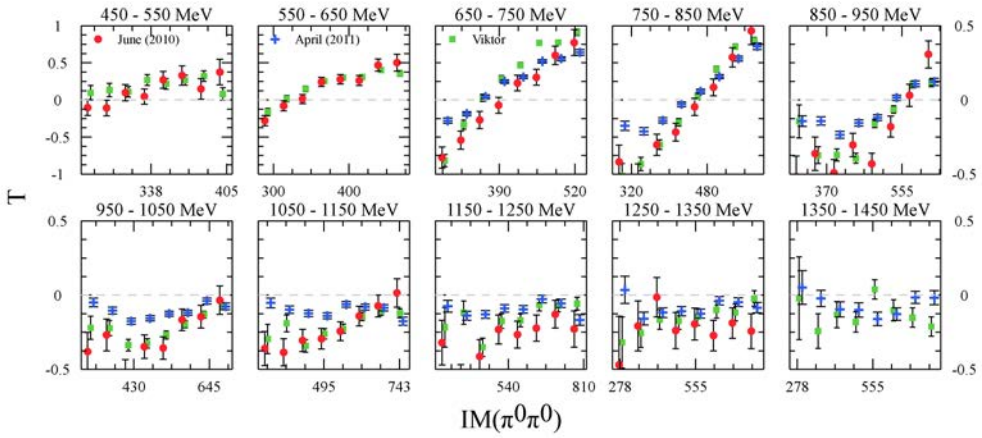

Figure A.35.: Results of the polarisation observable T for the invariant mass of the double π^0 mesons a function of the incident beam energy from 450 up to 1450 MeV. The measured results for the hydrogen normalisation method for the butanol data (June 2010 and April 2011) are shown by the red points and blue cross (shifted by $\pm 2.5\%$), respectively. The green squares show the measured result of V. L. Kashevarov [113] by the carbon subtraction method analysed over the cluster size.

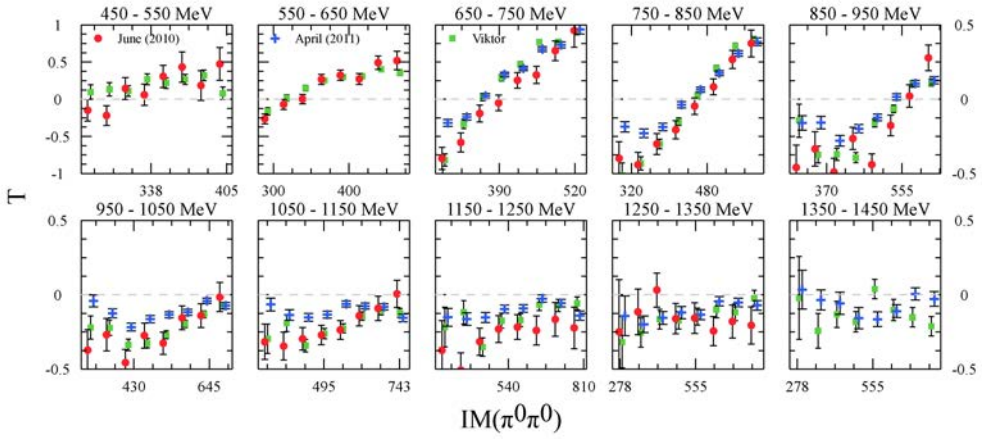

Figure A.36.: Results of the polarisation observable T for the invariant mass of the double π^0 mesons as a function of the incident beam energy from 450 up to 1450 MeV. The measured results for the carbon subtraction method for the butanol data (June 2010 and April 2011) are shown by the red points and blue cross (shifted by $\pm 2.5\%$), respectively. The green squares show the measured result of V. L. Kahevarov [113] by the carbon subtraction method analysed over the cluster size.

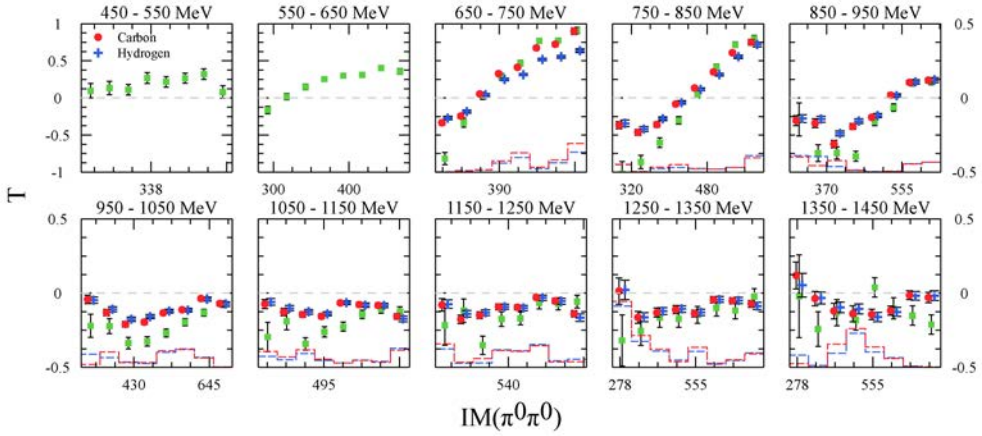

Figure A.37.: Results of the polarisation observable T of the butanol April 2011 data for the invariant mass of the double π^0 mesons as a function of the incident beam energy from 450 up to 1450 MeV. The polarisation observable result T for the carbon subtraction method and the hydrogen normalisation method are shown by the red points and blue cross (shifted by $\pm 2.5\%$), respectively. For the comparison with the measured results of the cluster size analysis the results of V. L. Kashevarov [113] are shown by the green squares. The systematic uncertainties are indicated by the same colored lines like the measurement methods.

Results of the Invariant Mass of the Pions and the Proton

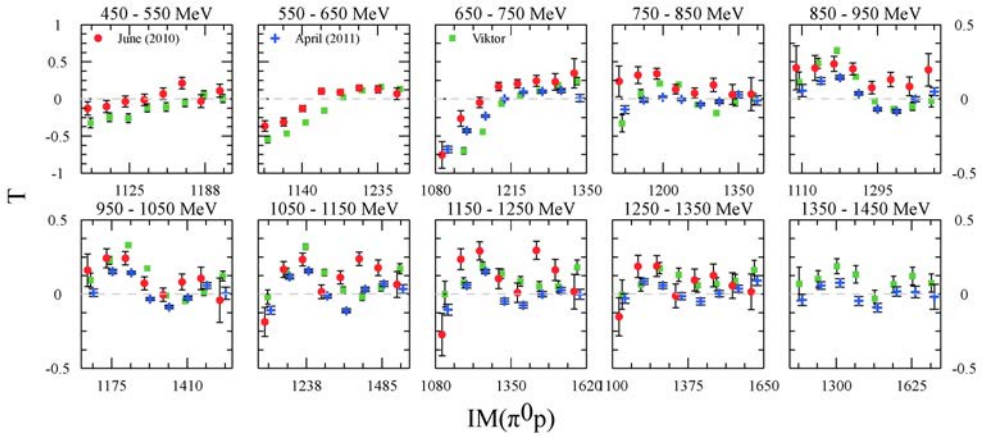

Figure A.38.: Results of the polarisation observable T for the invariant mass of each π^0 meson and the recoil proton as a function of the incident beam energy from 450 up to 1450 MeV. The measured results for the hydrogen normalisation method for the butanol data (June 2010 and April 2011) are shown by the red points and blue cross (shifted by $\pm 2.5\%$), respectively. The green squares show the measured result of V. L. Kashevarov [113] by the carbon subtraction method analysed over the cluster size.

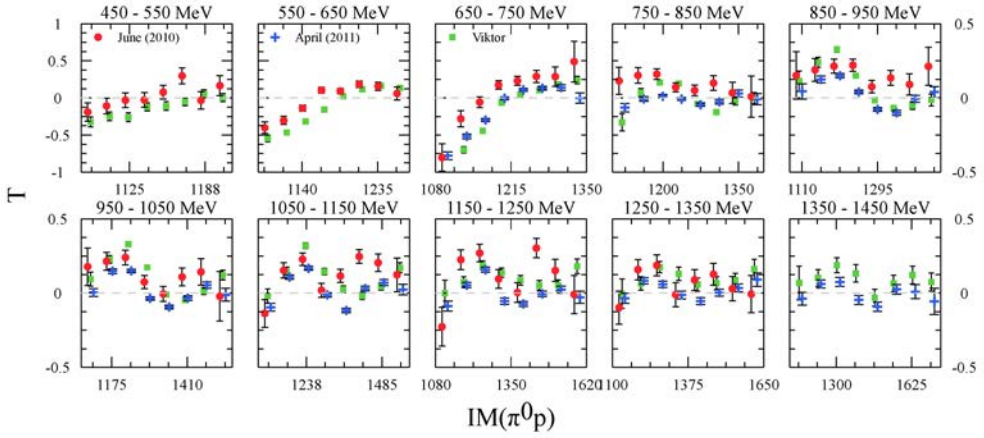

Figure A.39.: Results of the polarisation observable T for the invariant mass of each π^0 meson and the recoil proton as a function of the incident beam energy from 450 up to 1450 MeV. The measured results for the carbon subtraction method for the butanol data (June 2010 and April 2011) are shown by the red points and blue cross (shifted by $\pm 2.5\%$), respectively. The green squares show the measured result of V. L. Kahevarov [113] by the carbon subtraction method analysed over the cluster size.

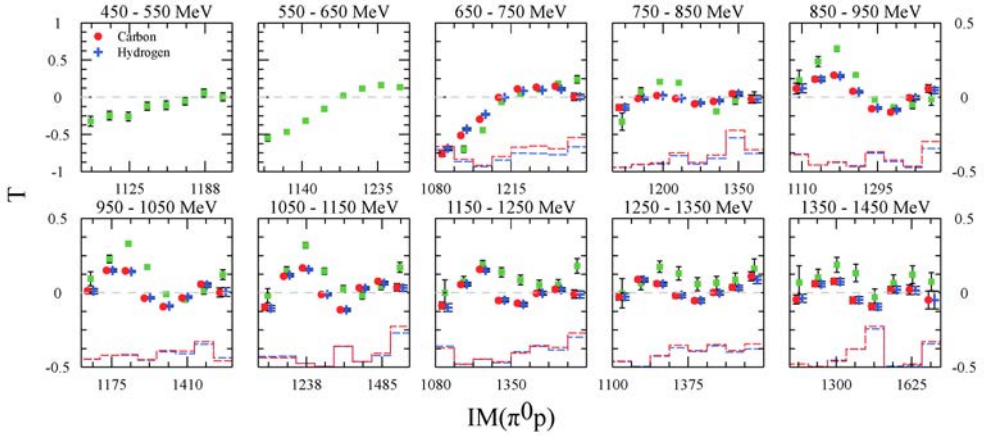

Figure A.40.: Results of the polarisation observable T of the butanol April 2011 data for the invariant mass of each π^0 meson and the recoil proton as a function of the incident beam energy from 450 up to 1450 MeV. The polarisation observable result T for the carbon subtraction method and the hydrogen normalisation method are shown by the red points and blue cross, respectively. For the comparison with the measured results of the cluster size analysis the results of V. L. Kashevarov [113] are shown by the green squares. The systematic uncertainties are indicated by the same colored lines like the measurement methods.

A.6 Polarisation Observable T for the Different Nucleon Polarisation

In this section, the results of the polarisation observable T for only one target polarisation spin state, vertically up or down, as a function of the incident beam energy from 450 up to 1450 MeV for both butanol data are presented. For a correct determined detector efficiency the asymmetry of the experimental setup should be cancels out and the calculation of the polarisations observable T for both spin polarisation should be the same. Since in both butanol data some angle dependent inconsistencies occur through the used charged particle detectors this results show some derivations, mainly for the butanol June data 2010 .

A.6.1 Results of the Pions

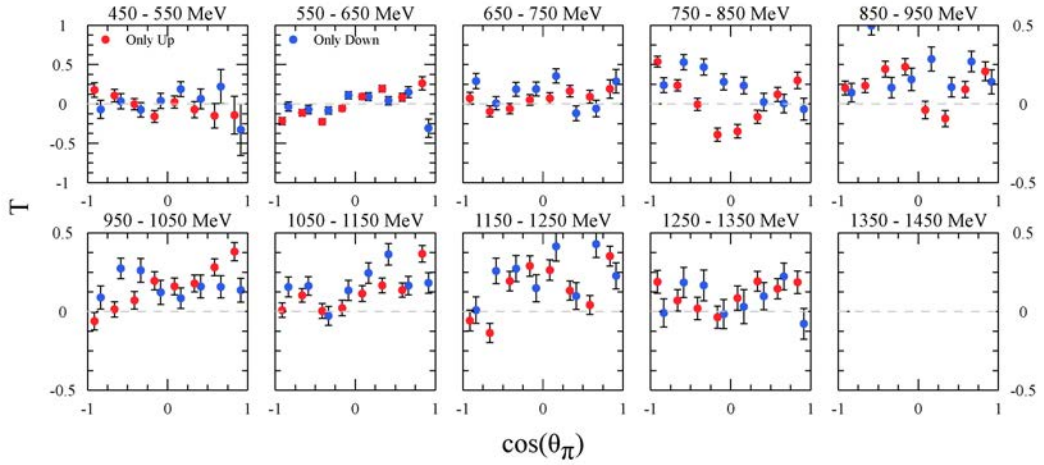

Figure A.41.: Results of the polarisation observable T in the representation of the $cos\theta_{\pi^0}$ angle of the double π^0 mesons as a function of the incident photon beam energy from 450 up to 1450 MeV. The results of the polarisation observable T for the butanol June 2010 data for the calculation over the nucleon target spin up and spin down is shown by the red points and blue points, respectively.

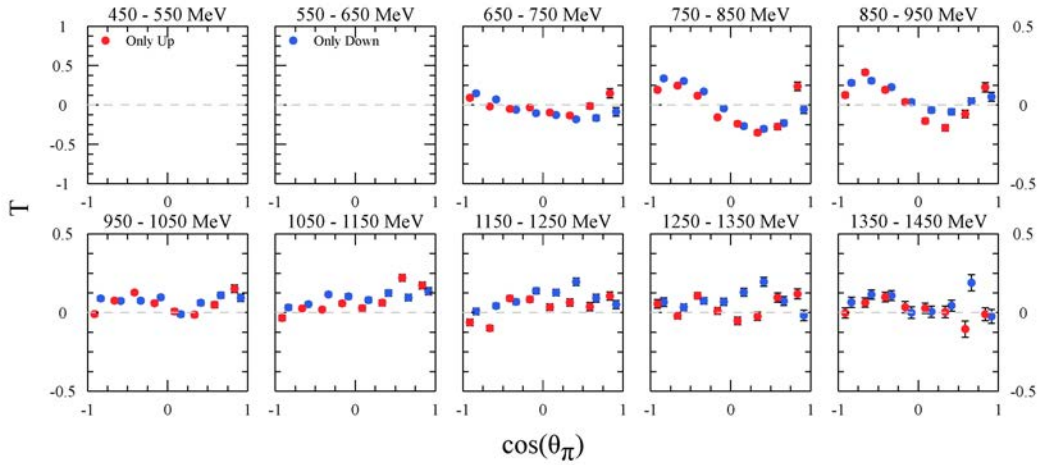

Figure A.42.: Incident beam energy $E_\gamma = 450 - 1450$ MeV dependent result of the polarisation observable T for the $cos\theta_{\pi^0}$ angle of the double π^0 mesons. The results of the polarisation observable T for the butanol April 2011 data for the calculation over the nucleon target spin up and spin down is shown by the red points and blue points, respectively.

A.6.2 Results of the Proton

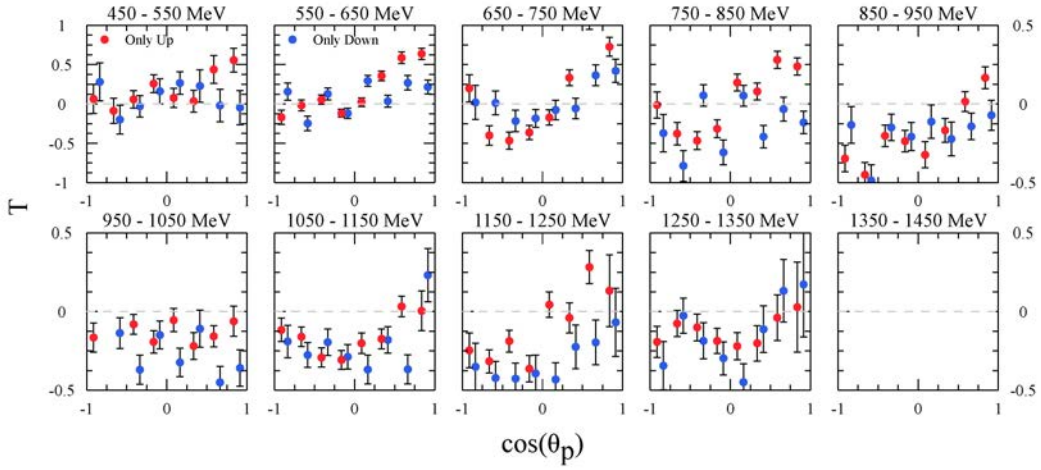

Figure A.43.: Results of the polarisation observable T for the $cos\theta_p$ angle of the recoil proton as a function of the incident photon beam energy from 450 up to 1450 MeV. The red and the blue points indicate the result of the polarisation observable T for the butanol June 2010 data calculated over the nucleon target spin up and spin down, respectively.

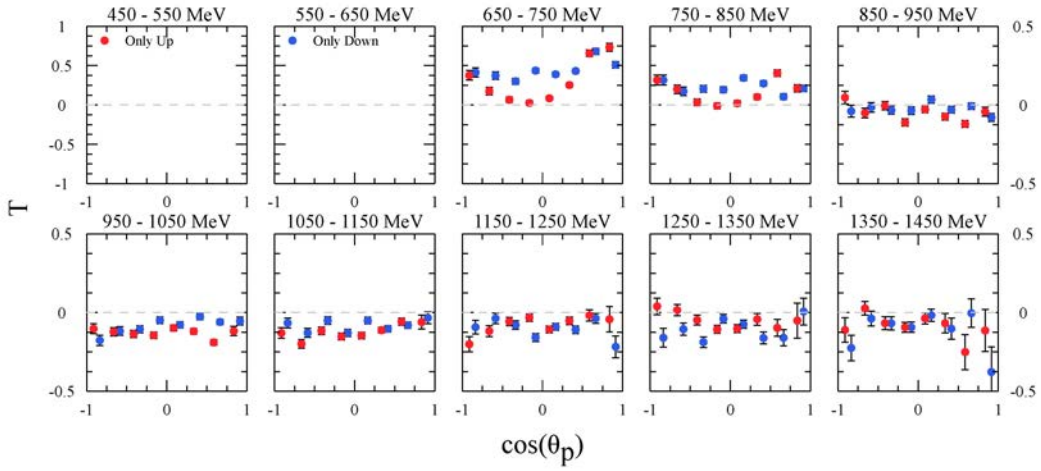

Figure A.44.: Incident beam energy $E_\gamma = 450 - 1450$ MeV dependent result of the polarisation observable T for the $cos\theta_p$ angle of the recoil proton. The red and the blue points indicate the result of the polarisation observable T for the butanol April 2011 calculated over the nucleon target spin up and spin down, respectively.

A.6.3 Results of the Invariant Mass of the Pions

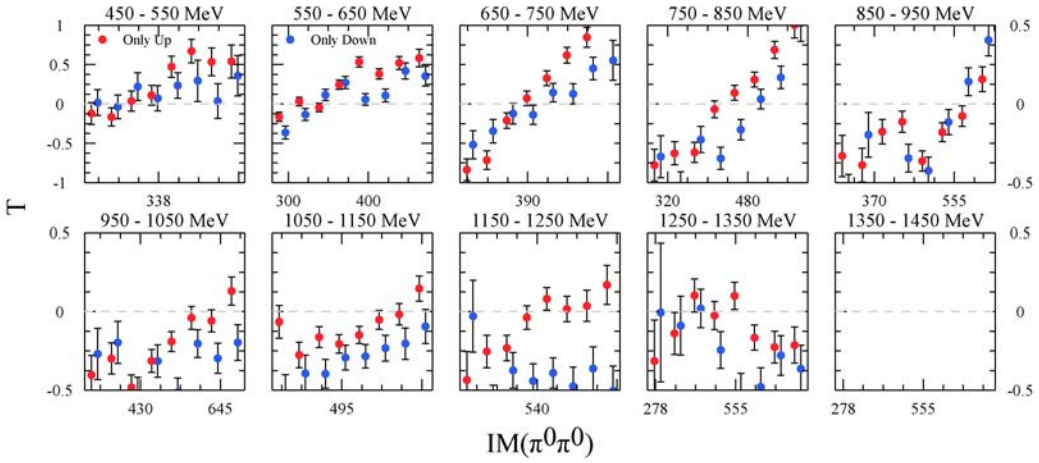

Figure A.45.: Results of the polarisation observable T in the representation of the invariant mass of the double π^0 mesons as a function of the incident photon beam energy from 450 up to 1450 MeV. The results of the polarisation observable T for the butanol June 2010 data for the calculation over the nucleon target spin up and spin down is shown by the red points and blue points, respectively.

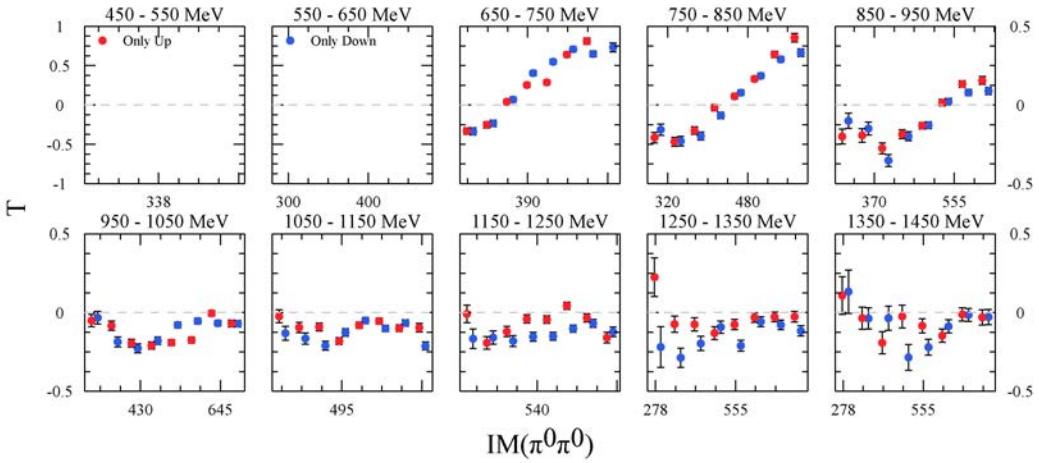

Figure A.46.: Incident beam energy $E_\gamma = 450 - 1450$ MeV dependent result of the polarisation observable T for the invariant mass of the double π^0 mesons. The results of the polarisation observable T for the butanol April 2011 data for the calculation over the nucleon target spin up and spin down is shown by the red points and blue points, respectively.

A.6.4 Results of the Invariant Mass of the Pions and the Proton

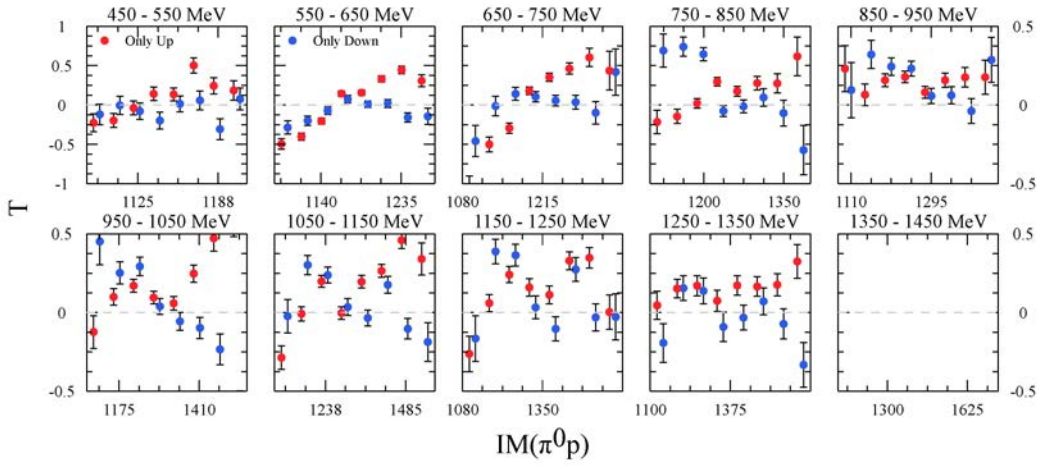

Figure A.47.: Results of the polarisation observable T for the invariant mass of each π^0 meson and the recoil proton as a function of the incident photon beam energy from 450 up to 1450 MeV. The red and the blue points indicate the result of the polarisation observable T for the butanol June 2010 data calculated over the nucleon target spin up and spin down, respectively.

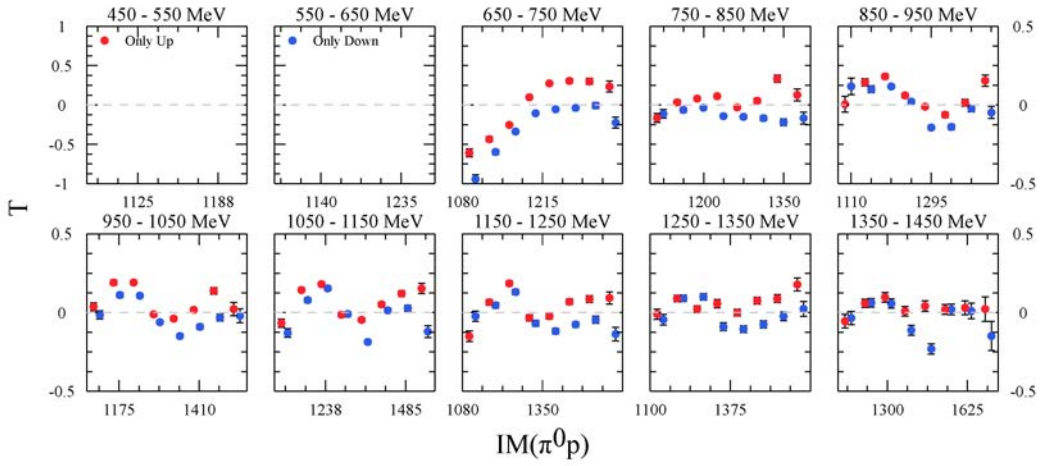

Figure A.48.: Incident beam energy $E_\gamma = 450 - 1450$ MeV dependent result of the polarisation observable T for the invariant mass of each π^0 meson and the recoil proton. The red and the blue points indicate the result of the polarisation observable T for the butanol April 2011 data calculated over the nucleon target spin up and spin down, respectively.

A.7 Check of other Asymmetry Contribution of the Polarisation Observable T

Since for the butanol data (June 2010 and April 2011) problems occur in the detector efficiency by angle dependent inconsistencies between the data and the simulation the T asymmetry was fitted with a cosine function instead of a sine function to determine the influence of the detector setup generated asymmetry contribution. For a correct detector efficiency correction the asymmetry of the detector setup should not contribute to the measurement of the polarisation observable T and the wrong fitted result should be zero for all energy representation of the $cos\theta_{\pi^0}$, $cos\theta_p$ angles of each π^0 mesons or recoil proton and for the invariant masses of the double π^0 mesons and the recoil proton. The presented results in this Section show that especially for the butanol June 2010 the asymmetry of the detector setup has a little contribution to the measured polarisation observable T results through the not identified problems with the PID detector.

A.7.1 Results of the Pions

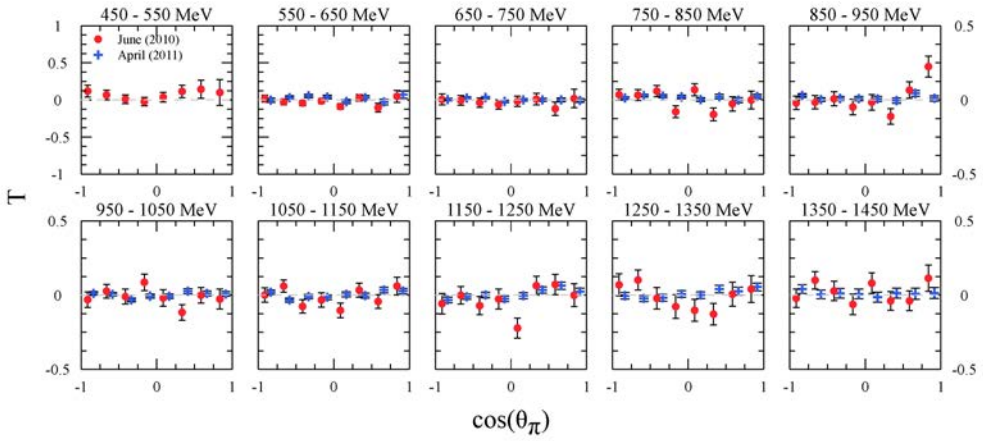

Figure A.49.: Result of polarisation observable T fitted with a cos function instead of the sine function for each π^0 meson in the representation of the $cos\theta_{\pi^0}$ angle as a function of the incident photon beam energy from 450 up to 1450 MeV. The results of the butanol data (June 2010 and April 2011) are shown by the red points and blue cross, respectively.

A.7.2 Results of the Proton

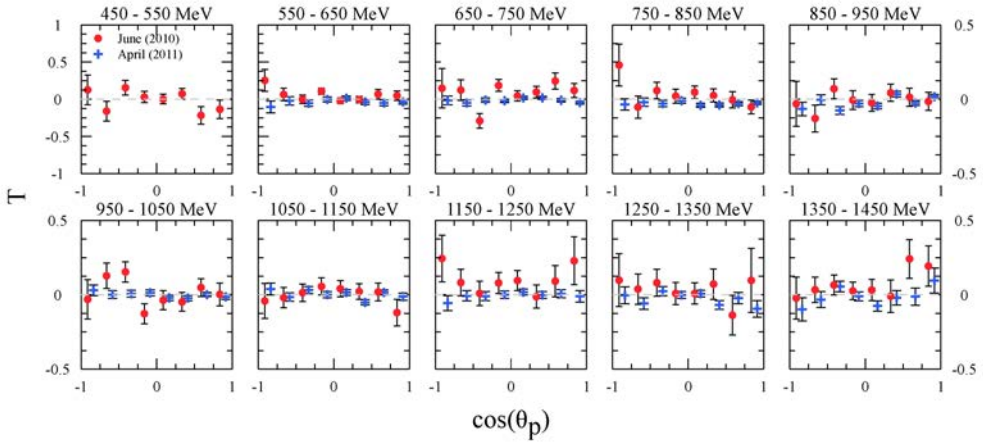

Figure A.50.: Incident photon beam energy $E_\gamma = 450 - 1450$ MeV result of the polarisation observable T fitted with a cosine function instead of the sin function for the recoil proton in the representation of the $cos\theta_p$ angle. The red points and the blue cross show the results of the butanol June 2010 and April 2011 data.

A.7.3 Results of the Invariant Mass of the Pions

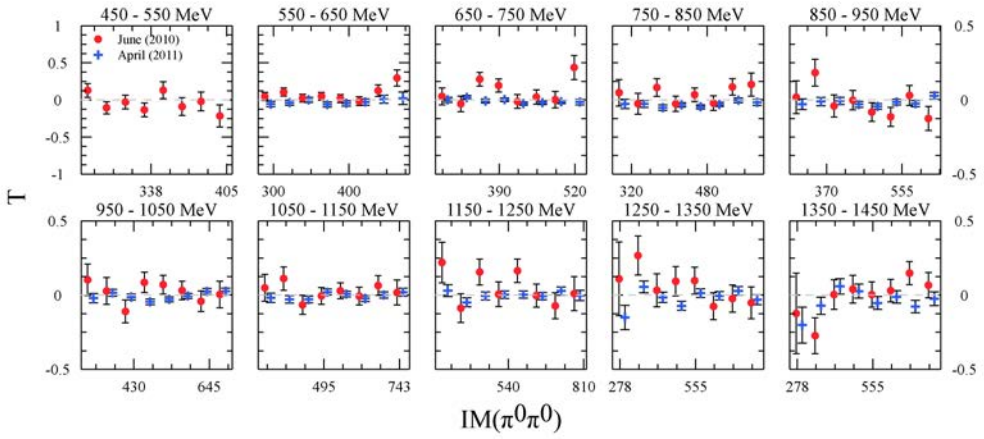

Figure A.51.: Results of the polarisation observable T fittet with a sine function instead of the sin function for the double π^0 mesons in the representation of the invariant mass as a function of the incident photon beam energy from 450 up to 1450 MeV. The results of the butanol June 2010 and April 2011 data are shown by the red points and blue cross, respectively.

A.7.4 Results of the Invariant Mass of the Pions and the Proton

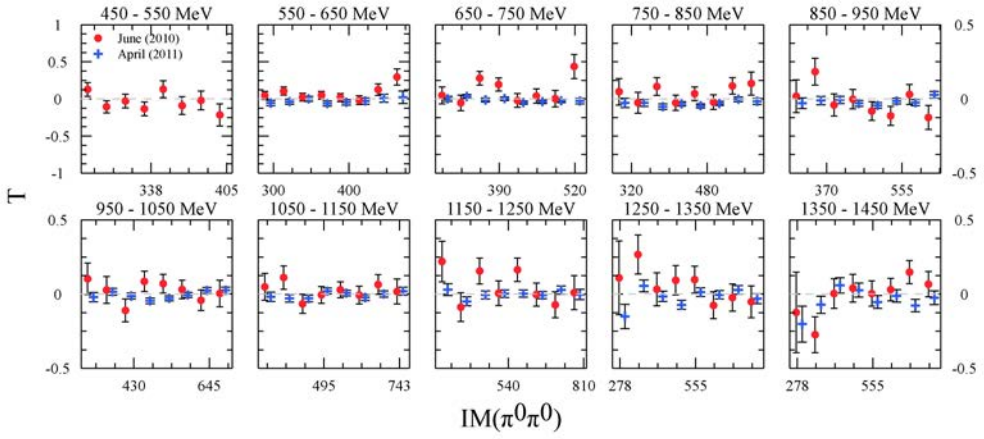

Figure A.52.: Incident photon beam energy $E_\gamma = 450 - 1450$ MeV result of the polarisation observable T fitted with a cosine function instead of the sin function for the recoil proton in the representation of the invariant mass of each π^0 meson and the recoil proton. The red points and the blue cross show the results of the butanol June 2010 and April 2011 data, respectively.

A.8 Data Tables

$E_\gamma[MeV]$	σ [μb]	Δ_{stat} [μb]	Δ_{sys} [μb]	$E_\gamma[MeV]$	σ [μb]	Δ_{stat} [μb]	Δ_{sys} [μb]
456.3	0.3993	0.0065	3.5058	950.0	7.2045	0.0176	0.2097
469.0	0.6250	0.0058	2.2274	962.7	7.4919	0.0184	0.2027
481.6	0.9291	0.0064	1.5051	975.3	7.7737	0.0193	0.1964
494.3	1.3031	0.0071	1.0783	988.0	8.0993	0.0232	0.1935
507.0	1.7834	0.0079	0.7928	1000.6	8.4511	0.0197	0.1812
519.6	2.3594	0.0097	0.6069	1013.3	8.7910	0.0199	0.1744
532.3	3.0095	0.0097	0.4757	1025.9	9.0776	0.0211	0.1703
544.9	3.5768	0.0102	0.4016	1038.6	9.2975	0.0217	0.1668
557.6	4.2194	0.0109	0.3420	1051.3	9.5358	0.0215	0.1625
570.3	4.8156	0.0125	0.3032	1063.9	9.6449	0.0225	0.1617
582.9	5.3781	0.0124	0.2712	1076.6	9.7453	0.0246	0.1622
595.6	5.9654	0.0138	0.2468	1089.2	9.8386	0.0226	0.1587
608.2	6.4735	0.0142	0.2281	1101.9	9.6738	0.0221	0.1609
620.9	6.9575	0.0151	0.2135	1114.6	9.5123	0.0227	0.1642
633.5	7.4712	0.0152	0.1990	1127.2	8.9950	0.0231	0.1740
646.2	7.8535	0.0158	0.1901	1139.9	8.5381	0.0228	0.1830
658.9	8.3753	0.0167	0.1793	1152.5	8.0874	0.0219	0.1922
671.5	8.8252	0.0163	0.1697	1165.2	7.8366	0.0214	0.1976
684.2	9.2764	0.0167	0.1619	1177.9	7.4165	0.0209	0.2082
696.8	9.7114	0.0172	0.1551	1190.5	7.0989	0.0208	0.2173
709.5	10.0816	0.0178	0.1500	1203.2	6.8389	0.0203	0.2249
722.2	9.9495	0.0203	0.1545	1215.8	6.6286	0.0204	0.2321
734.8	10.2562	0.0356	0.1648	1228.5	6.4087	0.0205	0.2402
747.5	10.0986	0.0198	0.1518	1241.1	5.9476	0.0214	0.2604
760.1	9.7659	0.0243	0.1616	1253.8	6.1372	0.0193	0.2488
772.8	8.9996	0.0335	0.1855	1266.5	5.9822	0.0208	0.2578
785.4	8.6138	0.0184	0.1763	1279.1	5.3387	0.0206	0.2886
798.1	8.0524	0.0174	0.1874	1291.8	5.8996	0.0213	0.2623
810.8	7.6411	0.0174	0.1975	1304.4	5.7876	0.0215	0.2678
823.4	7.3438	0.0264	0.2177	1317.1	5.7105	0.0193	0.2675
836.1	7.0237	0.0193	0.2175	1329.8	5.7508	0.0217	0.2698
848.7	6.8308	0.0182	0.2221	1342.4	5.1334	0.0211	0.3012
861.4	6.6465	0.0184	0.2285	1355.1	5.4598	0.0200	0.2811
874.1	6.5700	0.0211	0.2353	1367.7	5.7931	0.0215	0.2676
886.7	6.5911	0.0315	0.2503	1380.4	5.2238	0.0211	0.2959
899.4	6.5761	0.0168	0.2285	1393.0	5.3547	0.0223	0.2908
912.0	6.6797	0.0167	0.2248	1405.7	5.5162	0.0204	0.2790
924.7	6.8438	0.0171	0.2200	1418.4	5.2648	0.0228	0.2967
937.3	7.0018	0.0177	0.2159	1431.0	5.5986	0.0240	0.2812

H-Butanol April (2011)				H-Butanol June (2010)			
$E_\gamma[MeV]$	σ [μb]	Δ_{stat} [μb]	Δ_{sys} [μb]	$E_\gamma[MeV]$	σ [μb]	Δ_{stat} [μb]	Δ_{sys} [μb]
456.3	0.5374	0.1339	2.1831				
469.0	0.8180	0.1997	1.1342				
481.6	0.7452	0.0763	1.2884				
494.3	1.2502	0.0878	0.7869				
507.0	1.5991	0.0976	0.6493				
519.6	2.1317	0.1125	0.4784				
532.3	3.1883	0.1486	0.3031				
544.9	3.8866	0.1363	0.2473				
557.6	4.2248	0.1345	0.2478				
570.3	4.0005	0.2368	0.3273				
582.9	5.3748	0.1462	0.1925				
595.6	5.9905	0.1755	0.1756				
608.2	6.3025	0.2082	0.1723				
620.9	7.1626	0.1735	0.1463				
633.5	7.6194	0.1939	0.1358	633.5	6.4538	0.3158	0.2616
646.2	8.6054	0.1939	0.1183	646.2	7.6429	0.1896	0.2224
658.9	8.6386	0.1847	0.1217	658.9	8.2880	0.1967	0.2054
671.5	9.0818	0.1968	0.1142	671.5	8.3812	0.1860	0.2024
684.2	9.1332	0.1996	0.1166	684.2	8.5546	0.1796	0.2005
696.8	9.0627	0.2963	0.1264	696.8	9.5926	0.1802	0.1792
709.5	10.1623	0.3300	0.1024	709.5	9.5970	0.1862	0.1784
722.2	10.9909	0.3052	0.0928	722.2	10.0697	0.2219	0.1694
734.8	10.9525	0.2799	0.0909	734.8	10.3277	0.2330	0.1662
747.5	10.6102	0.2334	0.0989	747.5	9.5966	0.1616	0.1837
760.1	10.4780	0.2302	0.0956	760.1	9.2338	0.2090	0.1922
772.8	9.6456	0.2891	0.1085	772.8	8.8642	0.2391	0.1942
785.4	8.3578	0.2912	0.1401	785.4	8.3173	0.1526	0.2191
810.8	7.6844	0.2188	0.2877	798.1	8.2491	0.1751	0.2155
823.4	7.6393	0.1950	0.1474	810.8	7.4046	0.1477	0.2545
836.1	7.3849	0.2169	0.1355	823.4	7.3808	0.2246	0.2472
848.7	6.7162	0.2081	0.1569	836.1	6.7815	0.1516	0.2841
861.4	6.5335	0.2071	0.1765	848.7	6.3416	0.1499	0.3106
874.1	6.4587	0.2705	0.1789	861.4	6.2503	0.1536	0.3247
886.7	6.0611	0.3995	0.1765	874.1	6.4845	0.2030	0.3038
899.4	6.9266	0.2160	0.1959	886.7	6.3794	0.3448	0.3093
912.0	6.8668	0.2135	0.1685	899.4	6.4664	0.1464	0.3056
924.7	6.9491	0.2214	0.1720	912.0	6.7000	0.1473	0.2968
937.3	7.5636	0.2292	0.1718	924.7	6.4291	0.1518	0.3216
950.0	6.7134	0.3113	0.1561	937.3	6.8771	0.1581	0.2973
962.7	6.8868	0.3084	0.1823	950.0	6.4264	0.2441	0.3400
975.3	8.0425	0.3003	0.1820	962.7	7.4287	0.2224	0.2670
988.0	8.5719	0.2680	0.1460	975.3	7.6490	0.1963	0.2615
1000.6	8.3816	0.2974	0.1393	988.0	8.1285	0.1644	0.2472
1013.3	9.0085	0.2534	0.1503	1000.6	8.3980	0.1723	0.2389
1038.6	9.3048	0.3007	0.1258	1013.3	8.1253	0.1783	0.2608
1051.3	9.1817	0.4132	0.2688	1025.9	9.4182	0.1834	0.2133
1076.6	10.0326	0.2928	0.1239	1038.6	9.3021	0.1901	0.2187
1089.2	9.9643	0.2865	0.1360	1051.3	9.2593	0.2630	0.2200
1101.9	9.7096	0.2843	0.0972	1063.9	9.7479	0.2402	0.2084
1114.6	8.8248	0.2801	0.1051	1076.6	9.5674	0.3329	0.2198
1127.2	9.4544	0.3152	0.1161	1089.2	9.6607	0.2119	0.2145
1139.9	8.6046	0.2936	0.1178	1101.9	10.3409	0.1951	0.1921
1152.5	8.7160	0.3363	0.1374	1114.6	9.5747	0.2204	0.2166
1165.2	7.7170	0.2866	0.1269	1127.2	9.8404	0.2450	0.2093
1177.9	7.3209	0.2919	0.1376	1139.9	8.6912	0.2320	0.2454
1190.5	7.1876	0.2728	0.1364	1152.5	8.4059	0.2441	0.2574
1203.2	7.8203	0.3107	0.1594	1165.2	7.8530	0.2293	0.2848
1215.8	7.4114	0.3157	0.1728	1177.9	7.5460	0.2379	0.3042
1228.5	6.7862	0.3556	0.1764	1190.5	7.2141	0.2229	0.3226
1241.1	6.6144	0.3133	0.1591	1203.2	7.4748	0.2117	0.2949
1253.8	6.3690	0.2958	0.1724	1215.8	6.8603	0.2494	0.3431
1266.5	6.4279	0.2767	0.1818	1228.5	6.8894	0.2536	0.3330
1279.1	6.2825	0.2814	0.1858	1241.1	6.5203	0.2403	0.3715
1291.8	6.1443	0.3058	0.2029	1253.8	6.3929	0.2276	0.3692
1304.4	5.7139	0.2774	0.1930	1266.5	6.4891	0.2343	0.3647

550 - 650 MeV	Carbon			Hydrogen		
$cos(\theta_\pi)$	F	Δ_{stat} [μb]	Δ_{sys} [μb]	F	Δ_{stat} [μb]	Δ_{sys} [μb]
-0.9	0.1133	0.1188	-0.4698	0.1230	0.1284	-0.4672
-0.6	0.1513	0.0950	-0.4596	0.1723	0.1071	-0.4540
-0.4	0.1133	0.0883	-0.4698	0.1139	0.0941	-0.4696
-0.1	0.1162	0.0874	-0.4690	0.1079	0.0916	-0.4712
0.1	0.1745	0.0922	-0.4534	0.1923	0.0963	-0.4487
0.4	0.2590	0.1071	-0.4309	0.2440	0.1118	-0.4349
0.6	0.2691	0.1480	-0.4282	0.2331	0.1373	-0.4378
0.9	-0.3354	0.1965	-0.4105	-0.4204	0.2246	-0.3878

650 - 750 MeV	Carbon			Hydrogen		
$cos(\theta_\pi)$	F	Δ_{stat} [μb]	Δ_{sys} [μb]	F	Δ_{stat} [μb]	Δ_{sys} [μb]
-0.9	0.0595	0.0411	0.0159	0.0667	0.0469	0.0178
-0.6	0.1072	0.0368	0.0286	0.1222	0.0422	0.0326
-0.4	0.0799	0.0356	0.0213	0.0900	0.0400	0.0240
-0.1	0.0488	0.0357	0.0130	0.0571	0.0392	0.0152
0.1	0.0368	0.0389	0.0098	0.0395	0.0417	0.0106
0.4	-0.0527	0.0443	0.0141	-0.0557	0.0446	0.0149
0.6	-0.0921	0.0513	0.0246	-0.0991	0.0503	0.0264
0.9	-0.0522	0.0690	0.0139	-0.1072	0.0751	0.0286

750 - 850 MeV	Carbon			Hydrogen		
$cos(\theta_\pi)$	F	Δ_{stat} [μb]	Δ_{sys} [μb]	F	Δ_{stat} [μb]	Δ_{sys} [μb]
-0.9	-0.0873	0.0356	0.0233	-0.1049	0.0394	0.0280
-0.6	-0.0324	0.0360	0.0087	-0.0357	0.0381	0.0095
-0.4	0.0628	0.0368	0.0168	0.0689	0.0388	0.0184
-0.1	0.0046	0.0392	0.0012	0.0104	0.0421	0.0028
0.1	0.1549	0.0415	0.0413	0.1702	0.0443	0.0454
0.4	0.0741	0.0431	0.0198	0.0707	0.0435	0.0189
0.6	0.0068	0.0481	0.0018	-0.0099	0.0452	0.0027
0.9	-0.0719	0.0587	0.0192	-0.0546	0.0562	0.0146

850 - 950 MeV	Carbon			Hydrogen		
$cos(\theta_\pi)$	F	Δ_{stat} [μb]	Δ_{sys} [μb]	F	Δ_{stat} [μb]	Δ_{sys} [μb]
-0.9	-0.0194	0.0394	0.0052	-0.0279	0.0441	0.0075
-0.6	-0.0330	0.0400	0.0088	-0.0404	0.0417	0.0108
-0.4	-0.0233	0.0412	0.0062	-0.0189	0.0434	0.0051
-0.1	0.0871	0.0462	0.0233	0.0894	0.0452	0.0239
0.1	0.1765	0.0465	0.0471	0.1822	0.0503	0.0486
0.4	0.0971	0.0467	0.0259	0.0980	0.0472	0.0262
0.6	0.2361	0.0501	0.0630	0.2277	0.0454	0.0608
0.9	0.0376	0.0607	0.0100	0.0435	0.0574	0.0116

950 - 1050 MeV	Carbon			Hydrogen		
$cos(\theta_\pi)$	F	Δ_{stat} [μb]	Δ_{sys} [μb]	F	Δ_{stat} [μb]	Δ_{sys} [μb]
-0.9	-0.1607	0.0415	0.0429	-0.1571	0.0454	0.0419
-0.6	-0.1253	0.0366	0.0335	-0.1405	0.0400	0.0375
-0.4	-0.0222	0.0399	0.0059	-0.0283	0.0408	0.0075
-0.1	0.0573	0.0434	0.0153	0.0634	0.0442	0.0169
0.1	0.0714	0.0445	0.0191	0.0797	0.0431	0.0213
0.4	0.1216	0.0422	0.0325	0.1125	0.0420	0.0300
0.6	0.1643	0.0427	0.0439	0.1754	0.0452	0.0468
0.9	-0.0830	0.0526	0.0221	-0.0788	0.0496	0.0210

1050 - 1150 MeV	Carbon			Hydrogen		
$cos(\theta_\pi)$	F	Δ_{stat} [μb]	Δ_{sys} [μb]	F	Δ_{stat} [μb]	Δ_{sys} [μb]
-0.9	-0.0586	0.0354	0.0156	-0.0660	0.0397	0.0176
-0.6	-0.0700	0.0309	0.0187	-0.0704	0.0328	0.0188
-0.4	0.0129	0.0338	0.0034	0.0083	0.0334	0.0022
-0.1	0.0440	0.0361	0.0117	0.0424	0.0357	0.0113
0.1	-0.0229	0.0367	0.0061	-0.0213	0.0363	0.0057
0.4	0.0369	0.0362	0.0099	0.0376	0.0364	0.0100
0.6	0.0142	0.0354	0.0038	0.0158	0.0372	0.0042
0.9	0.0229	0.0435	0.0061	0.0243	0.0407	0.0065

1150 - 1250 MeV	Carbon			Hydrogen		
$cos(\theta_\pi)$	F	Δ_{stat} [μb]	Δ_{sys} [μb]	F	Δ_{stat} [μb]	Δ_{sys} [μb]
-0.9	-0.0025	0.0481	0.0007	-0.0013	0.0462	0.0004
-0.6	0.0468	0.0413	0.0125	0.0437	0.0394	0.0117
-0.4	0.0617	0.0427	0.0165	0.0745	0.0446	0.0199
-0.1	0.0049	0.0471	0.0013	0.0071	0.0476	0.0019
0.1	0.0081	0.0467	0.0022	0.0046	0.0463	0.0012
0.4	-0.0031	0.0443	0.0008	0.0057	0.0444	0.0015
0.6	-0.1048	0.0481	0.0280	-0.1244	0.0461	0.0332
0.9	-0.1048	0.0532	0.0280	-0.0940	0.0498	0.0251

1250 - 1350 MeV	Carbon			Hydrogen		
$cos(\theta_\pi)$	F	Δ_{stat} [μb]	Δ_{sys} [μb]	F	Δ_{stat} [μb]	Δ_{sys} [μb]
-0.9	0.0623	0.0500	0.0166	0.0813	0.0533	0.0217
-0.6	0.0721	0.0447	0.0193	0.0628	0.0452	0.0168
-0.4	0.1174	0.0485	0.0313	0.1128	0.0472	0.0301
-0.1	-0.0105	0.0530	0.0028	-0.0088	0.0472	0.0023
0.1	-0.1306	0.0495	0.0349	-0.1262	0.0531	0.0337
0.4	-0.1245	0.0494	0.0332	-0.1249	0.0459	0.0333
0.6	-0.1637	0.0545	0.0437	-0.1412	0.0472	0.0377
0.9	-0.1670	0.0600	0.0446	-0.1574	0.0544	0.0420

1350 - 1450 MeV	Carbon			Hydrogen		
$cos(\theta_\pi)$	F	Δ_{stat} [μb]	Δ_{sys} [μb]	F	Δ_{stat} [μb]	Δ_{sys} [μb]
-0.9	-0.0182	0.0375	0.0049	0.0351	0.1758	0.0094
-0.6	0.1100	0.0370	0.0294	0.2700	0.1569	0.0721
-0.4	0.0004	0.0408	0.0001	-0.0496	0.1602	0.0132
-0.1	-0.0230	0.0410	0.0061	0.2287	0.1646	0.0610
0.1	0.0417	0.0421	0.0111	0.0204	0.1528	0.0055
0.4	0.0210	0.0428	0.0056	0.0687	0.1529	0.0183
0.6	-0.0370	0.0471	0.0099	-0.0154	0.1618	0.0041
0.9	-0.0380	0.0471	0.0101	-0.1544	0.1579	0.0412

550 - 650 MeV	June (2010)			April (2011)		
$cos(\theta_\pi)$	F	Δ_{stat} [μb]	Δ_{sys} [μb]	F	Δ_{stat} [μb]	Δ_{sys} [μb]
-0.9	0.1230	0.1284	-0.4672			
-0.6	0.1723	0.1071	-0.4540			
-0.4	0.1139	0.0941	-0.4696			
-0.1	0.1079	0.0916	-0.4712			
0.1	0.1923	0.0963	-0.4487			
0.4	0.2440	0.1118	-0.4349			
0.6	0.2331	0.1373	-0.4378			
0.9	-0.4204	0.2246	-0.3878			

650 - 750 MeV	June (2010)			April (2011)		
$cos(\theta_\pi)$	F	Δ_{stat} [μb]	Δ_{sys} [μb]	F	Δ_{stat} [μb]	Δ_{sys} [μb]
-0.9	0.0937	0.0633	0.0250	0.0396	0.0201	0.0106
-0.6	0.1821	0.0572	0.0486	0.0624	0.0170	0.0166
-0.4	0.1240	0.0543	0.0331	0.0560	0.0160	0.0150
-0.1	0.0444	0.0529	0.0119	0.0698	0.0162	0.0186
0.1	0.0402	0.0564	0.0107	0.0389	0.0173	0.0104
0.4	-0.0613	0.0597	0.0164	-0.0502	0.0204	0.0134
0.6	-0.1451	0.0654	0.0387	-0.0531	0.0280	0.0142
0.9	-0.0419	0.0964	0.0112	-0.1726	0.0444	0.0461

750 - 850 MeV	June (2010)			April (2011)		
$cos(\theta_\pi)$	F	Δ_{stat} [μb]	Δ_{sys} [μb]	F	Δ_{stat} [μb]	Δ_{sys} [μb]
-0.9	-0.1271	0.0529	0.0339	-0.0828	0.0177	0.0221
-0.6	-0.0386	0.0512	0.0103	-0.0328	0.0170	0.0088
-0.4	0.1151	0.0521	0.0307	0.0227	0.0174	0.0060
-0.1	-0.0366	0.0568	0.0098	0.0573	0.0181	0.0153
0.1	0.2328	0.0597	0.0621	0.1075	0.0193	0.0287
0.4	0.1115	0.0581	0.0298	0.0299	0.0204	0.0080
0.6	0.0179	0.0591	0.0048	-0.0378	0.0245	0.0101
0.9	-0.1250	0.0711	0.0334	0.0157	0.0355	0.0042

850 - 950 MeV	June (2010)			April (2011)		
$cos(\theta_\pi)$	F	Δ_{stat} [μb]	Δ_{sys} [μb]	F	Δ_{stat} [μb]	Δ_{sys} [μb]
-0.9	0.0532	0.0590	0.0142	-0.1091	0.0201	0.0291
-0.6	0.0290	0.0563	0.0077	-0.1098	0.0178	0.0293
-0.4	-0.0318	0.0587	0.0085	-0.0060	0.0180	0.0016
-0.1	0.0636	0.0607	0.0170	0.1152	0.0203	0.0307
0.1	0.1983	0.0681	0.0529	0.1661	0.0206	0.0443
0.4	0.0197	0.0626	0.0053	0.1763	0.0235	0.0471
0.6	0.2878	0.0587	0.0768	0.1676	0.0259	0.0447
0.9	-0.0004	0.0737	0.0001	0.0873	0.0341	0.0233

950 - 1050 MeV	June (2010)			April (2011)		
$cos(\theta_\pi)$	F	Δ_{stat} [μb]	Δ_{sys} [μb]	F	Δ_{stat} [μb]	Δ_{sys} [μb]
-0.9	-0.1544	0.0622	0.0412	-0.1597	0.0162	0.0426
-0.6	-0.1839	0.0549	0.0491	-0.0971	0.0133	0.0259
-0.4	-0.0481	0.0561	0.0128	-0.0085	0.0139	0.0023
-0.1	0.0831	0.0605	0.0222	0.0438	0.0158	0.0117
0.1	0.0415	0.0581	0.0111	0.1180	0.0183	0.0315
0.4	0.1068	0.0563	0.0285	0.1183	0.0189	0.0316
0.6	0.2323	0.0604	0.0620	0.1184	0.0209	0.0316
0.9	-0.1600	0.0661	0.0427	0.0025	0.0237	0.0007

1050 - 1150 MeV	June (2010)			April (2011)		
$cos(\theta_\pi)$	F	Δ_{stat} [μb]	Δ_{sys} [μb]	F	Δ_{stat} [μb]	Δ_{sys} [μb]
-0.9	0.0103	0.0532	0.0028	-0.1424	0.0181	0.0380
-0.6	-0.0925	0.0444	0.0247	-0.0483	0.0134	0.0129
-0.4	0.0055	0.0453	0.0015	0.0111	0.0136	0.0030
-0.1	0.0273	0.0481	0.0073	0.0575	0.0151	0.0154
0.1	-0.1038	0.0485	0.0277	0.0612	0.0169	0.0163
0.4	0.0460	0.0475	0.0123	0.0292	0.0200	0.0078
0.6	0.0242	0.0480	0.0065	0.0074	0.0213	0.0020
0.9	0.0538	0.0529	0.0144	-0.0051	0.0226	0.0014

1150 - 1250 MeV	June (2010)			April (2011)		
$cos(\theta_\pi)$	F	Δ_{stat} [μb]	Δ_{sys} [μb]	F	Δ_{stat} [μb]	Δ_{sys} [μb]
-0.9	-0.0095	0.0623	0.0025	0.0068	0.0199	0.0018
-0.6	0.0733	0.0537	0.0196	0.0141	0.0151	0.0038
-0.4	0.0939	0.0610	0.0251	0.0550	0.0162	0.0147
-0.1	-0.0441	0.0649	0.0118	0.0584	0.0175	0.0156
0.1	0.0298	0.0626	0.0080	-0.0205	0.0192	0.0055
0.4	-0.0071	0.0592	0.0019	0.0186	0.0211	0.0050
0.6	-0.1870	0.0609	0.0499	-0.0618	0.0231	0.0165
0.9	-0.1834	0.0661	0.0490	-0.0047	0.0246	0.0013

1250 - 1350 MeV	June (2010)			April (2011)		
$cos(\theta_\pi)$	F	Δ_{stat} [μb]	Δ_{sys} [μb]	F	Δ_{stat} [μb]	Δ_{sys} [μb]
-0.9	0.0479	0.0715	0.0128	0.1148	0.0240	0.0306
-0.6	0.0580	0.0611	0.0155	0.0676	0.0185	0.0180
-0.4	0.1872	0.0641	0.0500	0.0384	0.0185	0.0102
-0.1	-0.0348	0.0632	0.0093	0.0173	0.0214	0.0046
0.1	-0.2131	0.0714	0.0569	-0.0393	0.0233	0.0105
0.4	-0.1711	0.0599	0.0457	-0.0788	0.0251	0.0210
0.6	-0.2404	0.0607	0.0642	-0.0419	0.0276	0.0112
0.9	-0.2933	0.0710	0.0783	-0.0215	0.0298	0.0057

1350 - 1450 MeV	June (2010)			April (2011)		
$cos(\theta_\pi)$	F	Δ_{stat} [μb]	Δ_{sys} [μb]	F	Δ_{stat} [μb]	Δ_{sys} [μb]
-0.9				-0.0202	0.0305	0.0054
-0.6				0.1075	0.0257	0.0287
-0.4				0.0022	0.0238	0.0006
-0.1				-0.0185	0.0280	0.0049
0.1				0.0431	0.0283	0.0115
0.4				0.0318	0.0325	0.0085
0.6				-0.0583	0.0435	0.0156
0.9				-0.0397	0.0359	0.0106

550 - 650 MeV	June (2010)			April (2011)		
$cos(\theta_\pi)$	F	Δ_{stat} [μb]	Δ_{sys} [μb]	F	Δ_{stat} [μb]	Δ_{sys} [μb]
-0.9	0.1133	0.1188	-0.4698			
-0.6	0.1513	0.0950	-0.4596			
-0.4	0.1133	0.0883	-0.4698			
-0.1	0.1162	0.0874	-0.4690			
0.1	0.1745	0.0922	-0.4534			
0.4	0.2590	0.1071	-0.4309			
0.6	0.2691	0.1480	-0.4282			
0.9	-0.3354	0.1965	-0.4105			

650 - 750 MeV	June (2010)			April (2011)		
$cos(\theta_\pi)$	F	Δ_{stat} [μb]	Δ_{sys} [μb]	F	Δ_{stat} [μb]	Δ_{sys} [μb]
-0.9	0.0928	0.0566	0.0248	0.0263	0.0128	0.0070
-0.6	0.1706	0.0506	0.0455	0.0438	0.0120	0.0117
-0.4	0.1159	0.0488	0.0309	0.0440	0.0122	0.0117
-0.1	0.0426	0.0489	0.0114	0.0550	0.0128	0.0147
0.1	0.0433	0.0531	0.0116	0.0303	0.0141	0.0081
0.4	-0.0630	0.0604	0.0168	-0.0423	0.0166	0.0113
0.6	-0.1455	0.0700	0.0388	-0.0386	0.0193	0.0103
0.9	-0.0280	0.0955	0.0075	-0.0764	0.0201	0.0204

750 - 850 MeV	June (2010)			April (2011)		
$cos(\theta_\pi)$	F	Δ_{stat} [μb]	Δ_{sys} [μb]	F	Δ_{stat} [μb]	Δ_{sys} [μb]
-0.9	-0.1168	0.0487	0.0312	-0.0577	0.0126	0.0154
-0.6	-0.0394	0.0491	0.0105	-0.0255	0.0132	0.0068
-0.4	0.1051	0.0500	0.0280	0.0206	0.0143	0.0055
-0.1	-0.0409	0.0531	0.0109	0.0502	0.0158	0.0134
0.1	0.2117	0.0560	0.0565	0.0981	0.0175	0.0262
0.4	0.1189	0.0574	0.0317	0.0294	0.0204	0.0078
0.6	0.0504	0.0641	0.0135	-0.0368	0.0227	0.0098
0.9	-0.1491	0.0807	0.0398	0.0052	0.0196	0.0014

850 - 950 MeV	June (2010)			April (2011)		
$cos(\theta_\pi)$	F	Δ_{stat} [μb]	Δ_{sys} [μb]	F	Δ_{stat} [μb]	Δ_{sys} [μb]
-0.9	0.0418	0.0537	0.0112	-0.0806	0.0146	0.0215
-0.6	0.0284	0.0545	0.0076	-0.0944	0.0153	0.0252
-0.4	-0.0395	0.0557	0.0105	-0.0071	0.0171	0.0019
-0.1	0.0661	0.0627	0.0176	0.1081	0.0185	0.0289
0.1	0.1914	0.0627	0.0511	0.1615	0.0199	0.0431
0.4	0.0231	0.0623	0.0062	0.1711	0.0222	0.0457
0.6	0.3211	0.0666	0.0857	0.1511	0.0241	0.0403
0.9	0.0166	0.0831	0.0044	0.0586	0.0213	0.0156

950 - 1050 MeV	June (2010)			April (2011)		
$cos(\theta_\pi)$	F	Δ_{stat} [μb]	Δ_{sys} [μb]	F	Δ_{stat} [μb]	Δ_{sys} [μb]
-0.9	-0.1876	0.0572	0.0501	-0.1338	0.0134	0.0357
-0.6	-0.1571	0.0502	0.0419	-0.0936	0.0128	0.0250
-0.4	-0.0349	0.0546	0.0093	-0.0094	0.0141	0.0025
-0.1	0.0719	0.0595	0.0192	0.0426	0.0152	0.0114
0.1	0.0402	0.0609	0.0107	0.1027	0.0160	0.0274
0.4	0.1244	0.0569	0.0332	0.1189	0.0181	0.0317
0.6	0.2163	0.0573	0.0577	0.1123	0.0189	0.0300
0.9	-0.1652	0.0726	0.0441	-0.0007	0.0165	0.0002

1050 - 1150 MeV	June (2010)			April (2011)		
$cos(\theta_\pi)$	F	Δ_{stat} [μb]	Δ_{sys} [μb]	F	Δ_{stat} [μb]	Δ_{sys} [μb]
-0.9	0.0028	0.0478	0.0008	-0.1201	0.0146	0.0320
-0.6	-0.0905	0.0416	0.0242	-0.0494	0.0136	0.0132
-0.4	0.0148	0.0455	0.0040	0.0110	0.0146	0.0029
-0.1	0.0305	0.0487	0.0081	0.0575	0.0154	0.0153
0.1	-0.1033	0.0493	0.0276	0.0575	0.0163	0.0153
0.4	0.0484	0.0481	0.0129	0.0255	0.0176	0.0068
0.6	0.0238	0.0464	0.0063	0.0047	0.0189	0.0012
0.9	0.0515	0.0589	0.0138	-0.0057	0.0175	0.0015

1150 - 1250 MeV	June (2010)			April (2011)		
$cos(\theta_\pi)$	F	Δ_{stat} [μb]	Δ_{sys} [μb]	F	Δ_{stat} [μb]	Δ_{sys} [μb]
-0.9	-0.0100	0.0656	0.0027	0.0050	0.0181	0.0013
-0.6	0.0769	0.0560	0.0205	0.0167	0.0167	0.0044
-0.4	0.0608	0.0577	0.0162	0.0626	0.0177	0.0167
-0.1	-0.0511	0.0640	0.0136	0.0609	0.0181	0.0163
0.1	0.0330	0.0634	0.0088	-0.0169	0.0188	0.0045
0.4	-0.0212	0.0594	0.0056	0.0149	0.0200	0.0040
0.6	-0.1563	0.0642	0.0417	-0.0534	0.0224	0.0142
0.9	-0.2002	0.0723	0.0535	-0.0093	0.0209	0.0025

1250 - 1350 MeV	June (2010)			April (2011)		
$cos(\theta_\pi)$	F	Δ_{stat} [μb]	Δ_{sys} [μb]	F	Δ_{stat} [μb]	Δ_{sys} [μb]
-0.9	0.0275	0.0679	0.0073	0.0971	0.0199	0.0259
-0.6	0.0729	0.0604	0.0195	0.0714	0.0184	0.0191
-0.4	0.1931	0.0655	0.0515	0.0418	0.0203	0.0112
-0.1	-0.0396	0.0719	0.0106	0.0185	0.0208	0.0049
0.1	-0.2245	0.0670	0.0599	-0.0368	0.0204	0.0098
0.4	-0.1730	0.0661	0.0462	-0.0759	0.0228	0.0203
0.6	-0.2805	0.0728	0.0749	-0.0470	0.0250	0.0125
0.9	-0.3267	0.0816	0.0872	-0.0073	0.0233	0.0020

1350 - 1450 MeV	June (2010)			April (2011)		
$cos(\theta_\pi)$	F	Δ_{stat} [μb]	Δ_{sys} [μb]	F	Δ_{stat} [μb]	Δ_{sys} [μb]
-0.9				-0.0182	0.0265	0.0049
-0.6				0.1100	0.0262	0.0294
-0.4				0.0004	0.0288	0.0001
-0.1				-0.0230	0.0290	0.0061
0.1				0.0417	0.0298	0.0111
0.4				0.0210	0.0302	0.0056
0.6				-0.0370	0.0333	0.0099
0.9				-0.0380	0.0333	0.0101

550 - 650 MeV	Carbon			Hydrogen		
$cos(\theta_p)$	F	Δ_{stat} [μb]	Δ_{sys} [μb]	F	Δ_{stat} [μb]	Δ_{sys} [μb]
-0.9	0.4596	0.3640	-0.3773	0.2620	0.2232	-0.4301
-0.6	0.0486	0.2049	-0.4870	0.0686	0.1770	-0.4817
-0.4	-0.2115	0.1369	-0.4435	-0.2064	0.1528	-0.4449
-0.1	-0.1696	0.1050	-0.4547	-0.2201	0.1312	-0.4413
0.1	-0.1066	0.0951	-0.4716	-0.1272	0.1310	-0.4661
0.4	-0.2496	0.1090	-0.4334	-0.3380	0.1391	-0.4098
0.6	0.0953	0.1634	-0.4745	0.1282	0.1794	-0.4658
0.9	0.0136	0.1522	-0.4964	-0.0514	0.1640	-0.4863

650 - 750 MeV	Carbon			Hydrogen		
$cos(\theta_p)$	F	Δ_{stat} [μb]	Δ_{sys} [μb]	F	Δ_{stat} [μb]	Δ_{sys} [μb]
-0.9	0.2373	0.1467	0.0633	0.2001	0.1029	0.0534
-0.6	0.0372	0.0787	0.0099	0.0500	0.0723	0.0134
-0.4	-0.0373	0.0564	0.0100	-0.0446	0.0664	0.0119
-0.1	0.0377	0.0452	0.0101	0.0469	0.0518	0.0125
0.1	-0.1122	0.0387	0.0299	-0.1488	0.0534	0.0397
0.4	-0.0845	0.0435	0.0226	-0.1022	0.0587	0.0273
0.6	-0.1099	0.0605	0.0293	-0.1679	0.0651	0.0448
0.9	-0.0783	0.0517	0.0209	-0.0824	0.0613	0.0220

750 - 850 MeV	Carbon			Hydrogen		
$cos(\theta_p)$	F	Δ_{stat} [μb]	Δ_{sys} [μb]	F	Δ_{stat} [μb]	Δ_{sys} [μb]
-0.9	-0.2378	0.1376	0.0635	-0.1730	0.0901	0.0462
-0.6	-0.0702	0.0755	0.0187	-0.0716	0.0718	0.0191
-0.4	-0.0080	0.0557	0.0021	-0.0014	0.0610	0.0004
-0.1	-0.0269	0.0470	0.0072	-0.0466	0.0554	0.0124
0.1	-0.0008	0.0418	0.0002	0.0084	0.0548	0.0022
0.4	-0.1247	0.0440	0.0333	-0.1653	0.0558	0.0441
0.6	-0.2203	0.0530	0.0588	-0.2653	0.0592	0.0708
0.9	-0.1824	0.0454	0.0487	-0.2343	0.0499	0.0625

850 - 950 MeV	Carbon			Hydrogen		
$cos(\theta_p)$	F	Δ_{stat} [μb]	Δ_{sys} [μb]	F	Δ_{stat} [μb]	Δ_{sys} [μb]
-0.9	-0.1960	0.1320	0.0523	-0.1510	0.0909	0.0403
-0.6	-0.0742	0.0813	0.0198	-0.0576	0.0672	0.0154
-0.4	-0.2434	0.0609	0.0650	-0.2318	0.0624	0.0619
-0.1	-0.0340	0.0564	0.0091	0.0011	0.0587	0.0003
0.1	0.0023	0.0500	0.0006	-0.0052	0.0750	0.0014
0.4	-0.0910	0.0511	0.0243	-0.1103	0.0634	0.0294
0.6	-0.2555	0.0527	0.0682	-0.2947	0.0584	0.0787
0.9	-0.2249	0.0529	0.0600	-0.2584	0.0574	0.0690

950 - 1050 MeV	Carbon			Hydrogen		
$cos(\theta_p)$	F	Δ_{stat} [μb]	Δ_{sys} [μb]	F	Δ_{stat} [μb]	Δ_{sys} [μb]
-0.9	-0.1085	0.1049	0.0290	-0.1128	0.0776	0.0301
-0.6	-0.0283	0.0677	0.0076	-0.0178	0.0579	0.0047
-0.4	-0.0022	0.0549	0.0006	-0.0037	0.0600	0.0010
-0.1	-0.0398	0.0538	0.0106	-0.0484	0.0563	0.0129
0.1	-0.0222	0.0512	0.0059	-0.0173	0.0609	0.0046
0.4	-0.0560	0.0502	0.0149	-0.0737	0.0655	0.0197
0.6	0.0362	0.0468	0.0097	0.0243	0.0558	0.0065
0.9	0.0274	0.0600	0.0073	0.0128	0.0685	0.0034

1050 - 1150 MeV	Carbon			Hydrogen		
$cos(\theta_p)$	F	Δ_{stat} [μb]	Δ_{sys} [μb]	F	Δ_{stat} [μb]	Δ_{sys} [μb]
-0.9	0.0128	0.0876	0.0034	0.0101	0.0600	0.0027
-0.6	-0.0357	0.0526	0.0095	-0.0312	0.0480	0.0083
-0.4	0.0412	0.0453	0.0110	0.0380	0.0478	0.0101
-0.1	-0.0610	0.0434	0.0163	-0.0524	0.0427	0.0140
0.1	-0.0813	0.0412	0.0217	-0.0878	0.0511	0.0234
0.4	0.0155	0.0392	0.0041	0.0217	0.0479	0.0058
0.6	0.0516	0.0440	0.0138	0.0601	0.0481	0.0160
0.9	-0.0110	0.0656	0.0029	-0.0126	0.0757	0.0034

1150 - 1250 MeV	Carbon			Hydrogen		
$cos(\theta_p)$	F	Δ_{stat} [μb]	Δ_{sys} [μb]	F	Δ_{stat} [μb]	Δ_{sys} [μb]
-0.9	-0.0673	0.1108	0.0180	-0.0337	0.0770	0.0090
-0.6	0.0580	0.0636	0.0155	0.0719	0.0601	0.0192
-0.4	0.1135	0.0583	0.0303	0.1000	0.0555	0.0267
-0.1	-0.0708	0.0501	0.0189	-0.0688	0.0562	0.0184
0.1	-0.0802	0.0466	0.0214	-0.0840	0.0509	0.0224
0.4	0.0159	0.0543	0.0042	0.0382	0.0611	0.0102
0.6	-0.0329	0.0729	0.0088	-0.0431	0.0706	0.0115
0.9	0.1309	0.1107	0.0349	0.1242	0.1288	0.0331

1250 - 1350 MeV	Carbon			Hydrogen		
$cos(\theta_p)$	F	Δ_{stat} [μb]	Δ_{sys} [μb]	F	Δ_{stat} [μb]	Δ_{sys} [μb]
-0.9	0.2585	0.1197	0.0690	0.1480	0.0838	0.0395
-0.6	0.0822	0.0700	0.0219	0.0758	0.0602	0.0202
-0.4	0.1101	0.0612	0.0294	0.0817	0.0531	0.0218
-0.1	-0.0393	0.0505	0.0105	-0.0377	0.0555	0.0101
0.1	-0.0564	0.0479	0.0150	-0.0743	0.0586	0.0198
0.4	0.1265	0.0683	0.0338	0.1448	0.0804	0.0386
0.6	0.0571	0.0890	0.0152	0.0468	0.0898	0.0125
0.9	-0.0446	0.1431	0.0119	-0.0834	0.1555	0.0223

1350 - 1450 MeV	Carbon			Hydrogen		
$cos(\theta_p)$	F	Δ_{stat} [μb]	Δ_{sys} [μb]	F	Δ_{stat} [μb]	Δ_{sys} [μb]
-0.9	-0.0841	0.0963	0.0225	0.1372	0.2668	0.0366
-0.6	-0.0188	0.0674	0.0050	-0.1897	0.1959	0.0506
-0.4	-0.0679	0.0449	0.0181	-0.1652	0.1767	0.0441
-0.1	-0.0852	0.0379	0.0228	-0.2837	0.1601	0.0757
0.1	-0.0430	0.0429	0.0115	0.0535	0.2005	0.0143
0.4	-0.1012	0.0608	0.0270	-0.3057	0.2919	0.0816
0.6	0.0323	0.0723	0.0086	0.3023	0.3407	0.0807
0.9	0.0791	0.1050	0.0211	0.3414	0.5261	0.0911

550 - 650 MeV	June (2010)			April (2011)		
$cos(\theta_p)$	F	Δ_{stat} [μb]	Δ_{sys} [μb]	F	Δ_{stat} [μb]	Δ_{sys} [μb]
-0.9	0.2620	0.2232	-0.4301			
-0.6	0.0686	0.1770	-0.4817			
-0.4	-0.2064	0.1528	-0.4449			
-0.1	-0.2201	0.1312	-0.4413			
0.1	-0.1272	0.1310	-0.4661			
0.4	-0.3380	0.1391	-0.4098			
0.6	0.1282	0.1794	-0.4658			
0.9	-0.0514	0.1640	-0.4863			

650 - 750 MeV	June (2010)			April (2011)		
$cos(\theta_p)$	F	Δ_{stat} [μb]	Δ_{sys} [μb]	F	Δ_{stat} [μb]	Δ_{sys} [μb]
-0.9	0.2848	0.1378	0.0760	0.1154	0.0466	0.0308
-0.6	0.0369	0.0949	0.0098	0.0632	0.0379	0.0169
-0.4	-0.1095	0.0890	0.0292	0.0203	0.0301	0.0054
-0.1	0.0691	0.0692	0.0184	0.0248	0.0239	0.0066
0.1	-0.2138	0.0727	0.0571	-0.0837	0.0204	0.0223
0.4	-0.1310	0.0802	0.0350	-0.0734	0.0218	0.0196
0.6	-0.1865	0.0869	0.0498	-0.1493	0.0303	0.0398
0.9	-0.1772	0.0808	0.0473	0.0124	0.0314	0.0033

750 - 850 MeV	June (2010)			April (2011)		
$cos(\theta_p)$	F	Δ_{stat} [μb]	Δ_{sys} [μb]	F	Δ_{stat} [μb]	Δ_{sys} [μb]
-0.9	-0.2100	0.1183	0.0561	-0.1359	0.0472	0.0363
-0.6	-0.1634	0.0935	0.0436	0.0203	0.0394	0.0054
-0.4	-0.0179	0.0806	0.0048	0.0150	0.0306	0.0040
-0.1	-0.0966	0.0740	0.0258	0.0035	0.0254	0.0009
0.1	0.0703	0.0741	0.0188	-0.0535	0.0226	0.0143
0.4	-0.2318	0.0753	0.0619	-0.0987	0.0235	0.0264
0.6	-0.3403	0.0790	0.0908	-0.1903	0.0276	0.0508
0.9	-0.2822	0.0654	0.0753	-0.1864	0.0264	0.0498

850 - 950 MeV	June (2010)			April (2011)		
$cos(\theta_p)$	F	Δ_{stat} [μb]	Δ_{sys} [μb]	F	Δ_{stat} [μb]	Δ_{sys} [μb]
-0.9	-0.1030	0.1172	0.0275	-0.1991	0.0528	0.0531
-0.6	-0.0718	0.0878	0.0192	-0.0433	0.0364	0.0116
-0.4	-0.3338	0.0826	0.0891	-0.1298	0.0309	0.0347
-0.1	0.0229	0.0777	0.0061	-0.0206	0.0292	0.0055
0.1	0.0721	0.1027	0.0193	-0.0826	0.0266	0.0220
0.4	-0.1211	0.0859	0.0323	-0.0994	0.0255	0.0265
0.6	-0.3612	0.0784	0.0964	-0.2281	0.0259	0.0609
0.9	-0.4014	0.0763	0.1071	-0.1155	0.0276	0.0308

950 - 1050 MeV	June (2010)			April (2011)		
$cos(\theta_p)$	F	Δ_{stat} [μb]	Δ_{sys} [μb]	F	Δ_{stat} [μb]	Δ_{sys} [μb]
-0.9	-0.1569	0.1038	0.0419	-0.0687	0.0357	0.0183
-0.6	0.0020	0.0767	0.0005	-0.0375	0.0287	0.0100
-0.4	0.0243	0.0812	0.0065	-0.0318	0.0248	0.0085
-0.1	-0.1163	0.0763	0.0310	0.0194	0.0225	0.0052
0.1	0.0846	0.0835	0.0226	-0.1191	0.0211	0.0318
0.4	-0.0762	0.0905	0.0203	-0.0713	0.0198	0.0190
0.6	0.0675	0.0767	0.0180	-0.0189	0.0187	0.0050
0.9	0.0198	0.0936	0.0053	0.0058	0.0253	0.0015

1050 - 1150 MeV	June (2010)			April (2011)		
$cos(\theta_p)$	F	Δ_{stat} [μb]	Δ_{sys} [μb]	F	Δ_{stat} [μb]	Δ_{sys} [μb]
-0.9	0.0263	0.0777	0.0070	-0.0060	0.0342	0.0016
-0.6	-0.0028	0.0621	0.0008	-0.0595	0.0273	0.0159
-0.4	0.1026	0.0633	0.0274	-0.0267	0.0235	0.0071
-0.1	-0.0554	0.0565	0.0148	-0.0493	0.0214	0.0132
0.1	-0.1298	0.0696	0.0346	-0.0459	0.0196	0.0122
0.4	0.0634	0.0650	0.0169	-0.0200	0.0190	0.0053
0.6	0.0200	0.0647	0.0053	0.1002	0.0210	0.0267
0.9	-0.0977	0.1017	0.0261	0.0726	0.0335	0.0194

1150 - 1250 MeV	June (2010)			April (2011)		
$cos(\theta_p)$	F	Δ_{stat} [μb]	Δ_{sys} [μb]	F	Δ_{stat} [μb]	Δ_{sys} [μb]
-0.9	-0.0186	0.1011	0.0050	-0.0487	0.0405	0.0130
-0.6	0.1481	0.0800	0.0395	-0.0043	0.0288	0.0011
-0.4	0.1893	0.0741	0.0505	0.0108	0.0260	0.0029
-0.1	-0.0689	0.0765	0.0184	-0.0687	0.0216	0.0183
0.1	-0.0828	0.0691	0.0221	-0.0851	0.0204	0.0227
0.4	0.0673	0.0839	0.0180	0.0091	0.0206	0.0024
0.6	-0.0854	0.0951	0.0228	-0.0007	0.0306	0.0002
0.9	0.2009	0.1706	0.0536	0.0475	0.0640	0.0127

1250 - 1350 MeV	June (2010)			April (2011)		
$cos(\theta_p)$	F	Δ_{stat} [μb]	Δ_{sys} [μb]	F	Δ_{stat} [μb]	Δ_{sys} [μb]
-0.9	0.2507	0.1074	0.0669	0.0453	0.0499	0.0121
-0.6	0.1769	0.0786	0.0472	-0.0253	0.0325	0.0067
-0.4	0.1861	0.0697	0.0497	-0.0226	0.0281	0.0060
-0.1	-0.0363	0.0747	0.0097	-0.0391	0.0239	0.0104
0.1	-0.1428	0.0796	0.0381	-0.0057	0.0228	0.0015
0.4	0.3257	0.1094	0.0869	-0.0361	0.0312	0.0096
0.6	0.0828	0.1198	0.0221	0.0108	0.0420	0.0029
0.9	-0.1623	0.2064	0.0433	-0.0046	0.0760	0.0012

1350 - 1450 MeV	June (2010)			April (2011)		
$cos(\theta_p)$	F	Δ_{stat} [μb]	Δ_{sys} [μb]	F	Δ_{stat} [μb]	Δ_{sys} [μb]
-0.9				-0.0665	0.0729	0.0178
-0.6				-0.0314	0.0414	0.0084
-0.4				-0.0787	0.0347	0.0210
-0.1				-0.0836	0.0264	0.0223
0.1				-0.0251	0.0308	0.0067
0.4				-0.1075	0.0491	0.0287
0.6				0.0299	0.0936	0.0080
0.9				0.0956	0.1972	0.0255

550 - 650 MeV	June (2010)			April (2011)		
$cos(\theta_p)$	F	Δ_{stat} [μb]	Δ_{sys} [μb]	F	Δ_{stat} [μb]	Δ_{sys} [μb]
-0.9	0.4596	0.3640	-0.3773			
-0.6	0.0486	0.2049	-0.4870			
-0.4	-0.2115	0.1369	-0.4435			
-0.1	-0.1696	0.1050	-0.4547			
0.1	-0.1066	0.0951	-0.4716			
0.4	-0.2496	0.1090	-0.4334			
0.6	0.0953	0.1634	-0.4745			
0.9	0.0136	0.1522	-0.4964			

650 - 750 MeV	June (2010)			April (2011)		
$cos(\theta_p)$	F	Δ_{stat} [μb]	Δ_{sys} [μb]	F	Δ_{stat} [μb]	Δ_{sys} [μb]
-0.9	0.3537	0.2025	0.0944	0.1209	0.0454	0.0323
-0.6	0.0133	0.1063	0.0035	0.0611	0.0327	0.0163
-0.4	-0.0906	0.0764	0.0242	0.0160	0.0228	0.0043
-0.1	0.0590	0.0616	0.0158	0.0163	0.0171	0.0044
0.1	-0.1595	0.0525	0.0426	-0.0649	0.0157	0.0173
0.4	-0.1100	0.0594	0.0294	-0.0590	0.0162	0.0158
0.6	-0.1329	0.0837	0.0355	-0.0869	0.0175	0.0232
0.9	-0.1625	0.0718	0.0434	0.0058	0.0135	0.0016

750 - 850 MeV	June (2010)			April (2011)		
$cos(\theta_p)$	F	Δ_{stat} [μb]	Δ_{sys} [μb]	F	Δ_{stat} [μb]	Δ_{sys} [μb]
-0.9	-0.3310	0.1875	0.0884	-0.1445	0.0518	0.0386
-0.6	-0.1604	0.0998	0.0428	0.0200	0.0380	0.0054
-0.4	-0.0370	0.0736	0.0099	0.0210	0.0281	0.0056
-0.1	-0.0579	0.0628	0.0155	0.0040	0.0220	0.0011
0.1	0.0423	0.0564	0.0113	-0.0439	0.0180	0.0117
0.4	-0.1725	0.0594	0.0460	-0.0770	0.0187	0.0205
0.6	-0.3124	0.0728	0.0834	-0.1282	0.0178	0.0342
0.9	-0.2672	0.0628	0.0713	-0.0975	0.0136	0.0260

850 - 950 MeV	June (2010)			April (2011)		
$cos(\theta_p)$	F	Δ_{stat} [μb]	Δ_{sys} [μb]	F	Δ_{stat} [μb]	Δ_{sys} [μb]
-0.9	-0.1876	0.1790	0.0501	-0.2044	0.0528	0.0545
-0.6	-0.1101	0.1077	0.0294	-0.0384	0.0401	0.0102
-0.4	-0.3533	0.0801	0.0943	-0.1335	0.0317	0.0356
-0.1	-0.0526	0.0758	0.0141	-0.0153	0.0252	0.0041
0.1	0.0729	0.0669	0.0195	-0.0682	0.0229	0.0182
0.4	-0.0973	0.0686	0.0260	-0.0847	0.0226	0.0226
0.6	-0.3366	0.0720	0.0898	-0.1744	0.0189	0.0465
0.9	-0.3773	0.0728	0.1007	-0.0726	0.0170	0.0194

950 - 1050 MeV	June (2010)			April (2011)		
$cos(\theta_p)$	F	Δ_{stat} [μb]	Δ_{sys} [μb]	F	Δ_{stat} [μb]	Δ_{sys} [μb]
-0.9	-0.1364	0.1432	0.0364	-0.0807	0.0390	0.0215
-0.6	-0.0118	0.0912	0.0032	-0.0448	0.0293	0.0120
-0.4	0.0265	0.0736	0.0071	-0.0309	0.0247	0.0082
-0.1	-0.1049	0.0728	0.0280	0.0254	0.0218	0.0068
0.1	0.0702	0.0697	0.0187	-0.1146	0.0197	0.0306
0.4	-0.0429	0.0682	0.0115	-0.0691	0.0195	0.0184
0.6	0.0866	0.0645	0.0231	-0.0143	0.0147	0.0038
0.9	0.0491	0.0829	0.0131	0.0057	0.0184	0.0015

1050 - 1150 MeV	June (2010)			April (2011)		
$cos(\theta_p)$	F	Δ_{stat} [μb]	Δ_{sys} [μb]	F	Δ_{stat} [μb]	Δ_{sys} [μb]
-0.9	0.0313	0.1174	0.0084	-0.0057	0.0396	0.0015
-0.6	-0.0146	0.0684	0.0039	-0.0567	0.0290	0.0151
-0.4	0.1051	0.0594	0.0281	-0.0226	0.0239	0.0060
-0.1	-0.0821	0.0577	0.0219	-0.0400	0.0211	0.0107
0.1	-0.1142	0.0551	0.0305	-0.0484	0.0191	0.0129
0.4	0.0476	0.0525	0.0127	-0.0166	0.0178	0.0044
0.6	0.0184	0.0599	0.0049	0.0849	0.0167	0.0227
0.9	-0.0732	0.0897	0.0195	0.0512	0.0237	0.0137

1150 - 1250 MeV	June (2010)			April (2011)		
$cos(\theta_p)$	F	Δ_{stat} [μb]	Δ_{sys} [μb]	F	Δ_{stat} [μb]	Δ_{sys} [μb]
-0.9	-0.0732	0.1491	0.0195	-0.0614	0.0482	0.0164
-0.6	0.1257	0.0837	0.0336	-0.0097	0.0330	0.0026
-0.4	0.2102	0.0775	0.0561	0.0167	0.0283	0.0045
-0.1	-0.0682	0.0669	0.0182	-0.0734	0.0236	0.0196
0.1	-0.0832	0.0633	0.0222	-0.0773	0.0186	0.0206
0.4	0.0239	0.0736	0.0064	0.0078	0.0220	0.0021
0.6	-0.0584	0.0999	0.0156	-0.0074	0.0258	0.0020
0.9	0.1990	0.1521	0.0531	0.0627	0.0372	0.0167

1250 - 1350 MeV	June (2010)			April (2011)		
$cos(\theta_p)$	F	Δ_{stat} [μb]	Δ_{sys} [μb]	F	Δ_{stat} [μb]	Δ_{sys} [μb]
-0.9	0.4465	0.1613	0.1192	0.0705	0.0515	0.0188
-0.6	0.1940	0.0927	0.0518	-0.0297	0.0349	0.0079
-0.4	0.2359	0.0815	0.0630	-0.0157	0.0289	0.0042
-0.1	-0.0313	0.0680	0.0083	-0.0473	0.0215	0.0126
0.1	-0.1066	0.0649	0.0284	-0.0062	0.0194	0.0017
0.4	0.2762	0.0928	0.0737	-0.0232	0.0271	0.0062
0.6	0.0966	0.1211	0.0258	0.0176	0.0341	0.0047
0.9	-0.0759	0.1957	0.0202	-0.0133	0.0512	0.0035

1350 - 1450 MeV	June (2010)			April (2011)		
$cos(\theta_p)$	F	Δ_{stat} [μb]	Δ_{sys} [μb]	F	Δ_{stat} [μb]	Δ_{sys} [μb]
-0.9				-0.0841	0.0681	0.0225
-0.6				-0.0188	0.0476	0.0050
-0.4				-0.0679	0.0318	0.0181
-0.1				-0.0852	0.0268	0.0228
0.1				-0.0430	0.0304	0.0115
0.4				-0.1012	0.0430	0.0270
0.6				0.0323	0.0511	0.0086
0.9				0.0791	0.0743	0.0211

550 - 650 MeV	Carbon			Hydrogen		
$IM(\pi^\phi\pi^\phi)$	F	Δ_{stat} [μb]	Δ_{sys} [μb]	F	Δ_{stat} [μb]	Δ_{sys} [μb]
292.5	-0.5019	0.1372	-0.3660	-0.5213	0.1441	-0.3608
317.5	-0.4067	0.1354	-0.3914	-0.4256	0.1386	-0.3864
342.5	-0.1917	0.1290	-0.4488	-0.1752	0.1395	-0.4532
367.5	0.1676	0.1283	-0.4553	0.1361	0.1447	-0.4637
392.5	-0.1944	0.1336	-0.4481	-0.1933	0.1520	-0.4484
417.5	0.2961	0.1475	-0.4210	0.3229	0.1758	-0.4138
442.5	0.3118	0.1882	-0.4168	0.3002	0.1998	-0.4199
467.5	0.7798	0.2673	-0.2918	0.7834	0.2720	-0.2909

650 - 750 MeV	Carbon			Hydrogen		
$IM(\pi^\phi\pi^\phi)$	F	Δ_{stat} [μb]	Δ_{sys} [μb]	F	Δ_{stat} [μb]	Δ_{sys} [μb]
296.3	-0.2207	0.0643	0.0589	-0.2383	0.0725	0.0636
328.8	-0.0909	0.0594	0.0243	-0.1330	0.0652	0.0355
361.3	-0.1254	0.0527	0.0335	-0.1649	0.0593	0.0440
393.8	-0.1298	0.0505	0.0346	-0.1372	0.0547	0.0366
426.3	-0.0432	0.0509	0.0115	-0.0471	0.0534	0.0126
458.8	0.0941	0.0546	0.0251	0.1067	0.0591	0.0285
491.3	0.1441	0.0625	0.0385	0.1699	0.0713	0.0453
523.8	0.0354	0.0902	0.0094	0.0527	0.1071	0.0141

750 - 850 MeV	Carbon			Hydrogen		
$IM(\pi^\phi\pi^\phi)$	F	Δ_{stat} [μb]	Δ_{sys} [μb]	F	Δ_{stat} [μb]	Δ_{sys} [μb]
300.0	0.0993	0.0892	0.0265	0.0749	0.0929	0.0200
340.0	-0.0085	0.0703	0.0023	-0.0155	0.0757	0.0041
380.0	-0.1173	0.0583	0.0313	-0.1170	0.0621	0.0312
420.0	-0.0908	0.0507	0.0242	-0.1191	0.0523	0.0318
460.0	-0.0988	0.0456	0.0264	-0.1154	0.0503	0.0308
500.0	-0.1586	0.0481	0.0423	-0.1686	0.0493	0.0450
540.0	-0.1768	0.0543	0.0472	-0.1824	0.0567	0.0487
580.0	-0.1634	0.0758	0.0436	-0.1722	0.0788	0.0460

850 - 950 MeV	Carbon			Hydrogen		
$IM(\pi^\phi\pi^\phi)$	F	Δ_{stat} [μb]	Δ_{sys} [μb]	F	Δ_{stat} [μb]	Δ_{sys} [μb]
303.1	-0.3710	0.0975	0.0990	-0.3094	0.1007	0.0826
349.4	-0.0271	0.0802	0.0072	-0.0320	0.0777	0.0085
395.6	-0.0432	0.0656	0.0115	-0.0664	0.0668	0.0177
441.9	-0.0465	0.0572	0.0124	-0.0540	0.0651	0.0144
488.1	-0.1136	0.0552	0.0303	-0.0787	0.0535	0.0210
534.4	-0.0977	0.0556	0.0261	-0.1054	0.0587	0.0281
580.6	-0.2241	0.0593	0.0598	-0.2219	0.0610	0.0592
626.9	-0.3253	0.0705	0.0868	-0.3231	0.0720	0.0862

950 - 1050 MeV	Carbon			Hydrogen		
$IM(\pi^\phi\pi^\phi)$	F	Δ_{stat} [μb]	Δ_{sys} [μb]	F	Δ_{stat} [μb]	Δ_{sys} [μb]
306.9	-0.2905	0.0851	0.0775	-0.2447	0.0795	0.0653
360.6	-0.0267	0.0719	0.0071	-0.0500	0.0742	0.0133
414.4	0.1429	0.0601	0.0382	0.1180	0.0619	0.0315
468.1	0.0120	0.0542	0.0032	0.0082	0.0554	0.0022
521.9	0.0991	0.0506	0.0265	0.1133	0.0550	0.0303
575.6	-0.0100	0.0487	0.0027	-0.0220	0.0592	0.0059
629.4	-0.0772	0.0551	0.0206	-0.0730	0.0619	0.0195
683.1	-0.1775	0.0703	0.0474	-0.1510	0.0675	0.0403

1050 - 1150 MeV	Carbon			Hydrogen		
$IM(\pi^\phi\pi^\phi)$	F	Δ_{stat} [μb]	Δ_{sys} [μb]	F	Δ_{stat} [μb]	Δ_{sys} [μb]
310.9	-0.1365	0.0679	0.0364	-0.1797	0.0720	0.0480
372.8	-0.0024	0.0583	0.0006	-0.0128	0.0574	0.0034
434.7	-0.0472	0.0475	0.0126	-0.0374	0.0495	0.0100
496.6	0.1182	0.0428	0.0316	0.1118	0.0455	0.0298
558.4	-0.0017	0.0406	0.0005	-0.0029	0.0411	0.0008
620.3	0.0213	0.0444	0.0057	0.0267	0.0471	0.0071
682.2	-0.0475	0.0492	0.0127	-0.0477	0.0499	0.0127
744.1	-0.0402	0.0628	0.0107	-0.0508	0.0615	0.0136

1150 - 1250 MeV	Carbon			Hydrogen		
$IM(\pi^\phi\pi^\phi)$	F	Δ_{stat} [μb]	Δ_{sys} [μb]	F	Δ_{stat} [μb]	Δ_{sys} [μb]
313.8	-0.2436	0.0953	0.0650	-0.2514	0.1011	0.0671
381.3	0.1323	0.0678	0.0353	0.1649	0.0681	0.0440
448.8	-0.1045	0.0613	0.0279	-0.1127	0.0659	0.0301
516.3	0.0740	0.0583	0.0197	0.0735	0.0532	0.0196
583.8	0.0546	0.0551	0.0146	0.0476	0.0463	0.0127
651.3	0.0221	0.0540	0.0059	0.0125	0.0615	0.0033
718.8	0.0189	0.0617	0.0050	0.0214	0.0679	0.0057
786.3	-0.0491	0.0798	0.0131	-0.0229	0.0787	0.0061

1250 - 1350 MeV	Carbon			Hydrogen		
$IM(\pi^\phi\pi^\phi)$	F	Δ_{stat} [μb]	Δ_{sys} [μb]	F	Δ_{stat} [μb]	Δ_{sys} [μb]
284.7	-0.0041	0.1677	0.0011	-0.0236	0.2081	0.0063
354.1	-0.0377	0.0882	0.0101	-0.0197	0.0820	0.0053
423.4	0.0200	0.0753	0.0053	-0.0303	0.0730	0.0081
492.8	0.0890	0.0669	0.0238	0.0996	0.0590	0.0266
562.2	0.0431	0.0607	0.0115	0.0394	0.0575	0.0105
631.6	0.1007	0.0606	0.0269	0.1066	0.0652	0.0285
700.9	-0.0091	0.0617	0.0024	-0.0305	0.0634	0.0081
770.3	0.0902	0.0722	0.0241	0.0742	0.0707	0.0198

1350 - 1450 MeV	Carbon			Hydrogen		
$IM(\pi^\phi\pi^\phi)$	F	Δ_{stat} [μb]	Δ_{sys} [μb]	F	Δ_{stat} [μb]	Δ_{sys} [μb]
284.7	-0.0322	0.1513	0.0086	-0.3732	0.6176	0.0996
354.1	-0.0937	0.0730	0.0250	0.0698	0.2923	0.0186
423.4	-0.0749	0.0644	0.0200	0.1790	0.2412	0.0478
492.8	0.0923	0.0594	0.0246	0.1422	0.2140	0.0379
562.2	-0.0087	0.0546	0.0023	-0.4420	0.2098	0.1180
631.6	-0.0536	0.0533	0.0143	-0.0177	0.1897	0.0047
700.9	-0.1023	0.0517	0.0273	-0.3744	0.1858	0.0999
770.3	-0.1005	0.0576	0.0268	0.0128	0.1987	0.0034

550 - 650 MeV	June (2010)			April (2011)		
$IM(\pi^\phi\pi^\phi)$	F	Δ_{stat} [μb]	Δ_{sys} [μb]	F	Δ_{stat} [μb]	Δ_{sys} [μb]
292.5	-0.5213	0.1441	-0.3608			
317.5	-0.4256	0.1386	-0.3864			
342.5	-0.1752	0.1395	-0.4532			
367.5	0.1361	0.1447	-0.4637			
392.5	-0.1933	0.1520	-0.4484			
417.5	0.3229	0.1758	-0.4138			
442.5	0.3002	0.1998	-0.4199			
467.5	0.7834	0.2720	-0.2909			

650 - 750 MeV	June (2010)			April (2011)		
$IM(\pi^\phi\pi^\phi)$	F	Δ_{stat} [μb]	Δ_{sys} [μb]	F	Δ_{stat} [μb]	Δ_{sys} [μb]
296.3	-0.3243	0.0965	0.0866	-0.1523	0.0348	0.0407
328.8	-0.1045	0.0871	0.0279	-0.1615	0.0301	0.0431
361.3	-0.1291	0.0792	0.0345	-0.2006	0.0275	0.0536
393.8	-0.2028	0.0736	0.0541	-0.0716	0.0240	0.0191
426.3	-0.1011	0.0716	0.0270	0.0070	0.0240	0.0019
458.8	0.1381	0.0798	0.0369	0.0752	0.0248	0.0201
491.3	0.2015	0.0968	0.0538	0.1383	0.0285	0.0369
523.8	-0.0487	0.1458	0.0130	0.1542	0.0411	0.0411

750 - 850 MeV	June (2010)			April (2011)		
$IM(\pi^\phi\pi^\phi)$	F	Δ_{stat} [μb]	Δ_{sys} [μb]	F	Δ_{stat} [μb]	Δ_{sys} [μb]
300.0	0.1721	0.1229	0.0459	-0.0223	0.0464	0.0059
340.0	-0.0300	0.0990	0.0080	-0.0011	0.0407	0.0003
380.0	-0.2032	0.0816	0.0542	-0.0309	0.0325	0.0082
420.0	-0.0677	0.0684	0.0181	-0.1705	0.0281	0.0455
460.0	-0.1035	0.0669	0.0276	-0.1273	0.0243	0.0340
500.0	-0.2891	0.0663	0.0772	-0.0480	0.0219	0.0128
540.0	-0.3179	0.0765	0.0849	-0.0469	0.0240	0.0125
580.0	-0.2033	0.1067	0.0543	-0.1411	0.0320	0.0377

850 - 950 MeV	June (2010)			April (2011)		
$IM(\pi^\phi\pi^\phi)$	F	Δ_{stat} [μb]	Δ_{sys} [μb]	F	Δ_{stat} [μb]	Δ_{sys} [μb]
303.1	-0.5242	0.1331	0.1399	-0.0946	0.0507	0.0253
349.4	-0.0326	0.0989	0.0087	-0.0313	0.0480	0.0083
395.6	0.0405	0.0862	0.0108	-0.1732	0.0385	0.0462
441.9	-0.0634	0.0865	0.0169	-0.0447	0.0316	0.0119
488.1	-0.0914	0.0706	0.0244	-0.0659	0.0274	0.0176
534.4	-0.1216	0.0793	0.0325	-0.0892	0.0245	0.0238
580.6	-0.2853	0.0829	0.0762	-0.1584	0.0239	0.0423
626.9	-0.4483	0.0979	0.1197	-0.1978	0.0282	0.0528

950 - 1050 MeV	June (2010)			April (2011)		
$IM(\pi^\phi\pi^\phi)$	F	Δ_{stat} [μb]	Δ_{sys} [μb]	F	Δ_{stat} [μb]	Δ_{sys} [μb]
306.9	-0.3567	0.1051	0.0952	-0.1327	0.0400	0.0354
360.6	0.0285	0.0999	0.0076	-0.1285	0.0321	0.0343
414.4	0.2260	0.0829	0.0603	0.0101	0.0279	0.0027
468.1	0.0028	0.0746	0.0008	0.0136	0.0238	0.0036
521.9	0.1589	0.0750	0.0424	0.0678	0.0208	0.0181
575.6	-0.1066	0.0811	0.0285	0.0625	0.0207	0.0167
629.4	-0.0290	0.0852	0.0077	-0.1170	0.0203	0.0312
683.1	-0.1451	0.0928	0.0387	-0.1569	0.0221	0.0419

1050 - 1150 MeV	June (2010)			April (2011)		
$IM(\pi^\phi\pi^\phi)$	F	Δ_{stat} [μb]	Δ_{sys} [μb]	F	Δ_{stat} [μb]	Δ_{sys} [μb]
310.9	-0.1770	0.0943	0.0473	-0.1824	0.0384	0.0487
372.8	0.0643	0.0742	0.0171	-0.0899	0.0329	0.0240
434.7	-0.0944	0.0650	0.0252	0.0197	0.0260	0.0052
496.6	0.1500	0.0610	0.0400	0.0736	0.0207	0.0197
558.4	-0.0601	0.0549	0.0161	0.0544	0.0192	0.0145
620.3	0.0348	0.0633	0.0093	0.0186	0.0209	0.0050
682.2	-0.0917	0.0676	0.0245	-0.0036	0.0205	0.0010
744.1	0.0658	0.0832	0.0176	-0.1673	0.0252	0.0447

1150 - 1250 MeV	June (2010)			April (2011)		
$IM(\pi^\phi\pi^\phi)$	F	Δ_{stat} [μb]	Δ_{sys} [μb]	F	Δ_{stat} [μb]	Δ_{sys} [μb]
313.8	-0.3605	0.1351	0.0962	-0.1423	0.0471	0.0380
381.3	0.3704	0.0904	0.0989	-0.0406	0.0331	0.0108
448.8	-0.0892	0.0874	0.0238	-0.1362	0.0325	0.0364
516.3	0.0482	0.0715	0.0129	0.0989	0.0235	0.0264
583.8	0.1282	0.0617	0.0342	-0.0330	0.0218	0.0088
651.3	-0.0533	0.0837	0.0142	0.0783	0.0234	0.0209
718.8	0.1143	0.0930	0.0305	-0.0715	0.0240	0.0191
786.3	0.0532	0.1074	0.0142	-0.0990	0.0289	0.0264

1250 - 1350 MeV	June (2010)			April (2011)		
$IM(\pi^\phi\pi^\phi)$	F	Δ_{stat} [μb]	Δ_{sys} [μb]	F	Δ_{stat} [μb]	Δ_{sys} [μb]
284.7	0.0307	0.2742	0.0082	-0.0778	0.1068	0.0208
354.1	0.0205	0.1073	0.0055	-0.0600	0.0442	0.0160
423.4	0.0358	0.0956	0.0096	-0.0963	0.0390	0.0257
492.8	0.1787	0.0771	0.0477	0.0205	0.0320	0.0055
562.2	-0.0233	0.0749	0.0062	0.1021	0.0315	0.0272
631.6	0.1884	0.0881	0.0503	0.0248	0.0273	0.0066
700.9	-0.0447	0.0858	0.0119	-0.0164	0.0260	0.0044
770.3	0.2346	0.0952	0.0626	-0.0861	0.0308	0.0230

1350 - 1450 MeV	June (2010)			April (2011)		
$IM(\pi^\phi\pi^\phi)$	F	Δ_{stat} [μb]	Δ_{sys} [μb]	F	Δ_{stat} [μb]	Δ_{sys} [μb]
284.7				-0.0482	0.0923	0.0129
354.1				-0.0870	0.0625	0.0232
423.4				-0.0565	0.0511	0.0151
492.8				0.0296	0.0571	0.0079
562.2				-0.0116	0.0453	0.0031
631.6				-0.0326	0.0351	0.0087
700.9				-0.0997	0.0392	0.0266
770.3				-0.1071	0.0383	0.0286

550 - 650 MeV	June (2010)			April (2011)		
$IM(\pi^\phi\pi^\phi)$	F	Δ_{stat} [μb]	Δ_{sys} [μb]	F	Δ_{stat} [μb]	Δ_{sys} [μb]
292.5	-0.5019	0.1372	-0.3660			
317.5	-0.4067	0.1354	-0.3914			
342.5	-0.1917	0.1290	-0.4488			
367.5	0.1676	0.1283	-0.4553			
392.5	-0.1944	0.1336	-0.4481			
417.5	0.2961	0.1475	-0.4210			
442.5	0.3118	0.1882	-0.4168			
467.5	0.7798	0.2673	-0.2918			

650 - 750 MeV	June (2010)			April (2011)		
$IM(\pi^\phi\pi^\phi)$	F	Δ_{stat} [μb]	Δ_{sys} [μb]	F	Δ_{stat} [μb]	Δ_{sys} [μb]
296.3	-0.3244	0.0870	0.0866	-0.1170	0.0266	0.0312
328.8	-0.0589	0.0809	0.0157	-0.1229	0.0224	0.0328
361.3	-0.1021	0.0719	0.0272	-0.1487	0.0197	0.0397
393.8	-0.2045	0.0691	0.0546	-0.0550	0.0180	0.0147
426.3	-0.0882	0.0699	0.0236	0.0019	0.0169	0.0005
458.8	0.1326	0.0751	0.0354	0.0555	0.0182	0.0148
491.3	0.1825	0.0859	0.0487	0.1057	0.0207	0.0282
523.8	-0.0446	0.1243	0.0119	0.1153	0.0284	0.0308

750 - 850 MeV	June (2010)			April (2011)		
$IM(\pi^\phi\pi^\phi)$	F	Δ_{stat} [μb]	Δ_{sys} [μb]	F	Δ_{stat} [μb]	Δ_{sys} [μb]
300.0	0.2043	0.1192	0.0545	-0.0057	0.0415	0.0015
340.0	-0.0148	0.0943	0.0039	-0.0022	0.0315	0.0006
380.0	-0.2078	0.0788	0.0555	-0.0268	0.0244	0.0072
420.0	-0.0580	0.0688	0.0155	-0.1236	0.0202	0.0330
460.0	-0.0977	0.0617	0.0261	-0.0998	0.0187	0.0266
500.0	-0.2778	0.0656	0.0741	-0.0394	0.0183	0.0105
540.0	-0.3110	0.0738	0.0830	-0.0426	0.0212	0.0114
580.0	-0.1983	0.1034	0.0529	-0.1285	0.0281	0.0343

850 - 950 MeV	June (2010)			April (2011)		
$IM(\pi^\phi\pi^\phi)$	F	Δ_{stat} [μb]	Δ_{sys} [μb]	F	Δ_{stat} [μb]	Δ_{sys} [μb]
303.1	-0.6354	0.1310	0.1696	-0.1066	0.0430	0.0285
349.4	-0.0297	0.1082	0.0079	-0.0245	0.0342	0.0065
395.6	0.0331	0.0884	0.0088	-0.1196	0.0281	0.0319
441.9	-0.0540	0.0771	0.0144	-0.0389	0.0245	0.0104
488.1	-0.1649	0.0746	0.0440	-0.0622	0.0230	0.0166
534.4	-0.1173	0.0755	0.0313	-0.0782	0.0220	0.0209
580.6	-0.2836	0.0803	0.0757	-0.1646	0.0241	0.0439
626.9	-0.4567	0.0960	0.1219	-0.1939	0.0269	0.0518

950 - 1050 MeV	June (2010)			April (2011)		
$IM(\pi^\phi\pi^\phi)$	F	Δ_{stat} [μb]	Δ_{sys} [μb]	F	Δ_{stat} [μb]	Δ_{sys} [μb]
306.9	-0.4393	0.1157	0.1173	-0.1416	0.0331	0.0378
360.6	0.0528	0.0985	0.0141	-0.1061	0.0254	0.0283
414.4	0.2798	0.0822	0.0747	0.0060	0.0218	0.0016
468.1	0.0082	0.0739	0.0022	0.0159	0.0203	0.0042
521.9	0.1352	0.0691	0.0361	0.0630	0.0187	0.0168
575.6	-0.0777	0.0662	0.0207	0.0577	0.0187	0.0154
629.4	-0.0310	0.0751	0.0083	-0.1234	0.0209	0.0329
683.1	-0.1744	0.0965	0.0465	-0.1807	0.0243	0.0482

1050 - 1150 MeV	June (2010)			April (2011)		
$IM(\pi^\phi\pi^\phi)$	F	Δ_{stat} [μb]	Δ_{sys} [μb]	F	Δ_{stat} [μb]	Δ_{sys} [μb]
310.9	-0.1096	0.0906	0.0293	-0.1634	0.0319	0.0436
372.8	0.0743	0.0784	0.0198	-0.0791	0.0256	0.0211
434.7	-0.1078	0.0637	0.0288	0.0133	0.0215	0.0036
496.6	0.1620	0.0572	0.0432	0.0744	0.0200	0.0199
558.4	-0.0569	0.0542	0.0152	0.0535	0.0188	0.0143
620.3	0.0245	0.0595	0.0065	0.0180	0.0200	0.0048
682.2	-0.0945	0.0662	0.0252	-0.0004	0.0214	0.0001
744.1	0.0967	0.0847	0.0258	-0.1770	0.0267	0.0472

1150 - 1250 MeV	June (2010)			April (2011)		
$IM(\pi^\phi\pi^\phi)$	F	Δ_{stat} [μb]	Δ_{sys} [μb]	F	Δ_{stat} [μb]	Δ_{sys} [μb]
313.8	-0.2890	0.1294	0.0771	-0.1982	0.0378	0.0529
381.3	0.2966	0.0914	0.0792	-0.0320	0.0288	0.0085
448.8	-0.0985	0.0828	0.0263	-0.1104	0.0257	0.0295
516.3	0.0447	0.0790	0.0119	0.1032	0.0236	0.0276
583.8	0.1474	0.0743	0.0393	-0.0382	0.0235	0.0102
651.3	-0.0311	0.0727	0.0083	0.0753	0.0231	0.0201
718.8	0.1264	0.0828	0.0337	-0.0887	0.0275	0.0237
786.3	0.0189	0.1081	0.0050	-0.1171	0.0326	0.0313

1250 - 1350 MeV	June (2010)			April (2011)		
$IM(\pi^\phi\pi^\phi)$	F	Δ_{stat} [μb]	Δ_{sys} [μb]	F	Δ_{stat} [μb]	Δ_{sys} [μb]
284.7	0.1308	0.2252	0.0349	-0.1390	0.0746	0.0371
354.1	-0.0163	0.1193	0.0043	-0.0591	0.0367	0.0158
423.4	0.1237	0.1017	0.0330	-0.0838	0.0316	0.0224
492.8	0.1746	0.0903	0.0466	0.0035	0.0283	0.0009
562.2	-0.0091	0.0816	0.0024	0.0953	0.0266	0.0254
631.6	0.1691	0.0819	0.0451	0.0323	0.0254	0.0086
700.9	0.0051	0.0831	0.0014	-0.0233	0.0265	0.0062
770.3	0.2623	0.0975	0.0700	-0.0819	0.0302	0.0219

1350 - 1450 MeV	June (2010)			April (2011)		
$IM(\pi^\phi\pi^\phi)$	F	Δ_{stat} [μb]	Δ_{sys} [μb]	F	Δ_{stat} [μb]	Δ_{sys} [μb]
284.7				-0.0322	0.1070	0.0086
354.1				-0.0937	0.0516	0.0250
423.4				-0.0749	0.0455	0.0200
492.8				0.0923	0.0420	0.0246
562.2				-0.0087	0.0386	0.0023
631.6				-0.0536	0.0377	0.0143
700.9				-0.1023	0.0366	0.0273
770.3				-0.1005	0.0407	0.0268

550 - 650 MeV	Carbon			Hydrogen		
$IM(\pi^\phi p)$	F	Δ_{stat} [μb]	Δ_{sys} [μb]	F	Δ_{stat} [μb]	Δ_{sys} [μb]
1096.9	0.0696	0.1480	-0.4814	0.0509	0.1661	-0.4864
1120.6	-0.1466	0.1129	-0.4609	-0.1900	0.1135	-0.4493
1144.4	0.0807	0.1008	-0.4784	0.0969	0.1037	-0.4741
1168.1	0.1840	0.0886	-0.4509	0.2144	0.0996	-0.4428
1191.9	0.2414	0.0863	-0.4356	0.2628	0.0931	-0.4299
1215.6	0.1037	0.0963	-0.4723	0.1302	0.0965	-0.4652
1239.4	0.0572	0.1247	-0.4847	0.0433	0.1292	-0.4884
1263.1	0.1612	0.1940	-0.4570	0.1443	0.2094	-0.4615

650 - 750 MeV	Carbon			Hydrogen		
$IM(\pi^\phi p)$	F	Δ_{stat} [μb]	Δ_{sys} [μb]	F	Δ_{stat} [μb]	Δ_{sys} [μb]
1096.9	0.0991	0.0825	0.0265	0.1098	0.0870	0.0293
1130.6	0.1408	0.0510	0.0376	0.1585	0.0536	0.0423
1164.4	0.0842	0.0358	0.0225	0.0899	0.0377	0.0240
1198.1	0.0141	0.0294	0.0038	0.0217	0.0311	0.0058
1231.9	0.0247	0.0304	0.0066	0.0307	0.0325	0.0082
1265.6	0.0430	0.0408	0.0115	0.0387	0.0437	0.0103
1299.4	0.0699	0.0615	0.0187	0.0821	0.0730	0.0219
1333.1	-0.0818	0.1086	0.0218	-0.1146	0.1404	0.0306

750 - 850 MeV	Carbon			Hydrogen		
$IM(\pi^\phi p)$	F	Δ_{stat} [μb]	Δ_{sys} [μb]	F	Δ_{stat} [μb]	Δ_{sys} [μb]
1118.8	0.0745	0.0811	0.0199	0.0961	0.0780	0.0256
1156.3	0.1358	0.0472	0.0362	0.1449	0.0485	0.0387
1193.8	0.0771	0.0323	0.0206	0.0803	0.0324	0.0214
1231.3	0.0006	0.0283	0.0002	0.0014	0.0289	0.0004
1268.8	-0.0713	0.0321	0.0190	-0.0758	0.0338	0.0202
1306.3	-0.0315	0.0426	0.0084	-0.0358	0.0450	0.0095
1343.8	-0.0447	0.0611	0.0119	-0.0751	0.0769	0.0200
1381.3	-0.0927	0.1059	0.0247	-0.0929	0.1191	0.0248

850 - 950 MeV	Carbon			Hydrogen		
$IM(\pi^\phi p)$	F	Δ_{stat} [μb]	Δ_{sys} [μb]	F	Δ_{stat} [μb]	Δ_{sys} [μb]
1103.1	0.0058	0.1148	0.0015	-0.0048	0.1207	0.0013
1149.4	0.1248	0.0598	0.0333	0.0980	0.0592	0.0262
1195.6	0.1227	0.0376	0.0328	0.1246	0.0372	0.0333
1241.9	0.1082	0.0326	0.0289	0.1110	0.0335	0.0296
1288.1	-0.0711	0.0344	0.0190	-0.0704	0.0351	0.0188
1334.4	-0.0598	0.0414	0.0160	-0.0650	0.0415	0.0174
1380.6	0.0482	0.0525	0.0129	0.0412	0.0630	0.0110
1426.9	0.0707	0.0917	0.0189	0.0797	0.1046	0.0213

950 - 1050 MeV	Carbon			Hydrogen		
$IM(\pi^\phi p)$	F	Δ_{stat} [μb]	Δ_{sys} [μb]	F	Δ_{stat} [μb]	Δ_{sys} [μb]
1109.4	-0.0395	0.0707	0.0106	-0.0502	0.0783	0.0134
1168.1	-0.0056	0.0409	0.0015	-0.0043	0.0425	0.0011
1226.9	0.0377	0.0321	0.0101	0.0379	0.0328	0.0101
1285.6	-0.0304	0.0321	0.0081	-0.0272	0.0322	0.0073
1344.4	0.0185	0.0355	0.0049	0.0173	0.0338	0.0046
1403.1	-0.0608	0.0408	0.0162	-0.0688	0.0435	0.0184
1461.9	0.0166	0.0583	0.0044	0.0439	0.0705	0.0117
1520.6	0.0453	0.1160	0.0121	-0.0091	0.1647	0.0024

1050 - 1150 MeV	Carbon			Hydrogen		
$IM(\pi^\phi p)$	F	Δ_{stat} [μb]	Δ_{sys} [μb]	F	Δ_{stat} [μb]	Δ_{sys} [μb]
1110.9	0.0176	0.0589	0.0047	0.0203	0.0575	0.0054
1172.8	0.0499	0.0334	0.0133	0.0527	0.0330	0.0141
1234.7	0.0662	0.0279	0.0177	0.0674	0.0281	0.0180
1296.6	-0.0728	0.0313	0.0194	-0.0632	0.0320	0.0169
1358.4	-0.0445	0.0319	0.0119	-0.0394	0.0306	0.0105
1420.3	-0.0080	0.0326	0.0021	-0.0121	0.0331	0.0032
1482.2	-0.0368	0.0397	0.0098	-0.0280	0.0438	0.0075
1544.1	-0.1008	0.0649	0.0269	-0.1353	0.0838	0.0361

1150 - 1250 MeV	Carbon			Hydrogen		
$IM(\pi^\phi p)$	F	Δ_{stat} [μb]	Δ_{sys} [μb]	F	Δ_{stat} [μb]	Δ_{sys} [μb]
1113.8	0.0729	0.0782	0.0195	0.0685	0.0774	0.0183
1181.3	-0.0540	0.0403	0.0144	-0.0554	0.0385	0.0148
1248.8	-0.0213	0.0369	0.0057	-0.0165	0.0359	0.0044
1316.3	0.0323	0.0433	0.0086	0.0374	0.0407	0.0100
1383.8	0.0351	0.0418	0.0094	0.0366	0.0402	0.0098
1451.3	-0.0268	0.0409	0.0072	-0.0353	0.0426	0.0094
1518.8	-0.0634	0.0489	0.0169	-0.0592	0.0484	0.0158
1586.3	0.0310	0.0806	0.0083	0.0725	0.1058	0.0193

1250 - 1350 MeV	Carbon			Hydrogen		
$IM(\pi^\phi p)$	F	Δ_{stat} [μb]	Δ_{sys} [μb]	F	Δ_{stat} [μb]	Δ_{sys} [μb]
1134.4	-0.0763	0.0652	0.0204	-0.0753	0.0640	0.0201
1203.1	-0.0236	0.0422	0.0063	-0.0215	0.0392	0.0058
1271.9	-0.0323	0.0442	0.0086	-0.0346	0.0419	0.0092
1340.6	-0.0915	0.0496	0.0244	-0.0838	0.0470	0.0224
1409.4	0.0225	0.0466	0.0060	0.0175	0.0454	0.0047
1478.1	0.0017	0.0477	0.0005	0.0011	0.0482	0.0003
1546.9	-0.1974	0.0560	0.0527	-0.1916	0.0528	0.0511
1615.6	-0.0522	0.0824	0.0139	-0.0623	0.0799	0.0166

1350 - 1450 MeV	Carbon			Hydrogen		
$IM(\pi^\phi p)$	F	Δ_{stat} [μb]	Δ_{sys} [μb]	F	Δ_{stat} [μb]	Δ_{sys} [μb]
1140.6	0.0984	0.0485	0.0263	0.1890	0.2180	0.0505
1221.9	0.0659	0.0305	0.0176	0.2195	0.1221	0.0586
1303.1	0.0454	0.0359	0.0121	0.0719	0.1257	0.0192
1384.4	-0.0460	0.0376	0.0123	0.1009	0.1355	0.0269
1465.6	-0.0210	0.0386	0.0056	-0.1642	0.1207	0.0438
1546.9	-0.0832	0.0401	0.0222	-0.0574	0.1964	0.0153
1628.1	-0.0693	0.0519	0.0185	-0.1747	0.2124	0.0466
1709.4	-0.0671	0.0986	0.0179	-0.3584	0.2785	0.0957

550 - 650 MeV	June (2010)			April (2011)		
$IM(\pi^\phi p)$	F	Δ_{stat} [μb]	Δ_{sys} [μb]	F	Δ_{stat} [μb]	Δ_{sys} [μb]
1096.9	0.0509	0.1661	-0.4864			
1120.6	-0.1900	0.1135	-0.4493			
1144.4	0.0969	0.1037	-0.4741			
1168.1	0.2144	0.0996	-0.4428			
1191.9	0.2628	0.0931	-0.4299			
1215.6	0.1302	0.0965	-0.4652			
1239.4	0.0433	0.1292	-0.4884			
1263.1	0.1443	0.2094	-0.4615			

650 - 750 MeV	June (2010)			April (2011)		
$IM(\pi^\phi p)$	F	Δ_{stat} [μb]	Δ_{sys} [μb]	F	Δ_{stat} [μb]	Δ_{sys} [μb]
1096.9	0.1256	0.1161	0.0335	0.0940	0.0405	0.0251
1130.6	0.2164	0.0721	0.0578	0.1005	0.0233	0.0268
1164.4	0.1272	0.0506	0.0339	0.0526	0.0166	0.0140
1198.1	-0.0002	0.0420	0.0000	0.0437	0.0132	0.0117
1231.9	0.0200	0.0438	0.0053	0.0414	0.0139	0.0111
1265.6	0.1458	0.0587	0.0389	-0.0684	0.0191	0.0183
1299.4	0.2092	0.0991	0.0558	-0.0449	0.0290	0.0120
1333.1	-0.2601	0.1902	0.0694	0.0309	0.0571	0.0082

750 - 850 MeV	June (2010)			April (2011)		
$IM(\pi^\phi p)$	F	Δ_{stat} [μb]	Δ_{sys} [μb]	F	Δ_{stat} [μb]	Δ_{sys} [μb]
1118.8	0.0583	0.1041	0.0156	0.1338	0.0364	0.0357
1156.3	0.1590	0.0649	0.0424	0.1308	0.0223	0.0349
1193.8	0.1027	0.0432	0.0274	0.0580	0.0153	0.0155
1231.3	0.0225	0.0385	0.0060	-0.0197	0.0135	0.0053
1268.8	-0.0931	0.0452	0.0248	-0.0585	0.0155	0.0156
1306.3	0.0106	0.0602	0.0028	-0.0821	0.0207	0.0219
1343.8	-0.0765	0.1044	0.0204	-0.0737	0.0304	0.0197
1381.3	-0.2291	0.1602	0.0612	0.0433	0.0521	0.0116

850 - 950 MeV	June (2010)			April (2011)		
$IM(\pi^\phi p)$	F	Δ_{stat} [μb]	Δ_{sys} [μb]	F	Δ_{stat} [μb]	Δ_{sys} [μb]
1103.1	-0.0050	0.1601	0.0013	-0.0047	0.0590	0.0013
1149.4	0.1354	0.0790	0.0361	0.0606	0.0275	0.0162
1195.6	0.1336	0.0497	0.0357	0.1157	0.0171	0.0309
1241.9	0.1837	0.0449	0.0490	0.0383	0.0150	0.0102
1288.1	-0.1070	0.0469	0.0286	-0.0338	0.0160	0.0090
1334.4	-0.0871	0.0551	0.0232	-0.0429	0.0201	0.0115
1380.6	0.1463	0.0847	0.0390	-0.0638	0.0276	0.0170
1426.9	0.1157	0.1416	0.0309	0.0436	0.0428	0.0116

950 - 1050 MeV	June (2010)			April (2011)		
$IM(\pi^\phi p)$	F	Δ_{stat} [μb]	Δ_{sys} [μb]	F	Δ_{stat} [μb]	Δ_{sys} [μb]
1109.4	-0.0500	0.1070	0.0134	-0.0504	0.0283	0.0135
1168.1	-0.0466	0.0578	0.0124	0.0381	0.0163	0.0102
1226.9	0.0357	0.0448	0.0095	0.0402	0.0123	0.0107
1285.6	-0.0430	0.0436	0.0115	-0.0114	0.0130	0.0030
1344.4	0.0823	0.0458	0.0220	-0.0476	0.0137	0.0127
1403.1	-0.0780	0.0592	0.0208	-0.0596	0.0168	0.0159
1461.9	0.0340	0.0969	0.0091	0.0538	0.0236	0.0144
1520.6	-0.0486	0.2281	0.0130	0.0305	0.0468	0.0081

1050 - 1150 MeV	June (2010)			April (2011)		
$IM(\pi^\phi p)$	F	Δ_{stat} [μb]	Δ_{sys} [μb]	F	Δ_{stat} [μb]	Δ_{sys} [μb]
1110.9	-0.0441	0.0770	0.0118	0.0847	0.0259	0.0226
1172.8	0.1326	0.0442	0.0354	-0.0272	0.0151	0.0073
1234.7	0.1064	0.0374	0.0284	0.0284	0.0135	0.0076
1296.6	-0.1404	0.0426	0.0375	0.0141	0.0152	0.0038
1358.4	-0.0504	0.0409	0.0135	-0.0284	0.0142	0.0076
1420.3	0.0119	0.0442	0.0032	-0.0360	0.0152	0.0096
1482.2	-0.0019	0.0589	0.0005	-0.0541	0.0194	0.0145
1544.1	-0.2190	0.1129	0.0585	-0.0515	0.0358	0.0137

1150 - 1250 MeV	June (2010)			April (2011)		
$IM(\pi^\phi p)$	F	Δ_{stat} [μb]	Δ_{sys} [μb]	F	Δ_{stat} [μb]	Δ_{sys} [μb]
1113.8	0.0739	0.1047	0.0197	0.0632	0.0320	0.0169
1181.3	-0.1451	0.0520	0.0387	0.0343	0.0161	0.0091
1248.8	-0.0732	0.0483	0.0195	0.0402	0.0155	0.0107
1316.3	0.0721	0.0550	0.0192	0.0027	0.0172	0.0007
1383.8	0.0909	0.0544	0.0243	-0.0176	0.0164	0.0047
1451.3	-0.0483	0.0577	0.0129	-0.0222	0.0170	0.0059
1518.8	-0.0890	0.0650	0.0238	-0.0294	0.0213	0.0078
1586.3	0.1171	0.1447	0.0313	0.0278	0.0383	0.0074

1250 - 1350 MeV	June (2010)			April (2011)		
$IM(\pi^\phi p)$	F	Δ_{stat} [μb]	Δ_{sys} [μb]	F	Δ_{stat} [μb]	Δ_{sys} [μb]
1134.4	-0.1887	0.0860	0.0504	0.0382	0.0283	0.0102
1203.1	-0.0546	0.0522	0.0146	0.0115	0.0185	0.0031
1271.9	-0.0937	0.0556	0.0250	0.0244	0.0206	0.0065
1340.6	-0.1908	0.0623	0.0509	0.0231	0.0232	0.0062
1409.4	0.0806	0.0608	0.0215	-0.0456	0.0210	0.0122
1478.1	-0.0044	0.0654	0.0012	0.0066	0.0193	0.0018
1546.9	-0.3782	0.0701	0.1009	-0.0050	0.0256	0.0013
1615.6	-0.1029	0.1059	0.0275	-0.0216	0.0392	0.0058

1350 - 1450 MeV	June (2010)			April (2011)		
$IM(\pi^\phi p)$	F	Δ_{stat} [μb]	Δ_{sys} [μb]	F	Δ_{stat} [μb]	Δ_{sys} [μb]
1140.6				0.1008	0.0344	0.0269
1221.9				0.0675	0.0232	0.0180
1303.1				0.0423	0.0251	0.0113
1384.4				-0.0479	0.0276	0.0128
1465.6				-0.0162	0.0252	0.0043
1546.9				-0.0883	0.0284	0.0236
1628.1				-0.0772	0.0399	0.0206
1709.4				-0.0929	0.0855	0.0248

550 - 650 MeV	June (2010)			April (2011)		
$IM(\pi^\phi p)$	F	Δ_{stat} [μb]	Δ_{sys} [μb]	F	Δ_{stat} [μb]	Δ_{sys} [μb]
1096.9	0.0696	0.1480	-0.4814			
1120.6	-0.1466	0.1129	-0.4609			
1144.4	0.0807	0.1008	-0.4784			
1168.1	0.1840	0.0886	-0.4509			
1191.9	0.2414	0.0863	-0.4356			
1215.6	0.1037	0.0963	-0.4723			
1239.4	0.0572	0.1247	-0.4847			
1263.1	0.1612	0.1940	-0.4570			

650 - 750 MeV	June (2010)			April (2011)		
$IM(\pi^\phi p)$	F	Δ_{stat} [μb]	Δ_{sys} [μb]	F	Δ_{stat} [μb]	Δ_{sys} [μb]
1096.9	0.1330	0.1126	0.0355	0.0652	0.0305	0.0174
1130.6	0.2009	0.0697	0.0536	0.0807	0.0185	0.0215
1164.4	0.1281	0.0490	0.0342	0.0404	0.0126	0.0108
1198.1	-0.0046	0.0403	0.0012	0.0327	0.0099	0.0087
1231.9	0.0204	0.0417	0.0054	0.0290	0.0102	0.0077
1265.6	0.1365	0.0560	0.0364	-0.0504	0.0138	0.0135
1299.4	0.1753	0.0844	0.0468	-0.0356	0.0212	0.0095
1333.1	-0.1877	0.1485	0.0501	0.0242	0.0389	0.0065

750 - 850 MeV	June (2010)			April (2011)		
$IM(\pi^\phi p)$	F	Δ_{stat} [μb]	Δ_{sys} [μb]	F	Δ_{stat} [μb]	Δ_{sys} [μb]
1118.8	0.0267	0.1095	0.0071	0.1223	0.0339	0.0327
1156.3	0.1545	0.0639	0.0412	0.1171	0.0195	0.0313
1193.8	0.1058	0.0438	0.0282	0.0483	0.0132	0.0129
1231.3	0.0181	0.0384	0.0048	-0.0169	0.0113	0.0045
1268.8	-0.0948	0.0436	0.0253	-0.0477	0.0125	0.0127
1306.3	0.0041	0.0579	0.0011	-0.0671	0.0163	0.0179
1343.8	-0.0368	0.0829	0.0098	-0.0525	0.0246	0.0140
1381.3	-0.2206	0.1435	0.0589	0.0353	0.0429	0.0094

850 - 950 MeV	June (2010)			April (2011)		
$IM(\pi^\phi p)$	F	Δ_{stat} [μb]	Δ_{sys} [μb]	F	Δ_{stat} [μb]	Δ_{sys} [μb]
1103.1	0.0186	0.1547	0.0050	-0.0071	0.0493	0.0019
1149.4	0.1839	0.0805	0.0491	0.0656	0.0259	0.0175
1195.6	0.1359	0.0507	0.0363	0.1096	0.0159	0.0293
1241.9	0.1807	0.0441	0.0482	0.0356	0.0137	0.0095
1288.1	-0.1080	0.0465	0.0288	-0.0342	0.0141	0.0091
1334.4	-0.0840	0.0562	0.0224	-0.0356	0.0164	0.0095
1380.6	0.1427	0.0713	0.0381	-0.0463	0.0207	0.0124
1426.9	0.1167	0.1253	0.0311	0.0247	0.0337	0.0066

950 - 1050 MeV	June (2010)			April (2011)		
$IM(\pi^\phi p)$	F	Δ_{stat} [μb]	Δ_{sys} [μb]	F	Δ_{stat} [μb]	Δ_{sys} [μb]
1109.4	-0.0297	0.0962	0.0079	-0.0493	0.0274	0.0132
1168.1	-0.0455	0.0558	0.0122	0.0343	0.0155	0.0091
1226.9	0.0377	0.0439	0.0101	0.0377	0.0116	0.0101
1285.6	-0.0508	0.0439	0.0136	-0.0100	0.0116	0.0027
1344.4	0.0823	0.0486	0.0220	-0.0453	0.0124	0.0121
1403.1	-0.0702	0.0559	0.0187	-0.0514	0.0142	0.0137
1461.9	-0.0147	0.0798	0.0039	0.0480	0.0208	0.0128
1520.6	0.0640	0.1578	0.0171	0.0266	0.0447	0.0071

1050 - 1150 MeV	June (2010)			April (2011)		
$IM(\pi^\phi p)$	F	Δ_{stat} [μb]	Δ_{sys} [μb]	F	Δ_{stat} [μb]	Δ_{sys} [μb]
1110.9	-0.0584	0.0786	0.0156	0.0936	0.0276	0.0250
1172.8	0.1257	0.0447	0.0336	-0.0259	0.0151	0.0069
1234.7	0.1062	0.0374	0.0283	0.0261	0.0122	0.0070
1296.6	-0.1561	0.0421	0.0417	0.0105	0.0137	0.0028
1358.4	-0.0590	0.0428	0.0158	-0.0299	0.0143	0.0080
1420.3	0.0167	0.0439	0.0045	-0.0326	0.0140	0.0087
1482.2	-0.0252	0.0535	0.0067	-0.0483	0.0170	0.0129
1544.1	-0.1584	0.0868	0.0423	-0.0433	0.0298	0.0115

1150 - 1250 MeV	June (2010)			April (2011)		
$IM(\pi^\phi p)$	F	Δ_{stat} [μb]	Δ_{sys} [μb]	F	Δ_{stat} [μb]	Δ_{sys} [μb]
1113.8	0.0799	0.1051	0.0213	0.0660	0.0342	0.0176
1181.3	-0.1457	0.0545	0.0389	0.0378	0.0169	0.0101
1248.8	-0.0789	0.0501	0.0211	0.0363	0.0145	0.0097
1316.3	0.0659	0.0587	0.0176	-0.0013	0.0176	0.0004
1383.8	0.0909	0.0563	0.0243	-0.0207	0.0179	0.0055
1451.3	-0.0305	0.0555	0.0081	-0.0231	0.0164	0.0062
1518.8	-0.0977	0.0665	0.0261	-0.0291	0.0192	0.0078
1586.3	0.0433	0.1093	0.0116	0.0187	0.0323	0.0050

1250 - 1350 MeV	June (2010)			April (2011)		
$IM(\pi^\phi p)$	F	Δ_{stat} [μb]	Δ_{sys} [μb]	F	Δ_{stat} [μb]	Δ_{sys} [μb]
1134.4	-0.1877	0.0876	0.0501	0.0351	0.0291	0.0094
1203.1	-0.0582	0.0573	0.0155	0.0111	0.0170	0.0030
1271.9	-0.0900	0.0601	0.0240	0.0255	0.0173	0.0068
1340.6	-0.2061	0.0670	0.0550	0.0230	0.0206	0.0061
1409.4	0.0865	0.0626	0.0231	-0.0415	0.0205	0.0111
1478.1	-0.0025	0.0645	0.0007	0.0058	0.0200	0.0016
1546.9	-0.3887	0.0758	0.1037	-0.0062	0.0230	0.0016
1615.6	-0.0883	0.1121	0.0236	-0.0161	0.0322	0.0043

1350 - 1450 MeV	June (2010)			April (2011)		
$IM(\pi^\phi p)$	F	Δ_{stat} [μb]	Δ_{sys} [μb]	F	Δ_{stat} [μb]	Δ_{sys} [μb]
1140.6				0.0984	0.0343	0.0263
1221.9				0.0659	0.0215	0.0176
1303.1				0.0454	0.0254	0.0121
1384.4				-0.0460	0.0266	0.0123
1465.6				-0.0210	0.0273	0.0056
1546.9				-0.0832	0.0284	0.0222
1628.1				-0.0693	0.0367	0.0185
1709.4				-0.0671	0.0697	0.0179

550 - 650 MeV	Carbon			Hydrogen		
$cos(\theta_\pi)$	T	Δ_{stat} [μb]	Δ_{sys} [μb]	T	Δ_{stat} [μb]	Δ_{sys} [μb]
-0.9	-0.0368	0.0247	0.0482	-0.0318	0.0211	0.0363
-0.6	-0.0066	0.0205	0.0479	-0.0054	0.0175	0.0431
-0.4	-0.0440	0.0183	0.0285	-0.0399	0.0173	0.0290
-0.1	-0.0828	0.0179	0.1258	-0.0822	0.0176	0.1224
0.1	-0.0612	0.0202	0.0924	-0.0558	0.0185	0.0865
0.4	0.0071	0.0240	0.2453	0.0064	0.0223	0.2326
0.6	-0.0348	0.0339	0.1545	-0.0294	0.0281	0.1287
0.9	-0.0154	0.0604	0.0788	-0.0112	0.0321	0.0673

650 - 750 MeV	Carbon			Hydrogen		
$cos(\theta_\pi)$	T	Δ_{stat} [μb]	Δ_{sys} [μb]	T	Δ_{stat} [μb]	Δ_{sys} [μb]
-0.9	0.0597	0.0091	0.0283	0.0397	0.0060	0.0204
-0.6	0.0128	0.0077	0.0451	0.0092	0.0055	0.0323
-0.4	-0.0276	0.0073	0.0056	-0.0213	0.0057	0.0041
-0.1	-0.0343	0.0073	0.0360	-0.0276	0.0058	0.0284
0.1	-0.0558	0.0079	0.0156	-0.0455	0.0065	0.0123
0.4	-0.0789	0.0094	0.0244	-0.0642	0.0076	0.0200
0.6	-0.0450	0.0127	0.0755	-0.0325	0.0090	0.0555
0.9	0.0155	0.0197	0.1172	0.0075	0.0095	0.0578

750 - 850 MeV	Carbon			Hydrogen		
$cos(\theta_\pi)$	T	Δ_{stat} [μb]	Δ_{sys} [μb]	T	Δ_{stat} [μb]	Δ_{sys} [μb]
-0.9	0.1322	0.0095	0.0728	0.0955	0.0067	0.0511
-0.6	0.1377	0.0091	0.0295	0.1081	0.0069	0.0231
-0.4	0.0723	0.0089	0.0270	0.0637	0.0077	0.0229
-0.1	-0.0501	0.0096	0.0567	-0.0441	0.0083	0.0503
0.1	-0.1269	0.0101	0.0150	-0.1194	0.0093	0.0136
0.4	-0.1638	0.0108	0.0243	-0.1693	0.0109	0.0260
0.6	-0.1269	0.0134	0.0221	-0.1177	0.0122	0.0175
0.9	0.0457	0.0190	0.1462	0.0262	0.0106	0.0808

850 - 950 MeV	Carbon			Hydrogen		
$cos(\theta_\pi)$	T	Δ_{stat} [μb]	Δ_{sys} [μb]	T	Δ_{stat} [μb]	Δ_{sys} [μb]
-0.9	0.1022	0.0112	0.0779	0.0801	0.0086	0.0617
-0.6	0.1808	0.0107	0.0533	0.1575	0.0090	0.0461
-0.4	0.1047	0.0110	0.0170	0.0996	0.0102	0.0191
-0.1	0.0184	0.0116	0.0007	0.0168	0.0109	0.0014
0.1	-0.0674	0.0126	0.0694	-0.0644	0.0119	0.0655
0.4	-0.0944	0.0141	0.1018	-0.0936	0.0135	0.1017
0.6	-0.0172	0.0163	0.0809	-0.0184	0.0150	0.0891
0.9	0.0822	0.0204	0.0603	0.0559	0.0132	0.0382

950 - 1050 MeV	Carbon			Hydrogen		
$cos(\theta_\pi)$	T	Δ_{stat} [μb]	Δ_{sys} [μb]	T	Δ_{stat} [μb]	Δ_{sys} [μb]
-0.9	0.0400	0.0105	0.0991	0.0336	0.0088	0.0783
-0.6	0.0751	0.0089	0.0021	0.0714	0.0084	0.0026
-0.4	0.1016	0.0091	0.0520	0.1059	0.0093	0.0544
-0.1	0.0779	0.0104	0.0376	0.0734	0.0098	0.0360
0.1	-0.0015	0.0114	0.0174	-0.0006	0.0105	0.0215
0.4	0.0244	0.0119	0.0757	0.0246	0.0119	0.0732
0.6	0.0799	0.0134	0.0603	0.0798	0.0132	0.0571
0.9	0.1225	0.0164	0.0575	0.0858	0.0112	0.0435

1050 - 1150 MeV	Carbon			Hydrogen		
$cos(\theta_\pi)$	T	Δ_{stat} [μb]	Δ_{sys} [μb]	T	Δ_{stat} [μb]	Δ_{sys} [μb]
-0.9	-0.0005	0.0124	0.0662	-0.0013	0.0104	0.0562
-0.6	0.0396	0.0094	0.0269	0.0402	0.0096	0.0277
-0.4	0.0669	0.0094	0.0958	0.0735	0.0103	0.1042
-0.1	0.0804	0.0106	0.0440	0.0842	0.0109	0.0487
0.1	0.0536	0.0124	0.0512	0.0507	0.0113	0.0491
0.4	0.0938	0.0138	0.0620	0.0874	0.0127	0.0633
0.6	0.1583	0.0155	0.1258	0.1549	0.0139	0.1348
0.9	0.1537	0.0160	0.0383	0.1244	0.0126	0.0267

1150 - 1250 MeV	Carbon			Hydrogen		
$cos(\theta_\pi)$	T	Δ_{stat} [μb]	Δ_{sys} [μb]	T	Δ_{stat} [μb]	Δ_{sys} [μb]
-0.9	-0.0275	0.0152	0.0697	-0.0251	0.0136	0.0648
-0.6	-0.0284	0.0121	0.1414	-0.0294	0.0128	0.1495
-0.4	0.0792	0.0124	0.0219	0.0870	0.0134	0.0220
-0.1	0.1110	0.0131	0.0540	0.1218	0.0138	0.0517
0.1	0.0807	0.0149	0.0931	0.0874	0.0142	0.1061
0.4	0.1299	0.0171	0.1317	0.1297	0.0159	0.1361
0.6	0.0648	0.0182	0.0550	0.0680	0.0179	0.0541
0.9	0.0780	0.0185	0.0544	0.0693	0.0161	0.0520

1250 - 1350 MeV	Carbon			Hydrogen		
$cos(\theta_\pi)$	T	Δ_{stat} [μb]	Δ_{sys} [μb]	T	Δ_{stat} [μb]	Δ_{sys} [μb]
-0.9	0.0612	0.0198	0.0112	0.0488	0.0152	0.0072
-0.6	0.0067	0.0155	0.0540	0.0063	0.0145	0.0502
-0.4	0.0910	0.0148	0.0325	0.0999	0.0156	0.0307
-0.1	0.0390	0.0158	0.0588	0.0412	0.0160	0.0617
0.1	0.0382	0.0177	0.1820	0.0401	0.0162	0.2018
0.4	0.0862	0.0198	0.2194	0.0897	0.0183	0.2312
0.6	0.0844	0.0203	0.0225	0.0904	0.0213	0.0260
0.9	0.0501	0.0230	0.1368	0.0414	0.0180	0.1130

1350 - 1450 MeV	Carbon			Hydrogen		
$cos(\theta_\pi)$	T	Δ_{stat} [μb]	Δ_{sys} [μb]	T	Δ_{stat} [μb]	Δ_{sys} [μb]
-0.9	0.0314	0.0228	0.0685	0.0276	0.0209	0.0648
-0.6	0.0889	0.0207	0.0512	0.0960	0.0213	0.0517
-0.4	0.1031	0.0219	0.0095	0.1028	0.0220	0.0219
-0.1	0.0168	0.0256	0.0350	0.0211	0.0218	0.0383
0.1	0.0164	0.0242	0.0220	0.0226	0.0236	0.0110
0.4	0.0239	0.0251	0.0402	0.0257	0.0253	0.0514
0.6	0.0425	0.0365	0.2946	0.0615	0.0281	0.2190
0.9	-0.0176	0.0299	0.0145	-0.0166	0.0266	0.0106

550 - 650 MeV	Carbon			Hydrogen		
$cos(\theta_p)$	T	Δ_{stat} [μb]	Δ_{sys} [μb]	T	Δ_{stat} [μb]	Δ_{sys} [μb]
-0.9	0.3001	0.0507	0.2040	0.3611	0.0557	0.2699
-0.6	0.2004	0.0459	0.0932	0.1866	0.0412	0.0763
-0.4	0.0565	0.0339	0.3172	0.0559	0.0305	0.3009
-0.1	0.1006	0.0262	0.2291	0.0908	0.0250	0.2294
0.1	0.1975	0.0242	0.2378	0.1911	0.0236	0.2472
0.4	0.1839	0.0263	0.1162	0.1687	0.0240	0.1203
0.6	0.3579	0.0417	0.0513	0.2806	0.0295	0.0548
0.9	0.2799	0.0442	0.1912	0.1555	0.0226	0.0979

650 - 750 MeV	Carbon			Hydrogen		
$cos(\theta_p)$	T	Δ_{stat} [μb]	Δ_{sys} [μb]	T	Δ_{stat} [μb]	Δ_{sys} [μb]
-0.9	0.1975	0.0214	0.0188	0.2065	0.0210	0.0270
-0.6	0.1372	0.0167	0.0988	0.1289	0.0152	0.0934
-0.4	0.0917	0.0133	0.1172	0.0728	0.0105	0.0945
-0.1	0.1158	0.0108	0.2053	0.0855	0.0081	0.1610
0.1	0.1186	0.0098	0.1524	0.0971	0.0078	0.1330
0.4	0.1715	0.0099	0.0892	0.1386	0.0079	0.0814
0.6	0.3346	0.0145	0.0134	0.2085	0.0084	0.0036
0.9	0.3113	0.0166	0.1112	0.1245	0.0061	0.0457

750 - 850 MeV	Carbon			Hydrogen		
$cos(\theta_p)$	T	Δ_{stat} [μb]	Δ_{sys} [μb]	T	Δ_{stat} [μb]	Δ_{sys} [μb]
-0.9	0.1585	0.0224	0.0000	0.2125	0.0274	0.0198
-0.6	0.0935	0.0196	0.0137	0.0998	0.0201	0.0084
-0.4	0.0597	0.0154	0.0863	0.0624	0.0151	0.1038
-0.1	0.0457	0.0134	0.1026	0.0394	0.0116	0.0983
0.1	0.0914	0.0125	0.1612	0.0762	0.0104	0.1488
0.4	0.0939	0.0119	0.0857	0.0855	0.0107	0.0870
0.6	0.1272	0.0140	0.1498	0.0952	0.0101	0.1162
0.9	0.1058	0.0154	0.0000	0.0525	0.0075	0.0021

850 - 950 MeV	Carbon			Hydrogen		
$cos(\theta_p)$	T	Δ_{stat} [μb]	Δ_{sys} [μb]	T	Δ_{stat} [μb]	Δ_{sys} [μb]
-0.9	0.0038	0.0277	0.0867	-0.0059	0.0324	0.0826
-0.6	-0.0327	0.0218	0.0363	-0.0371	0.0241	0.0467
-0.4	-0.0188	0.0186	0.0279	-0.0286	0.0189	0.0219
-0.1	-0.0737	0.0167	0.0763	-0.0690	0.0151	0.0803
0.1	0.0033	0.0161	0.0629	-0.0012	0.0143	0.0690
0.4	-0.0519	0.0158	0.0429	-0.0459	0.0142	0.0343
0.6	-0.0639	0.0154	0.1134	-0.0462	0.0114	0.0846
0.9	-0.0612	0.0193	0.0360	-0.0359	0.0103	0.0251

950 - 1050 MeV	Carbon			Hydrogen		
$cos(\theta_p)$	T	Δ_{stat} [μb]	Δ_{sys} [μb]	T	Δ_{stat} [μb]	Δ_{sys} [μb]
-0.9	-0.1397	0.0230	0.0737	-0.1668	0.0254	0.0906
-0.6	-0.1200	0.0192	0.0043	-0.1294	0.0195	0.0247
-0.4	-0.1209	0.0164	0.0299	-0.1344	0.0161	0.0598
-0.1	-0.0964	0.0150	0.0961	-0.0952	0.0139	0.1175
0.1	-0.0885	0.0140	0.0196	-0.0891	0.0133	0.0326
0.4	-0.0727	0.0137	0.0933	-0.0730	0.0128	0.0872
0.6	-0.1248	0.0125	0.1302	-0.0993	0.0097	0.1010
0.9	-0.0859	0.0197	0.0629	-0.0563	0.0116	0.0488

1050 - 1150 MeV	Carbon			Hydrogen		
$cos(\theta_p)$	T	Δ_{stat} [μb]	Δ_{sys} [μb]	T	Δ_{stat} [μb]	Δ_{sys} [μb]
-0.9	-0.0979	0.0231	0.0632	-0.1219	0.0281	0.0943
-0.6	-0.1642	0.0195	0.0707	-0.1924	0.0208	0.0703
-0.4	-0.0833	0.0167	0.0651	-0.0874	0.0168	0.0774
-0.1	-0.1409	0.0163	0.0221	-0.1359	0.0150	0.0315
0.1	-0.0986	0.0152	0.0942	-0.0923	0.0138	0.0993
0.4	-0.1074	0.0130	0.0086	-0.1078	0.0129	0.0062
0.6	-0.0694	0.0152	0.0223	-0.0583	0.0122	0.0217
0.9	-0.0471	0.0291	0.0272	-0.0281	0.0170	0.0149

1150 - 1250 MeV	Carbon			Hydrogen		
$cos(\theta_p)$	T	Δ_{stat} [μb]	Δ_{sys} [μb]	T	Δ_{stat} [μb]	Δ_{sys} [μb]
-0.9	-0.1471	0.0328	0.1084	-0.2002	0.0356	0.1822
-0.6	-0.0775	0.0245	0.0800	-0.0892	0.0251	0.1080
-0.4	-0.0680	0.0191	0.0222	-0.0764	0.0211	0.0173
-0.1	-0.0953	0.0172	0.1266	-0.1010	0.0174	0.1117
0.1	-0.0993	0.0154	0.0163	-0.0988	0.0149	0.0126
0.4	-0.0805	0.0171	0.0567	-0.0802	0.0165	0.0613
0.6	-0.0274	0.0237	0.0197	-0.0244	0.0194	0.0076
0.9	-0.1300	0.0534	0.1746	-0.0879	0.0290	0.0907

1250 - 1350 MeV	Carbon			Hydrogen		
$cos(\theta_p)$	T	Δ_{stat} [μb]	Δ_{sys} [μb]	T	Δ_{stat} [μb]	Δ_{sys} [μb]
-0.9	-0.0604	0.0401	0.1998	-0.0856	0.0415	0.2452
-0.6	-0.0449	0.0261	0.1204	-0.0539	0.0281	0.0775
-0.4	-0.1177	0.0229	0.1407	-0.1255	0.0224	0.1311
-0.1	-0.0733	0.0187	0.0668	-0.0763	0.0172	0.0943
0.1	-0.0890	0.0182	0.0286	-0.0805	0.0160	0.0282
0.4	-0.1020	0.0267	0.1189	-0.0838	0.0215	0.0972
0.6	-0.1287	0.0376	0.0629	-0.1152	0.0281	0.0844
0.9	-0.0222	0.0701	0.0573	-0.0266	0.0442	0.0578

1350 - 1450 MeV	Carbon			Hydrogen		
$cos(\theta_p)$	T	Δ_{stat} [μb]	Δ_{sys} [μb]	T	Δ_{stat} [μb]	Δ_{sys} [μb]
-0.9	-0.1679	0.0563	0.1143	-0.2078	0.0568	0.1075
-0.6	-0.0056	0.0320	0.0650	-0.0069	0.0377	0.0727
-0.4	-0.0679	0.0295	0.0003	-0.0731	0.0263	0.0336
-0.1	-0.0937	0.0227	0.0003	-0.0971	0.0220	0.0086
0.1	-0.0268	0.0265	0.0202	-0.0275	0.0246	0.0196
0.4	-0.0855	0.0457	0.0349	-0.0887	0.0352	0.0700
0.6	-0.1278	0.0719	0.2475	-0.0822	0.0422	0.1648
0.9	-0.2460	0.1037	0.2636	-0.1704	0.0728	0.0246

550 - 650 MeV	Carbon			Hydrogen		
$IM(\pi^\phi\pi^\phi)$	T	Δ_{stat} [μb]	Δ_{sys} [μb]	T	Δ_{stat} [μb]	Δ_{sys} [μb]
292.5	-0.1099	0.0379	0.0045	-0.0805	0.0264	0.0049
317.5	0.0309	0.0340	0.0623	0.0270	0.0249	0.0522
342.5	0.1524	0.0328	0.2276	0.1094	0.0244	0.1829
367.5	0.0404	0.0321	0.1427	0.0316	0.0241	0.1052
392.5	0.2881	0.0298	0.1108	0.2819	0.0273	0.1168
417.5	0.2736	0.0307	0.0208	0.2997	0.0316	0.0251
442.5	0.2777	0.0348	0.1050	0.3305	0.0399	0.1202
467.5	0.4348	0.0443	0.0207	0.6470	0.0600	0.0482

650 - 750 MeV	Carbon			Hydrogen		
$IM(\pi^\phi\pi^\phi)$	T	Δ_{stat} [μb]	Δ_{sys} [μb]	T	Δ_{stat} [μb]	Δ_{sys} [μb]
296.3	-0.1673	0.0157	0.0024	-0.1358	0.0122	0.0017
328.8	-0.1218	0.0140	0.0090	-0.0925	0.0102	0.0109
361.3	0.0272	0.0121	0.0139	0.0216	0.0092	0.0154
393.8	0.1647	0.0112	0.0755	0.1264	0.0084	0.0598
426.3	0.2090	0.0109	0.1309	0.1574	0.0080	0.0995
458.8	0.3373	0.0119	0.0340	0.2598	0.0086	0.0235
491.3	0.3653	0.0140	0.0818	0.2791	0.0098	0.0635
523.8	0.4632	0.0216	0.1932	0.3224	0.0133	0.1350

750 - 850 MeV	Carbon			Hydrogen		
$IM(\pi^\phi\pi^\phi)$	T	Δ_{stat} [μb]	Δ_{sys} [μb]	T	Δ_{stat} [μb]	Δ_{sys} [μb]
300.0	-0.1821	0.0246	0.0504	-0.1698	0.0221	0.0523
340.0	-0.2315	0.0206	0.0037	-0.2100	0.0171	0.0035
380.0	-0.1799	0.0178	0.0340	-0.1405	0.0129	0.0222
420.0	-0.0416	0.0147	0.0492	-0.0305	0.0109	0.0303
460.0	0.0666	0.0118	0.0233	0.0583	0.0103	0.0243
500.0	0.1754	0.0115	0.0198	0.1573	0.0100	0.0199
540.0	0.3055	0.0133	0.0314	0.2788	0.0114	0.0304
580.0	0.3798	0.0184	0.0955	0.3638	0.0158	0.1120

850 - 950 MeV	Carbon			Hydrogen		
$IM(\pi^\phi\pi^\phi)$	T	Δ_{stat} [μb]	Δ_{sys} [μb]	T	Δ_{stat} [μb]	Δ_{sys} [μb]
303.1	-0.1507	0.0338	0.0997	-0.1355	0.0262	0.1116
349.4	-0.1716	0.0297	0.0431	-0.1428	0.0202	0.1054
395.6	-0.3141	0.0258	0.0773	-0.2402	0.0168	0.0381
441.9	-0.1925	0.0201	0.0129	-0.1561	0.0148	0.0142
488.1	-0.1306	0.0154	0.0025	-0.1193	0.0137	0.0043
534.4	0.0184	0.0150	0.0058	0.0157	0.0132	0.0045
580.6	0.1063	0.0141	0.0537	0.1092	0.0144	0.0571
626.9	0.1227	0.0171	0.0665	0.1243	0.0170	0.0661

950 - 1050 MeV	Carbon			Hydrogen		
$IM(\pi^\phi\pi^\phi)$	T	Δ_{stat} [μb]	Δ_{sys} [μb]	T	Δ_{stat} [μb]	Δ_{sys} [μb]
306.9	-0.0422	0.0280	0.0184	-0.0447	0.0208	0.0884
360.6	-0.1347	0.0215	0.1022	-0.1112	0.0166	0.0651
414.4	-0.2115	0.0188	0.0316	-0.1767	0.0141	0.0359
468.1	-0.1948	0.0169	0.0306	-0.1578	0.0129	0.0256
521.9	-0.1348	0.0139	0.1120	-0.1214	0.0122	0.1016
575.6	-0.1143	0.0135	0.1204	-0.1142	0.0125	0.1250
629.4	-0.0361	0.0128	0.0636	-0.0395	0.0136	0.0669
683.1	-0.0701	0.0148	0.0012	-0.0733	0.0156	0.0012

1050 - 1150 MeV	Carbon			Hydrogen		
$IM(\pi^\phi\pi^\phi)$	T	Δ_{stat} [μb]	Δ_{sys} [μb]	T	Δ_{stat} [μb]	Δ_{sys} [μb]
310.9	-0.0777	0.0304	0.1075	-0.0623	0.0226	0.0744
372.8	-0.1299	0.0244	0.0696	-0.1031	0.0178	0.0510
434.7	-0.1509	0.0189	0.1188	-0.1290	0.0154	0.0915
496.6	-0.1542	0.0161	0.0552	-0.1374	0.0141	0.0463
558.4	-0.0657	0.0139	0.0298	-0.0642	0.0134	0.0293
620.3	-0.0776	0.0138	0.0469	-0.0823	0.0144	0.0492
682.2	-0.0833	0.0151	0.0331	-0.0847	0.0152	0.0402
744.1	-0.1544	0.0185	0.1161	-0.1682	0.0195	0.1276

1150 - 1250 MeV	Carbon			Hydrogen		
$IM(\pi^\phi\pi^\phi)$	T	Δ_{stat} [μb]	Δ_{sys} [μb]	T	Δ_{stat} [μb]	Δ_{sys} [μb]
313.8	-0.0875	0.0420	0.1576	-0.0768	0.0283	0.1247
381.3	-0.1761	0.0289	0.0340	-0.1389	0.0216	0.0278
448.8	-0.1509	0.0238	0.0597	-0.1321	0.0188	0.0291
516.3	-0.0973	0.0194	0.1132	-0.0943	0.0177	0.1176
583.8	-0.0977	0.0175	0.1064	-0.1016	0.0178	0.1116
651.3	-0.0296	0.0169	0.1457	-0.0316	0.0177	0.1540
718.8	-0.0516	0.0178	0.0348	-0.0541	0.0207	0.0445
786.3	-0.1409	0.0225	0.0375	-0.1669	0.0254	0.0541

1250 - 1350 MeV	Carbon			Hydrogen		
$IM(\pi^\phi\pi^\phi)$	T	Δ_{stat} [μb]	Δ_{sys} [μb]	T	Δ_{stat} [μb]	Δ_{sys} [μb]
284.7	0.0031	0.0888	0.4440	0.0019	0.0661	0.4127
354.1	-0.1805	0.0400	0.2137	-0.1659	0.0304	0.1741
423.4	-0.1361	0.0307	0.1214	-0.1235	0.0239	0.1102
492.8	-0.1114	0.0282	0.0382	-0.1061	0.0222	0.0485
562.2	-0.1434	0.0238	0.1342	-0.1318	0.0213	0.1081
631.6	-0.0448	0.0215	0.0263	-0.0430	0.0204	0.0201
700.9	-0.0529	0.0213	0.0505	-0.0499	0.0208	0.0458
770.3	-0.0715	0.0232	0.0904	-0.0854	0.0247	0.0961

1350 - 1450 MeV	Carbon			Hydrogen		
$IM(\pi^\phi\pi^\phi)$	T	Δ_{stat} [μb]	Δ_{sys} [μb]	T	Δ_{stat} [μb]	Δ_{sys} [μb]
284.7	0.1209	0.0915	0.0248	0.0511	0.0803	0.0818
354.1	-0.0364	0.0487	0.0022	-0.0333	0.0401	0.0116
423.4	-0.1139	0.0526	0.1565	-0.0925	0.0355	0.0946
492.8	-0.1551	0.0546	0.2605	-0.1074	0.0342	0.2292
562.2	-0.1521	0.0341	0.1362	-0.1660	0.0324	0.1022
631.6	-0.1175	0.0298	0.0594	-0.1259	0.0302	0.0642
700.9	-0.0131	0.0295	0.0039	-0.0188	0.0295	0.0075
770.3	-0.0294	0.0345	0.0027	-0.0173	0.0329	0.0005

550 - 650 MeV	Carbon			Hydrogen		
$IM(\pi^\phi p)$	T	Δ_{stat} [μb]	Δ_{sys} [μb]	T	Δ_{stat} [μb]	Δ_{sys} [μb]
1096.9	-0.4191	0.0401	0.1686	-0.2943	0.0254	0.1246
1120.6	-0.2983	0.0310	0.1072	-0.1878	0.0188	0.0670
1144.4	-0.2384	0.0236	0.0488	-0.1876	0.0181	0.0382
1168.1	-0.0735	0.0203	0.0376	-0.0628	0.0172	0.0352
1191.9	0.0279	0.0183	0.1283	0.0246	0.0164	0.1140
1215.6	0.0786	0.0185	0.2512	0.0825	0.0190	0.2623
1239.4	0.0953	0.0234	0.2188	0.1019	0.0248	0.2354
1263.1	0.0581	0.0311	0.2253	0.0761	0.0416	0.3023

650 - 750 MeV	Carbon			Hydrogen		
$IM(\pi^\phi p)$	T	Δ_{stat} [μb]	Δ_{sys} [μb]	T	Δ_{stat} [μb]	Δ_{sys} [μb]
1096.9	-0.3887	0.0189	0.1670	-0.3455	0.0147	0.1461
1130.6	-0.2582	0.0111	0.0809	-0.2151	0.0088	0.0664
1164.4	-0.1479	0.0077	0.0418	-0.1147	0.0058	0.0326
1198.1	-0.0020	0.0061	0.1016	-0.0014	0.0046	0.0764
1231.9	0.0549	0.0063	0.1646	0.0412	0.0047	0.1232
1265.6	0.0673	0.0090	0.1716	0.0475	0.0063	0.1208
1299.4	0.0731	0.0133	0.1531	0.0522	0.0096	0.1135
1333.1	0.0023	0.0246	0.2291	0.0016	0.0175	0.1651

750 - 850 MeV	Carbon			Hydrogen		
$IM(\pi^\phi p)$	T	Δ_{stat} [μb]	Δ_{sys} [μb]	T	Δ_{stat} [μb]	Δ_{sys} [μb]
1118.8	-0.0694	0.0197	0.0264	-0.0680	0.0186	0.0290
1156.3	-0.0074	0.0115	0.0479	-0.0079	0.0108	0.0456
1193.8	0.0118	0.0079	0.0579	0.0101	0.0069	0.0510
1231.3	-0.0077	0.0072	0.1269	-0.0063	0.0060	0.1063
1268.8	-0.0452	0.0082	0.0605	-0.0381	0.0067	0.0505
1306.3	-0.0286	0.0110	0.1104	-0.0223	0.0086	0.0884
1343.8	0.0285	0.0164	0.2767	0.0248	0.0131	0.2271
1381.3	-0.0099	0.0269	0.1474	-0.0096	0.0227	0.1223

850 - 950 MeV	Carbon			Hydrogen		
$IM(\pi^\phi p)$	T	Δ_{stat} [μb]	Δ_{sys} [μb]	T	Δ_{stat} [μb]	Δ_{sys} [μb]
1103.1	0.0615	0.0361	0.1137	0.0611	0.0289	0.1171
1149.4	0.1222	0.0164	0.0435	0.1218	0.0159	0.0442
1195.6	0.1496	0.0104	0.0638	0.1436	0.0097	0.0604
1241.9	0.0409	0.0092	0.0386	0.0364	0.0081	0.0332
1288.1	-0.0773	0.0094	0.1331	-0.0713	0.0086	0.1231
1334.4	-0.1010	0.0119	0.0777	-0.0848	0.0096	0.0673
1380.6	-0.0036	0.0159	0.0350	-0.0031	0.0124	0.0272
1426.9	0.0532	0.0261	0.2027	0.0418	0.0198	0.1551

950 - 1050 MeV	Carbon			Hydrogen		
$IM(\pi^\phi p)$	T	Δ_{stat} [μb]	Δ_{sys} [μb]	T	Δ_{stat} [μb]	Δ_{sys} [μb]
1109.4	0.0113	0.0182	0.0515	0.0105	0.0179	0.0543
1168.1	0.1511	0.0109	0.0790	0.1505	0.0104	0.0789
1226.9	0.1491	0.0083	0.0838	0.1433	0.0078	0.0804
1285.6	-0.0362	0.0086	0.0501	-0.0330	0.0078	0.0454
1344.4	-0.0939	0.0088	0.1106	-0.0879	0.0081	0.1028
1403.1	-0.0366	0.0108	0.1082	-0.0303	0.0091	0.0908
1461.9	0.0531	0.0153	0.1702	0.0480	0.0135	0.1541
1520.6	0.0006	0.0304	0.0429	0.0024	0.0296	0.0623

1050 - 1150 MeV	Carbon			Hydrogen		
$IM(\pi^\phi p)$	T	Δ_{stat} [μb]	Δ_{sys} [μb]	T	Δ_{stat} [μb]	Δ_{sys} [μb]
1110.9	-0.0986	0.0187	0.0624	-0.1063	0.0194	0.0717
1172.8	0.1111	0.0105	0.0639	0.1176	0.0108	0.0732
1234.7	0.1672	0.0096	0.0262	0.1562	0.0088	0.0254
1296.6	-0.0117	0.0105	0.0047	-0.0113	0.0097	0.0051
1358.4	-0.1166	0.0102	0.1403	-0.1150	0.0099	0.1380
1420.3	0.0327	0.0108	0.0382	0.0300	0.0099	0.0350
1482.2	0.0741	0.0138	0.0933	0.0623	0.0116	0.0773
1544.1	0.0162	0.0249	0.2733	0.0135	0.0206	0.2292

1150 - 1250 MeV	Carbon			Hydrogen		
$IM(\pi^\phi p)$	T	Δ_{stat} [μb]	Δ_{sys} [μb]	T	Δ_{stat} [μb]	Δ_{sys} [μb]
1113.8	-0.0871	0.0239	0.1274	-0.0998	0.0263	0.1405
1181.3	0.0559	0.0127	0.0200	0.0579	0.0129	0.0196
1248.8	0.1583	0.0120	0.0549	0.1512	0.0111	0.0516
1316.3	-0.0511	0.0142	0.0353	-0.0487	0.0133	0.0295
1383.8	-0.0706	0.0125	0.0947	-0.0777	0.0137	0.1031
1451.3	-0.0034	0.0128	0.1441	-0.0031	0.0122	0.1380
1518.8	0.0203	0.0158	0.1326	0.0180	0.0138	0.1163
1586.3	-0.0219	0.0290	0.2299	-0.0223	0.0240	0.2029

1250 - 1350 MeV	Carbon			Hydrogen		
$IM(\pi^\phi p)$	T	Δ_{stat} [μb]	Δ_{sys} [μb]	T	Δ_{stat} [μb]	Δ_{sys} [μb]
1134.4	-0.0276	0.0233	0.0347	-0.0266	0.0229	0.0397
1203.1	0.0902	0.0147	0.0007	0.0860	0.0135	0.0045
1271.9	0.0612	0.0145	0.0778	0.0595	0.0139	0.0740
1340.6	-0.0166	0.0182	0.1479	-0.0150	0.0164	0.1302
1409.4	-0.0527	0.0160	0.1043	-0.0512	0.0158	0.1119
1478.1	0.0005	0.0162	0.1505	-0.0019	0.0150	0.1421
1546.9	0.0323	0.0186	0.1119	0.0278	0.0164	0.1005
1615.6	0.1006	0.0311	0.1550	0.0767	0.0241	0.1211

1350 - 1450 MeV	Carbon			Hydrogen		
$IM(\pi^\phi p)$	T	Δ_{stat} [μb]	Δ_{sys} [μb]	T	Δ_{stat} [μb]	Δ_{sys} [μb]
1140.6	-0.0448	0.0301	0.0211	-0.0372	0.0267	0.0200
1221.9	0.0609	0.0191	0.0037	0.0588	0.0179	0.0041
1303.1	0.0774	0.0215	0.0399	0.0755	0.0201	0.0453
1384.4	-0.0522	0.0220	0.1215	-0.0497	0.0215	0.1201
1465.6	-0.0951	0.0232	0.2731	-0.0900	0.0208	0.2576
1546.9	0.0198	0.0229	0.0006	0.0205	0.0217	0.0066
1628.1	0.0200	0.0335	0.0208	0.0158	0.0277	0.0122
1709.4	-0.0634	0.0605	0.1714	-0.0615	0.0605	0.1550

Bibliography

[1] E. Rutherford, "The Scattering of α and β Particles by Matter and the Structure of the Atom," *Philosophical Magazine Series 6*, vol. 21, 1911.

[2] J. Chadwick, "Possible existence of a neutron," *Nature 129*, 1932. doi: 10.1038/129312a0

[3] R. Frisch and O. Stern, "Über die magnetische Ablenkung von Wasserstoffmolekülen und das magnetische Moment des Protons," *Zeitschrift für Physik*, vol. 85, 1933. doi: 10.1007/BF01330773.

[4] R. MCAllister and R. Hofstadler, "Elastic-scattering of 188-MeV Electrons From the Proton and the α Particle," *Physical Review*, vol. 102, 1965. doi: 10.1103/PhysRev.102.851

[5] K. Bethge and U. Schröder, "Elementarteilchen und ihre Wechselwirkungen," *WILEY-VCH Verlag GmbH & KGaA, Weinheim (Dritte, erweiterte und überarbeitete Auflage)*, 2006.

[6] B. Krusche and S. Schadmand, "Study of Non-Strange Baryon Resonances with Meson Photoproduction," *Progress in Particle and Nuclear Physics*, vol. 51, 2003. doi: 10.1016/S0146-6410(03)00096-6

[7] S. Schadmand, "Double Pion Photoproduction from Nuclei," *Acta Phys.Hung. A*, vol. 26, pp. 159–166, 2005.

[8] F. Zehr, "Double pion photoproduction off the proton at threshold and in second resoance region," *Phd thesis (Univerität Basel, Basel)*, 2010. doi: 10.5451/unibas-005204836

[9] B. Krusche, "Photoproduction of mesons off nuclei," *The European Physical Journal Sepcial Topics*, vol. 198, pp. 199–238, 2011. doi:

10.1140/epjst/e2011-01491-2

[10] D. J. Gross and F. Wilczek, "Ultraviolet behavior of non-abelian gauge theories," *Physik Review Letter*, vol. 30, pp. 1343–1346, 1973. doi: 10.1103/PhysRevLett.30.1343

[11] S. Bethke, "Experimental tests of asymptotic freedom," *Progress in Particle and Nuclear Physics*, vol. 58, pp. 351–386, 2007. doi: 10.1016/j.ppnp.2006.06.001

[12] M. Gell-Mann, "Symmetries of Baryons and Mesons," *Physical Review*, vol. 125, pp. 1067–1084, 1962. doi: 10.1103/PhysRev.125.1067.

[13] M. Gell-Mann, "A schematic model of baryons and mesons," *Physics Letters*, vol. 8, pp. 214–215, 1964. doi: 10.1016/S0031-9163(64)92001-3

[14] G. Zweig, "An SU(3) model for strong interaction symmetry and its breaking. Version 2." *in Developments in the quark theory of hadrons. vol. 1. 1964-1978, edited by D. B. Lichtenberg and S.P. Rosen*, pp. 22–101, 1964. [Online]. Available: http://inspirehep.net/record/4674/files/cern-th-412.pdf

[15] K. A. Olive, "Review of Particle Physics," *Chinese Physics C*, vol. 38, p. 090001, 2014. doi: 10.1088/1674-1137/38/9/090001

[16] O. Greenberg, "Spin and Unitary-Spin Independence in a Paraquark Model of Baryons and Mesons," *Physical Review Letters*, vol. 13, pp. 598–602, 1964. doi: 10.1103/PhysRevLett.13.598.

[17] M. Y. Han and Y. Nambu, "Three-Triplet Model with Double SU(3) Symmetry," *Physical Review*, vol. 139, pp. B1006–B1010, 1965. doi: 10.1103/phys-Rev.139.B1006

[18] R. P. Feymann, "Very high-Energy Collisions of Hadrons," *Physical Review Letters*, vol. 23, pp. 1415–1417, 1969. doi: 10.1103/PhysRevLett.23.1415

[19] J. Bjorken and E. Paschos, "Inelastic Electron-Proton and γ-Proton Scattering and the Structure of the Nucleon," *Physical Review*, vol. 185, pp. 1975–1982, 1969. doi: 10.1103/PhysRev.185.1975

[20] J. I. Friedmann, "Deep Inelastic Scattering: Comparisons With The Quark Model," *Nobel Lecture, Massachusetts Institute of Technology, Cambridge, Massachusetts, USA*, 1990.

[21] D. Gross and F. Wilczec, "Ultraviolet Behavior of Non-Abelian Gauge Theories," *Physical Review Letters*, vol. 30, pp. 1346–1349, 1973. doi: 10.1103/PhysRevLett.30.1343

[22] H. Politzer, "Reliable Perturbative Results for Strong Interactions," *Physical Review Letters*, vol. 30, pp. 1346–1349, 1973. doi: 10.1103/PhysRevLett.30.1346

[23] O. Greenberg, "Spin and Unitary-Spin Independence in a Paraquark Model of Baryons and Mesosn," *Physical Review Letters*, vol. 13, p. 598, 1964. doi: 10.1103/PhysRevLett.13.598

[24] R. Dalitz, *Proceedings of the x11 Int. Conf. on High Energy Physics Berkeley, Calif.*, 1966.

[25] D. Faimann and A. Hendry, "Harmonic-Oscillator Model for Baryons," *Physical Review*, vol. 173, pp. 1720–1729, 1968. doi: 10.1103/PhysRev.173.1720

[26] N. Isgur and G. Karl, "P-wave baryons in the quark model," *Physical Review D*, vol. 18, pp. 4187–4205, 1978. doi: 10.1103/PhysRevD.18.4187.

[27] B. U.Loering and H. Petry, "The light-baryon spectrum in a relativistic quark model with instanton-induced quark forces," *The European Physical Journal A*, vol. 10, pp. 395–446, 2001. doi: 10.1007/s100500170105

[28] R. Edwards *et al.*, "Excited state baryon spectroscopy from lattice QCD," *Physical Review D*, vol. 84, pp. 074 508–29, 2011. doi: 10.1103/PhysRevD.84.074508

[29] B. Krusche, "Hadronenstruktur mit elektromagnetischer Wechselwirkung," *Lecture*, 2016.

[30] R. H. Landau, "Quantum Mechanics 2, Second Edition," *WILEY-VCH Verlag*, 2004. doi: ISBN-13:978-0-471-11608-0

[31] J. Griffiths, "Introduction to Qunatum Mechanics," *Pearson Prentice Hall*.

[32] G. C. M. G. F. Low and Y. Nambu, "Application of Dispersion Relations to Low-Energy Meson-Nucleon Scattering," *Physical Review*, vol. 106, p. 1337, 1957. doi: 10.1103/PhysRev.106.1337

[33] W. Pauli, "Zur Qunatenmechanik des magnetischen Elektrons," *Zeitschrift für Physik*, vol. Bd. 43, 1927.

[34] P.-B. Otte, "Erste Messung der Pi0-Photoproduktion an transversal polarisierten Protonen Nahe der Schwelle," *PhD thesis (Johannes Gutenberg Universitaet Mainz, (MAINZ))*, 2015.

[35] R. Walker, "Phenomenological Analysis of Single-Pion Photoproduction," *Physical Review C*, vol. 182, p. 1729, 1969. doi: 10.1103/PhysRev.182.1729

[36] I. Barker, A. Donnachie, and J. Storrow, "Complete Experiments in Pseudoscalar Photoproduction," *Nuclear Physics B*, vol. 95, pp. 347–356, 1975. doi: 10.1016/0550-3213(75)90049-8

[37] A. Sandorfi *et al.*, "Calculations of Polarization Observables in Pseudoscalar Meson Photo-production Reactions," *arXiv.org*, 2009. [Online]. Available: http://arxiv.org/abs/0912.3505.

[38] W. Roberts and T. Oed, "Polarization observables for two-pion production off the nucleon," *Physical Review C*, vol. 71, p. 055201, 2005. doi: 10.1103/PhysRevC.71.055201

[39] W. Chiang and F. Tabakin, "Completeness Rules for Spin Observables in Pseudoscalar Meson Photoproduction," pp. 2054–2066, 1997.

[40] M. Oberle *et al.*, "Measurement of the beam-helicity asymmetry I^0 in the photoproduction of $p^0p^{+/-}$-pairs off protons and off neutrons," *The European Physical Journal A*, vol. 50, p. 54, 2014. doi: 10.1140/epja/i2014-14054-5

[41] A. Fix and H. Ahrenövel, "Double-pion photoproduction on nucleon and deuteron," *The European Physical Journal A*, vol. 25, pp. 115–135, 2005. doi: 10.1140/epja/i2005-10067-5

[42] V. Kashevarov, "Target and beam-target asymmetry for $\gamma p \to \pi^0\pi^0 p$," *current not published*, 2016.

[43] A. Braghieri *et al.*, "Total cross section measurement for the three double pion photoproduction channels on the proton," *Physics Letters B*, vol. 363, pp. 46–50, 1995. doi: 10.1016/0370-2693(95)01189-W

[44] J. Ahrens *et al.*, "Intermediate resonance excitation in the $\gamma p \rightarrow p\pi^0\pi^0$ reaction," *Physics Letters B*, vol. 624, pp. 173–180, 2005. doi: 10.1016/j.physletb.2005.08.034

[45] F. Härter *et al.*, "Two neutral pion photoproduction off the proton between threshold and 800 MeV," *Physics Letters B*, vol. 401, pp. 229–233, 1997. doi: 10.1016/S0370-2693(97)00423-1

[46] A. V. Sarantsev *et al.*, "New results on the Roper resonance and the $P11$ partial wave," *Physics Letters B*, vol. 659, pp. 94–100, 2008. doi: 10.1016/j.physletb.2007.11.055

[47] M. Kotulla *et al.*, "Double π^0 photoproduction off the proton at threshold," *Physics Letters B*, vol. 578, pp. 63–68, 2004. doi: 10.1016/j.physletb.2003.10.056

[48] V. Kashevarov *et al.*, "Experimental study of the $\gamma p \rightarrow \pi^0\pi^0 p$ reaction with the Crystal Ball/TAOS detector system at the Mainz Microtron," *Physical Review C*, vol. 85, pp. 064 610–11, 2012. doi: 10.1103/PhysRevC.85.064610

[49] Y. Assafiri *et al.*, "Double π^0 Photoproduction on the Proton at GRAAL," *Physical Review Letters*, vol. 90, 2003. doi: 10.1103/PhysRevLett.90.222001

[50] A. Thiel *et al.*, "Three-Body Nature of N^* and Δ^* Resonances from Sequential Decay Chains," *Physical Review Letters*, vol. 114, pp. 091 803–5, 2015.

[51] V. Sokhoyan *et al.*, "Data on I^s and I^c in $\gamma p \rightarrow p\pi^0\pi^0$ reveal cascade decays of $N(1900)$ via $N(1520)\pi$," *Physics Letters B*, vol. 746, pp. 127–131, 2015. doi: 10.1016/j.physletb.2015.04.063

[52] V. Kashevarov *et al.*, "Experimental study of the $\gamma p \rightarrow \pi^0\pi^0 p$ reaction with the Crystall Ball/TAPS detector system at the Mainz Mictrotron," *Physical Review C*, vol. 85, pp. 064 610–11, 2012. doi: 10.1103/PhysRevC.85.064610

[53] A. Sarantsev *et al.*, "New results on the Roper resonance and the P_{11} partial wave," *Physical Letters B*, vol. 659, pp. 94–100, 2008. doi: 10.1016/j.physletb.2007.11.055

[54] Nachher *et al.*, "The role of $\Delta(1700)$ excitation and ρ production in double pion photoproduction," *Nuclear Physics A*, vol. 695, pp. 295–327, 2001. doi: 10.1016/S0375-9474(01)01110-1

[55] F. Zehr *et al.*, "Photoproduction of $\pi^0\pi^0$ and $\pi^0\pi^+$ -pairs off the proton from threshold to the second resonance region," *European Physical Journal A*, vol. 48, pp. 98–19, 2012. doi: 10.1140/epja/i2012-12098-1

[56] F. Zehr *et al.*, "Photoproduction of $\pi^0\pi^0$- and $\pi^0\pi^+$-pairs off the proton from threshold of the second resonance region," *The European Physical Journal A*, vol. 98, 2012. doi: 10.1140/epja/i2012-12098-1

[57] L. Roca, E. Oset, and M. V. Vacas, "The σ meson in a nuclear medium through two pion photoproduction," *Physical Letters B*, vol. 541, pp. 77–86, 2002. doi: 10.1016/S0370-2693(02)02188-3

[58] E. Gutz *et al.*, "High statistics study of the reaction $\gamma p \to p\pi^0\eta$," *The European Physical Journal A*, vol. 50, p. 74, 2014. doi: 10.1140/epja/i2014-14074-1

[59] A. Jankowiak, "The Mainz microtron MAMI - Past and future," *The European Physical Journal*, vol. 28, 2006. doi: 10.1140/epja/i2006-09-016-3

[60] K. Aulenbacher *et al.*, "The MAMI source of polarized electrons," *Nuclear Instruments and Methods in Physic Research Section A: Accelerators, Spectrometers, Detectors and Associated Equipment*, vol. 391, pp. 498–506, 1997. doi: 10.1016/S01689002(97)00528-7

[61] K. Aulenbacher, "Polarized beams for electron accelerators," *The European Physical Journal Special Topics*, vol. 198, pp. 361–380, 2011. doi: 10.1140/epjst/e2011-01499-6

[62] M. Dehn *et al.*, "The MAMI accelerator: The beauty of normal conduction multi-turn reciculators," *The European Physical Journal Special Topics*, vol. 198, pp. 19–47, 2011. doi: 10.1140/epjst/e2011-01481-4

[63] A. Thomas, C. Collaboration, and A. Collaboration, "Recent result from the A2 real photon facility at MAMI," *Chinese Physics C*, vol. 33, no. 12, p. 1120, 2009. [Online]. Available: http://stacks.iop.org/1674-1137/33/i=12/a=012

[64] Olsen, Haakon, and L. Maximom, "Photon and Electron Polarization in High-Energy Bremsstrahlung and Pair Production with Screening," *Physical Review*, vol. 114, pp. 887–904, 1959. doi: 10.1103/PhysRev.114.887. [Online]. Available: http://link.aps.org/doi/10.1103/PhysRev.114.887

[65] J. McGeorge *et al.*, "Upgrade of the Glasgow photon tagging spectrometer for Mainz MAMI-C," *The European Physical Journal A*, vol. 37, pp. 129–137, 2008. doi: 10.1140/epja/i2007-10606-0

[66] C. A2, "Mainz Microtron MAMI," *Proposal for an Experiment, Photoproduction of Pions off Polarized Neutrons*, 2009.

[67] A. Thomas, "Crystal Ball Hydrogen (Butanol) Target manuel," 2013.

[68] A. Thomas, "Review on the last developments on polarized targets at Mainz," *Annual Meeting of the GDR PH-QCD*, pp. 1–40, 2013. [Online]. Available: https://indico.in2p3.fr/event/9046/session/3/contribution/27/material/0/0.pdf

[69] A. Starostin *et al.*, "Measurement of $K^- \to p\eta\Lambda$ near threshold," *Physical Review C*, vol. 64, p. 055205, Oct 2001. doi: 10.1103/PhysRevC.64.055205. [Online]. Available: http://link.aps.org/doi/10.1103/PhysRevC.64.055205

[70] D. Watts, "The Crystal Ball and the TAPS Detectors at the MAMI Electron Beam Facility, in Calorimetry in particle physics," *the eleventh international conference*, pp. 116–123, 2005. doi: 10.1142/9789812701978_0015

[71] R. Novotny, "The electromagnetic calorimeter TAPS, in Calorimetry in high-energy physics.proceedings," *6th international conference*, pp. 683–692, 1996.

[72] A. R. Gabler *et al.*, "Response of TAPS to monochromatic photons with energies between 45 and 790 MeV," *Nuclear Instruments and Methods*, vol. 346, pp. 168–176, 1994. [Online]. Available: 10.1016/0168-9002(94)90701-3

[73] A. Mushkarenkov and P. Pedroni, "Multi-wire proportional chamber status," *CB meeting at Bosen*, 2011. [Online]. Available: https://wwwa2.kph.uni-mainz.de/intern/daqwiki/_media/experiment/detectors/mushkarenkov_bosen-2011.pdf

[74] A. Mushkarenkov, "Multi-wire proportional chamber," *CB meeting*. [Online]. Available: https://wwwa2.kph.uni-mainz.de/intern/daqwiki/_media/experiment/detectors/mwpc.pdf

[75] M. Dieterle *et al.*, "Photoproduction of π^0-pairs off protons and off neutrons," *The European Physical Journal A.*, vol. 52, p. 187, 2015. doi: 10.1140/epja/i2015-15142-8

[76] E. Bloom and C. Peck, "Physics with the Crystal Ball Detector," *Annual Review Nuclear Science*, vol. 33, p. 143, 1983. doi: 10.1146/annurev.ns.33.120183.001043

[77] B. Krusche, F. Pheron, and Y. Magrbhi, "Photoproduction of Mesons off Light Nuclei - the Search for η-Mesic Nuclei," *Acta Phys.Polon.B4*, pp. 2249–2260, 2010.

[78] D. Werthmueller, "Experimental study of nucleon resonance contribution to η-photoproduction on the neutron," *PhD thesis (Universität Basel), Basel*, 2014. doi: 10.5451/unibas-006230854

[79] P. Drexler *et al.*, "The new read-out electronics for the BaF2-colorimeter TAPS," vol. Vol. 1, IEEE, Nov. 2002. doi: 10.1109/NSSMIC.2002.1239381

[80] A. C. Website, "Institut für Kernphysik, Mainz, Germany," [Wednesday, 25-May-2011 19:00:00 EDT]. [Online]. Available: http://wwwa2.kph.uni-mainz.de/cb/pic_setup/cb4_k.jpg

[81] N. Mott, "The scattering of fast electrons by atomic nuclei," *Proceedings of the Royal Society A (London)*, vol. 124, 4 June 1929. doi: 10.1098/rspa.1929.0127

[82] M. Gowin, "Optimierung der laserinduzierten Photoemission zur Erzeugung polarisierter Elektronenstrahlen an der 50 keV-Quelle der Bonner Beschleunigeranlage ELSA," *PhD thesis (Rheinische Friedrich-Wilhelm-Universität Bonn, Bonn)*, 2001.

[83] J. Kessler, "Polarized Electrons," *Springer Series, 2 Aufl.*, 1985.

[84] W. Hillert, "Erzeugung eines Nutzstrahls spinpolarisierter Elektronen an der Beschleunigungsanlage ELSA," *PhD thesis (Rheinische Friedrich-Wilhelm-Universität Bonn, Bonn)*, 2000.

[85] L. Akosoy, "Polimetrie," *Lecture SS06 (Mainz)*. [Online]. Available: http://wwwa1.kph.uni-mainz.de/Vorlesungen/SS06/FP-Seminar/akasoy_polarimetrie.pdf

[86] C. Rohlof, "Entwicklung polarisierter Targets zur Messung der Gerasimov-Drell-Hearn-Summenregel an ELSA," *PhD thesis (Rheinische Friedrich-Wilhelm-Universität Bonn, Bonn)*, 2003.

[87] P. Klaer, "Polarisierte Targets," *Vortrag FP-Seminar SS06, Uni Mainz*, 2006. [Online]. Available: http://wwwa1.kph.uni-mainz.de/Vorlesungen/SS06/FP-Seminar/klaer_poltargets.pdf

[88] J. Bernhard, "Polarisierte Targets," *Vortrag im Rahmen des Seminars im Praktikum fuer Fortgeschrittene, Universiät Mainz*, 2005.

[89] R. Brun and F. Rademakers, "ROOT - An Object Oriented Data Analysis Framework," *Nuclear Instruments and Methods A*, vol. 389, 1997. doi: 10.1016/S0168-9002(97)00048-X

[90] J. R. M. Annand, "Data Analysis within an AcquRoot Framework," 2008. [Online]. Available: http://www.nuclear.gla.ac.uk/~acqusys/doc/AcquRoot.11.08.pdf

[91] I. Froehlich *et al.*, "Pluto: A Monte Carlo Simulation Tool for Hadronic Physics," *in Proceedings, 11th international workshop on advanced computing and analysing techniques in physics research acat*, 2007. [Online]. Available: http://axiv.org/abs/0708.2382v2

[92] L. Zana, D. Watts, and D. Glazier, "A2 Geant4 Simulation." [Online]. Available: http://ww2.ph.ed.ac.uk/nuclear/G4

[93] S. Agostinelli *et al.*, "GEANT4: A Simulation toolkit," *Nuclear Instruments and Methods A*, vol. 506, pp. 250–303, 2003. doi: 10.1016/S0168-9002(03)01368-8

[94] J. Allison *et al.*, "Geant4 developments and applications," *IEEE Transactions on Nuclear Science*, vol. 53, p. 270, 2006. doi: 10.1109/TNS.2006.869826

[95] D. Glazier, "A GEANT4 Simulation of the CrystalBall@MAMI," *CB Meeting 17 (University of Edinburgh)*, 2011. [Online]. Available: https://wwwa2.kph.uni-mainz.de/download/data_old_web/intern/cb17meeting/Glazier_CB_March2011.pdf

[96] Nighley, "jraph," *github.com*, 2016. [Online]. Available: http://github.com/nighley/jraph

[97] M. Unverzagt, "Energie-Eichung des Crystal-Barrel/TAPS-Experiments am MAMI," *Diploma thesis (Johannes Gutenberg-Universität Mainz, Mainz)*, 2004.

[98] V. Hejny, "Photoproduktion von eta-Mesonen an Helium 4," *PhD thesis (Justus-Liebig-Universität Giessen, Giesen)*, Oct. 1998.

[99] K. Molenaar, "Performance of TAPS in the Tagged Photon Beam of MAMI," *Diploma thesis (Rijksuniversiteit Groningen), Groningen*, 1992.

[100] M. Pfeiffer, "Photoproduction of η mesons from ^3He," *PhD thesis (Universität Giessen, Giessen)*, 2002.

[101] M. Unverzagt, "Bestimmung des Dalitz-Plot-Parameters α für den Zerfall $\eta \to 3\pi^0$ mit dem Crystal Ball am MAMI," *PhD thesis (Rheinischen Friedrich-Wilhelms-Universität Bonn, Bonn)*, 2008.

[102] U. S. K. Bethge, "Elementarteilchen und ihre Wechselwirkung," *WILEY-VCH Verlag GmbH & Co. KGaA, Weinheim*, 2006.

[103] M. Rörig, "Eichung des TAPS-Detektorsystems mit Höhenstrahlung," *Diploma thesis (Universität Giessen, Giessen)*, 1991.

[104] T.Jude, "Strangeness Photoproduction off the Proton at Threshold Energies," *PhD thesis (University of Edingburgh, Edingburgh)*, 2010.

[105] S. Brandt, "Datenanalyse," *Spektrum Akademischer Verlag*, vol. 4th ed., 1999.

[106] L. Witthauer *et al.*, "Quasi-free photoproduction of η-mesons off $3He$ nuclei," *The European Physical Journal A*, vol. 49, p. 154, 2013. doi: 10.1140/epja/i2013-13154-0

[107] L. Witthauer, "Measurement of the Cross Sections and Polarisation Observables in eta Photoproduction from Neutrons and Protons Bound in Light Nuclei," *PhD thesis (Universitaet Basel, Basel)*, 2015.

[108] S. Schumann, "Strahlungsbegleitete π^0-Photoproduktion am Proton," *PhD thesis (Rheinische Friedrich-Wilhelms-Universität Bonn, Bonn)*, 2007.

[109] M. Unverzagt, "Bestimmung des Dalitz-Plot Parameters α fuer den Zerfall $\eta \to 3\pi^0$ mit dem Crystal Ball am MAMI," *PhD thesis (Rheinische Friedrich-Wilhelm-Universität Bonn, Bonn)*, 2008.

[110] M. Dieterle, "Measurement of Polarization Observables in π^0 and $\pi^0\pi^0$ Photoproduction from Protons and Neutrons at MAMI and ELSA," *PhD thesis (Universität Basel, Basel)*, 2015.

[111] A. V. Anisovich, R. Beck, E. Klempt, V. A. Nikonov, A. V. Sarantsev, and U. Thoma, "Pion- and photo-induced transition amplitudes to ΛK, ΣK, and Nη," 2012.

[112] V. Sokhoyan *et al.*, "High statistics study of the reaction $\gamma p \to p2\pi^0$," *The European Physical Journal A*, vol. 51, p. 28, 2015. doi: 10.1140/epja/i2015-15187-7

[113] V. Kashevarov, *private Communication*.

[114] A. Sandorfi *et al.*, "Determining pseudoscalar meson photoproduction amplitudes from complete experiments," *Journal of Physics G: Nuclear and Particle Physics*, vol. 38, p. 053001, 2011. doi: 10.1088/0954-3899/38/5/053001